Model-Based Optimization of Combustion-Engine Control

Turesson, Gabriel

2018

Document Version:
Publisher's PDF, also known as Version of record

Link to publication

Citation for published version (APA):
Turesson, G. (2018). *Model-Based Optimization of Combustion-Engine Control*. [Doctoral Thesis (monograph), Department of Automatic Control]. Department of Automatic Control, Lund Institute of Technology, Lund University.

Total number of authors:
1

Model-Based Optimization of Combustion-Engine Control

Gabriel Turesson

LUND UNIVERSITY

Department of Automatic Control

The cover illustration shows heat-release data from a closed-loop experiment.

PhD Thesis TFRT-1120
ISBN 978-91-7753-705-2 (print)
ISBN 978-91-7753-706-9 (web)
ISSN 0280–5316

Department of Automatic Control
Lund University
Box 118
SE-221 00 LUND
Sweden

Printed in Sweden by Media-Tryck.
Lund 2018

Till Desire

Abstract

The work presented in this thesis is motivated by the need to reliably operate a compression-ignition engine in a partially premixed combustion (PPC) mode. Partially premixed combustion is a low temperature combustion concept, where the ignition delay is prolonged to enhance fuel-air mixing in the combustion chamber before the start of combustion. A premixed combustion process, in combination with high levels of exhaust-gas recirculation (EGR), gives low combustion temperatures, which decrease NO_x and soot formation. Lowered combustion temperatures also reduce heat-transfer losses which increase the thermodynamic engine efficiency. The ignition delay is, however, determined by chemical reactions rates, which are sensitive to temperature, gas-mixture composition, fuel properties and fuel-injection timing. This sensitivity makes PPC more challenging to operate compared to conventional diesel combustion. Challenges related to PPC include an increased sensitivity to operating conditions, decreased combustion-timing controllability, high pressure-rise rates, and low combustion efficiency at low engine loads. These challenges put high demands on the engine control system that needs to be able to adjust fuel-injection timings and durations to compensate for the combustion sensitivity.

Therefore, this thesis investigates closed-loop combustion control for reliable PPC operation. The feedback loop from pressure-sensor measurement to fuel-injection actuation is studied in particular. A common theme for the controllers presented is the use of models in the controller design. Either to evaluate controller performance in simulation, or to optimize engine performance online. The principle of model predictive control is used for its ability to incorporate modeled system behavior in the controller design, and to control multi-variable systems with input and output constraints.

The problem of tuning robust and noise insensitive combustion-timing controllers, and its dependence on fuel reactivity is studied in simulation. Simulation results reveal a nonlinear relation between start of injection and combustion timing that depends on both load and fuel reactivity. Optimization is used to find robust and noise-insensitive controller gains. Guidelines for combustion-timing controller tuning are also presented.

Low-order autoignition models are evaluated and compared for the purpose of model-based controller design. The comparison shows that a simple autoignition model is sufficient for control of the ignition delay when the cylinder-charge properties are varied. This model is then used by a model predictive controller to simultaneously control ignition delay and combustion timing in transient engine operation, using both gas-exchange and fuel-injection actuation.

The effects of pilot injection on the combustion processes are characterized experimentally. Experimental results show that a pilot injection can decrease the main-injection ignition delay and maintain the pressure-rise rate at an acceptable level. This is utilized by a presented fuel-injection controller that manages to control both combustion timing and pressure-rise rate.

Strategies for improving the low-load performance of PPC are studied experimentally, where results show that the selection of injection timings and the use of a pilot injection are important when maximizing the combustion efficiency. The suggested low-load controller demonstrated a 9 % efficiency increase during transient engine operation.

This thesis also investigates the design of a controller that utilizes the degrees of freedom enabled by multiple injections to efficiently fulfill constraints on cylinder pressure, NO_x emissions and exhaust temperature. A simulation study shows a potential 2 - 4 % indicated efficiency increase when two injections are used instead of one. These findings motivated the design of a hybrid multiple-injection controller that changes the number of injections depending on operating conditions. The controller designed was capable of reproducing the found efficiency increase experimentally with respect to constraints on pressure and NO_x emissions.

A model-predictive pressure controller is also introduced. The controller predicts how the cylinder pressure varies with fuel injection by taking advantage of the estimated heat-release rate and a cylinder-pressure model. This feature was used to adjust fuel-injection timings, durations, and number of injections, for efficient constraint fulfillment in transient engine operation. Experimental results demonstrate that the pressure controller can also be used for tracking of cycle-resolved in-cylinder pressure trajectories, as well as finding the most efficient combustion timing.

Heat-release analysis is an essential component in the pressure-sensor feedback loop. Methods for calibrating heat-release model parameters with the use of engine data, and methods for detecting combustion timings are therefore discussed in the thesis.

The experimental results presented were conducted on a heavy-duty Scania D13 engine with a modified gas-exchange system. The fuel used was a mixture (by volume) of 80 % gasoline and 20 % n-heptane, to elevate the fuel octane number and allow for longer ignition delays.

Acknowledgments

I would like to thank my supervisor, Rolf Johansson, for his consistent support and advice, for sharing his knowledge of scientific work, and for setting high standards in the project. My co-supervisor Per Tunestål has been very helpful with discussions and suggestions on theoretical and practical matters related both to combustion engines and control. Bo Bernhardsson gave interesting courses in control and optimization that contributed to the project.

The experimental work was done in collaboration with my colleague, Lianhao Yin. His knowledge about, and experience with laboratory work and programming made it possible for us to quickly build the test rig and conduct the experiments presented in the thesis. The technicians at the Division of Combustion Engines were very helpful in keeping the engine running and re-building the experimental platform when necessary. I am also grateful to Ola Stenlåås for taking a great interest in our project and for giving constructive feedback on our progress. I wish to express my gratitude to the colleagues who took their time and helped me with the proofreading of this thesis.

I also extend my acknowledgments to colleagues at the Department of Automatic Control and the Department of Energy Sciences for interesting discussions on research and related subjects, and to the technical and administrative staff at the departments for assistance on various subjects related to my research. Special thanks goes to Leif Andersson for his support in the finalization of this thesis.

Finally, I would like to thank my wife Desire, my family, and my friends for their encouragement and support.

Financial Support

The author would like to acknowledge the Competence Center for Combustion Processes (KCFP) and the Swedish Energy Agency for the financial support (project number 22485-3), Scania for supplying the experimental engine, and the KFCP PPC Control reference group for consistent feedback on the work. The author is also a member of the LCCC Linnaeus Center and the ELLIIT Excellence Center at Lund University.

Contents

Nomenclature

Symbol Descriptions

The table below summarizes the most frequently used notation in the thesis.

Notation	Description
A	Cylinder area
B	Cylinder bore
C_1 & C_2	Heat-transfer coefficients
c_p	Specific heat at constant pressure
c_v	Specific heat at constant volume
γ	Ratio of specific heats
dp_{max}	Maximum cylinder pressure derivative
E_a	Activation energy
η_{GIE}	Gross indicated efficiency
η_{NIE}	Net indicated efficiency
η_{th}	Thermodynamic efficiency
λ	Relative air/fuel ratio
ϕ	Fuel/air equivalence ratio
$\dot{m}_{\mathrm{air}}$	Air mass flow
$\dot{m}_{\mathrm{EGR}}$	EGR mass flow
$\dot{m}_f$	Fuel mass flow
m_f	Fuel mass
NO_x	Oxides of nitrogen
N_{speed}	Engine speed
p	In-cylinder pressure
p_{ex}	Exhaust-manifold pressure
p_{in}	Intake-manifold pressure
p_{IMEPg}	Gross indicated mean effective pressure
p_{IMEPn}	Net indicated mean effective pressure

p_{PMEP}	Indicated pumping losses
$p_{\max}$	Maximum cylinder pressure
p_{rail}	Common-rail pressure
$dQ_c/d\theta$	Heat-release rate
$dQ_{ht}/d\theta$	Heat-transfer rate
Q_{LHV}	Lower heating value
R^2	Coefficient of determination
$\tilde{R}$	Universal gas constant
R	Specific gas constant
r_c	Compression ratio
r_{EGR}	EGR ratio
r_p	Pilot ratio
S_p	Mean piston speed
T	In-cylinder temperature
T_c	Coolant temperature
T_{EVO}	Temperature at exhaust-valve opening
T_{IVC}	Temperature at intake-valve closing
T_{ex}	Exhaust-manifold temperature
T_{in}	Intake-manifold temperature
T_{res}	Residual-gas temperature
T_w	Wall-surface temperature
θ	Crank angle
θ_{CT}	Combustion timing
θ_{DOI}	Fuel-injection duration
θ_{EOC}	End of combustion
θ_{SOC}	Start of combustion
θ_{SOI}	Fuel-injection timing
$\Delta\theta_{\mathrm{TDC}}$	TDC offset
θ_x	Crank-angle of x % burnt
θ_{HP}	High-pressure EGR valve
θ_{LP}	Low-pressure EGR valve
θ_{cool}	Cool-path FTM valve
θ_{hot}	Hot-path FTM valve
τ	Ignition delay
u	System input
V_d	Displacement volume
V	Cylinder volume
x	System state
x^c	Constraint for x
x^r	Set point for x
$[x]$	Concentration of species x
y	System output
ω	Mean gas velocity

Abbreviation	**Description**
0D	Zero dimensional
BC	Boundary condition
CAD	Crank angle degree
CDC	Conventional diesel combustion
CFD	Computational fluid dynamics
DOI	Duration of injection
EGR	Exhaust gas recirculation
EVO	Exhaust valve opening
EKF	Extended Kalman filter
FTM	Fast thermal management
HC	Hydrocarbon
HCCI	Homogeneous charge compression ignition
IAE	Integrated absolute error
ICE	Internal combustion engine
IMEP	Indicated mean effective pressure
IVC	Inlet valve closing
KF	Kalman filter
LTC	Low temperature combustion
MPC	Model predictive control
MVM	Mean value model
NTC	Negative temperature coefficient
ON	Octane number
PF	Particle filter
PI	Proportional integral
PPC	Partially premixed combustion
PM	Particulate matter
PRF	Primary reference fuel
rpm	Revolutions per minute
RMSE	Root mean square error
SOC	Start of combustion
SOI	Start of injection
TDC	Top-dead-center
QP	Quadratic program
VI	Virtual instrument

1

Introduction

Combustion-engine technology has made tremendous advances during the last decades due to increasingly stringent demands for a reduction in both emission levels and fuel consumption. These demands have necessitated an increase in the number of engine sensors and actuators [Isermann, 2014]. At the same time, there has been an exponential growth in electronics, and the availability of computational power has increased [Leen and Heffernan, 2002; Broy et al., 2007]. These trends have opened up new possibilities for more intelligent engine-control systems, capable of monitoring the combustion process, and in real time, optimize actuator adjustments for clean and efficient combustion. Such control systems could be used to enable sensitive low-emission combustion concepts. Partially premixed combustion is a combustion concept that has previously been shown to provide high efficiency and low emissions simultaneously. Its sensitivity to chemical reaction rates has, however, made it challenging to operate. This thesis presents work on how to operate a compression-ignition engine in a partially-premixed combustion mode, with model-based control and pressure-sensor feedback. This thesis also investigates how feedback control can be used to optimize fuel injection for efficient fulfillment of constraints on cylinder pressure, NO_x emissions and exhaust temperature. Such methods could also be used to improve performance of conventional combustion concepts. The controllers and methods presented were evaluated experimentally using a modified heavy-duty engine, which was run on a high octane-number fuel to prolong ignition delays and enhance premixing of fuel and air.

This chapter provides background and motivation for the work presented in this thesis together with a description of the research contributions made.

1.1 Combustion-Engine Challenges

The internal combustion engine has revolutionized transportation since the 19th century. Today, the world's vehicle population consists of more than one billion cars, with a yearly production of 95 million, of which the vast majority is propulsed by a combustion engine [Sperling and Gordon, 2009; OICA, 2017]. The reason for its persistent popularity is a combination of simplicity, durability, low power-to-weight ratio, high power controllability and reasonable efficiency [Heywood, 1988]. Engine research and development are mainly focused on legislation-enforced emission reduction and the aim to reduce fuel consumption. This is due to toxic local emissions [Haagen-Smit, 1952; Sher, 1998], and the fact that the transportation sector contributes to 23 % of global green-house gas emissions [IPCC, 2014]. The European NO_x and soot-particle emission limits for heavy-duty engines during the past 20 years are presented in Fig. 1.1. Emissions of CO, unburned hydrocarbons (HC) and particle number count are also regulated. Forthcoming legislation is expected to include standards for greenhouse-gas emission levels as the European Union targets a 60 % greenhouse-gas emission reduction in the transportation sector by 2050, compared to the levels of 1990 [EC, 2016]. Battery-electric and fuel-cell vehicles are possible zero-emission alternatives to the internal combustion engine [Contestabile et al., 2011]. However, considering the large number of combustion engines on our roads today, mass production will probably continue for several years, especially in the heavy-duty sector [McKinsey, 2014; Askin et al., 2015]. In this scenario, technological combustion-engine advances in combination with hybridization and the usage of biofuels could constitute a cost-effective path towards reduced local and global emissions [Enkvist et al., 2007; Johansson et al., 2013].

Engine-technology advances for cleaner combustion includes high-pressure fuel-injection, exhaust-gas recirculation (EGR), and compression and cooling of inducted air [Majewski et al., 2006]. Exhaust filters and catalysts are also necessary for fulfillment of current legislation. The resulting engine complexity has led to an increase in the number of sensors and actuators which has promoted the development of more advanced engine-control systems. Focus has also been directed towards the development of new, clean and efficient combustion concepts. A number of such concepts utilize low temperature combustion, with low emission formation and heat-transfer rates, achieved through increased mixing of fuel and air in the combustion chamber. The following sections give a brief overview of fundamental engine principles and compare conventional diesel combustion with low temperature combustion.

1.2 Fundamental Engine Principles

The reciprocating internal combustion engine is a heat engine where combustion of fuel and air occurs inside a cylinder. The combustion fluids perform expansion work on a piston whose linear movement is converted to rotation of a crankshaft. The basic geometry of an engine cylinder is shown in Figure 1.2. The work presented in this thesis concerns the four stroke compression-ignition engine. The four-stroke cycle starts with air induction through the intake valves

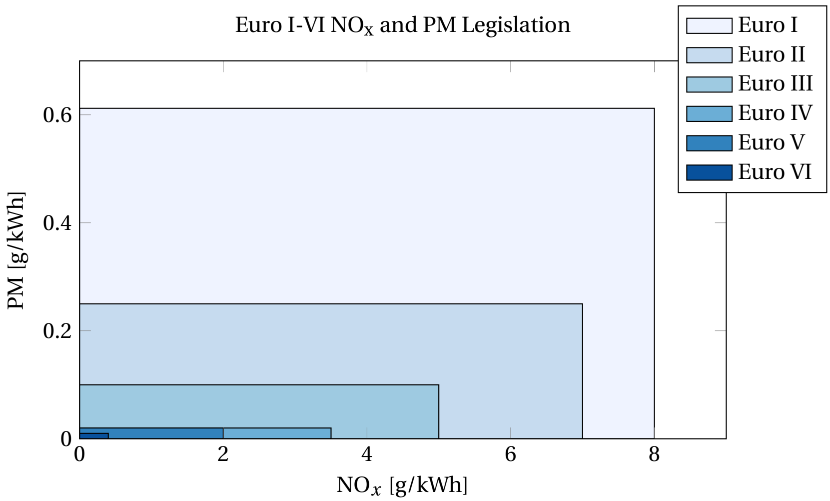

Figure 1.1 Legislated emission levels for heavy-duty vehicles in the European Union (Euro I-VI) during the past 20 years [EU, 2007]. The emission goals have been met by gradual improvements of emission control techniques and improved fuel quality. Improvements from Euro IV were done with the help of exhaust-gas after treatment.

due to downward motion of the piston. The air is then compressed during the compression stoke and fuel is injected as the piston approaches top-dead-center (TDC). At this point, the temperature is sufficiently high for autoignition to occur. Combustion leads to a pressure increase that generates work during the expansion stroke. Combustion products are then scavenged as the piston moves upward with the exhaust-valves open during the exhaust stroke. The four strokes and corresponding cylinder pressure and volume curves are presented in Figs. 1.3 and 1.4. The cylinder pressure was obtained from the engine used in the experimental work presented in the thesis, whereas the volume was computed from the cylinder geometry. Fuel injection is indicated by the injector-current pulse located before TDC.

Conventional Diesel Combustion

The following description of conventional diesel combustion (CDC) is based on the conceptual model presented by Dec [1997].

Conventional diesel combustion is initiated by high-pressure fuel injection into a compressed, hot (~1000 K) air charge, close to TDC. The injected fuel propagates into the combustion chamber and forms a conical jet of fuel droplets. The fuel jet becomes increasingly diluted with hot air and vaporizes as it expands. After a certain traveling distance along the jet axis (~20-25 mm), called

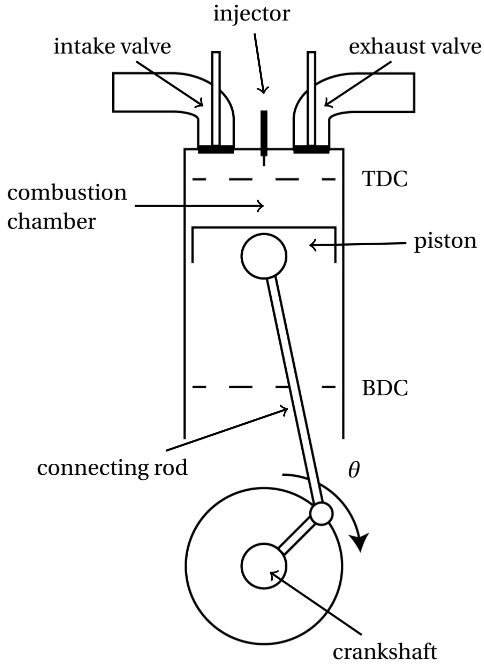

Figure 1.2 The basic geometry of an engine cylinder. Combustion of fuel and air in the combustion chamber leads to a pressure increase that generates linear piston motion. The linear motion is converted to rotational motion of the crankshaft. Flow of fuel and air are governed by poppet valves, a fuel injector and the motion of the piston. The acronyms TDC and BDC stand for top-dead-center and bottom-dead-center, indicating the top and bottom positions of the piston. Crank-angle degree is denoted θ.

the lift-off length, the fuel has vaporized completely. Chemical reactions are initiated all over the jet cross section after further air entrainment. Initial reactions are followed by rapid, rich, premixed combustion and the resulting temperature increase leads to formation of soot due to an excess of fuel. Air entrainment continues as the reacting fuel travels along the spray axis and a quasi-steady diffusion flame is formed along the jet periphery when stoichiometric conditions are reached. At this stage, the combustion rate is controlled by how fast the injected fuel is vaporized, mixed with air and supplied to the diffusion flame. This type of combustion is therefore referred to as mixing controlled. Temperature reaches its maximum in the vicinity of the flame which causes nitrogen to oxidize and form harmful NO_x emissions. High temperature in combination with availability of oxygen also result in soot oxidation which gives the characteristic diesel-flame luminosity. Furthermore, these conditions lead to almost complete oxidation of

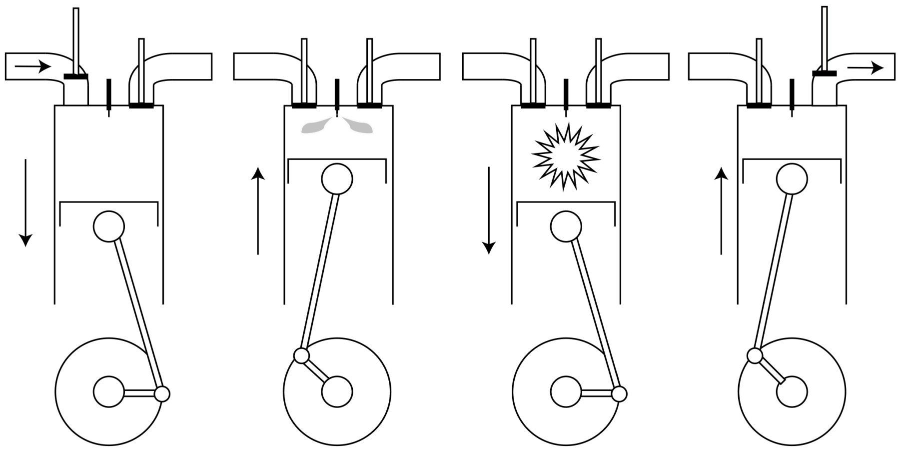

Figure 1.3 The principle of a four-stroke compression-ignition engine. Air is first inducted from the intake manifold during the intake stroke. The air is then compressed during the compression stoke and fuel is injected as the piston approaches TDC, when the cylinder temperature is sufficiently high for autoignition to occur. The fuel autoignites shortly after TDC and the resulting pressure increase generates work during the expansion stroke. The combustion products are then scavenged during the exhaust stroke, as the piston moves upward with the exhaust valves open.

CO and HC during the expansion stroke. This conceptual description of CDC is illustrated in Fig. 1.5, where two jet intersections are presented.

The left diagram in Fig. 1.5 shows a fuel jet 5 crank-angle degrees (CAD) after injection, where the liquid fuel has started to vaporize. Initial rich premixed combustion is indicated in purple. The diagram to the right shows the same jet 1.5 CAD later. A hot diffusion-flame front (green) has been established and surrounds a region of soot formation due to rich and hot conditions.

The temperature T, and the ratio of the actual fuel/air ratio to the stoichiometric fuel/air ratio ϕ have significant effect on soot formation and oxidation. Temperature also affects formation of NO_x. Emission characteristics can therefore be studied in a $\phi - T$ diagram, where emission-formation level curves are presented as a function of ϕ and T. Such diagrams have been generated from experimental data, and by simulating soot and NO_x concentrations at fixed ϕ and T for a given residence time [Aoyagi et al., 1980; Kamimoto and Bae, 1988; Kitamura et al., 2002; Kook et al., 2005]. A $\phi - T$ diagram for combustion of n-heptane, a fuel with similar properties to diesel, is presented in Fig. 1.6.

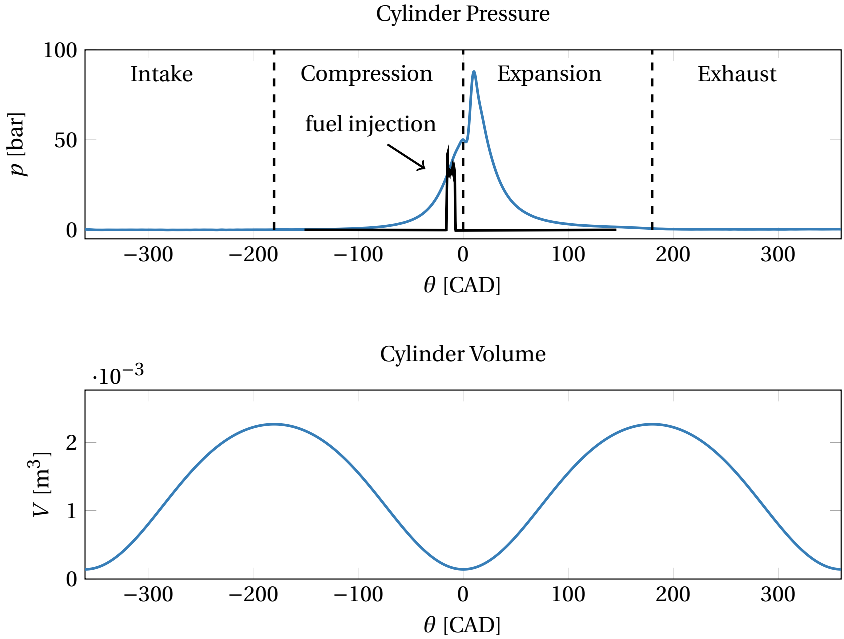

Figure 1.4 Cylinder pressure and volume during the engine cycle. The cylinder pressure was measured from the engine used for the experimental work presented in this thesis, whereas the volume was computed from the cylinder geometry. Fuel injection is indicated by the injector current pulse located before TDC.

The journey of a fuel particle along the diesel-jet axis is indicated by the orange trajectory in this diagram. The fuel/air mixture starts rich (high ϕ) with fairly low temperature after vaporization (1). Premixed rich combustion is then initiated as the fuel mixes with air ($\phi \sim 2-4$). Temperature increases steeply and the rich, high-T, soot-formation region is reached (2). The fuel becomes increasingly diluted and the temperature peaks at the diffusion flame boundary at close to stoichiometric conditions (3). The lean, high-T region is favorable for thermal NO_x formation and the availability of oxygen promotes soot oxidation as the burned mixture cools down during the expansion stroke (4). The intersection of the NO_x-formation zone with the soot-oxidation zone leads to a fundamental diesel-combustion trade-off between NO_x and soot emissions. If NO_x formation is to be avoided, soot oxidation will simultaneously decrease with higher soot-emission levels as a result.

It should be noted, however, that this conceptual model only gives a qualitative understanding of diesel-combustion characteristics. In reality, there is a distribution of ϕ and T around the trajectory in Fig. 1.6, [Kitamura et al., 2002].

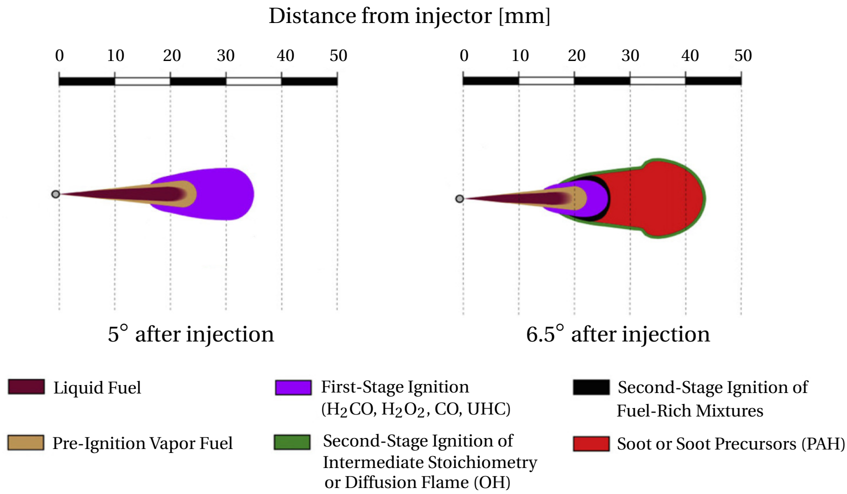

Figure 1.5 Conceptual model of conventional diesel combustion. The left diagram shows a fuel jet 5 crank-angle degrees (CAD) after injection, where liquid fuel has vaporized and mixed with air. Initial premixed combustion is indicated in purple. The diagram to the right shows the same jet 1.5 CAD later, where a hot diffusion-flame front (green) has been established. Source: [Musculus, 2006].

1.3 Low Temperature Combustion

Combustion concepts with improved paths through the $\phi - T$ diagram have been under intense study during the past decades. Low temperature combustion (LTC) concepts utilize enhanced fuel-air mixing to increase the combustion-zone heat capacity. The increased heat capacity lowers combustion temperatures and makes it possible to avoid the emission-formation regions in Fig. 1.6.

HCCI

The interest in LTC emerged with the discovery of homogeneous charge compression ignition (HCCI). A concept where a diluted homogeneous charge is inducted and autoignitioned by compression. It was first studied in two-stroke engines [Onishi et al., 1979] and was later shown to yield low emission levels in combination with high efficiencies in the low-load operating region of a four-stroke engine [Epping et al., 2002]. The blue line in Fig. 1.6 indicates the path taken by a fuel element in the case of ideal HCCI combustion. It is assumed that the fuel is completely mixed with air prior to the start of combustion, $\phi < 1$. The HCCI trajectory shows lean, premixed combustion that avoids the soot forma-

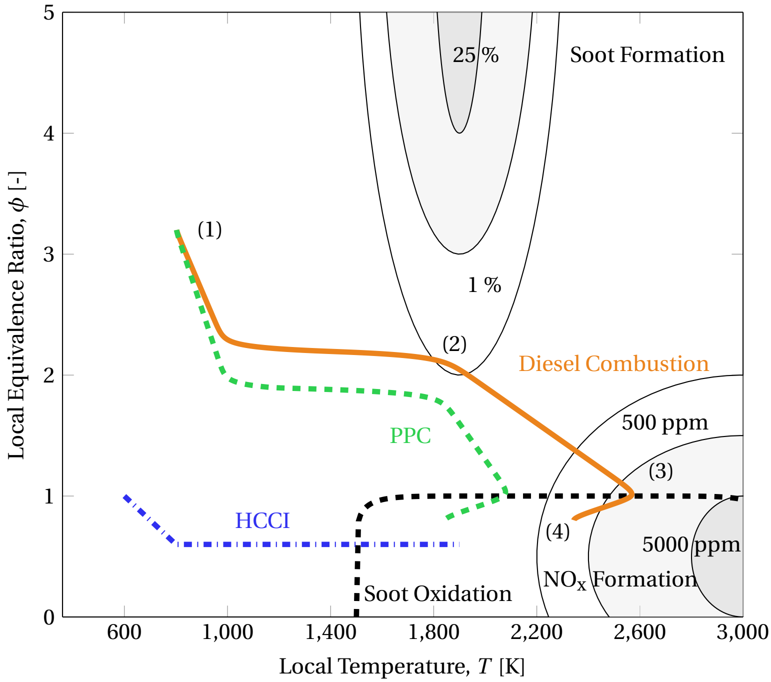

Figure 1.6 Emission formation as a function of ϕ and T. Combustion paths for HCCI, PPC and conventional diesel combustion are indicated by the blue, green and orange lines. The increased dilution of fuel with air in HCCI and PPC gives a higher combustion-zone heat capacity. This reduces T and ϕ, and the emission-formation zones can be avoided. Source: [Kitamura et al., 2002; Kook et al., 2005].

tion region. Furthermore, the reduced temperature results in low NO_x-emission levels. In HCCI, the combustion timing is completely determined by chemical autoignition kinetics as compared to injection-controlled diesel combustion. Combustion timing can therefore only be controlled by varying the temperature and mixture composition during the compression stroke. This poses a challenge with respect to combustion-timing sensitivity and controllability. Alternative combustion-timing strategies, such as variable-valve timing [Agrell et al., 2003], variable compression ratio [Haraldsson et al., 2002] and dual-fuel operation [Olsson et al., 2001] have been proposed to control the combustion timing in HCCI. Another challenge with HCCI is the limited operating range due to violent combustion rates during high-load operation [Olsson et al., 2004].

PPC

Low temperature combustion can also be obtained by prolonging the ignition delay of conventional diesel combustion. This can be done by diluting the inducted air charge with EGR, and by injecting fuel earlier during the compression stroke, or later during the expansion stroke when the temperature is lower [Takeda and Keiichi, 1995; Kimura et al., 1999; Akihama et al., 2001]. With direct injection, the fuel-air mixture obtained is not as homogeneous as in HCCI. On the other hand, combustion timing is only to a limited degree controlled by chemical kinetics. Emission levels can therefore be reduced with maintained combustion controllability. These concepts are commonly referred to as partially premixed, and has been applied by means of different techniques, leading to a number of names and abbreviations existing in the literature. Examples are MK, PCCI and RCCI [Kimura et al., 1999; Kanda et al., 2005; Kokjohn et al., 2011]. This thesis addresses topics related to a concept called partially premixed combustion (PPC). The conceptual model developed by Musculus [2006] is summarized below for the purpose of describing PPC.

In PPC, the fuel takes an intermediate path through the $\phi - T$ diagram. This is illustrated by the green line in Fig. 1.6. Injection occurs earlier during the compression stroke, which increases the fuel-traveling distance prior to vaporization due to reduced mixture temperature and density. The reduced temperature and increased EGR dilution extend the ignition delay and make it possible for the majority of the fuel to vaporize before the start of combustion. Increased mixing leads to a more spatially distributed fuel jet as compared to CDC. Combustion is therefore initiated more uniformly over the jet cross section. The increased combustion-zone heat capacity reduces combustion temperature, and the simultaneous reduction of ϕ and T reduces formation of both NO_x and soot. Two PPC fuel-jet intersections are presented in Fig. 1.7. Here, the fuel starts to react later (12 CAD after injection) as compared to Fig. 1.5, which allows for complete fuel vaporization before the start of combustion. The fuel jet also occupies a larger region during combustion. This leads to an increased dilution with smaller regions of soot formation.

It has been proven difficult to obtain sufficient ignition delay for premixed combustion with diesel fuels at high-load conditions [Noehre et al. 2006]. This could be remedied by increasing the fuel autoignition resistance. Gasoline PPC was introduced by Hildingsson et al. [2006] who showed that longer ignition delays could be achieved even at high-load conditions. At the author's engine laboratory, Manente et al. [2010c] showed that gasoline PPC could achieve gross indicated efficiencies between 52 and 55 % from idle to 26 bar (indicated mean effective pressure), with Euro VI compatible emission levels. This was achieved with EGR ratios at 50 %, ϕ at 0.75, and an advanced fuel-injection strategy. Simulation results in [Fridriksson et al., 2011] attributed the high efficiency obtained to low heat-transfer losses resulting from low combustion temperatures. These

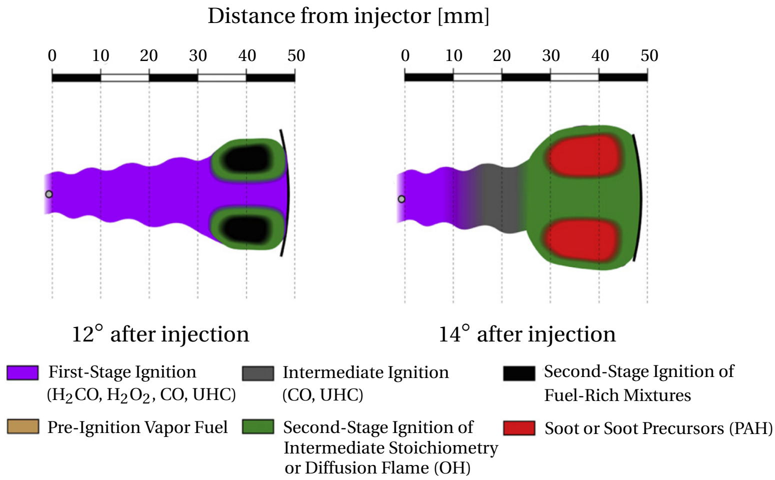

Figure 1.7 Conceptual model of low load, single-injection, and EGR-diluted partially premixed combustion (PPC). In PPC, the fuel reacts later compared to conventional diesel combustion, see Fig. 1.5. This allows for complete fuel vaporization before the start of combustion. The fuel jet also occupies a larger region during combustion, which leads to increased dilution with smaller regions of soot formation. Source: [Musculus, 2006].

results were the main motivation for the work presented in this thesis.

The increased dependency on chemical kinetics makes PPC more sensitive to operating conditions, as compared to CDC. Variations in temperature, dilution and fuel reactivity might lead to undesired combustion in the emission-formation regions in Fig. 1.6. Other PPC challenges include violent combustion rates, increased cylinder-to-cylinder variation, and misfire if the fuel does not ignite properly. This thesis therefore studies the problem of controlling PPC. With the objective of advancing the concept from manual operation in steady state, towards autonomous and transient operation in a multi-cylinder engine.

1.4 Engine Control

Automatic control concerns automatic operation and regulation of systems. For most control problems, the state of the system to be controlled x is influenced by a control input u, and information about x can be obtained from a measured output y. Controller design addresses the problem of deciding u in order for the

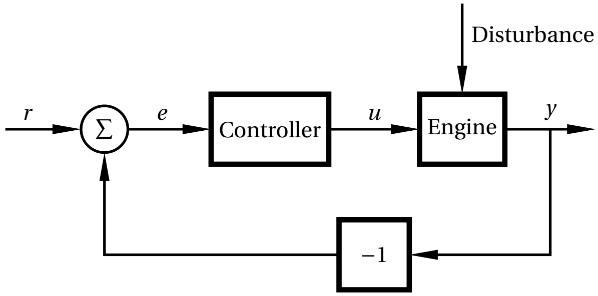

Figure 1.8 A system controlled in closed loop. The controller decides u based on deviation between the measured system output y and a set point r.

specified system-performance requirements to be fulfilled. Engine-performance requirements are related to efficient, durable and reliable operation subject to constraints on emission and noise levels. At a price that is competitive for mass production.

Compression-ignition engines have traditionally been controlled in open-loop, where the injected fuel amount has been determined by the accelerator-pedal position, engine speed and air-fuel ratio as opposed to generated work output. Fuel-injection timings are commonly computed from calibrated maps [Guzzella and Onder, 2009]. In closed-loop control, the control action is dependent on the measured process output, see Fig. 1.8. Closed-loop controllers have the advantage of making the system more resilient to external disturbances and variation in system components. Examples related to combustion engines are variations in fuel and gas-mixture properties, driving patterns, and aging of hardware components [Saracino et al., 2015]. Potential disadvantages with closed-loop control are possible dynamic instabilities and the introduction of sensor noise into the system. This imposes controller-design challenges in terms of trade-offs between achievable system performance and robustness [Åström and Murray, 2010].

The work presented in this thesis investigates how timings and durations of fuel-injection pulses should be decided to control the combustion processes with the use of in-cylinder pressure measurement. For this control problem, the main actuator is a solenoid injector, connected to a common-rail fuel system. The injected fuel quantity is determined by the common-rail pressure and the opening duration of the injector nozzle. Injector-opening timings and durations are determined by current pulses sent to the injector solenoid. The possibility to divide the fuel among several injection events gives additional degrees of freedom for combustion control. A detailed description of the workings of a solenoid injection is provided in [Bosch, 2011].

The cylinder pressure is perhaps the most fundamental variable available for direct measurement in an internal combustion engine. In this thesis it is measu-

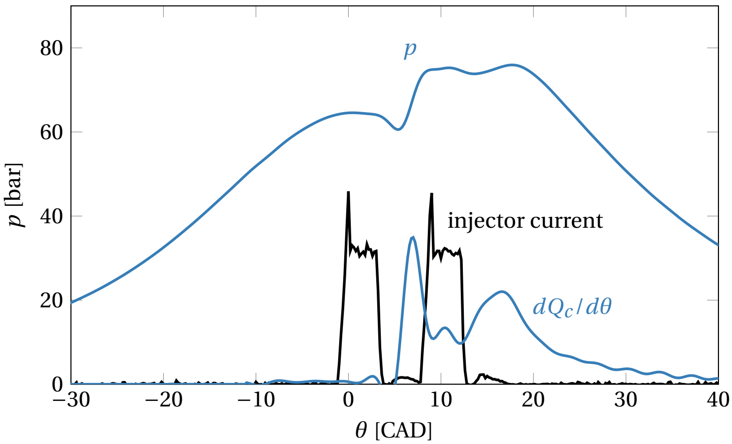

Figure 1.9 This thesis investigates the problem of how to decide timings and durations of fuel-injection pulses to control the combustion processes and the in-cylinder pressure p. This is a control problem with several degrees of freedom and a highly informative measured system output as feedback signal.

red with piezoelectric pressure transducers, mounted in the cylinder head. These sensors utilize the piezoelectric effect where a charge is generated when a piezoelectric crystal is exposed to a force. The measured in-cylinder pressure can be used to compute indicated engine work, heat-release rate and NO_x formation. The heat-release rate $dQ_c/d\theta$ can be used to compute combustion timings and ignition delays, which are important indicators for efficiency and emission formation. Although cylinder pressure sensing is a widely used in engine research, development, and calibration, in-cylinder pressure sensors have not yet reached widespread use in production vehicles due to high technical demands and associated cost. Recent announcements still indicate that cylinder pressure sensing might be used in future production vehicles [BorgWarner, 2014; Nagatsu et al., 2017]. There are several reviews describing the potential use for pressure sensors in engine control and diagnostics, see [Powell, 1993; Iorio et al., 2003; Eriksson and Thomasson, 2017].

Cycle-resolved input and output signals are presented as a function of θ in Fig. 1.9. The figure shows injector-current pulses, the measured in-cylinder pressure p and the computed heat-release rate $dQ_c/d\theta$.

Favorable cylinder boundary conditions in terms of intake temperature, pressure and composition were in this work obtained by regulating mass flows through EGR paths and a charge-air cooler. This was done by actuating valve positions in the gas-exchange system. Sensors in the gas-exchange system measured temperatures, pressures, air-mass flow and exhaust oxygen concentration. A more detailed description of the experimental setup and the gas-exchange system is given in chapters 2 and 5.

Control of Partially Premixed Combustion

Partially premixed combustion is sensitive to the cylinder-mixture temperature and composition. This puts high demands on the engine-control system, where actuators have to be accurately set for satisfactory performance. A feedback loop from measured cylinder pressure to fuel injection could significantly reduce combustion sensitivity. The foremost objective of this feedback loop is to reduce combustion-timing sensitivity through injection-timing adjustment for efficient delivery of the desired work output. If combustion occurs too early during the compression stroke, pressure buildup would contribute negatively to the produced work output. If combustion on the other hand occurs too late, there is a risk of incomplete combustion as a result of too lean and cold fuel-air mixtures. It is also of interest to regulate the ignition delay to ensure sufficient fuel-air mixing.

Too high combustion rates is another known issue with PPC and other premixed combustion concepts. This problem can be solved by introducing a pilot injection that reduces the ignition delay and the main-injection combustion rate. Feedback control can be used to ensure a sufficient pilot amount for acceptable combustion rates. These PPC-related control challenges are illustrated in Fig. 1.10 together with performance improvements achieved with fuel-injection adjustment. These challenges and corresponding feedback-controller designs will be described in greater detail in chapters 6 to 9.

Optimal Control

A common theme for the work presented in this thesis is to represent control problems as mathematical optimization problems with the system input u as the optimization variable

$$\begin{aligned} \underset{u}{\text{minimize}} \quad & J(u,x) \\ \text{subject to} \quad & g(u,x,y) = 0 \\ & f(u,x) \le 0 \end{aligned} \tag{1.1}$$

The cost function J is used to represent controller objectives such as set-point tracking and minimization of fuel consumption. The equality constraint determines the relation between input, state and output and is a model of the system to be controlled. The function g can also incorporate system dynamics by including time derivatives or difference equations with respect to x. The inequality constraint describes constraints and limitations with respect to x and u. This problem representation is convenient for engine-control purposes where it is often desirable to minimize fuel consumption and load set-point deviation without violating constraints with respect to cylinder pressure, emissions and actuator limitations. High engine efficiency typically demands operation close to, or on the boundary of admissible x and u.

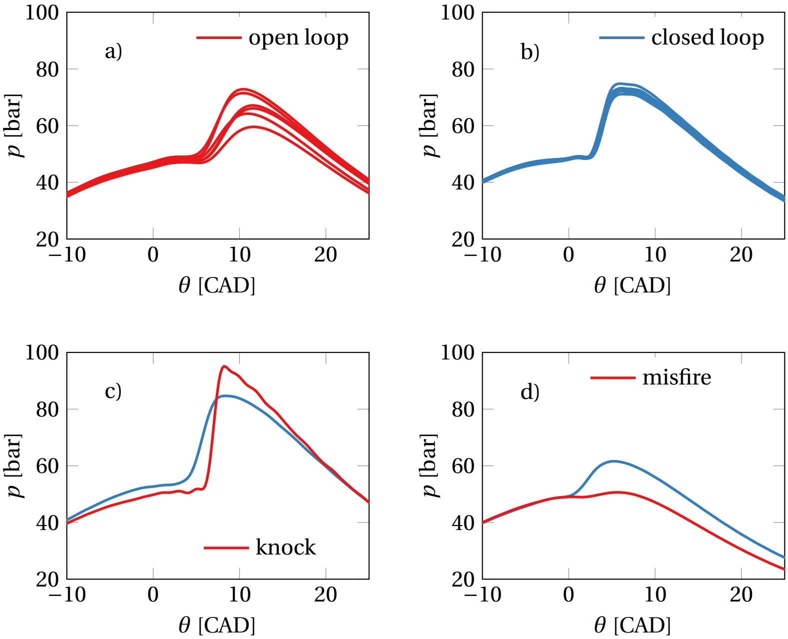

Figure 1.10 This thesis investigates the use of closed-loop control for reliable PPC operation. Presented controller designs manage to: Reduce cylinder-to-cylinder variation for consistent and efficient work output with sufficient ignition delay; Compare (a) where same injection durations and timing are actuated to the different cylinder, with (b), where work output and combustion timings are regulated in closed loop; Control the pressure-rise rate with pilot-injection adjustment to avoid knock and maintain an efficient combustion timing (c); Improve low-load operation by adjusting intake conditions and fuel injection to avoid misfire and incomplete combustion (d).

The approach taken here was to let the controller repeatedly solve (1.1) on a cycle-to-cycle basis with respect to measured y and a time horizon of future inputs, states and outputs. This optimal-control technique is called model predictive control (MPC) and has gained attention in several context, for example process control, automotive applications and combustion-engine control. Model predictive control will be described in greater detail in Chapter 3.

Chapters 10 to 12 of this thesis investigates the optimization problem of how pressure-sensor feedback and actuation of a number of fuel injections could be combined to efficiently fulfill constraints on cylinder pressure, NO_x formation and exhaust-gas temperature. The aim of this investigation was to design a controller capable of automatically finding efficient fuel-injection timings, durations and number of injections, as a function of the engine operating point.

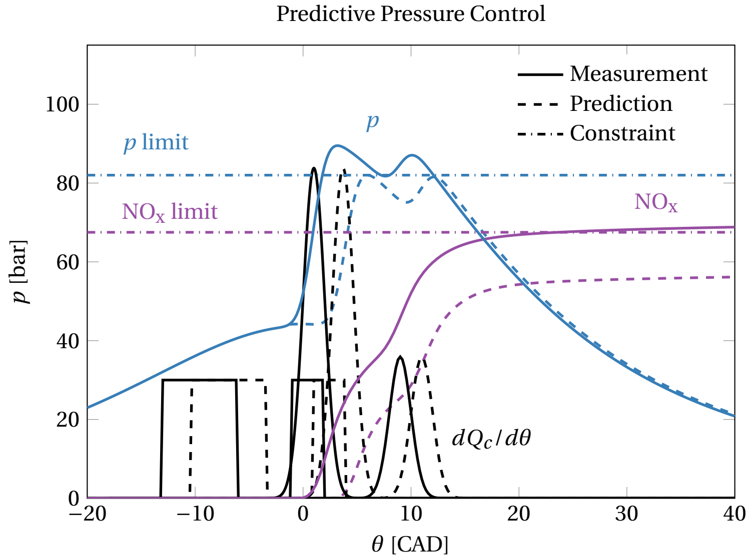

Figure 1.11 Fuel-injection optimization for efficient fulfillment of pressure and NO_x-emission constraints is studied in this thesis. This figure illustrates the predictive controller technique introduced in chapters 11 and 12. The controller predicts how future-cycle pressure (dashed) varies with fuel injection with the use of a pressure model and the previous-cycle pressure measurement (solid). The prediction is used to optimize fuel-injection timings and durations so that constraints on p and NO_x are efficiently fulfilled (dash-dotted).

Two types of controllers were studied. The first controller was designed with simple proportional/integral controller components and heuristic constraint handling. The second controller employed the MPC principle and utilized methods for cylinder-pressure approximation and heat-release analysis to predict how the cylinder pressure varies with fuel-injection parameters. This principle is illustrated in Fig. 1.11, where a controller predicts future-cycle fuel-injection adjustment and cylinder-pressure variation (dashed) based on a pressure model and the measured pressure from the previous cycle (solid). This allows the controller to repeatedly optimize fuel-injection timings and durations on a cycle-to-cycle basis, so that the predicted engine outputs efficiently fulfill specified constraints (dash-dotted).

1.5 Outline and Contributions

The thesis begins with two chapters that introduce the models and control principles used. The introductory chapters are followed by chapters on heat-release analysis and the experimental platform. The main contributions of the thesis are presented in chapters 6 to 12, where chapters 6 to 9 cover engine experiments and controller designs related to partially premixed combustion. Chapters 10 to 12 are focused on fuel-injection optimization and constraint fulfillment, where the results are also applicable to conventional compression-ignition engines.

A more detailed description of the chapters are given below along with references to publications on which they are based. Preliminary versions of parts of the research presented in this thesis was published in the licentiate thesis by the author:

Ingesson, G. (2015). *Model-Based Control of Gasoline Partially Premixed Combustion.* Licentiate Thesis TFRT-3268. Dept. of Automatic Control, Lund University, Lund, Sweden.

Note that the author's previous surname was Ingesson.

Chapter 2

This chapter presents models used for simulation, state estimation and controller design. It includes control-oriented models of the gas-exchange system and in-cylinder processes. Model-calibration results are also presented. The main contribution of this chapter is an evaluation of low-order ignition-delay models for the purpose of control. The results show that a fairly simple model can be used to predict the relation between intake conditions and ignition delay. The relation between injection timing and ignition delay when the gain from injection timing to ignition delay changes sign was, however, not adequately captured by the models considered.

Related Publication

Ingesson, G., L. Yin, R. Johansson, and P. Tunestål (2017). "An investigation on ignition-delay modeling for control". *Int. J. Powertrains* **6**:3, pp. 282–306.

Chapter 3

The control principles used are presented in this chapter with emphasis on model predictive control. This chapter also presents the state-estimation methods used to estimate heat-release model parameters and EGR mass flow in subsequent chapters.

Chapter 4

This chapter introduces heat-release analysis methods used to extract combustion information from in-cylinder pressure measurement. A heat-release detection method for multimodal heat-release feedback is also presented. The problem of calibrating unknown heat-release model parameters is represented as a state-estimation problem. With this representation, a particle filter and an extended Kalman filter are evaluated for on-line estimation of cylinder-wall surface temperature, TDC offset and a convective heat-transfer parameter.

Related Publication

Ingesson, G., L. Yin, R. Johansson, and P. Tunestål (2016). "Evaluation of nonlinear estimation methods for calibration of a heat-release model". *SAE Int. J. Engines* **9**:2, pp. 1191–1200.

Chapter 5

The setup used in the experimental work is presented in this chapter. Engine specifications, sensors and actuators are presented together with a description of the control-system architecture.

Chapter 6

Chapter 6 investigates proportional-integral (PI) combustion-timing controller design as a function of fuel reactivity, indicated by the fuel octane number. The investigation was done through simulation and describes how PI controllers should be tuned for maximized disturbance rejection subject to constraints on robustness and cycle-to-cycle variation. The obtained results present challenges and limiting factors for combustion-timing controller performance.

Related Publication

Ingesson, G., L. Yin, R. Johansson, and P. Tunestål (2018). "Proportional–integral controller design for combustion-timing feedback, from n-heptane to iso-octane in compression–ignition engines". *J. Dynamic Systems, Measurement, and Control* **140**:5, p. 054502.

Chapter 7

This chapter covers simultaneous control of ignition delay and combustion timing through combined actuation of fuel injection and valve positions in the gas-exchange system. The suggested model predictive controller utilizes a physics-based ignition-delay model, previously presented and calibrated in Chapter 2. The controller was evaluated experimentally and was shown capable of tracking set points with respect to cylinder-individual combustion timings and the cylinder-mean ignition delay during engine load and speed changes.

Related Publication

Ingesson, G., L. Yin, R. Johansson, and P. Tunestål (2015). "Simultaneous control of combustion timing and ignition delay in multi-cylinder partially premixed combustion". *SAE Int. J. Engines* **8**:5, pp. 2089–2098.

Chapter 8

Chapter 8 investigates the effects of pilot injection for control of the pressure-rise rate. An experimental evaluation on how pilot injection affects emission levels and efficiency is first presented. The experimental results are then used to design a model predictive controller with the objective to fulfill an upper limit on pressure-rise rate, and to track combustion-timing and engine-load set points. Experimental controller-evaluation results are also presented.

Related Publication

Ingesson, G., L. Yin, R. Johansson, and P. Tunestål (2016). "A double-injection control strategy for partially premixed combustion". In: *Proc. 8th IFAC Symposium on Advances in Automotive Control (AAC 2016)*. Vol. 49. 11. Norrköping, Sweden, pp. 353–360.

Chapter 9

Chapter 9 explores control strategies for improved combustion efficiency at low-load operation. The results presented were based on experimental engine data. Saturation of the fuel-injection timing and the introduction of a pilot injection increased the indicated efficiency. Gas-exchange actuation for avoidance of low-efficiency regions in a $\phi - T$ diagram was found through simulation of a calibrated gas-exchange system model.

Related Publication

Ingesson, G., L. Yin, R. Johansson, and P. Tunestål (2016). "Control of the low-load region in partially premixed combustion". In: *Proc. J. Physics: Conference Series*. Vol. 744. 1. Southampton, England.

Chapter 10

Chapter 10 investigates potential efficiency improvements with multimodal heat-release rates, when constraints on maximum cylinder pressure, NO_x and exhaust temperature are imposed. A simulation study showing an efficiency increase with two injections is first presented. The simulation results suggest a heuristic hybrid fuel-injection controller that varies the number of injections depending on operating conditions. Experimental controller-performance results in both steady state and transient operation are presented. The experimental result showed a 4-5 % efficiency improvement with respect to pressure and NO_x constraints, compared to that of a single-injection controller

Related Publications

Ingesson, G., L. Yin, R. Johansson, and P. Tunestål (2017). "Efficiency optimal, maximum-pressure control in compression-ignition engines". In: *Proc. American Control Conf. (ACC 2017)*. Seattle, WA, USA, pp. 4753–4759.

Ingesson, G., L. Yin, R. Johansson, and P. Tunestål (2018). “Design and evaluation of a multiple-injection controller for efficient fulfillment of NOx and exhaust-temperature constraints”. *submitted to SAE Int. J. Engines.*

Chapter 11

This chapter introduces a model-based pressure-prediction method. The novelty of this method lies in the use of the estimated heat-release rate to predict how the cylinder pressure varies with injection timing. This is a computationally cheap alternative to heat-release modeling. This chapter also presents how this method can be used to find efficiency-optimal injection timings with respect to constraints on maximum pressure and pressure-rise rate.

Related Publication

Ingesson, G., L. Yin, R. Johansson, and P. Tunestål (2015). “A model-based injection-timing strategy for combustion-timing control”. *SAE Int. J. Engines* **8**:3, pp. 1012–1020.

Chapter 12

This chapter presents how the pressure-prediction method in Chapter 11 can be used in a model predictive control framework to efficiently fulfill constraints on in-cylinder pressure, NO_x and exhaust temperature with multiple injections. This controller objective was previously studied in Chapter 10, but was revised here with a model-based approach. An alternative model predictive control formulation for pressure set-point tracking is also presented. The controllers presented rely on a heat-release detection method, capable of separating the heat-release rate among several injections. Model-based methods for adding and removing injections are also discussed.

Related Publication

Turesson, G., L. Yin, R. Johansson, and P. Tunestål (2018). “Predictive pressure control with multiple injections”. *submitted to E-CoSM 2018, Changchun, China.*

Chapter 13

The thesis is concluded in Chapter 13, where aspects on future research are also discussed.

Authors Contributions

The author was the foremost contributor to the publications listed above. The author was the main contributor to the work related to modeling, control and experimental evaluation. This includes problem formulation, as well as developing, implementing, testing, and evaluating controller designs. The author wrote the papers himself with input from the co-authors. All authors jointly determined the general direction of the research, for example, that focus should be directed towards control problems related to fuel-injection and its effect on the combustion processes. Lianhao Yin was the main contributor to the design of the experimental platform used in the thesis. This includes design of the test-cell setup, control-system and data-acquisition architecture.

2

Modeling

The increasing demands for reduced fuel consumption, emissions levels and improved driveability lead to more actuators, sensors and complex control functions. With the increasing engine complexity in mind, a systematic implementation of the engine-control system requires mathematical models for simulation, calibration and controller design [Isermann, 2014, Atkinsson, 2009].

Model-based control is a controller-design approach where a mathematical model describing physical or empirical system knowledge is utilized. A model can be used off-line to evaluate controller performance in simulation, and in this way provide suitable controller parameters and reduce the experimental workload. A model can also be used on-line to provide the controller with information about predicted system behavior in real time. Both approaches to model-based controller design were adopted in this work.

2.1 Control-Oriented Modeling

Engine modeling can be done at different levels of detail and complexity and involves several disciplines such as thermodynamics, chemical kinetics and fluid mechanics. Computational fluid dynamics (CFD) modeling is the most complex and detailed modeling approach. CFD utilizes numerical algorithms to solve partial differential equations describing dynamical fluid flow with high spatial and temporal resolution, whilst incorporating chemical reactions with up to hundreds of species and reactions. This resolves details of gas dynamics, multi-phase flows, and turbulence-chemistry interactions. Applications for CFD modeling include design of combustion-chamber geometry, fuel-spray properties and in-cylinder flow patterns, related to engine development as an alternative and complement to experimental testing [Han et al., 2002; Szekely et al., 2004; Shi et al., 2011]. CFD is also used in engine research to give physical explanation for experimental results. However, simulation times from hours to several months make CFD modeling unsuitable for controller design, where simulation tests have to be done over a large number of engine cycles and test cases. For on-line control applications, computational times have to be in the range of milliseconds to meet the hard timing constraints of engine actuation.

Zero-dimensional (0D) models are an alternative of lower complexity. They represent mean variables over a larger space, such as the average pressure and temperature in the combustion-chamber volume. These models are commonly derived from first principles, where fuel injection, fuel/air mixing and combustion are represented as sub-models with empirical parameters. Short computational times allow for engine simulation over complete drive cycles and real-time applications. Examples of such models are presented in [Kiencke and Nielsen, 2000; Isermann al., 2014; Eriksson and Nielsen, 2014]. Albeit spatial resolution is lost, zero-dimensional models are able to accurately predict engine data with high temporal resolution, see [Kiencke and Nielsen, 2000; Chmela et al., 2007; Widd et al., 2012].

Models with high temporal resolution are not always directly applicable for controller design. Fuel-injection timings and durations are for instance only set once every engine cycle. It would therefore be sufficient for a fuel-injection controller to utilize a model describing how the engine state changes from one cycle to the next. Cycle-to-cycle models can be obtained by sampling crank-angle resolved models or by deriving empirical models from engine data. Examples of physics-based and empirical cycle-to-cycle models can be found in [Guzella and Onder, 2009] and [Henningsson et al., 2012], respectively.

The dynamics of the fuel-delivery and gas-exchange systems have longer time constants than the cycle-resolved combustion processes. This can be exploited by neglecting discrete engine cycles and instead model slower engine dynamics by averaging over several engine cycles and viewing faster processes as static relations [Eriksson and Nielsen, 2014]. These models are typically of low spatial resolution and are referred to as mean-value models (MVM) [Hendricks, 1986], or control-oriented models due to their usefulness in control applications.

The modeling detail required is a trade-off between computational complexity and the possible increase in controller performance. It also depends on application requirements. For the purpose of closed-loop controller design, it is usually sufficient to model the system behavior in the vicinity of the desired bandwidth of the closed-loop system. This is because feedback control makes the closed-loop system robust to model errors and disturbances of lower frequencies. High-frequency components are commonly filtered out and may in those cases be neglected by the model.

The modeling approach adopted in this work is illustrated in Fig. 2.1. In-cylinder processes were modeled using a crank-angle-resolved zero-dimensional model, derived from first principles of thermodynamics. Combustion was modeled with empirical expressions for global chemical-reaction rates, triggered by the event of fuel injection. This model was occasionally simplified through linearization or sampling for cycle-to-cycle controller design.

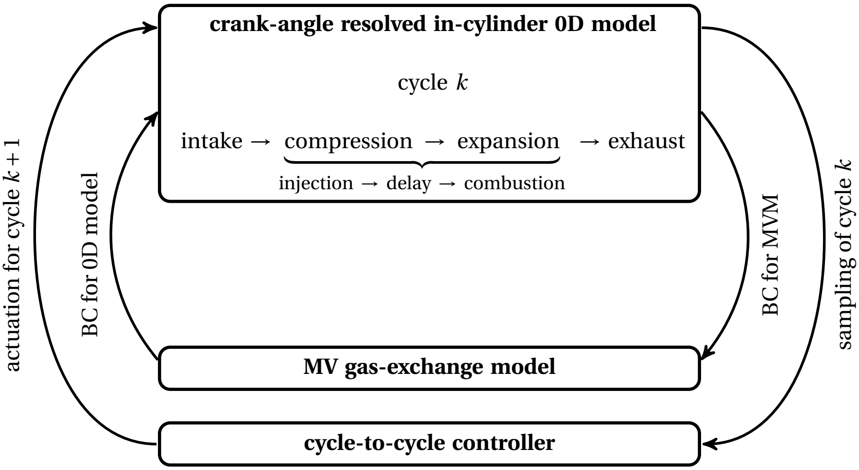

Figure 2.1 The modeling approach adopted in this work was to represent the in-cylinder processes with a crank-angle resolved zero-dimensional (0D) model with empirical expressions for chemical reaction rates. Cylinder boundary conditions (BC) are determined by the states of the intake and exhaust manifolds, obtained from a mean-value gas-exchange model. Controller sampling and actuation occur in-between consecutive engine cycles.

A mean-value model was used to model states of the intake and exhaust manifolds which determine the boundary conditions for the in-cylinder model.

These models will be described in greater detail in the following sections. First, the crank-angle resolved in-cylinder pressure and temperature model is presented. The mean-value gas-exchange model is presented subsequently. Then, ignition-delay models of different complexity are presented and evaluated. Finally, an NO_x-formation model is presented. System identification was conducted in order to obtain unknown model parameters from engine data. Identification experiments and results are also presented below.

2.2 In-Cylinder Model

The main objective of this thesis is to investigate model-based combustion control though fuel-injection actuation. Models for heat-release estimation and prediction of how the cylinder pressure depends on fuel injection are therefore essential controller components. The models used for this purpose is based on the assumption that the in-cylinder gas during the closed part of the engine cycle is an open thermodynamic system with the combustion chamber as the system boundary, see Fig. 2.2.

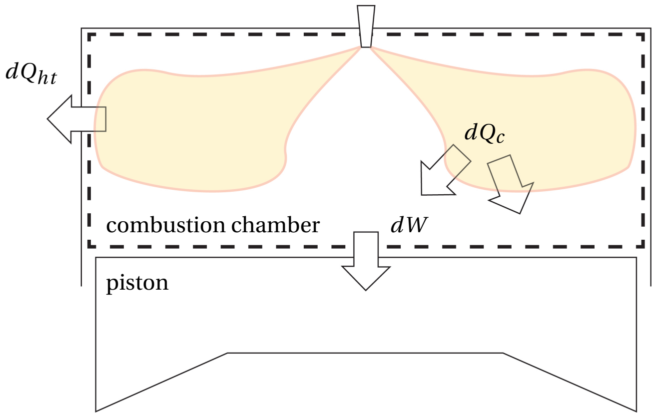

Figure 2.2 Open system boundary for the combustion chamber. The combustion is modeled as a release of heat dQ_c, whereas the cylinder gas performs work on the piston dW, and heat dQ_{ht} is transferred to the cylinder walls.

The first law of thermodynamics for this system states

$$dU = dQ - dW + \sum_i h_i dm_i \tag{2.1}$$

where dU is the change in system internal energy, dQ is the heat added to the system, dW is the work done by the system, and $\sum_i h_i dm_i$ is the enthalpy flux across the system boundary. The combustion is modeled as a release of heat, which gives that the heat added to the system dQ is the difference between released chemical energy dQ_c and heat transferred to the cylinder walls

$$dQ = dQ_c - dQ_{ht} \tag{2.2}$$

With the piston work given by pdV, the first law can be rewritten as

$$dU = dQ_c - dQ_{ht} - pdV + \sum_i h_i dm_i \tag{2.3}$$

Under the assumption of ideal gas, a change in internal energy is given by

$$dU = mc_v dT + udm \tag{2.4}$$

where m is the system mass, c_v is the heat-capacity at constant volume and u is the specific internal energy. The ideal-gas law, where R is the specific gas constant

$$pV = mRT \tag{2.5}$$

provides a differential in T

$$dT = \frac{1}{mR}(Vdp + pdV - RTdm) \tag{2.6}$$

by assuming a constant R. Now, by inserting (2.4) and (2.6) into (2.3), and substituting

$$c_v = \frac{R}{\gamma - 1} \tag{2.7}$$

where γ is the ratio of specific heats $\gamma = c_p/c_v$, the following differential in p can be derived

$$dp = -\frac{\gamma}{V} p dV + \frac{\gamma - 1}{V}(dQ_c - dQ_{ht} + \sum_i h_i dm_i) + \frac{1}{V}(RT - (\gamma - 1)u)dm \tag{2.8}$$

From (2.8), the simplified differential equation in p is obtained

$$\frac{dp}{d\theta} = -\frac{\gamma}{V}\frac{dV}{d\theta}p + \frac{\gamma - 1}{V}\left(\frac{dQ_c}{d\theta} - \frac{dQ_{ht}}{d\theta}\right) \tag{2.9}$$

if m is assumed to be constant, and the crank angle θ is chosen as the independent variable. In this work, (2.9) was used to analyze $dQ_c/d\theta$ from measured p. A more detailed description of heat-release analysis is given in Chapter 4. Model (2.9) was also used to simulate p with initial conditions and $dQ_c/d\theta$ as input in Chapter 10.

The assumption of a uniform ideal gas with constant mass and composition is a useful approximation that is adequate for many engineering applications. In reality, liquid fuel is injected into the cylinder. The fuel vaporizes and mixes with air to produce a nonuniform fuel and air distribution, where the chemical composition changes during combustion. Flows to and from cooling crevice regions have a significant effect but was also neglected here. More detailed models that take into account for mass flow to crevice volumes, radiation, and thermal boundary layers are presented in [Heywood, 1988]. Models that divide the combustion chamber into multiple zones, instead of one, can be found in [Fiveland and Assanis, 2001; Nilsson and Eriksson, 2001].

The following sections describe how the different components of (2.9) were modeled.

Cylinder Geometry

The cylinder volume V was modeled as a slider-crank mechanism

$$V = V_c + \frac{V_d}{2}\left(R_v + 1 - \cos(\frac{\pi}{180}\theta) - \sqrt{R_v^2 - \sin^2(\frac{\pi}{180}\theta)}\right) \tag{2.10}$$

where V_d and V_c are displacement and clearance volumes, and R_v is the ratio of the connecting-rod length to the crank radius.

Temperature

The in-cylinder temperature T was computed from the ideal-gas equation using the conditions at intake-valve closing (IVC)

$$T = \frac{pVT_{\mathrm{IVC}}}{p_{\mathrm{IVC}}V_{\mathrm{IVC}}} \tag{2.11}$$

The temperature T_{IVC} was computed as a weighted average of the intake-manifold gas temperature T_{in} and the trapped residual-gas temperature T_{res}

$$T_{\mathrm{IVC}} = \frac{c_v^{\mathrm{in}} T_{\mathrm{in}} + c_v^{\mathrm{res}} \alpha\chi T_{\mathrm{res}}}{c_v^{\mathrm{in}} + c_v^{\mathrm{res}} \alpha\chi} \tag{2.12}$$

where c_v^{in} and c_v^{res} are specific heats of inducted charge and residual gases, α is the mass ratio between trapped residuals and inducted gases and χ is a measure of residual-gas temperature decrease during gas exchange. The residual gas temperature T_{res} was computed from the exhaust-valve-opening temperature of the previous cycle.

Ratio of Specific Heats

The ratio of specific heats $\gamma = c_p/c_v$ is determined by the cylinder-gas composition and temperature. In this work, γ was held constant for less sensitive computations, such as determining the combustion-timing. The ratio γ was computed with NASA specific-heat polynomials as a function of in-cylinder gas temperature and composition when an increased model accuracy was needed.

The gas composition is non-trivial to compute during combustion and was therefore interpolated between the unburned and burned gas composition during combustion, using the computed heat-release rate, EGR ratio, and the stoichiometry of the overall chemical reaction

$$\begin{aligned}
&\mathrm{C}_x\mathrm{H}_y + \frac{1}{\phi_n}\left(x+\frac{y}{4}\right)(\mathrm{O}_2 + 3.773\mathrm{N}_2) \rightarrow \\
&\qquad x\mathrm{CO}_2 + \frac{y}{2}\mathrm{H}_2\mathrm{O} + \left(\frac{1}{\phi_n} - \left(x+\frac{y}{4}\right)\right)\mathrm{O}_2 + \frac{1}{\phi_n}3.773\left(x+\frac{y}{4}\right)\mathrm{N}_2
\end{aligned} \tag{2.13}$$

where y/x is the fuel hydrogen to carbon ratio and ϕ_n is the molar equivalence ratio.

Heat-Transfer Model

The convective heat-transfer rate from in-cylinder gas to piston, cylinder head and walls $dQ_{ht}/d\theta$ was modeled using Newton's law of cooling

$$\frac{dQ_{ht}}{d\theta} = \frac{h_c A}{60 N_{\mathrm{speed}}}(T - T_w) \tag{2.14}$$

where T_w is the wall-surface temperature, A is the combustion-chamber surface area and N_{speed} is engine speed in revolutions per minute (rpm). The convection coefficient h_c is an empirical [Woschni, 1967] expression

$$h_c = 3.26 B^{0.2} p^{0.8} T^{-0.55} \omega^{0.8} \tag{2.15}$$

derived from a Nusselt-Reynolds correlation, as presented in [Heywood, 1988]. Here, B is the cylinder bore and ω the mean cylinder-gas velocity, where ω was modeled according to

$$\omega = C_1 S_p + C_2 \frac{V_d T_{\text{IVC}}}{p_{\text{IVC}} V_{\text{IVC}}} (p - p_m) \tag{2.16}$$

The first term in (2.16) relates gas motion to the mean piston speed S_p, and the second term captures the effect of charge-density variation during combustion, where p_m is the cylinder pressure of a motored cycle. The empirical parameters C_1 and C_2 are engine dependent, where $C_2 = 0$ before the start of combustion. The problem of estimating C_2 from cylinder-pressure data is investigated in Chapter 4. Similar global heat-transfer models presented in [Annand, 1963; Hohenberg, 1979] are also commonly used to model (2.14).

Cylinder-Wall Temperature

The cylinder-wall surface temperature T_w is determined by the heat flux from in-cylinder gases to the engine coolant with temperature T_c. The cylinder wall, cylinder head and piston were modeled as a single mass with conductive coefficient k_c, thickness L_c, mass m_c and specific heat c_p. By assuming that the inner wall temperature is in steady state and that the outer-wall surface on the coolant side has fixed temperature T_c, the following dynamic equation for T_w can be derived

$$\frac{dT_w}{d\theta} = -\frac{2A(h_c + k_c/L_c)}{m_c c_p 60 N_{\text{speed}}} T_w + \frac{2Ah_c}{m_c c_p 60 N_{\text{speed}}} (T + T_c) \tag{2.17}$$

During the intake and exhaust strokes, T was assumed to be constant and equal to intake- and exhaust-manifold temperatures. This model was previously presented and used in [Roelle et al., 2006; Widd et al., 2008].

Heat-Release Rate

The heat-release rate $dQ_c/d\theta$ is difficult to model from first principles due to its dependency on a multitude of factors such as chemical combustion rates, fuel-injection profile and fuel-air mixing rates. The approach adopted in Chapter 11 was to utilize the heat-release rate computed from cylinder-pressure measurements to predict how p varies with fuel injection. This method can not be used to simulate p. A Wiebe [1970] expression for the accumulated heat-release

$$\frac{Q_c(\theta)}{Q_{\text{tot}}} = \begin{cases} 1 - \exp\left(-a\left(\dfrac{\theta-\theta_{\text{SOC}}}{\Delta\theta}\right)^{b+1}\right) & \text{for } \theta \geq \theta_{\text{SOC}} \\ 0 & \text{otherwise} \end{cases} \tag{2.18}$$

was therefore used, mainly because of its simplicity, as an input to simulate (2.9) in Chapter 10. In (2.18), θ_{SOC} is the start of combustion, and the parameters $\Delta\theta$, a and b relate to the duration and shape of the heat-release profile.

Load and Efficiency Definitions

The measured in-cylinder pressure was used to compute the engine work output and efficiency. The gross- and net-indicated mean effective pressures, p_{IMEPg} and p_{IMEPn} are normalized measures of the work done on the piston by the cylinder gas during the closed part of the cycle and during the complete cycle. These quantities were here defined as

$$\begin{aligned} p_{\text{IMEPg}} &= \frac{1}{V_d}\int_{\text{IVC}}^{\text{EVO}} p\,dV \\ p_{\text{IMEPn}} &= \frac{1}{V_d}\oint p\,dV \end{aligned} \tag{2.19}$$

The gross mean effective pressure p_{IMEPg} is more commonly defined by

$$p_{\text{IMEPg}} = \frac{1}{V_d}\int_{\text{BDC}_1}^{\text{BDC}_2} p\,dV \tag{2.20}$$

where the integral is taken over the complete compression and expansion strokes. The difference between (2.19) and (2.20) is determined by engine valve timings and intake and exhaust manifold pressures. The reason for using the definition in (2.19) was to distinguish the efficiency of the closed part of the cycle and to evaluate efficiency in simulation without a gas-exchange model. Both p_{IMEPg} and p_{IMEPn} were used as feedback variables to control the engine load. For this purpose, the difference between (2.19) and (2.20) has negligible effect.

With (2.19) and (2.20) computed, fuel-conversion efficiencies to indicated work are given by

$$\begin{aligned} \eta_{\text{GIE}} &= \frac{p_{\text{IMEPg}} V_d}{m_f Q_{\text{LHV}}} \\ \eta_{\text{NIE}} &= \frac{p_{\text{IMEPn}} V_d}{m_f Q_{\text{LHV}}} \end{aligned} \tag{2.21}$$

where m_f is the injected fuel mass and Q_{LHV} is the lower heating value of the fuel. These efficiencies were frequently used to evaluate simulated and measured engine efficiency. The gross efficiency η_{GIE} is of interest if the combustion and thermodynamic efficiencies of the closed part of the engine cycle are of interest, whereas η_{NIE} also accounts for pumping losses during gas exchange.

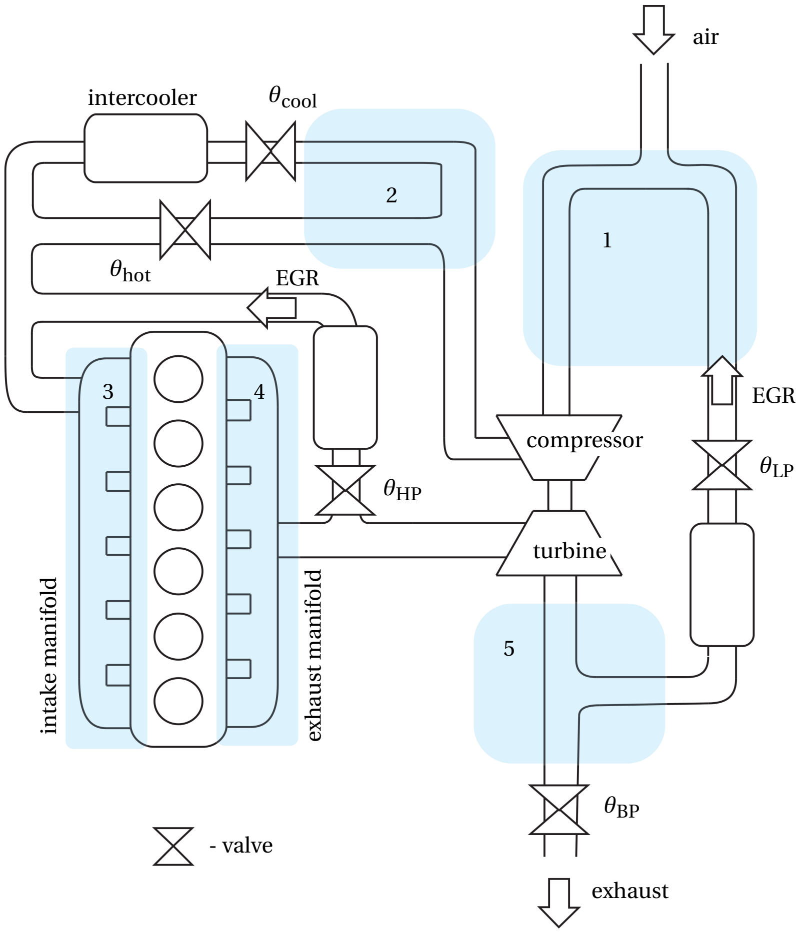

Figure 2.3 Engine gas-exchange system layout. The engine was boosted by a fixed-geometry turbocharger. Exhaust-gas recirculation was supplied by a high and a low-pressure path, and the intake temperature was controlled by the gas flow through a charge-air cooler prior to the intake manifold. The gas-exchange system was modeled as 5 interconnected adiabatic volumes (indicated by the blue regions). Gas flows through the EGR paths and the thermal management system were controlled by actuating valve positions, denoted θ_x. The engine layout is further described in Chapter 5.

2.3 Gas-Exchange System

A layout of the gas-exchange system used in the experimental work is presented in Fig. 2.3. Air enters from above and is compressed by a turbocharger. The air then either goes through a charge-air cooler or directly to the intake manifold. The mass-flow ratio between these paths is determined by the position of two valves. These paths will later be referred to as the fast thermal-management part (FTM) of the gas-exchange system. After leaving the exhaust manifold, the exhaust gases either enter the cooled high-pressure EGR path or expands through the turbine. After the turbine, some of the exhaust goes through a cooled low-pressure EGR path, and the remaining exhaust gas passes through a back-pressure valve to the exhaust pipe. Mass flows through the EGR paths are determined by the EGR-valve positions.

Gas-Exchange Dynamics

A gas-exchange system model was used in Chapter 9 to design a low-load PPC controller. The main objective of the model was to describe in-cylinder temperature and mass in the low-load operating range of the engine, in order to compute optimal valve-position actuation in simulation. The gas-exchange system was modeled as five adiabatic ideal-gas control volumes, interconnected with restrictions, denoted 1 to 5 in Fig. 2.3. Under this assumption, the dynamic equations with respect to pressure p_i and temperature T_i in volume V_i are given by [Eriksson and Nielsen, 2014]

$$\begin{aligned} \frac{dp_i}{dt} &= \frac{RT_i}{V_i}(\dot{m}_{\text{in}} - \dot{m}_{\text{out}}) + \frac{p_i}{T_i}\frac{dT_i}{dt} \\ \frac{dT_i}{dt} &= \frac{RT_i}{V_i p_i c_{v,i}}(\dot{m}_{\text{in}} c_{v,i}(T_{\text{in}} - T_i) + R(\dot{m}_{\text{in}} T_{\text{in}} - \dot{m}_{\text{out}} T_i)) \end{aligned} \tag{2.22}$$

Here, $\dot{m}_{\text{in}}$ and $\dot{m}_{\text{out}}$ are in- and outgoing mass flows, and $c_{v,i}$ is the gas specific heat at constant volume. States in the intake and exhaust manifolds are also denoted X_{in} and X_{ex} in this thesis. Mass flow from V_i to V_j, $\dot{m}_{ij}$, was modeled as turbulent compressible flow through a restriction, where $\dot{m}_{ij}$ is given by [Heywood, 1988]

$$\dot{m}_{ij} = \frac{A_{ij} p_i}{\sqrt{RT_i}} \left(\frac{p_j}{p_i}\right)^{1/\gamma_i} \sqrt{\frac{2\gamma_i}{\gamma_i - 1}\left(1 - \left(\frac{p_j}{p_i}\right)\right)^{(\gamma_i - 1)/\gamma_i}} \tag{2.23}$$

Here, A_{ij} is the effective flow area and γ_i is the ratio of specific heats which is different for air and exhaust. If the pressure ratio is too low

$$\frac{p_j}{p_i} < \left(\frac{2}{\gamma_i + 1}\right)^{\dfrac{\gamma_i}{\gamma_i - 1}} \tag{2.24}$$

the flow becomes choked, and the expression for $\dot{m}_{ij}$ is given by

$$\dot{m}_{ij} = \frac{A_{ij} p_i}{\sqrt{RT_i}} \gamma_i^{1/2} \left(\frac{2}{\gamma_i + 1}\right)^{\dfrac{\gamma_i + 1}{2(\gamma_i - 1)}} \tag{2.25}$$

The effective flow area A_{ij} was in the case of a valve restriction determined by the valve angle θ_{ij} according to an empirical expression

$$A_{ij} = A_{ij}^0 \left(1 - e^{-k_{A_{ij}}(\theta_{ij} - \theta_{ij}^0)}\right) \tag{2.26}$$

The mass flow from the intake manifold to the cylinders $\dot{m}_{\text{cyl}}^{\text{in}}$ was modeled using a volumetric efficiency η_v, the intake-manifold density and the engine displacement rate

$$\dot{m}_{\text{cyl}}^{\text{in}} = \eta_v \cdot \frac{p_3}{RT_3} \cdot \frac{V_d N_{\text{speed}}}{120} \tag{2.27}$$

The volumetric efficiency was approximated by assuming displacement of new charge by residual gas

$$\eta_v = \frac{r_c - \left(\frac{p_4}{p_3}\right)^{1/\gamma}}{r_c - 1} \tag{2.28}$$

where r_c is the engine compression ratio. The cylinder-out mass flow was then obtained by adding the fuel flow $\dot{m}_f$

$$\dot{m}_{\text{cyl}}^{\text{out}} = \dot{m}_{\text{cyl}}^{\text{in}} + \dot{m}_f \tag{2.29}$$

The turbocharger model used was a simplification of the model presented in [Wahlström and Eriksson, 2011]. First, the following relation for the turbine power P_t

$$P_t = \eta_{\text{t}} P_t^s \tag{2.30}$$

was assumed where η_t is the turbine thermodynamic efficiency and P_t^s is the power obtained from isentropic expansion over the turbine

$$P_t^s = c_{p,4} T_4 \left(1 - \left(\frac{p_5}{p_4}\right)^{1-1/\gamma_4}\right) \dot{m}_{45} \tag{2.31}$$

where $\dot{m}_{45}$ is the mass flow over the turbine, modeled using (2.23). The compressor power P_c was then related to P_t through a mechanical efficiency η_m and the static relation

$$P_c = \eta_m P_t \tag{2.32}$$

The compressor power P_c was in turn related to the power of isentropic compression over the compressor P_c^s

$$P_c^s = \eta_c P_c \tag{2.33}$$

where P_c^s is a function of the compressor mass flow $\dot{m}_{12}$

$$P_c^s = c_{p,1} T_1 \left(\left(\frac{p_2}{p_1}\right)^{1-1/\gamma_1} - 1\right) \dot{m}_{12} \tag{2.34}$$

We can now solve for $\dot{m}_{12}$ which gives

$$\dot{m}_{12} = \frac{\eta_{\text{tc}} c_{p,4} T_4 \left(1 - \left(\dfrac{p_5}{p_4}\right)^{1-1/\gamma_4}\right)}{c_{p,1} T_1 \left(\left(\dfrac{p_2}{p_1}\right)^{1-1/\gamma_1} - 1\right)} \dot{m}_{45} \tag{2.35}$$

where η_{tc} is the overall efficiency of the turbocharger

$$\eta_{\text{tc}} = \eta_c \eta_m \eta_t \tag{2.36}$$

More detailed turbocharger models include dynamics and experimentally obtained maps describing turbine and compressor efficiencies. The approach taken here was instead to calibrate a constant η_{tc} over a limited engine operating range. Engine-out temperature T_{EO} and cooler-out flow temperatures T_{EGR}, T_{CO} were modeled using empirical polynomials

$$\begin{aligned} T_{\text{EO}}(T_3, m_f) &= c_{\text{EO}}(T_3, m_f) \\ T_{\text{CO}}^{ij}(T_i, \dot{m}_{ij}) &= c_{\text{CO}}^{ij}(T_i, \dot{m}_{ij}) \end{aligned} \tag{2.37}$$

The unknown model parameters were identified with respect to engine data by first calibrating the polynomial coefficients in c_X and $k_{A_{ij}}$ in (2.26) with respect to local flow and temperature data. The remaining unknown parameters

$$\vartheta = \begin{pmatrix} A_{\text{atm},1} & A_{23}^1 & A_{23}^2 & A_{43} & A_{45} & A_{51} & A_{5,\text{atm}} & \eta_{\text{tc}} \end{pmatrix}^T \tag{2.38}$$

were then computed by minimizing the model-output error cost function

$$V(\vartheta) = \sum_{i=1}^{5} \alpha_i \| p_i^m - p_i \|_2^2 + \beta_i \| T_i^m - T_i \|_2^2 \tag{2.39}$$

where p_i^m, T_i^m are measured pressure and temperature data, and p_i, T_i are corresponding model outputs. The importance of capturing different outputs are determined by the tuning parameters α_i and β_i. Cost function (2.39) was minimized subject to

$$\eta_{\text{tc}} \le 1 \tag{2.40}$$

and measured boundary conditions p_{atm}, T_{atm}. Model output and measured data are shown in Fig. 2.4 for a local minimizer of (2.39) ϑ^*, where ϑ^* was found using the MATLAB nonlinear-optimization toolbox. The data presented in Fig. 2.4 are combined sequences of steady-state data with different θ_{Cool} and θ_{HP} positions for p_{IMEP} between 1 and 5 bar. The tuning parameters were set to prioritize model fit with respect to the intake-manifold state. In Fig. 2.4, it can be seen that the model managed to predict in-cylinder temperature at the start of injection $T_{\theta_{\text{SOI}}}$ and the relative air-fuel ratio λ, which was the main purpose of the model when used in Chapter 9.

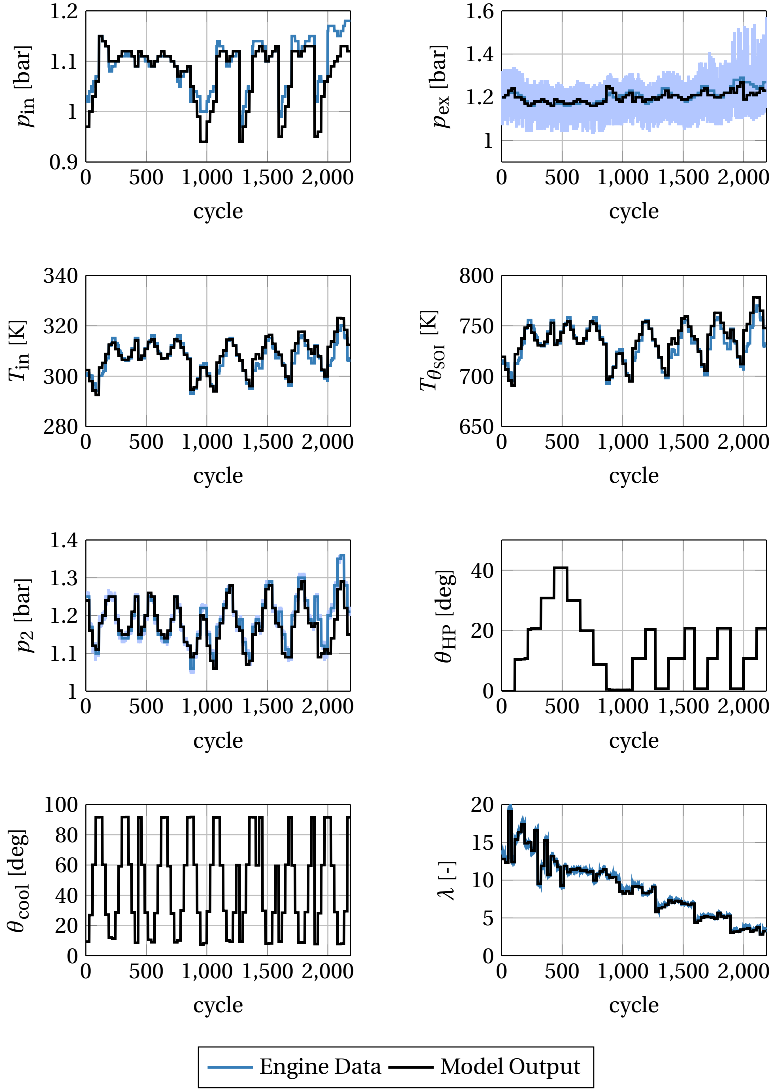

Figure 2.4 Model output (black) and measured data (blue) for a local minimizer ϑ^* of (2.39). The light blue color indicates cycle-to-cycle variation in the intake and exhaust manifolds. The engine data presented are combined sequences of steady-state data with different θ_{Cool} and θ_{EGR} positions for p_{IMEPn} from 1 to 5 bar. The model managed to capture in-cylinder temperature at the start of injection $T_{\theta_{SOI}}$ and the relative air-fuel ratio λ.

Cylinder Oxygen Concentration

The EGR mass flow reduces the cylinder oxygen concentration, which in turn affects chemical reaction rates and the ignition delay. The oxygen concentration was for this reason an important ignition-delay model input and was computed from air-flow measurements and estimated EGR mass flow according to the following description. The oxygen concentration at intake-valve closing $[O_2]_{IVC}$ is determined by the oxygen in the inducted air, EGR, and residual gas

$$[O_2]_{IVC} = \chi_{O_2}^{air} \frac{120\dot{m}_{air}}{6M_{air}V_d N_{speed}} + \chi_{O2}^{ex} \left(\frac{120\dot{m}_{EGR}}{6M_{ex}V_d N_{speed}} + \frac{m_{res}}{M_{ex}V_d} \right) \tag{2.41}$$

where $\dot{m}_{air}$ is the measured engine air flow, M_{air}, M_{ex}, $\chi_{O_2}^{air}$ and $\chi_{O_2}^{ex}$ are molar masses and oxygen molar fractions of air and exhaust. The latter was computed from λ-sensor measurements. A Kalman filter [Kalman, 1960] (see Chapter 3) was then used to estimate the EGR mass flow from both EGR paths $\dot{m}_{EGR}$ with the use of the intake-manifold pressure model

$$\frac{dp_{in}}{dt} = \frac{RT_{in}}{V_{in}}(\dot{m}_{air} + \dot{m}_{EGR} - \dot{m}_{cyl}^{in}) + \frac{p_{in}}{T_{in}}\frac{dT_{in}}{dt} \tag{2.42}$$

A similar EGR-estimation technique was presented in [Lee et al., 2013]. The residual-gas mass m_{EGR} was computed using the state in the exhaust manifold at exhaust valve opening (EVO)

$$m_{res} = \frac{p_{ex}V_{EVO}}{RT_{ex}} \tag{2.43}$$

This method was used to compute $[O_2]_{IVC}$ online in Chapter 7, where $[O_2]_{IVC}$ was used to predict ignition-delay variation.

2.4 Ignition-Delay Modeling

The ignition delay is an important variable in PPC where it should be kept sufficiently long for the fuel to mix with the cylinder-gas mixture before the start of combustion. In a direct-injection combustion engine, the ignition delay depends on physical processes such as fuel atomization, vaporization and the mixing of fuel and air in the cylinder. It also depends on chemically controlled autoignition reactions [Heywood, 1988]. Here, the ignition delay τ is defined as the time in milliseconds between θ_{SOI} and the crank angle of 10 % heat released θ_{10}, which was used as an indicator for ignition, see Fig. 2.5

$$\tau = \frac{\theta_{10} - \theta_{SOI}}{0.006N_{speed}} \tag{2.44}$$

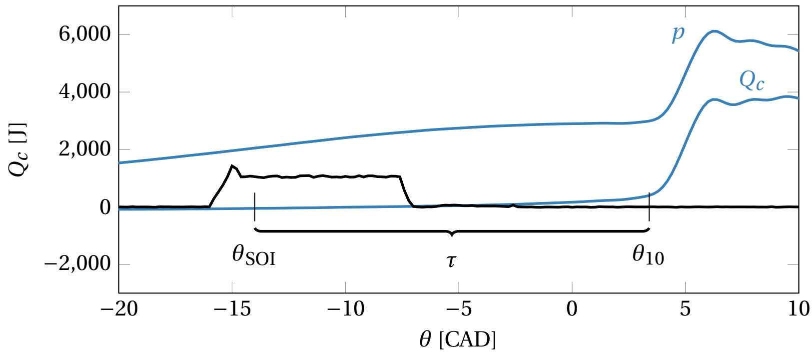

Figure 2.5 The ignition delay τ was defined as the time between the start of injection θ_{SOI} and the crank angle of 10 % heat released θ_{10}. This indicator for the start of combustion was computed from the accumulated heat release Q_c. The start of injection was here determined by the rising flank of the injector-current pulse and a hydraulic injector delay.

For the purpose of controller design, autoignition models that correlate τ with the cylinder-gas state were studied under the assumption that the chemically controlled part of τ contributes most to its variability. This assumption is valid for longer τ where the relative importance of autoignition is high. The relative importance of physical factors becomes more important for shorter τ [Heywood, 1988].

Detailed reaction mechanisms for larger hydrocarbons consist of thousands of species and tens of thousands of reactions [Lu and Law, 2009]. Model complexity can be reduced by removing or lumping reactions of less importance, or by building empirical models that uses a sufficient number of species and reactions to capture experimental τ data. A well-known example of the latter is the global reaction mechanism with five representative species and eight reactions developed by Halstead et al. [1975, 1977]. This model was able to accurately predict two-stage ignition of alkanes under engine-like conditions in a rapid compression machine.

The empirical modeling approach was adopted in this work, where three different low-order models denoted M1, M2 and M3 with increasing complexity were evaluated. An additional model, M4, derived from chemical-reaction simulations by Delvescovo et al. [2016] was used to simulate τ for different octane numbers, for the purpose of evaluating the fuel-reactivity effect on combustion-timing controller design. A reason for using simpler ignition-delay models was the need to simulate in the order of 10^7 engine cycles when evaluating different controller parameters in Chapter 6. Another reason was the requirement for computational times below the engine-cycle duration when regulating τ in Chapter 7. Models M1 to M4 are presented in the following sections.

Evaluation of M1, M2 and M3

The three low-order autoignition models, M1, M2, and M3, were evaluated for the purpose of model-based control. The evaluation was done by studying how well these models, when calibrated, could predict experimental τ data for different injection timings, intake temperatures and oxygen concentrations, in the low-to-mid load and speed range of the engine. The complexity of linearizing the models for controller design was also investigated. Another reason for evaluation the models was to gain a better understanding of the model complexity needed to predict experimental data.

These models are based on the fact that the reaction rate for a chemical reaction with two species, B and C, is proportional to the concentrations of the reactants via a rate coefficient k_{reac}

$$\frac{d[B]}{dt} = -k_{\text{reac}}[B][C] \tag{2.45}$$

The rate coefficient is usually modeled with a temperature dependent Arrhenius expression

$$k_{\text{reac}} = Ae^{-E_a/\tilde{R}T} \tag{2.46}$$

where A is a collision-frequency constant, $\tilde{R}$ is the universal gas constant, and E_a is an activation energy. Although combustion proceeds in multiple steps, a useful approximation can be obtained by modeling the reaction rate as a single mechanism [Turns, 1996]

$$\frac{d[C_xH_y]}{dt} = -A[C_xH_y]^a[O_2]^b e^{-E_a/\tilde{R}T} \tag{2.47}$$

where $[C_xH_y]$ and $[O_2]$ are fuel and oxygen concentrations, and a and b are empirical parameters.

M1

The first model is given by the following inverted reaction-rate expression

$$\tau = A\overline{[\mathrm{O_2}]}^{\alpha}\,\overline{[\mathrm{C_xH_y}]}^{\beta}\,\bar{p}^{\zeta} S_p^{\delta} e^{E_a/\tilde{R}\bar{T}} \tag{2.48}$$

where A, E_a, α, β, ζ and δ are fuel-dependent empirical parameters, and the notation $\bar{X}$ denote the average X between θ_{SOI} and θ_{10}, under the assumption that all fuel has been injected. The unknown model parameters

$$\vartheta_{M1} = [A, E_a, \alpha, \beta, \zeta, \delta]^T \tag{2.49}$$

are to be identified from engine data.

Similar models were presented by [Heywood, 1988] and were used by Kempinski and Rife [1981] and also by Donald and Eyzat [1978] to parameterize τ for different fuels and engines.

M2

The second model is a crank-angle resolved extension of M1 where it is assumed that combustion starts when

$$\int_{\theta_{\mathrm{SOI}}}^{\theta_{\mathrm{SOI}}+\tau} A[\mathrm{O_2}]^{\alpha}[\mathrm{C_xH_y}]^{\beta} p^{\zeta} S_p^{\delta} e^{-E_a/\tilde{R}T} d\theta = 1 \tag{2.50}$$

is fulfilled. The integral relation can be interpreted as an autoignition criterion, where combustion is initiated when a critical number of radicals is reached [Chiang and Stefanopoulou, 2009]. The unknown model parameters are here given by

$$\vartheta_{M2} = [A, E_a, \alpha, \beta, \zeta, \delta]^T \tag{2.51}$$

This model was previously presented by Thurns [1996] and Chmela et al. [2007] among others.

M3

The third model is a two-stage reaction model with empirically determined reaction rates as presented in [Westbrook and Dryer, 1981]

$$\begin{aligned} \mathrm{C_xH_y} + \left(\frac{x}{2} + \frac{y}{4}\right)\mathrm{O_2} &\xrightarrow{k_1} x\mathrm{CO} + \frac{y}{2}\mathrm{H_2O} \\ \mathrm{CO} + \frac{1}{2}\mathrm{O_2} &\xrightarrow{k_2} \mathrm{CO_2} \end{aligned} \tag{2.52}$$

Here, the fuel C_xH_y reacts with O_2 to form CO and H_2O in the first reaction, CO is then oxidized to CO_2 in the second reaction. Reaction rates are given by the following differential equations

$$\begin{aligned} \frac{d[\mathrm{C_xH_y}]}{dt} &= -k_1[\mathrm{C_xH_y}]^{\beta}[\mathrm{O_2}]^{\alpha} \\ \frac{d[\mathrm{O_2}]}{dt} &= -\left(\frac{x}{2} + \frac{y}{4}\right)k_1[\mathrm{C_xH_y}]^{\beta}[\mathrm{O_2}]^{\alpha} - k_2[\mathrm{CO}][\mathrm{O_2}]^{1/2} \\ \frac{d[\mathrm{CO}]}{dt} &= xk_1[\mathrm{C_xH_y}]^{\beta}[\mathrm{O_2}]^{\alpha} - k_2[\mathrm{CO}][\mathrm{O_2}]^{1/2} \\ \frac{d[\mathrm{CO_2}]}{dt} &= k_2[\mathrm{CO}][\mathrm{O_2}]^{1/2} \end{aligned} \tag{2.53}$$

Initial conditions for (2.53) are given by the global cylinder oxygen and fuel concentrations after fuel injection. The reaction-rate parameters k_i are empirical expressions on the form

$$k_i = A_i S_p^{\delta_i} e^{-E_a^i/\tilde{R}T} \tag{2.54}$$

Finally, the heat-release rate of the reactions is computed from

$$\frac{dQ_c}{dt} = V(Q_1 k_1[\mathrm{C_xH_y}]^{\beta}[\mathrm{O_2}]^{\alpha} + k_2 Q_2[\mathrm{CO}][\mathrm{O_2}]^{1/2}) \tag{2.55}$$

Table 2.1 Investigated operating points for model calibration and evaluation.

	L1S1	L2S1	L1S2	L2S2
N_{speed} [rpm]	1200	1200	1500	1500
p_{IMEPg} [bar]	5	10	5	10
T_{in} [°C]	20 - 40	22 - 60	22 - 50	38 - 85
$[O_2]_{\text{IVC}}$ [mol/m^3]	7.5 - 9.5	9.5 - 11.5	7.5 - 10	8.5 - 13
θ_{SOI} [CAD]	-25 - (-5)	-10 - 2	-25 - 5	-15 - 0

where Q_1 and Q_2 are the lower heating values per mole of fuel and CO in (2.53). Combustion is assumed to start when Q_c has reached 10 % of the expected total heat released Q_c^{tot}. For M3, unknown model parameters are given by

$$\vartheta_{M3} = [A_1, A_2, E_a^1, E_a^2, \alpha, \beta, \delta_1, \delta_2]^T \tag{2.56}$$

Ignition-Delay Experiments

Ignition-delay experiments were conducted at the four operating points obtained by combining $p_{\text{IMEPg}} = 5, 10$ bar and $N_{\text{speed}} = 1200, 1500$ rpm, see Table 2.1. Suitable θ_{SOI} were found at each operating point with EGR valves closed and both thermal-management valves opened at 45°. A layout of the experimental engine setup showing valve locations was presented in the section covering gas-exchange modeling above, see Fig. 2.3.

In order to investigate the τ response to different engine inputs, θ_{SOI}, thermal-management ($\theta_{\text{cool/hot}}$) and EGR-valve positions ($\theta_{\text{HP/LP}}$) were varied manually in steps during a total of 12000 cycles at each operating point.

The thermal-management valve positions were changed by setting

$$\theta_{\text{cool}} = \cos^{-1}(1 - \cos(\theta_{\text{hot}})) \tag{2.57}$$

and varying θ_{hot} in order to keep an approximately constant total valve-opening area. The low-pressure EGR path was used to adjust EGR flow at the higher load operating points while the high-pressure EGR path was used at the lower load operating points. The reason for doing so was an insufficient pressure difference over the high-pressure EGR valve at higher loads. The resulting data can be viewed in Figs. 2.6-2.9 where T_{in}, $[O_2]_{\text{IVC}}$, θ_{SOI} and τ for one of the six cylinders are presented.

The first half of the cycles τ^{ID} were used for model calibration and the other half τ^{VAL} for model validation. This approach of evaluating model performance is called cross validation and is a technique for evaluating how well parameter-identification results generalize to an independent data set. This is done to avoid overfitting with respect to the identification data set [Geisser, 1993].

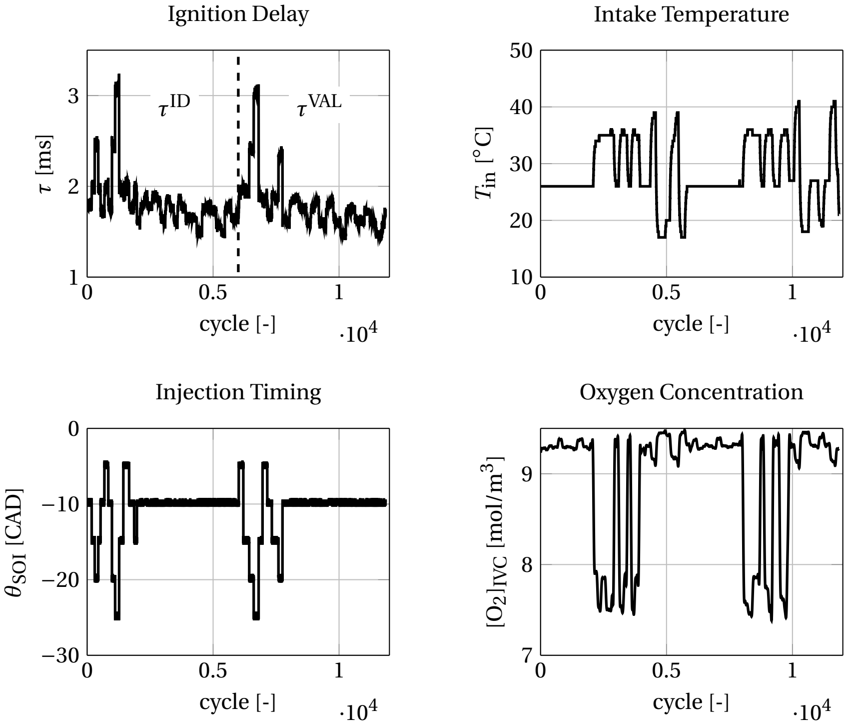

Figure 2.6 Experiment data at operating point L1S1, top left: τ [ms], top right: T_{in} [C], bottom left: θ_{SOI} [CAD ATDC] and bottom right: $[O_2]_{\mathrm{IVC}}$ [mol/m^3].

Parameter Identification

Sum-of-squares model-error cost functions $J_{Mx}(\tau^{\mathrm{ID}}, \vartheta_{Mx})$ were minimized for each model with respect to ϑ_{M1-3} and the identification data set τ^{ID} to identify suitable model parameters.

M1 If logarithms are applied to both sides of (2.48), the problem of minimizing the sum of squares

$$J_{M1}(\tau^{\mathrm{ID}}, \vartheta_{M1}) = \sum_{i=1}^{N} \left(\ln(\tau_i^{\mathrm{ID}}) - \ln(\tau_i^{M1})\right)^2 \tag{2.58}$$

with respect to ϑ_{M1} is a linear regression, where the index i denotes sample number and N is the number of samples. In the following notation

$$\mathbf{y} = \begin{pmatrix} \ln(\tau_1^{M1}) & \dots & \ln(\tau_N^{M1}) \end{pmatrix}^T \tag{2.59}$$

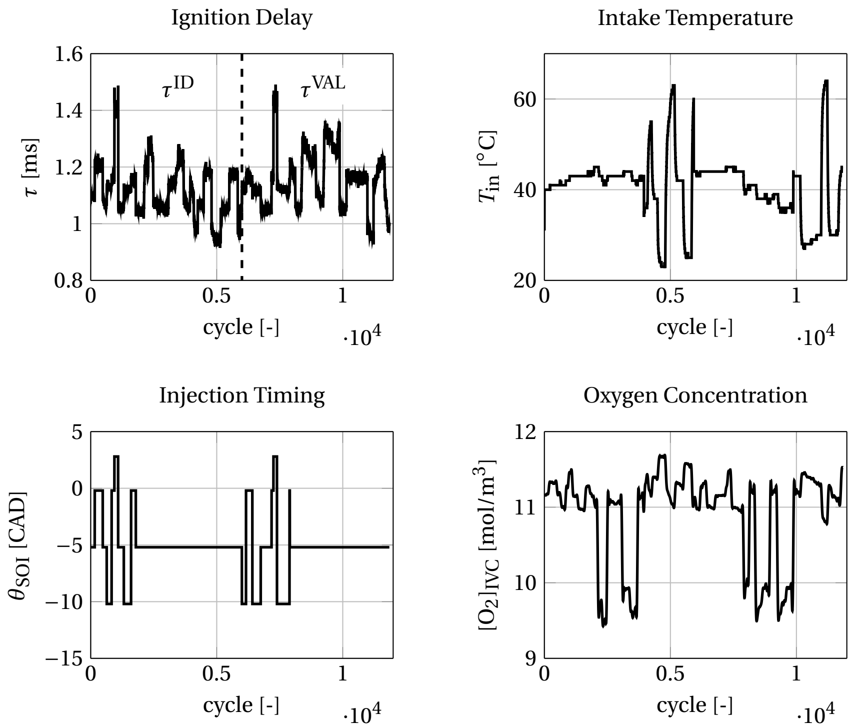

Figure 2.7 Experiment data at operating point L2S1.

$$\Phi = \begin{pmatrix} 1 & \dfrac{1}{\tilde{R}\bar{T}_1} & \ln(\overline{[\mathrm{O_2}]}_1) & \ln(\overline{[\mathrm{C_xH_y}]}_1) & \ln(\bar{p}_1) & \ln(S_{p_1}) \\ \vdots & \vdots & \vdots & \vdots & \vdots & \vdots \\ 1 & \dfrac{1}{\tilde{R}\bar{T}_N} & \ln(\overline{[\mathrm{O_2}]}_N) & \ln(\overline{[\mathrm{C_xH_y}]}_N) & \ln(\bar{p}_N) & \ln(S_{p_N}) \end{pmatrix} \tag{2.60}$$

the minimizer of (2.58), $\vartheta^* = \begin{pmatrix} \ln(A^*) & E_a^* & \alpha^* & \beta^* & \zeta^* & \delta^* \end{pmatrix}^T$, is given by

$$\vartheta^* = (\Phi^T\Phi)^{-1}\Phi^T\mathbf{y} \tag{2.61}$$

Linear-regression problems and the least-squares method are described in greater detail in [Johansson, 1993].

M2 For the second model, parameters were found by minimizing

$$J_{M2}(\tau^{\mathrm{ID}}, \vartheta_{M2}) = \sum_{i=1}^{N} \left(\int_{\theta_{\mathrm{SOI}}}^{\theta_{\mathrm{SOI}}+\tau_i^{\mathrm{ID}}} A[\mathrm{O_2}]_i^{\alpha}[\mathrm{C_xH_y}]_i^{\beta} p_i^{\zeta} S_{p,i}^{\delta} e^{-E_a/(\tilde{R}T_i)}\, dt - 1 \right)^2 \tag{2.62}$$

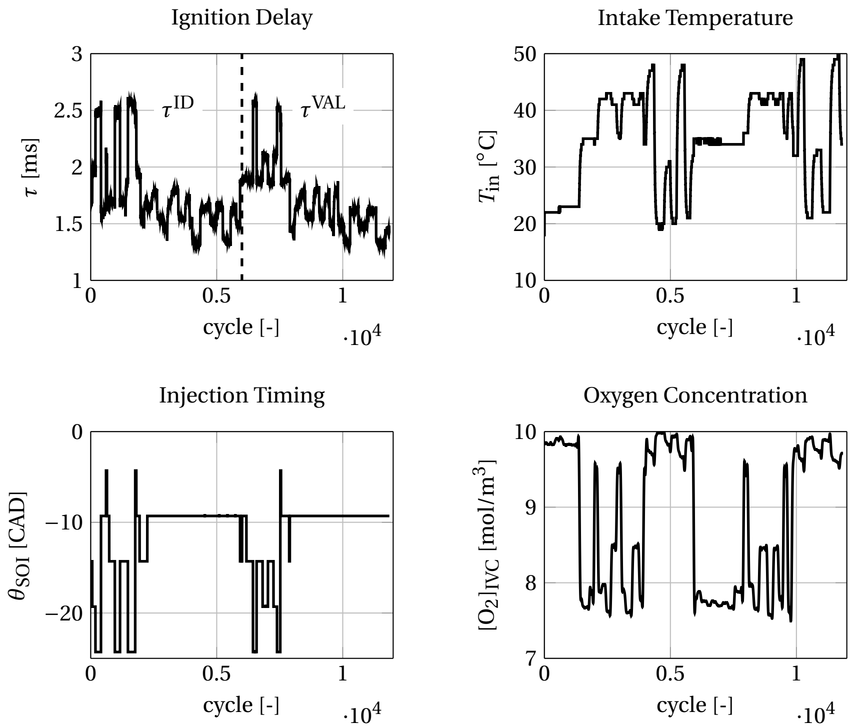

Figure 2.8 Experiment data at operating point L1S2.

This is not a linear regression, without a closed-form expression for the minimizer. The cost function was therefore minimized numerically, using the MATLAB Optimization Toolbox. In order to avoid local minima, (2.62) was minimized with respect to different initial parameters.

M3 The reaction-rate parameters of the third model were found using the same numerical procedure as for M2. The chemical reactions were simulated by approximating the derivatives in (2.53) using the forward-Euler method and a sufficiently small step size, $h = 0.01$ ms. The model parameters were then found by minimizing

$$J_{M3}(\tau^{\mathrm{ID}}, \vartheta_{M3}) = \sum_{i=1}^{N} \left(Q_{c,i}^{M3}(\theta_{10,i}^{\mathrm{ID}}) - 0.1 m_{f,i} Q_{\mathrm{LHV}} \right)^2 \tag{2.63}$$

where $Q_{c,i}^{M3}(\theta_{10,i}^{\mathrm{VAL}})$ is the modeled accumulated heat-release at θ_{10} in the identification-data set, and $m_{f,i} Q_{\mathrm{LHV}}$ is the injected fuel energy, computed from fuel-flow measurements.

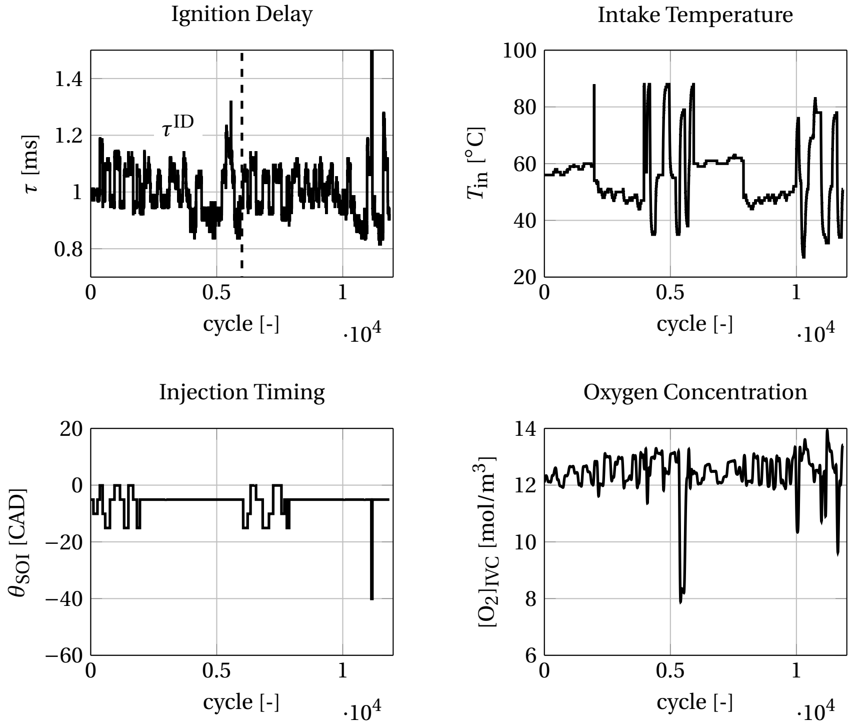

Figure 2.9 Experiment data at operating point L2S2. Unfortunately, the last 2000 cycles of τ^{ID} were corrupted due to a malfunctioning thermal-management valve. This part of τ^{ID} was therefore replaced with the last 2000 cycles of τ^{VAL}. Note the unintentional decrease in θ_{SOI} after cycle 11000. It was decided to be keep these data points in the sets τ^{ID} and τ^{VAL}.

Model Evaluation

The three models were evaluated by how well they could explain variation in the validation-data set τ^{VAL} in two different ways:

- By how well a model calibrated by τ^{ID} from one operating point could predict τ^{VAL} from the same operating point. During model calibration, the speed dependence was removed ($\delta = 0$). The load dependence was also removed by setting $\beta = 0$ in M1-2 and $\beta = 1$ in M3. Furthermore, M1 and M2 were investigated with and without pressure dependence, i.e., with ζ free and $\zeta = 0$.

- By how well a model calibrated with the complete τ^{ID} data set could predict the complete τ^{VAL} data set. Now, β and δ were free parameters during model calibration.

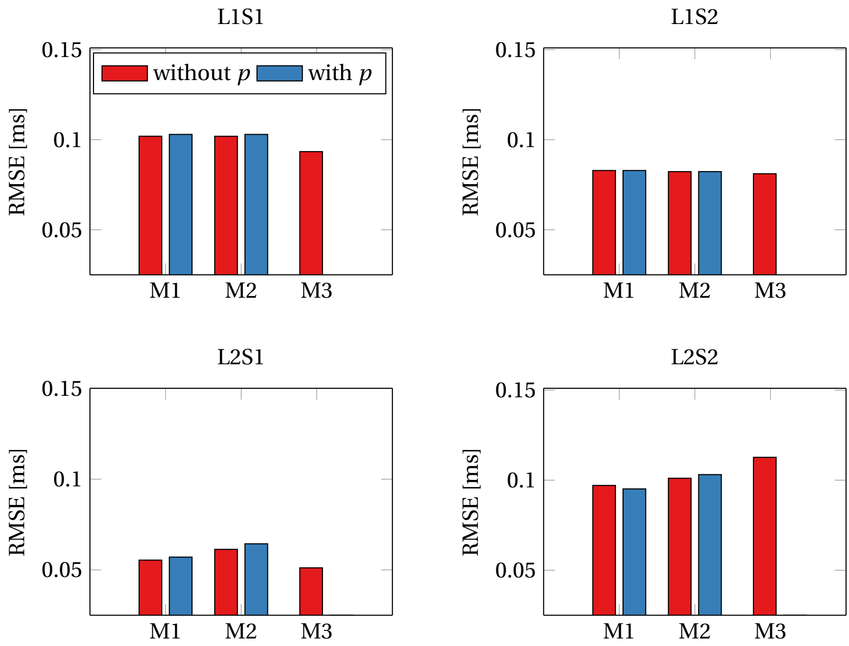

Figure 2.10 Model RMSE with respect to validation data for M1, M2 and M3 at each operating point. Including p dependence in M1 and M2 did not give any improvement. Increasing model complexity from M1 to M2 and M3 did not necessarily yield a smaller prediction error.

The reason for evaluating the models with respect to these two aspects was to determine if there is an incentive to use multiple models with fewer parameters, instead of having one model that covers all operating points with more parameters. Model performance was evaluated by computing the root-mean-square error

$$\mathrm{RMSE}_{Mx} = \sqrt{\frac{1}{N}\sum_{i=1}^{N}(\tau_i^{Mx} - \tau_i^{\mathrm{VAL}})^2} \tag{2.64}$$

where τ^{Mx} is the model output and τ^{VAL} is measured τ in the validation-data set.

Individual Operating Points

Model RMSE scores with respect to individual operating points are presented in Fig. 2.10. The blue and red bars indicate RMSE with and without p dependence.

It can be seen that including p did not improve performance significantly. It rather increased error slightly, which could be a sign of overparameterization. Increasing model complexity from M1 to M2 decreased performance at L2S1 and

Table 2.2 Complexity in number of arithmetic operations where addition, subtraction and multiplication are all considered to be one operation. N is the number of samples between θ_{SOI} and θ_{10}, and τ/h is the ratio of τ and the step size used in the forward-Euler approximation. From the author's experience, h should be smaller than 0.05 ms. * = crank angle resolution of 0.2 CAD, and τ = 10 CAD. ** = $\tau/h = 300$.

Model	Arithmetic Operations	Example
M1	$7N$	750^*
M2	$43N$	2150^*
M3	$105\tau/h$	31500^{**}

L2S2 but not at L1S1 and L1S2. Increasing model complexity from M2 to M3 improved model performance in all operating points but L2S2.

For a more detailed analysis, the model outputs are displayed together with τ^{VAL} in Figs. 2.11-2.14, where the gray dots indicate τ^{VAL} and the red, blue and green lines are model outputs from M1, M2 and M3 without pressure dependence.

In Fig. 2.11, the model outputs did not follow τ^{VAL} well around cycles 100 and 1000. This occured when θ_{SOI} was delayed at cycles 6100 and 7000 in Fig. 2.8. The same behavior is found in Fig. 2.12 from cycle 1 to 800, in Fig. 2.13 at cycle 200, and in Fig. 2.14 at cycles 500 and 1500. As θ_{SOI} was delayed close to TDC, the computed T during τ increased which caused the models to predict a decreased τ. Instead, the measured τ^{VAL} increased. Hence, the models were incapable of anticipating the point where a delayed θ_{SOI} started to increase τ. This behavior can clearly be seen in Fig. 2.12 at cycle 1400, where an increase in θ_{SOI} resulted in a large increase in τ^{VAL}. The models were overall better at predicting τ^{VAL} during variations in T_{IVC}, $[O_2]_{\text{IVC}}$ and θ_{SOI} for early θ_{SOI}, see cycle 750 in Fig. 2.11.

Similar model outputs for M1, M2 and M3 in Figs. 2.11-2.14 indicate that controller designs based on the different models would yield comparable performance.

All operating points

The models were also calibrated with the complete τ^{ID} data set to see how well one model could predict the overall τ behavior. The parameters β and δ were free parameters during identification for model M1-2, and β and δ_1 were free parameters during identification for M3. The RMSE scores are presented in Fig. 2.15, where the green bars indicate total RMSE for the individual operating-point models in Fig. 2.10 for comparison.

Increasing model complexity from M1 to M3 resulted in an increased RMSE, and using operating-point individual models gave a slight reduction in RMSE. Modeled τ for all operating points is presented together with τ^{VAL} in Fig. 2.16.

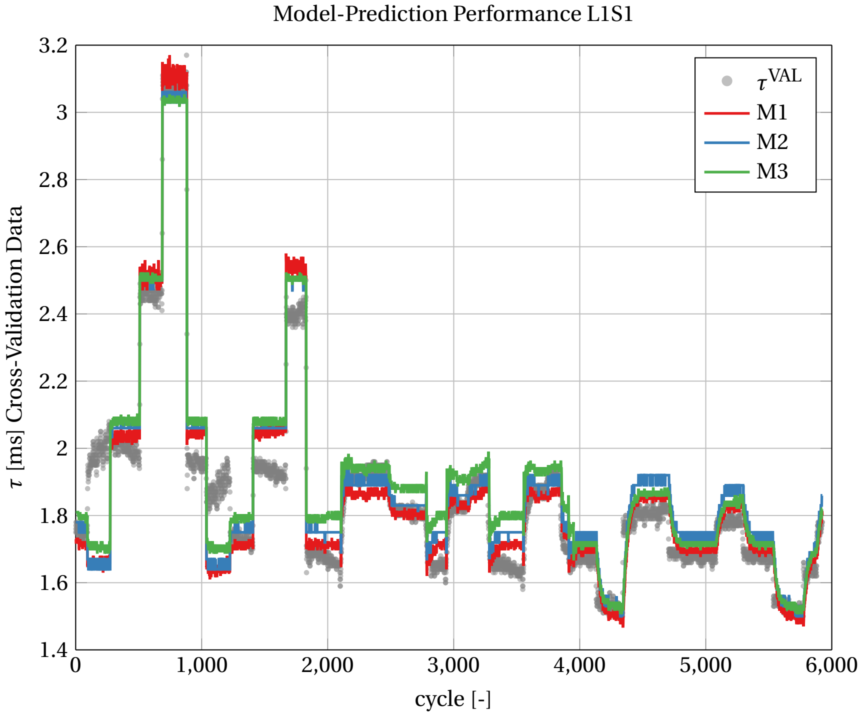

Figure 2.11 Modeled τ together with τ^{VAL} from operating point L1S1. It can be noted that the models did not follow τ^{VAL} well at cycles 100 and 1000. M1 had overall comparable performance to M2 and M3.

Linearization for Control Purposes

For the purpose of model-based controller design, it is of interest to linearize the models with respect to the system inputs T_{IVC}, $[\text{O}_2]_{\text{IVC}}$ and θ_{SOI}, at an arbitrary operating point

$$X^0 = \begin{pmatrix} T^0_{\text{IVC}} & [\text{O}_2]^0_{\text{IVC}} & \theta^0_{\text{SOI}} \end{pmatrix}^T \tag{2.65}$$

to obtain a linear cycle-to-cycle model on the form

$$\tau(k+1) = \tau(k) + \frac{\partial \tau(X^0)}{\partial T_{\text{IVC}}} \Delta T_{\text{IVC}}(k) + \frac{\partial \tau(X^0)}{\partial [\text{O}_2]_{\text{IVC}}} \Delta [\text{O}_2]_{\text{IVC}}(k) + \frac{\partial \tau(X^0)}{\partial \theta_{\text{SOI}}} \Delta \theta_{\text{SOI}}(k) \tag{2.66}$$

where Δ is the forward-difference operator and k denotes cycle index. The linear model could then easily be incorporated in controller design frameworks

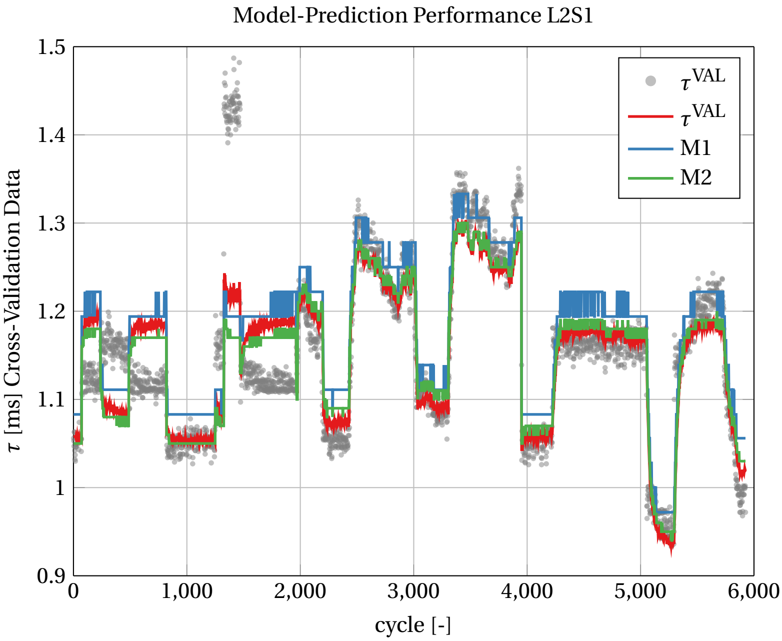

Figure 2.12 Modeled τ together with τ^{VAL} from operating point L2S1. The model mismatch at cycle 1400 is an example of where θ_{SOI} was increased and the models underestimated τ^{VAL}. The models were overall better at predicting τ^{VAL} during variations in T_{IVC}, $[\mathrm{O}_2]_{\mathrm{IVC}}$ and θ_{SOI} for early θ_{SOI}.

such as linear quadratic Gaussian (LQG) control [Kalman, 1960] or linear model predictive control [Maciejowski, 2002]. Linearization of M1, M2 and M3 can be conducted by approximating the partial derivatives numerically

$$\frac{\partial \tau(X^0)}{\partial X} \approx \frac{\tau(X^0 + \Delta X) - \tau(X^0)}{\Delta X} \tag{2.67}$$

The computational complexity of (2.67) in terms of arithmetic operations are presented in Table 2.2 for the different models. Addition, subtraction, multiplication and taking powers were counted as one operation. In Table 2.2, N is the number of samples between θ_{SOI} and θ_{10}, τ/h is the ratio of τ to the step size h used in the forward-Euler approximation when simulating M3. From the author's experience, h should be smaller than 0.05 ms. The values in Table 2.2 are by no means shown to be the most efficient implementation of (2.67), nevertheless, they originate from the implementation used in this work. The results show that M1 and M2 are superior in terms of simplicity, at least if (2.67) should be computed by a controller every engine cycle.

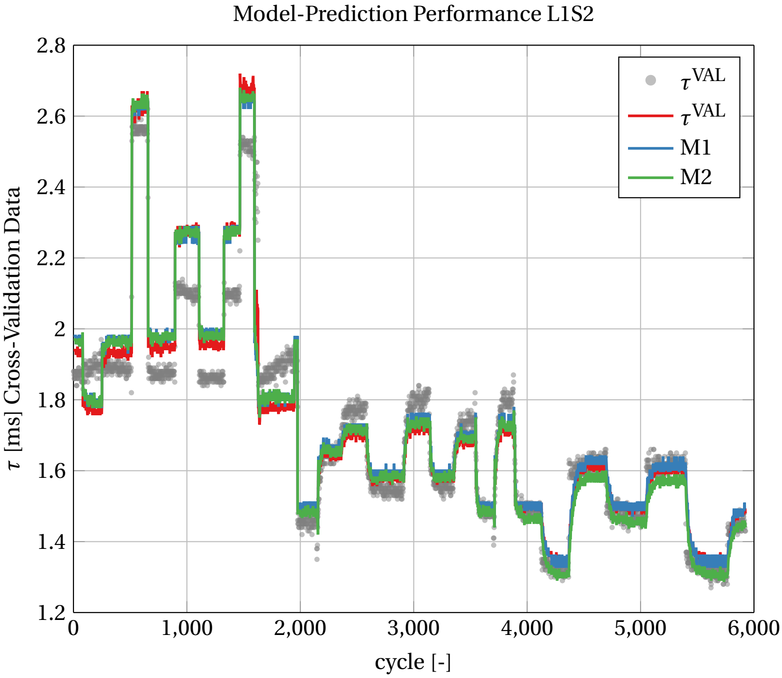

Figure 2.13 Modeled τ together with τ^{VAL} from operating point L1S2.

Discussion

The models could not accurately detect when an increase in θ_{SOI} started to give an increase in τ. If this was caused by errors in the estimated cylinder-gas state, errors in the heat-release analysis or by the fact that the models did not account for spatial and physical effects is not known. Model performance was however more acceptable when θ_{SOI} was advanced earlier during the compression stroke and when T_{IVC} and $[O_2]_{\mathrm{IVC}}$ were varied. This implies that it is easier to obtain satisfactory controller performance when regulating τ using T_{IVC} and $[O_2]_{\mathrm{IVC}}$, unless θ_{SOI} is sufficiently far away from TDC. When evaluating performance for all operating points simultaneously (see Fig. 2.16), model performance decreased with complexity. Small improvements could be obtained when using four local models instead of one global model.

The results were somewhat unambiguous when comparing model performance, and it was only worthwhile to increase model complexity in some cases, (see L1S1, L2S1, Fig. 2.10). When studying Figs. 2.11-2.14, it can be seen that model performance did not differ significantly in most cases. When taking into account for the computational cost of linearization, M1 was superior to M2 and M3 (see Table 2.2). Furthermore, M1 had a closed-form expression (2.61) for

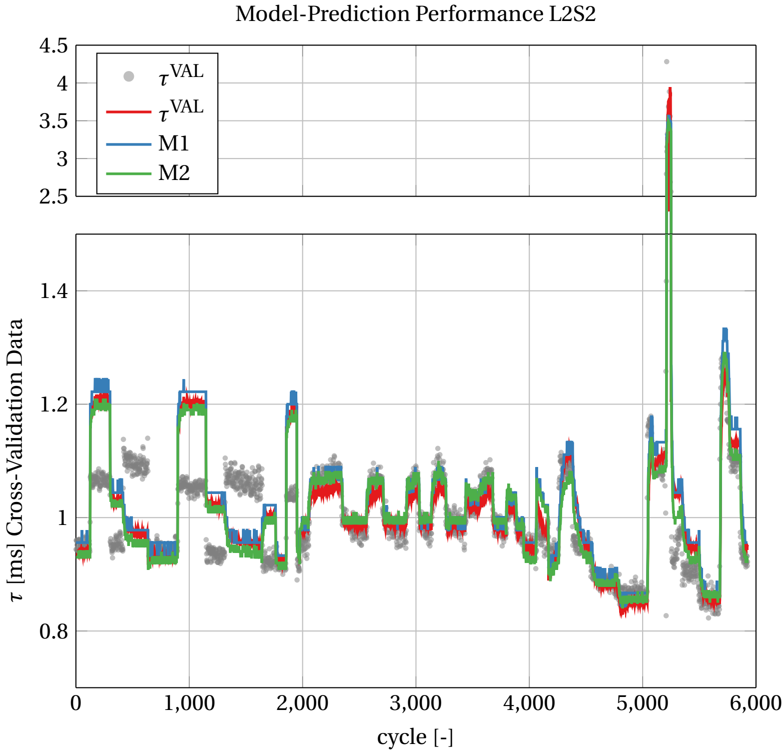

Figure 2.14 Modeled τ together with τ^{VAL} from operating point L2S2. Note that the models were able to predict the steep increase in τ as θ_{SOI} was decreased around cycle 5250. The reason for this was that cycles 4000-6000 at L2S2 were included τ^{ID}, see Fig. 2.9.

parameter calibration. Based on these findings, M1 was the suitable choice for model-based controller design, and was therefore used by the model predictive controller in Chapter 7.

These models did not include effects from cylinder-wall temperature, fuel vaporization, atomization and fuel-spray interaction with the combustion chamber walls. If carefully modeled, these effects are believed to improve the model performance. However, information from these effects were not easily accessible from the sensors available, making the validation of these effects difficult.

M4

The ignition-delay models presented above did not take fuel reactivity into account. One of the main motivators for closed-loop combustion control is the possibility to handle fuel variation. The octane-number dependent τ correlation

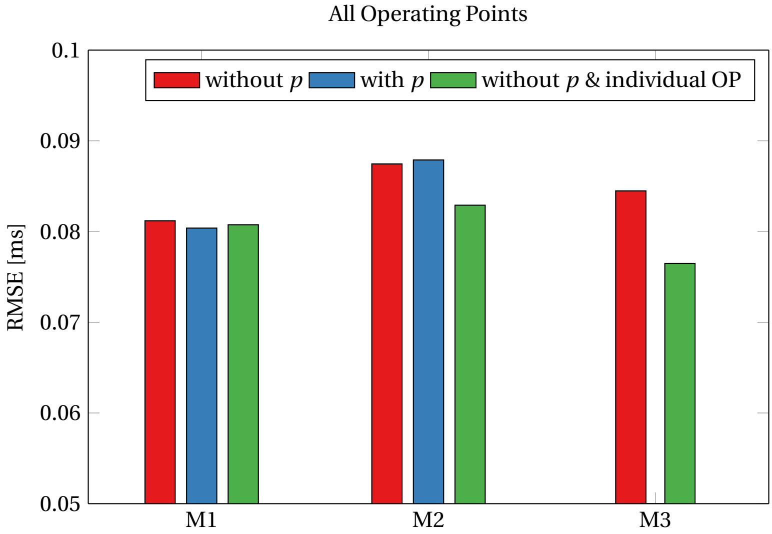

Figure 2.15 RMSE with respect to validation data. Increasing the model complexity from M1 to M2 and M3 increased RMSE, and using individual operating-point models gave a slight reduction in RMSE. Increased prediction performance could therefore be obtained by switching between different models instead of using one model for all operating points.

presented by Delvescovo et al. [2016]

$$\tau = \phi^{\alpha(T,\mathrm{PRF})} p^{\beta(T,\mathrm{PRF})} x_{O_2}^{\zeta(T,\mathrm{PRF})} e^{\Lambda(T,\mathrm{PRF})} \tag{2.68}$$

was therefore used in Chapter 6 to investigate how the fuel reactivity affects controller design. This model was developed for primary-reference fuel (PRF) blends from PRF0 (n-heptane) to PRF100 (iso-octane) and was calibrated with data from constant-volume simulations in Cantera, using a reduced gasoline-surrogate kinetic mechanism. Note that the PRF value and octane number are equal per definition. In (2.68), ϕ denotes equivalence ratio, p denotes pressure, and x_{O_2} is the mole fraction of oxygen of the inducted gas. The parameters α, β, ζ and Λ are temperature-dependent polynomials multiplied with a PRF-dependent exponential expression, yielding roll-off at low temperatures. Delvescovo et al. [2016] calibrated the polynomial coefficients with respect to simulated τ data at the following conditions

- initial temperatures from 570-1860 K
- initial pressures from 10-100 bar
- mole fractions of oxygen from 12.6 % to 21 %

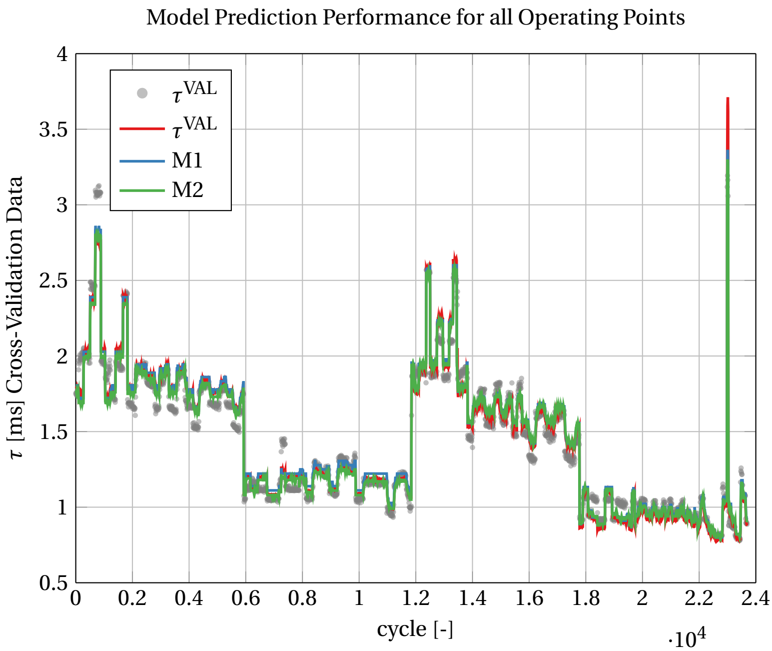

Figure 2.16 Modeled τ together with τ^{VAL} for all operating points.

- equivalence ratios from 0.30-1.5
- PRF blends from PRF0 to PRF100

to capture a wide range of engine-like operating conditions. With (2.68), the start of combustion θ_{SOC} was computed using a Livengood-Wu integration criterion [Livengood and Wu, 1955]

$$\int_{\theta_{SOI}}^{\theta_{SOC}} \frac{1}{\tau} dt = 1 \tag{2.69}$$

2.5 NO$_x$-formation Model

Oxides of nitrogen NO_x are regulated engine pollutants which are mainly produced by reactions between nitrogen and oxygen during combustion and expansion. A NO_x model was used both as a virtual sensor to provide a controller with the previous-cycle NO_x-emission level, and as a predictive model for NO_x regulation below an upper limit. For these purposes, the computation time needs to be sufficiently short for cycle-to-cycle control. A model that fulfills this requirement is the two-zone (burned and unburned gas) combustion model coupled with the Zeldovich mechanism

$$\begin{aligned} O + N_2 &\rightarrow NO + N \\ N + O_2 &\rightarrow NO + O \end{aligned} \tag{2.70}$$

that was previously developed for combustion-control purposes in [Egnell, 2001; Murić et al., 2014]. This model assumes NO_x formation through the thermal-formation path alone. Less dominant formation paths include reactions between nitrogen and unburnt hydrocarbons and reactions with nitrogen components in the fuel [Fenimore, 1971]. More detailed NO_x-formation models incorporate fuel-air mixing and the cylinder air-to-fuel ratio distribution, which affect the combustion temperature. An extensive NO_x-modeling review can be found in [Miller and Bowman, 1989].

The model used here separates the cylinder gases into a burned zone and an unburned zone. The unburned zone contains fuel, air and EGR, whilst the burned zone contains combustion products. When fuel and air react at a local air-fuel ratio, λ_{local}, the reaction products are moved from the unburned zone to the burned zone where combustion chemistry is assumed to be in equilibrium after combustion. The local air-fuel ratio λ_{local} was here used as a model-calibration parameter. Under these assumptions, the mass m_{bz} and temperature T_{bz} of the burned zone change every crank-angle increment $\Delta\theta$ according to

$$\begin{aligned} m_{bz}(\theta + \Delta\theta) &= m_{bz}(\theta) + \frac{1}{Q_{\text{LHV}}} \frac{dQ_c(\theta)}{d\theta}(1 + \lambda_{\text{local}} + r_{\text{EGR}})\Delta\theta \\ T_{bz}(\theta + \Delta\theta) &= T_{bz}(\theta) \left(\frac{p(\theta + \Delta\theta)}{p(\theta)}\right)^{\frac{\gamma - 1}{\gamma}} + \frac{1}{m_{bz}(\theta)c_p} \frac{dQ_c(\theta)}{d\theta}\Delta\theta \end{aligned} \tag{2.71}$$

where $dQ_c/d\theta$ is the heat-release rate, and r_{EGR} is the EGR ratio. The unburned-zone temperature T_{uz} changes due to isentropic compression and expansion alone

$$T_{uz}(\theta + \Delta\theta) = T_{uz}(\theta) \left(\frac{p(\theta + \Delta\theta)}{p(\theta)}\right)^{\frac{\gamma - 1}{\gamma}} \tag{2.72}$$

The NO-formation rate in the burned zone is given by

$$\frac{d[\text{NO}]}{dt} = \frac{2r_1\left(1 - \left(\frac{[\text{NO}]}{[\text{NO}]_e}\right)^2\right)}{1 + \frac{[\text{NO}]}{[\text{NO}]_e}\frac{r_1}{r_2}} - \frac{[\text{NO}]}{V}\frac{dV}{dt} \tag{2.73}$$

according to the Zeldovich mechanism [Zeldovich et al., 1947]. This expression assumes radical species in equilibrium where NO and O equilibrium concentrations, $[\text{NO}]_e$ and $[\text{O}]_e$, can be computed from combustion-product composition, temperature and equilibrium concentrations of the water-gas shift reaction. The last term in (2.73) is due to the time-varying cylinder volume. and the reaction rates r_1 and r_2 are given by

$$\begin{aligned} r_1 &= 7.6 \times 10^{13} [\mathrm{O}]_e [\mathrm{N}_2]_e e^{-38000/T_{bz}} \\ r_2 &= 1.5 \times 10^{9} [\mathrm{NO}]_e [\mathrm{O}]_e e^{-19500/T_{bz}} \end{aligned} \tag{2.74}$$

Formation of NO_2 is typically an order of magnitude smaller than NO and was therefore not modeled explicitly. The model could however anticipate the total amount of NO_x since NO_2 is formed from NO. For a more detailed description of this model, see [Egnell, 2001; Murić et al., 2014].

Model Calibration

The NO_x-model was calibrated with respect to experimental data. Figure 2.17 shows modeled NO_x coincidence with measured NO_x concentrations, obtained from engine experiments. The data originate from operating points at p_{IMEP} = 5 and 10 bar with 0 and 30 % EGR, with combustion timings from 0 to 15 CAD, pilot-injection durations from 0 to 0.4 ms, and with diesel ($\times$) and gasoline ($\circ$) fuel.

In Fig. 2.17, performance was found to degrade for low NO_x concentrations, especially with high EGR ratios where the model underestimated the measured NO_x emissions. An explanation for this could be that other formation paths become more important at these operating points. Possible improvement could be obtained by also including the N_2O formation path as described in [Gong and Rutland, 2013], which improves NO_x prediction at lower combustion temperatures. It can also be seen that model errors were larger for gasoline compared to diesel. The reason for this is unknown and deserves further investigation.

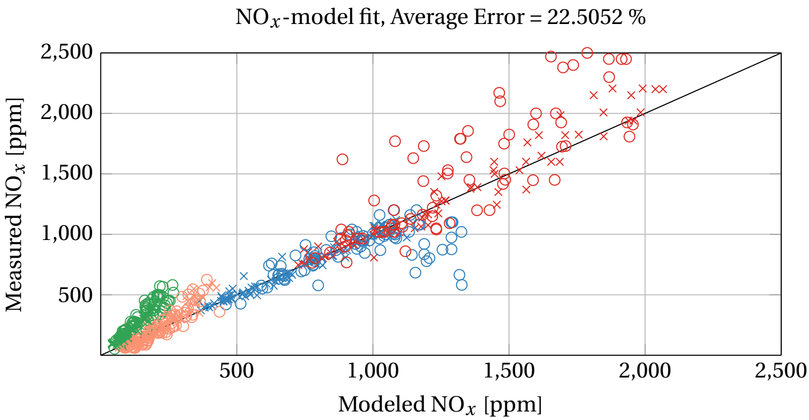

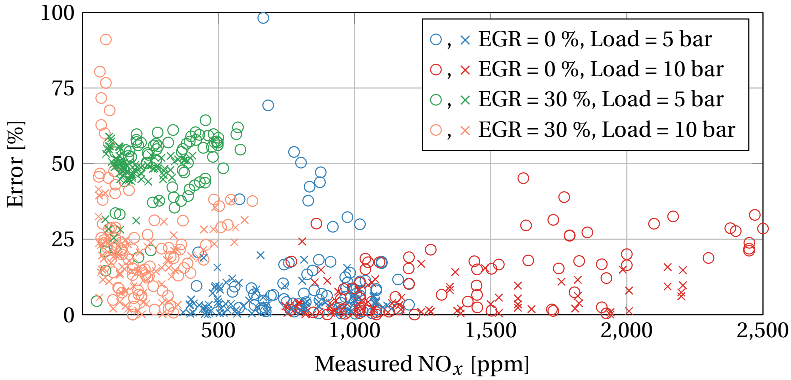

Figure 2.17 The NO_x model was calibrated at p_{IMEP} = 5 and 10 bar and 1200 rpm, with 0 and 30 % EGR, combustion timings from 0 to 15 CAD, pilot-injection durations from 0 to 0.4 ms, and with diesel (×) and gasoline (∘) fuel.

3

Control and Estimation Methods

This chapter gives a brief overview of the control and state-estimation methods used in the thesis.

3.1 Control Concepts

PI Control

The PI (Proportional Integral) controller is the most common solution to practical control problems [Åström and Hägglund, 2006]. A discrete-time PI controller, suitable for cycle-to-cycle control, is given by

$$u(k+1) = k_p e(k) + k_I \sum_{i=0}^{k-1} e(i) \tag{3.1}$$

where u is the controller output, e is the control-error, i.e., the system-output deviation from a set point, k is the cycle index, and k_p and k_I are controller gains. The controller in (3.1) is obtained by discretizing the continuous PI controller counterpart with a forward-Euler approximation.

The PI controller was used for many different purposes in this work. It was used to control p_{IMEP} by adjusting the fuel-injection duration, and to control the common-rail pressure p_{rail} by adjusting the inlet-metering valve position, which determines the fuel-flow to the common-rail volume. Chapter 6 investigates robust PI-controller tuning for combustion-timing control, and a hybrid PI controller was used in Chapter 10 for simultaneous tracking and constraint fulfillment with multiple injections.

PI controllers were used because of their simplicity with respect to tuning and implementation. A simple controller design is attractive if performance requirements are met. Previous research have also shown that PI control is a suitable option for combustion-control purposes [Bengtsson, 2004; Hanson, 2010].

Model Predictive Control

Model predictive control (MPC) is a control technique where a system model

$$\begin{aligned} \boldsymbol{x}(k+1) &= f(\boldsymbol{x}(k), \boldsymbol{u}(k)) \\ \boldsymbol{y}(k) &= h(\boldsymbol{x}(k)) \end{aligned} \tag{3.2}$$

is used to solve a finite horizon optimal-control problem every sample. Here, we denote the system state $\boldsymbol{x} \in \mathbb{R}^n$, the system input $\boldsymbol{u} \in \mathbb{R}^m$ and the measured output $\boldsymbol{y} \in \mathbb{R}^p$. The solution to the optimal-control problem is an open-loop sequence $U = \{\boldsymbol{u}(k)\}$ from $k = 1$ to H_c, where H_c is the control horizon, and $k = 0$ is the current sample. The first input of the optimal open-loop sequence $\boldsymbol{u}^*(1)$ is then repeatedly actuated. The input sequence is optimal in the sense that it minimizes a cost function

$$J(\boldsymbol{u}(k), \boldsymbol{y}(k)) = \sum_{k=1}^{H_p} J_y(\boldsymbol{y}(k)) + \sum_{k=1}^{H_c} J_u(\boldsymbol{u}(k)) + \rho_\epsilon \epsilon^2 \tag{3.3}$$

which consists of output costs $J_y(k)$ over a prediction horizon H_p and input costs $J_u(k)$ over a control horizon H_u. The output cost at sample k

$$J_y(\boldsymbol{y}(k)) = \sum_{j=1}^{p} \omega_{y_j} (y_j^r(k) - y_j(k))^2 \tag{3.4}$$

is the sum of the squared set-point deviations $y_j^r(k) - y_j(k)$ for each output y_j and corresponding set point y_j^r, scaled with a cost weight ω_{y_j}. The input cost at sample k

$$J_u(\boldsymbol{u}(k)) = \sum_{j=1}^{m} \omega_{u_j} u_j(k)^2 + \omega_{\Delta u_j} \Delta u_j(k)^2 \tag{3.5}$$

is the square sum of both absolute input values u_j and changes Δu_j with corresponding weights ω_{u_j} and $\omega_{\Delta u_j}$. The positive cost weights ω_x are controller design parameters that determine how the controller prioritizes different output errors and control actions.

Feedback is introduced by minimizing (3.3) subject to the system initial conditions $\boldsymbol{x}(0) = \boldsymbol{x}_0$, obtained from measurement or state estimation. The main feature of MPC is its ability to incorporate constraints with respect to inputs, outputs and states in the optimization problem

$$\begin{aligned} -\epsilon\eta_{\min}^{y} + y_{\min} &\le \boldsymbol{y}(k) \le y_{\max} + \epsilon\eta_{\max}^{y} \\ -\epsilon\eta_{\min}^{x} + x_{\min} &\le \boldsymbol{x}(k) \le x_{\max} + \epsilon\eta_{\max}^{x} \\ -\epsilon\eta_{\min}^{u} + u_{\min} &\le \boldsymbol{u}(k) \le u_{\max} + \epsilon\eta_{\max}^{u} \\ -\epsilon\eta_{\min}^{\Delta u} + \Delta u_{\min} &\le \Delta\boldsymbol{u}(k) \le \Delta u_{\max} + \epsilon\eta_{\max}^{\Delta u} \end{aligned} \tag{3.6}$$

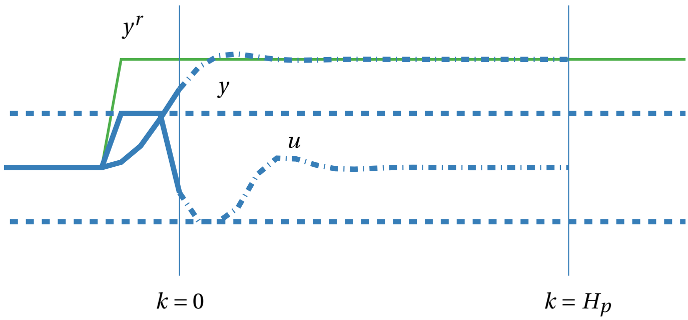

Figure 3.1 Illustration of the model predictive control principle for a one-dimensional system, where $H_p = H_c$. At the current sample $k = 0$ with measured output y, the computed future optimal control sequence u gives an optimal output sequence with respect to the prediction horizon H_p (dash-dotted). The first output of the optimal input sequence is then actuated to the system at the next time step. This procedure is then repeated every sample. In this example, the objective is to track a set-point signal y^r subject to constraints on the input (dashed).

The positive variable ϵ and vectors η determine costs for constraint violation. When $\eta = 0$, the solution U^* is not allowed to violate the constraint, but when $\eta \neq 0$, the constraint can be violated with additional cost, determined by the cost weight ρ_ϵ in (3.3). The design choice of having $\eta > 0$ was used in Chapter 8 to ensure existence of feasible solutions. The principle of MPC is illustrated in Fig. 3.1 for a single-input / single-output system where the objective is to track a set point y^r, subject to constraints on the input (dashed).

If the system dynamics are linear, the optimization problem of minimizing (3.3) subject to the equality constraints in (3.2), and the inequality constraint in (3.6) is a quadratic-programming (QP) problem

$$\begin{aligned} \underset{\boldsymbol{x}}{\text{minimize}} \quad & \frac{1}{2}\boldsymbol{x}^T H \boldsymbol{x} + f^T \boldsymbol{x} \\ \text{subject to} \quad & A\boldsymbol{x} \leq b \\ & A_{\text{eq}}\boldsymbol{x} = b_{\text{eq}} \end{aligned} \tag{3.7}$$

A QP is a convex optimization problem, which means that it has many beneficial properties [Boyd and Vandenberghe, 2008]. The most important being that a local optimal point is also globally optimal. A QP can be solved efficiently with custom-made solvers, often within a few milliseconds and sometimes even faster [Mattingley and Boyd, 2012]. In this thesis, QPs were obtained by linearizing the system equations, see below. Linearization was then recomputed every engine cycle to update the optimization-problem approximation. More details on the MPC implementation are presented in Chapter 5.

MPC has previously been applied to a wide range of problems including chemical-process control [Maciejowski, 2002], supply-chain management [Cho et al., 2003] and finance [Dawid, 2005]. MPC has also been used to control HCCI and PPC engines where it was chosen primarily for its MIMO and constraint-handling capabilities [Bengtsson et al., 2006; Widd et al., 2009; Lewander et al., 2008].

In this work, MPC was chosen for its ability to handle input and output constraints. For the control problems investigated, there were constraints on valve positions, cylinder pressure, exhaust temperature and NO_x emissions. With active constraints, MPC obtains nonlinear properties that are not obtainable with standard linear controller designs such as LQR or PID [Maciejowski, 2002]. The MPC framework is also convenient when the system is large, as in Chapter 7. In this case, tuning of the cost function weights ω_x is an intuitive way of formulating the controller objectives. An optimization framework is also well suited for engine control, since the controller objective does not always involve set-point tracking. An example of this is investigated in Chapter 11, where the objective is to maximize η_{GIE} subject to pressure constraints.

Linearization

Linear model predictive control requires linear system models. Most of the models presented in Chapter 2 are however nonlinear. In order to enable linear controller design, one can linearize the system dynamics at the current operating point. Given a nonlinear discrete-time model on the form

$$\begin{aligned} \boldsymbol{x}(k+1) &= f(\boldsymbol{x}(k), \boldsymbol{u}(k)) \\ \boldsymbol{y}(k) &= h(\boldsymbol{x}(k)) \end{aligned} \tag{3.8}$$

a linear model approximation

$$\begin{aligned} \Delta\boldsymbol{x}(k+1) &= A\Delta\boldsymbol{x}(k) + B\Delta\boldsymbol{u}(k) \\ \Delta\boldsymbol{y}(k) &= C\Delta\boldsymbol{x}(k) \end{aligned} \tag{3.9}$$

is obtained from the partial derivatives

$$\begin{aligned} A_{ij} &= \frac{\partial f_i}{\partial x_j}(\boldsymbol{x}_0, \boldsymbol{u}_0), \qquad B_{ij} = \frac{\partial f_i}{\partial u_j}(\boldsymbol{x}_0, \boldsymbol{u}_0) \\ C_{ij} &= \frac{\partial h_i}{\partial x_j}(\boldsymbol{x}_0, \boldsymbol{u}_0) \end{aligned} \tag{3.10}$$

where $\Delta\boldsymbol{x}(k)$, $\Delta\boldsymbol{u}(k)$ and $\Delta\boldsymbol{y}(k)$ are deviations from the linearization point $\boldsymbol{x}_0$, $\boldsymbol{u}_0$, $\boldsymbol{y}_0$. Linearization was used in Chapter 7 to linearize an ignition-delay model, and in Chapter 11 to linearize the cylinder-pressure model presented in Chapter 2. Since the linear approximation is only accurate close to the linearization point, (3.10) was recomputed every engine cycle.

3.2 State Estimation

The objective in state estimation is to estimate the system state $\boldsymbol{x}$ given measurements $\boldsymbol{y}$. With the probabilistic representation of a dynamic system with state $\boldsymbol{x}(k)$, measured output $\boldsymbol{y}(k)$ and input $\boldsymbol{u}(k)$

$$\begin{aligned} \boldsymbol{x}(k+1) &\sim p(\boldsymbol{x}(k+1)|\boldsymbol{x}(k),\boldsymbol{u}(k)) \\ \boldsymbol{y}(k) &\sim p(\boldsymbol{y}(k)|\boldsymbol{x}(k)) \\ \boldsymbol{x}_0 &\sim p(\boldsymbol{x}_0) \end{aligned} \tag{3.11}$$

the state-estimation problem amounts to evaluate the probability density function of $\boldsymbol{x}(k)$ given previous measurement $\boldsymbol{y}(k)$

$$p(\boldsymbol{x}(k)|\boldsymbol{y}(k),\boldsymbol{y}(k-1),\dots,\boldsymbol{y}(0)) \tag{3.12}$$

Here, the notation $\boldsymbol{x} \sim p(\boldsymbol{x}|\boldsymbol{y})$ indicates that $\boldsymbol{x}$ is distributed according to the conditional probability-density function p of $\boldsymbol{x}$, given $\boldsymbol{y}$.

The Kalman Filter

For the case when the system in (3.11) is linear

$$\begin{aligned} \boldsymbol{x}(k+1) &= A\boldsymbol{x}(k)+B\boldsymbol{u}(k)+\boldsymbol{v}(k) \\ \boldsymbol{y}(k) &= C\boldsymbol{x}(k)+\boldsymbol{e}(k) \end{aligned} \tag{3.13}$$

and perturbed with additive Gaussian noise with zero mean and covariance matrices Q and R

$$\begin{aligned} \boldsymbol{v}(k) &\sim N(0,Q) \\ \boldsymbol{e}(k) &\sim N(0,R) \end{aligned} \tag{3.14}$$

the estimation problem has an analytic solution, and the Kalman Filter (KF) provides an optimal algorithm for iteratively estimating $\boldsymbol{x}(k)$, see Algorithm 1 [Kalman, 1960]. The Kalman filter is used in Chapter 7 to estimate the EGR mass flow for $[O_2]_{IVC}$ computation, and in Chapter 8 to filter cycle-to-cycle variation in pressure-rise rate and combustion timing.

If the system (3.11) is nonlinear on the form

$$\begin{aligned} \boldsymbol{x}(k+1) &= f(\boldsymbol{x}(k),\boldsymbol{u}(k))+\boldsymbol{v}(k) \\ \boldsymbol{y}(k) &= h(\boldsymbol{x}(k))+\boldsymbol{e}(k) \end{aligned} \tag{3.15}$$

Algorithm 1 Kalman Filter

Initialize $\hat{\boldsymbol{x}}(0)$ and $P(0)$
while $k > 0$ **do**
    $\hat{\boldsymbol{x}}(k|k-1) = A\hat{\boldsymbol{x}}(k-1|k-1) + B\boldsymbol{u}(k-1)$
    $P(k|k-1) = AP(k-1|k-1)A^T + Q$
    $\boldsymbol{e}(k) = \boldsymbol{y}(k) - C\hat{\boldsymbol{x}}(k|k-1)$
    $S(k) = CP(k|k-1)C^T + R$
    $K(k) = P(k|k-1)C^T S^{-1}(k)$
    $\hat{\boldsymbol{x}}(k|k) = \hat{\boldsymbol{x}}(k|k-1) + K(k)\boldsymbol{e}(k)$
    $P(k|k) = (I - K(k)C)P(k|k-1)$
end while

the Kalman filter is unfortunately not directly applicable. There are however well-established methods for solving nonlinear estimation problems. The extended Kalman filter (EKF) and the particle filter (PF) are examples of such methods. They were used in Chapter 4 for automatic calibration of the heat-release model presented in Chapter 2.

The Extended Kalman Filter

The EKF provides an approximate solution to the estimation problem by linearizing (3.15) at the current estimate in order for the iterative KF procedure to be applied [Julier and Uhlmann, 2004]. The EKF is presented in Algorithm 2.

Algorithm 2 Extended Kalman Filter

Initialize $\hat{\boldsymbol{x}}(0)$ and $P(0)$
while $k > 0$ **do**
    $\hat{\boldsymbol{x}}(k|k-1) = f(\hat{\boldsymbol{x}}(k-1|k-1)|\boldsymbol{u}(k-1))$
    $A(k-1) = \frac{\partial f}{\partial \boldsymbol{x}}|_{\hat{\boldsymbol{x}}(k|k-1),\boldsymbol{u}(k-1)}$
    $P(k|k-1) = A(k-1)P(k-1|k-1)A(k-1)^T + Q$
    $\boldsymbol{e}(k) = \boldsymbol{y}(k) - h(\hat{\boldsymbol{x}}(k|k-1))$
    $C(k) = \frac{\partial h}{\partial \boldsymbol{x}}|_{\hat{\boldsymbol{x}}(k|k-1)}$
    $S(k) = C(k)P(k|k-1)C^T(k) + R$
    $K(k) = P(k|k-1)C(k)^T S^{-1}(k)$
    $\hat{\boldsymbol{x}}(k|k) = \hat{\boldsymbol{x}}(k|k-1) + K(k)\boldsymbol{e}(k)$
    $P(k|k) = (I - K(k)C(k))P(k|k-1)$
end while

The Particle Filter

The PF is a sequential Monte Carlo sampling method that aims to approximate the conditional distribution in (3.12) numerically. The PF consists of a set of N_p sampled particles $\boldsymbol{x}^i(k)$ with corresponding weights ω^i. Together, they provide a point-mass approximation

$$p(\boldsymbol{x}(k)|\boldsymbol{y}(k)) \approx \sum_{i=1}^{N_p} \omega^i(k)\delta(\boldsymbol{x}(k) - \boldsymbol{x}^i(k)) \tag{3.16}$$

where $\delta(\cdot)$ is the Dirac delta function. The PF performs the sampling procedure using a sequential Monte Carlo technique where particles $\boldsymbol{x}^i(k+1)$ are sampled sequentially, given the old particles $\boldsymbol{x}^i(k)$, and a proposal distribution $q(\boldsymbol{x}(k+1)|\boldsymbol{x}^i(k))$. After each time step, the weights are updated to represent the desired probability density function in (3.12). When choosing $q(\boldsymbol{x}(k+1)|\boldsymbol{x}^i(k)) = p(\boldsymbol{x}(k+1)|\boldsymbol{x}^i(k), \boldsymbol{u}(k))$, the update rule for the weights becomes $\omega^i(k+1) = \omega^i(k)p(\boldsymbol{y}(k+1)|\boldsymbol{x}^i(k+1))$. To avoid particle depletion, meaning that only a few weights contribute to (3.16), the particles have to be resampled according to the weight distribution. This procedure puts more particles into areas of high probability and discards particles in regions of low probability. The resampling step is commonly conducted when the ratio of the number of effective particles N_{eff}

$$N_{\text{eff}} = \frac{1}{\sum_{i=1}^{N_p}(\omega^i)^2} \tag{3.17}$$

to N_p becomes too low. This estimation method is referred to as the bootstrap PF and was first introduced by [Gordon et al., 1993], see Algorithm 3.

Algorithm 3 The Particle Filter

```
1: Draw N_p particles x^i(0) from the initial distribution p(x(0)) and initialize the
   weights ω(0)^i = 1/N_p
2: while k > 0 do
3:     Update the particles x^i(k) by sampling p(x(k)|x^i(k−1), u(k−1))
4:     Update the weights ω^i(k) = ω^i(k−1) p(y(k)|x^i(k)) and renormalize
5:     if N_eff < x_frac N_p then
6:         Draw new particles from the distribution defined by {ω^i(k)}_{i=1...N_p}
7:         Reinitialize the weights ω^i(k) = 1/N_p
8:     end if
9: end while
```

4

Heat-Release Analysis

4.1 Introduction

Heat-release analysis refers to the use of physical models, such as the pressure model introduced in Chapter 2, to infer information about the combustion processes from cylinder-pressure measurements. This information is commonly used for engine diagnostics, research, control and simulation. Pioneering work on methods for inferring the heat-release rate from measured in-cylinder pressure were presented in [Rassweiler and Withrow, 1938; Krieger and Borman, 1966; Gatowski et al., 1984]. From a feedback-control perspective, heat-release analysis provides the possibility to regulate combustion timing and ignition delay on a cycle-to-cycle basis.

Heat-Release Analysis

In this work, the heat-release rate $dQ_c/d\theta$ is computed from the measured pressure p by rearranging (2.9)

$$\frac{dQ_c}{d\theta} = \frac{\gamma}{\gamma-1}p\frac{dV}{d\theta} + \frac{1}{\gamma-1}V\frac{dp}{d\theta} + \frac{dQ_{ht}}{d\theta} \tag{4.1}$$

Crank angles of x% burned θ_x are commonly used indicators for the timing and duration of the combustion process. These are obtained from the accumulated heat release

$$Q_c(\theta) = \int_{\theta_{\mathrm{IVC}}}^{\theta} \frac{dQ_c}{d\theta}\,d\theta \tag{4.2}$$

and the relation

$$x = 100\frac{Q_c(\theta_x)}{\max\limits_{\theta} Q_c(\theta)} \tag{4.3}$$

In this work, θ_{10} was used to compute τ and θ_{50} was used to indicate combustion timing. The difference $\theta_{90} - \theta_{10}$ is a commonly used measure for the duration of combustion. Figure 4.1 illustrates how these quantities are obtained from measured p and estimated $dQ_c/d\theta$.

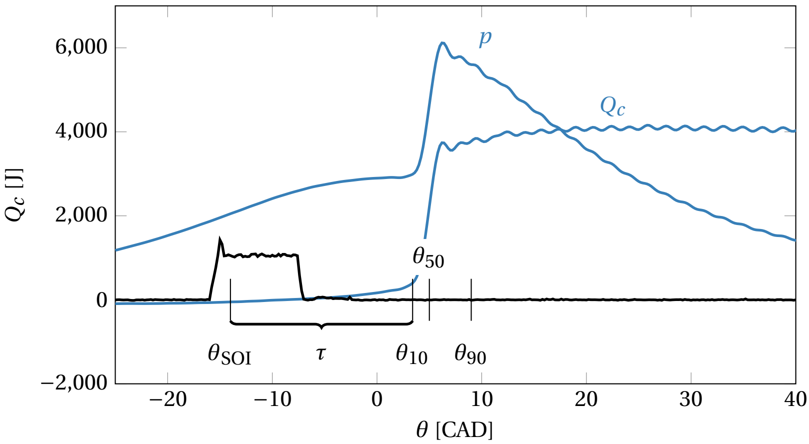

Figure 4.1 The accumulated heat-release Q_c is obtained from the measured in cylinder pressure p and (4.1). It provides important feedback variables, such as the combustion timing θ_{50} and the ignition delay τ.

With multiple large injections and a multimodal heat-release rate, it is no longer sufficient to have θ_{50} as a combustion-timing indicator. Peak detection was therefore used instead to extract combustion timings θ^i_{CT}, under the assumption that each injection contributes to a heat-release impulse. Here, i denotes injection index where $i = 1, \ldots, M$, with M injections. Detection was conducted by computing the M largest maxima of $dQ_c/d\theta$, larger than a threshold dQ_t, and with a minimum separation in θ. The separation criterion was included since diffusion combustion has a characteristic double-peak heat-release rate that could result in additional peaks detected. The peak-detection method also accounted for the ordering of injections when allocating combustion timings to injections. The use of threshold criteria for detection is a commonly used approach in signal processing, where the threshold-magnitude used is a trade-off between the probabilities of having false positives and false negatives [Kay, 1998].

It is sometimes necessary to separate $dQ_c/d\theta$ among different injections. For this purpose, $dQ_c/d\theta$ was assumed to consist of the heat-release generated from the different injections according to

$$\frac{dQ_c}{d\theta} = \sum_{i=1}^{M} \frac{dQ_c^i}{d\theta} \tag{4.4}$$

The procedure used for obtaining $dQ_c^i/d\theta$ from $dQ_c/d\theta$ was to first detect the M most significant peaks, as described above. With the peaks detected, $dQ_c/d\theta$

was separated in different intervals according to

$$\frac{d\hat{Q}_c^i}{d\theta} = \begin{cases} \frac{dQ_c}{d\theta} & \text{if } l_i \le \theta \le d_i \\ 0 & \text{otherwise} \end{cases} \tag{4.5}$$

where the bounds l_i and d_i were determined from computed minima in-between detected peaks. In order to obtain more physical heat-release shapes, $d\hat{Q}_i/d\theta$ were smoothed through a zero-phase filter, and normalized so that (4.4) is fulfilled

$$\frac{dQ_c^i}{d\theta} = \Big(\sum_{i=1}^{M} \frac{d\hat{Q}_c^i}{d\theta}\Big)^{-1} \frac{d\hat{Q}_c^i}{d\theta} \frac{dQ_c}{d\theta} \tag{4.6}$$

The separation method is illustrated in Fig. 4.2 for a multimodal heat-release rate with three injections. This method is later used in chapters 10 and 12, where combustion feedback with multiple injections is investigated.

The proposed combustion-detection method is fairly simplistic and was developed out of necessity. Suggested further development is to instead use a statistical method where a probabilistic combustion model is utilized in combination with fuel-injection information.

Model Parameters

The heat-release model in (4.1) has a set of unknown parameters that have to be tuned for satisfactory performance. These parameters can be tuned manually with knowledge of the appearance of physical heat-release rates and the influence of the different model components. This procedure is, however, time consuming and has to be redone from time to time.

The development of automatic calibration methods has been an active research area during the past decades, where methods for calibrating pressure-sensor offset [Tunestål et al., 2001; Brunt and Pond, 1997], polytropic coefficients [Manente et al., 2008; Randolph, 1990], volume-curve offset [Stas, 2004; Tunestål, 2001] and compression ratio [Klein et al., 2006] have been presented. In [Klein, 2007], an off-line method for calibration of a large set of parameters simultaneously was presented and studied in detail. It was, however, concluded by Eriksson [1998], that all model parameters might not be identifiable simultaneously. This indicates that a calibration problem involving a large set of parameters is not easily solved.

This chapter investigates on-line calibration of a subset of the model parameters in (4.1). The task is first formulated as a nonlinear estimation problem, where unknown states of a dynamic system are to be estimated given a statistical model and sensor measurements. The formulated estimation problem is then solved using the extended Kalman filter (EKF) and the bootstrap particle filter (PF),

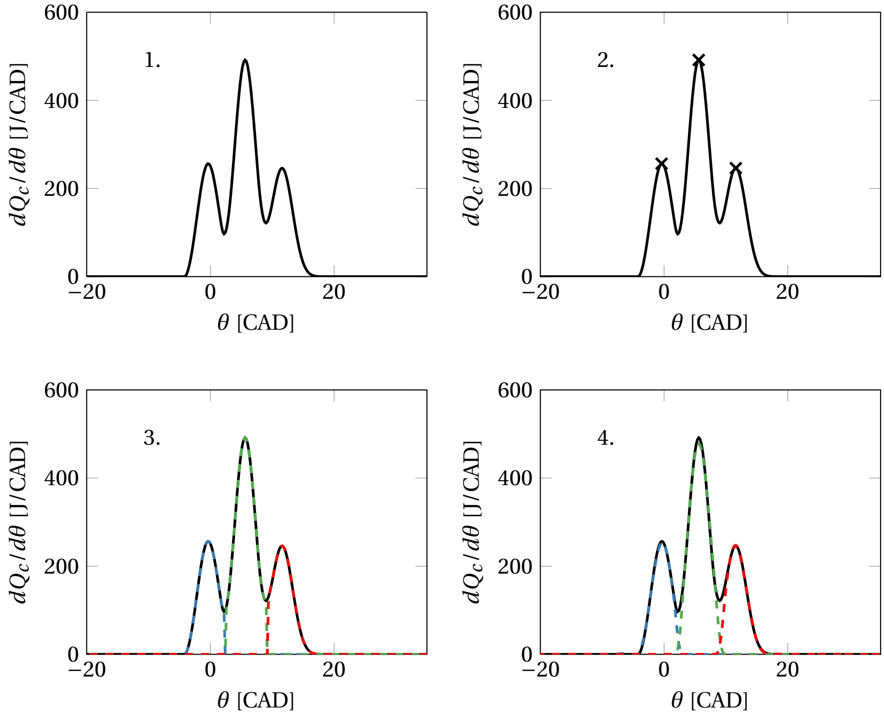

Figure 4.2 A method for separating $dQ_c/d\theta$ among several injections. The heat-release rate is first obtained from the measured pressure signal (1). The M most significant peaks are then detected (2). The detected peaks constitute the combustion timings θ^i_{CT}. The heat release is then separated in different intervals (3) according to detected peak locations. The heat-release rates $d\hat{Q}^i_c/d\theta$ in the different intervals are then filtered and normalized (4).

described in Chapter 3. These filters lend themselves nicely for real-time applications because of their sequential processing of measured data. The problem representation provides a general framework for which any parameter combination could be estimated as long as the system is observable.

The chapter is outlined as follows: The estimation-problem formulation and filter configurations are introduced in Secs. 4.2 to 4.3. Filter-performance results with respect to simulated and experimental data are then given in Secs. 4.4 to 4.5. Discussion and conclusions are presented in Secs. 4.6 and 4.7.

4.2 Problem Formulation

The problem considered was to estimate the TDC offset $\theta_{\Delta\mathrm{TDC}}$, the convective heat-transfer coefficient C_2 (see (2.16)), and the cylinder-wall surface temperature T_w from cylinder-pressure data. The heat-release model is given by

$$\frac{dQ_c}{d\theta} = \frac{\gamma}{\gamma-1}p\frac{dV}{d\theta} + \frac{1}{\gamma-1}V\frac{dp}{d\theta} + \frac{dQ_{ht}}{d\theta} \tag{4.7}$$

where γ is determined from NASA polynomials and $dQ_{ht}/d\theta$ is given by the Woschni heat-transfer model in (2.14-2.16). It was concluded in [Brunt, 1997] that the p_{IMEP} error from $\theta_{\Delta\mathrm{TDC}}$ is 3 to 10 % per CAD. The parameter C_2 was chosen over C_1 due to its greater impact on heat-transfer rate as shown in [Klein, 2008]. The wall-surface temperature T_w, has previously been shown to be an important state for describing the slower combustion-timing dynamics in low temperature combustion [Blom 2008]. If these parameters are set correctly, the accumulated heat release should be zero before the start of combustion θ_{SOC} and constant at the value of released fuel energy after the end of combustion θ_{EOC}. The validity of this assumption is affected by measurement noise and model errors. Given the correct model-parameters, the computed accumulated heat release is assumed to be on the form

$$Q_c(\theta) = \begin{cases} \epsilon_1 & \theta \le \theta_{\mathrm{SOC}} \\ Q_c^{\mathrm{tot}} + d + \epsilon_2 & \theta \ge \theta_{\mathrm{EOC}} \end{cases} \tag{4.8}$$

where $\epsilon_1 \sim N(0,\sigma_1^2)$ and $\epsilon_2 \sim N(0,\sigma_2^2)$ are i.i.d normally distributed noise processes, with standard deviations σ_i. They are introduced to represent sensor noise and unmodeled effects. The mean injected fuel energy Q_c^{tot} is assumed to be known and determined by the injection duration and common-rail pressure. The variable $d \sim N(0,\sigma_d^2)$ is a random offset accounting for stochastic variation in the injected fuel energy.

Nonlinear State-Space Model with Gaussian Noise

Prior knowledge of the unknown states was modeled as a Gaussian distribution

$$\begin{pmatrix} C_2^0 & \theta_{\Delta\mathrm{TDC}}^0 & T_w^0 \end{pmatrix}^T \sim N(\boldsymbol{\mu}_0, \Sigma_0) \tag{4.9}$$

where $\boldsymbol{\mu}_0$ is an initial guess with corresponding covariance Σ_0. Dynamic cycle-to-cycle variation was represented by the state-space model

$$\begin{pmatrix} C_2(k+1) \\ \theta_{\Delta\mathrm{TDC}}(k+1) \\ T_w(k+1) \end{pmatrix} = \begin{pmatrix} 1 & 0 & 0 \\ 0 & 1 & 0 \\ 0 & 0 & \Phi \end{pmatrix} \begin{pmatrix} C_2(k) \\ \theta_{\Delta\mathrm{TDC}}(k) \\ T_w(k) \end{pmatrix} + \begin{pmatrix} 0 \\ 0 \\ \Gamma_1 T + \Gamma_2 T_c \end{pmatrix} + \boldsymbol{v}(k) \tag{4.10}$$

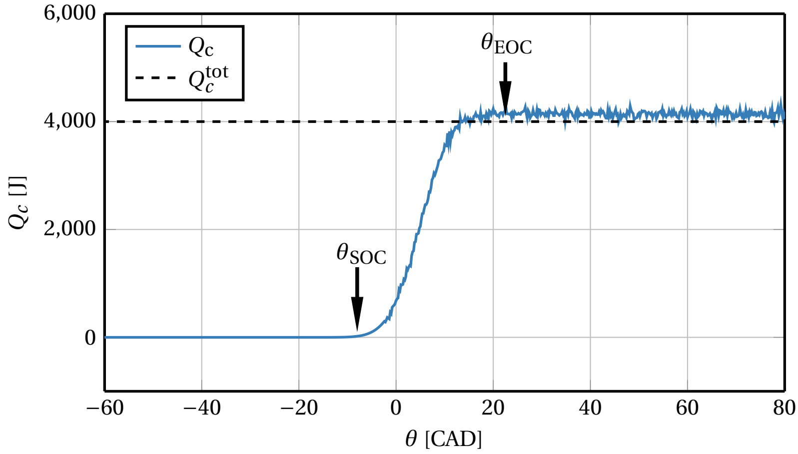

Figure 4.3 A realization of the statistical model in (4.9-4.13). The dashed line represents the expected accumulated heat release before and after combustion without stochastic variation. Deviation from this value is due to an offset d and noise processes ϵ_1, and ϵ_2 for which $\sigma_1^2 = 0$, $\sigma_2^2 = 2500$. It is assumed that the injected fuel energy Q_c^{tot}, the start and end of combustion θ_{SOC} and θ_{EOC} are available.

where T_w evolves according to the heat-transfer model presented in Sec. 2.2

$$\begin{aligned} \Phi &= e^{\oint A_w(\theta)d\theta} \\ \Gamma_1 T + \Gamma_2 T_c &= \oint e^{\int_{\theta_{BDC}}^{\vartheta} A_w(\vartheta)d\vartheta} B_w(\theta)(T + T_c)d\theta \end{aligned} \tag{4.11}$$

The uncertainty in C_2 and $\theta_{\Delta TDC}$ was modeled as a random walk driven by a Gaussian process

$$\boldsymbol{v}(k) \sim N(0, \Sigma_1) \tag{4.12}$$

The covariance matrix in (4.12), Σ_1, is a measure of the model uncertainty, and was here chosen as a diagonal matrix with elements representing the state uncertainty. The model generates a Q_c output every engine cycle according to

$$\begin{aligned} \frac{dQ_c}{d\theta} &= \frac{\gamma}{\gamma-1} p \frac{dV}{d\theta} + \frac{1}{\gamma-1} V \frac{dp}{d\theta} + \frac{dQ_{ht}}{d\theta} \\ Q_c(\theta) &= \int_{\theta_{IVC}}^{\theta} \frac{dQ_c}{d\theta} d\theta \end{aligned} \tag{4.13}$$

where a realization of (4.13) with the correct model parameters is shown in Fig. 4.3. Equations (4.9)-(4.13) are on the form

$$\begin{aligned} \boldsymbol{x}(k+1) &= f(\boldsymbol{x}(k), \boldsymbol{u}(k)) + \boldsymbol{v}(k) \\ \boldsymbol{y}(k) &= h(\boldsymbol{x}(k)) + \boldsymbol{e}(k) \\ \boldsymbol{x}(0) &= \boldsymbol{\mu}_0 + \boldsymbol{e}_0 \end{aligned} \tag{4.14}$$

where the state-update equation is given by (4.10), and the system-output equation by (4.13). The objective is now to estimate $\boldsymbol{x}(k)$ given measurements $\boldsymbol{y}(k),\dots,\boldsymbol{y}(0)$. In our case, $\boldsymbol{y}(k)$ is not obtained from sensor measurement. It is instead given by the deterministic part of (4.8), which is the expected heat-release rate before θ_{SOC} and after θ_{EOC}, given the fuel energy Q_c^{tot}.

Observability

It is crucial to evaluate the system observability when conducting state-estimation. Observability is a measure of how well the system state $\boldsymbol{x}(k)$ can be inferred from knowledge of the system output $\boldsymbol{y}(k)$, and was introduced to linear-system theory by Kalman [1959]. In order to apply the concept of observability to the system in (4.10-4.13), a linearization

$$\begin{aligned} \Delta\boldsymbol{x}(k+1) &= A(k)\Delta\boldsymbol{x}(k) + B(k)\Delta\boldsymbol{u}(k) \\ \Delta\boldsymbol{y}(k) &= C(k)\Delta\boldsymbol{x}(k) \end{aligned} \tag{4.15}$$

was conducted at the operating point presented in Table 4.1. In our case, observability was investigated by evaluating

$$C(k)_{ij} = \frac{\partial h_i(\boldsymbol{x}(k))}{\partial x_j} \tag{4.16}$$

Since $A(k) \approx I_{3x3}$, and the observability matrix $\mathcal{O}$ is given by

$$\mathcal{O} = \begin{pmatrix} C \\ C \\ C \end{pmatrix} \tag{4.17}$$

The system (4.15) is observable if $\mathcal{O}$, or in this case C, has 3 independent rows. A rescaled $C(k)$ is presented in Fig. 4.4, where it can be seen that $\theta_{\Delta\text{TDC}}$ has a relatively large asymmetric affect on Q_c around TDC. Changes in C_2 and T_w determine the final Q_c value, whereas T_w also affects Q_c during the compression stroke. The linear-system approximation (4.15) is observable since the curves in Fig. 4.4 are linearly independent. Despite this fact, it can be seen that negatively correlated variation in C_2 and T_w might be difficult to detect due to their similar effect on Q_c after TDC. Johansson [2006] presented similar results for guidance in manual tuning of heat-release model parameters.

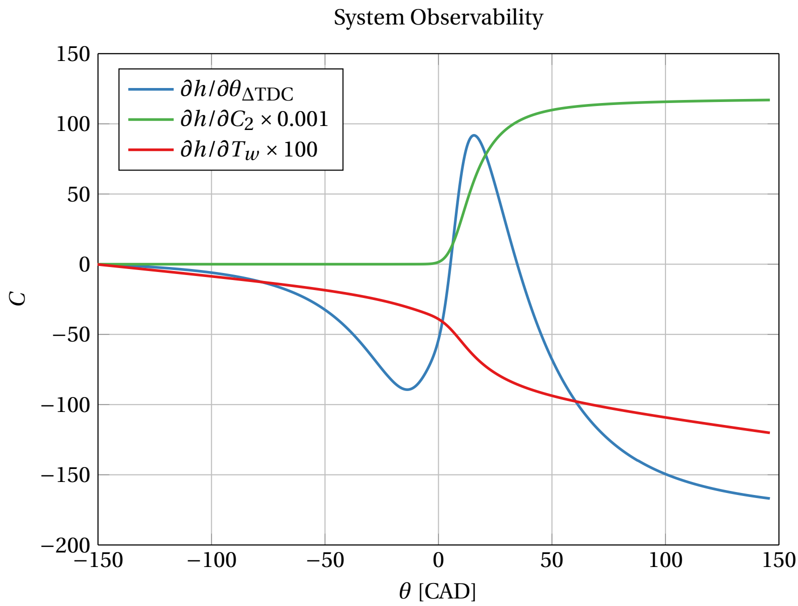

Figure 4.4 Computed C when linearizing (4.10-4.13) at the operating point in Table 4.1. The parameters affect Q_c differently: $\theta_{\Delta\mathrm{TDC}}$ affects Q_c asymmetrically around TDC; C_2 determines the final Q_c level; T_w reduces Q_c both before and after TDC.

4.3 Filter Configurations

The remainder of this chapter covers implementation and evaluation of an extended Kalman filter (EKF) (see Algorithm 2) and a particle filter (see Algorithm 3) for the purpose of estimating the unknown parameters. Partial derivatives ($\partial f/\partial x$ and $\partial h/\partial x$) necessary for the EKF were obtained through numerical differentiation of (4.10) and (4.13). The probability density functions $p(\boldsymbol{x}(k+1)|\boldsymbol{x}(k),\boldsymbol{u}(k))$ and $p(\boldsymbol{y}(k+1)|\boldsymbol{x}(k+1))$, necessary for the PF, were given by (4.8), (4.10) and (4.13) directly. Measurements $\boldsymbol{y}(k)$ were given by the deterministic part of (4.8).

In order to reduce computational effort, (4.8) was downsampled from a resolution of 0.2 CAD to 1 CAD and considered 50 samples before θ_{SOC} and 50 samples after θ_{EOC}. Computation times below 1 ms per iteration were obtained for the EKF with compiled Matlab code. To obtain comparable runtimes with the PF, the number of particles N_p was set to 250, which enabled the PF to run under 5 ms. The particle number N_p is a trade-off between performance and computation time. This trade-off was however not investigated here. Particle resampling was done when the number of effective particles N_{eff} was below $0.25N_p$.

4.4 Simulation Results

The filters were evaluated with respect to consistency and rate of convergence, sensitivity to statistical assumptions and model-parameter errors. This was done with respect to simulated pressure traces generated from the model

$$\frac{dp}{d\theta} = -\frac{\gamma}{V}\frac{dV}{d\theta}p + \frac{\gamma-1}{V}\left(\frac{dQ_c}{d\theta} - \frac{dQ_{ht}}{d\theta}\right), \qquad p(\theta_{\mathrm{IVC}}) = p_{\mathrm{in}} \tag{4.18}$$

using the MATLAB ode23s solver, the model parameters in Table 4.1 and the noise densities

$$\sigma_1 = 25,\ \sigma_2 = 25,\ \sigma_d = 100$$

$$\Sigma_0 = \begin{pmatrix} 9/4 & 0 & 0 \\ 0 & 2.5\times10^{-7} & 0 \\ 0 & 0 & 625 \end{pmatrix} \tag{4.19}$$

$$\Sigma_1 = \begin{pmatrix} 0.0625 & 0 & 0 \\ 0 & 1\times10^{-8} & 0 \\ 0 & 0 & 6.25 \end{pmatrix}$$

Convergence

Filter consistency and rate of convergence were evaluated by initializing the EKF and the PF with correct model parameters according to Table 4.1, apart from the incorrect initial filter states

$$\begin{aligned} \boldsymbol{x}_0^1 &= \left(1,\ 0.0095,\ 595\right)^T \\ \boldsymbol{x}_0^2 &= \left(-1,\ 0.002,\ 336\right)^T \end{aligned} \tag{4.20}$$

with the true state being

$$\boldsymbol{x}^* = \left(0,\ 0.0032,\ 465\right)^T \tag{4.21}$$

Figure 4.5 shows simulation results where the mean filter state and standard deviation of 25 realizations are presented as a function of engine cycle for the initial conditions $\boldsymbol{x}_0^1$ (dashed) and $\boldsymbol{x}_0^2$ (solid). Note that the cycle-axis scales are different for the two filters. It can be seen that the filters converged to the correct state and that the EKF had a higher convergence rate, where the PF convergence rate probably could have been improved by increasing N_p. It can also be seen that the $\theta_{\Delta\mathrm{TDC}}$ estimates had very fast initial transients, which indicates a relatively high filter sensitivity to $\theta_{\Delta\mathrm{TDC}}$ errors. Filter RMSE at cycle k

$$\mathrm{RMSE}(k) = \sqrt{\frac{1}{N}\sum_{i=1}^{N}(\hat{\boldsymbol{x}}_i(k) - \boldsymbol{x}^*)^2} \tag{4.22}$$

is indicated by the black lines in Fig. 4.6 for $N = 25$.

Table 4.1 Nominal operating point for filter evaluation. The heat-release rate, $dQ_c/d\theta$, was chosen as a Gaussian function with a standard deviation of 5 CAD.

Boundary Conditions		Combustion Properties	
p_{in} [bar]	1.3	θ_{50} [CAD]	5
T_{in} [K]	303	$\dfrac{dQ_c/d\theta}{Q_c^{\text{tot}}}$ [-]	$N(5,5)$
λ [-]	2	Q_c^{tot} [J]	4×10^3
r_{EGR} [-]	0		
T_{ex} [K]	400		
Cylinder Geometry		**Heat-Transfer Parameters**	
r_c [-]	16	C_1 [-]	2.28
V_d [m^3]	2.1×10^3	C_2 [m/(sK)]	0.0032
B [mm]	130	T_w [K]	465
L [mm]	160	T_c [K]	333
IVC [CAD]	-151	$m_c c_p$ [J/K]	1150
EVC [CAD]	146	k_c [J/(mK)]	45
$\theta_{\Delta\text{TDC}}$ [CAD]	0	L_c [m]	0.025

Sensitivity to Model Uncertainty, Σ_1

Sensitivity to the assumed model uncertainty was investigated by scaling the covariance matrix of the noise term acting on (4.10) Σ_1 a factor of 16. The resulting RMSE (red) is compared to the nominal RMSE (black) in Fig. 4.6. An increase in the assumed model uncertainty gave a higher convergence rate, but a slightly larger steady-state error.

Sensitivity to Q_c Noise Levels, σ_x

Sensitivity to the assumed Q_c noise variance was investigated by scaling σ_1, σ_2 and σ_d a factor of 4. The resulting RMSE is indicated by the red lines in Fig. 4.7 together with the nominal RMSE in black. An increased assumed Q_c noise variance clearly decreased the convergence rate.

Sensitivity to σ_d was also tested by setting $\sigma_d = 0$ whilst σ_2 was set to $\sqrt{25^2 + 100^2}$. This corresponds to precise knowledge of the injected fuel energy but with increased variation from unstructured, Gaussian uncertainty. The resulting RMSE is shown in Fig 4.8, where convergence with the modified noise model is shown in red. Assuming Gaussian noise before and after combustion clearly

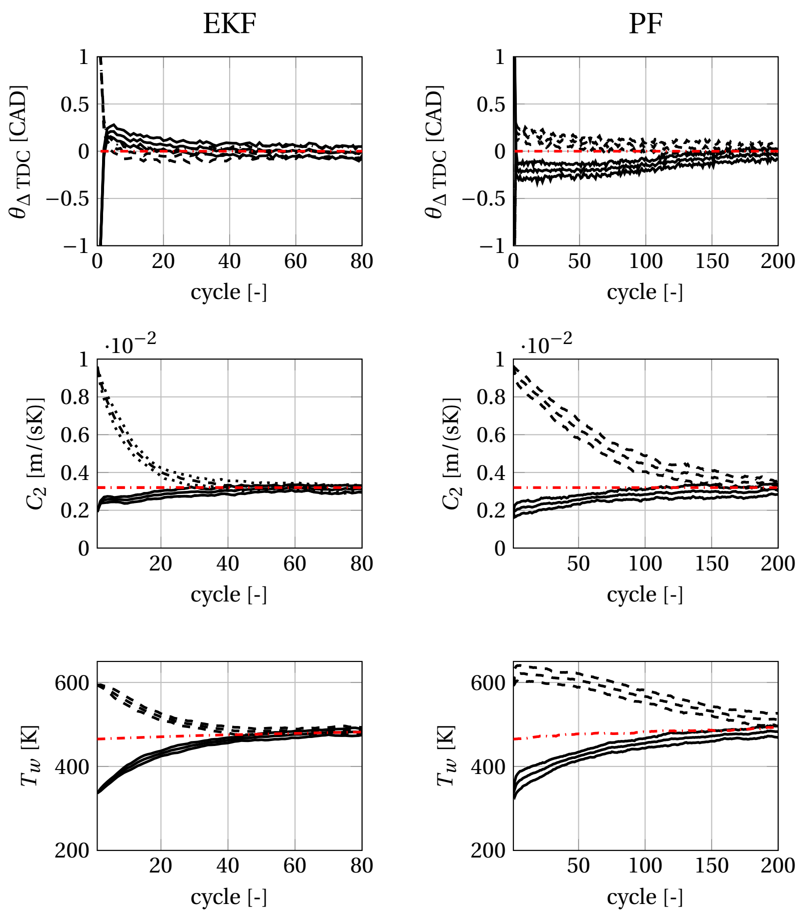

Figure 4.5 Filter convergence with initial conditions x_0^1 (dashed) and x_0^2 (solid). True state values are indicated in red. Note the different scales on the cycle-axes for the two filters. It can be seen that the filters converged to the correct state (red, dash-dotted) and that the EKF had a higher convergence rate. Also note that $\theta_{\Delta\mathrm{TDC}}$ estimates had faster initial transients. This indicates a relatively high filter sensitivity to $\theta_{\Delta\mathrm{TDC}}$ errors.

degrades performance when there is a stochastic offset d. Another observation is that the EKF had a large transient and a larger steady-state RMSE.

Overall, the filters behaved as one would expect. An increase in the assumed model uncertainty increased convergence rates. For the EKF, the measurement equation contributed more to the state estimate in relation to the model dynamics, and for the PF, a larger particle spread was made each sample which incre-

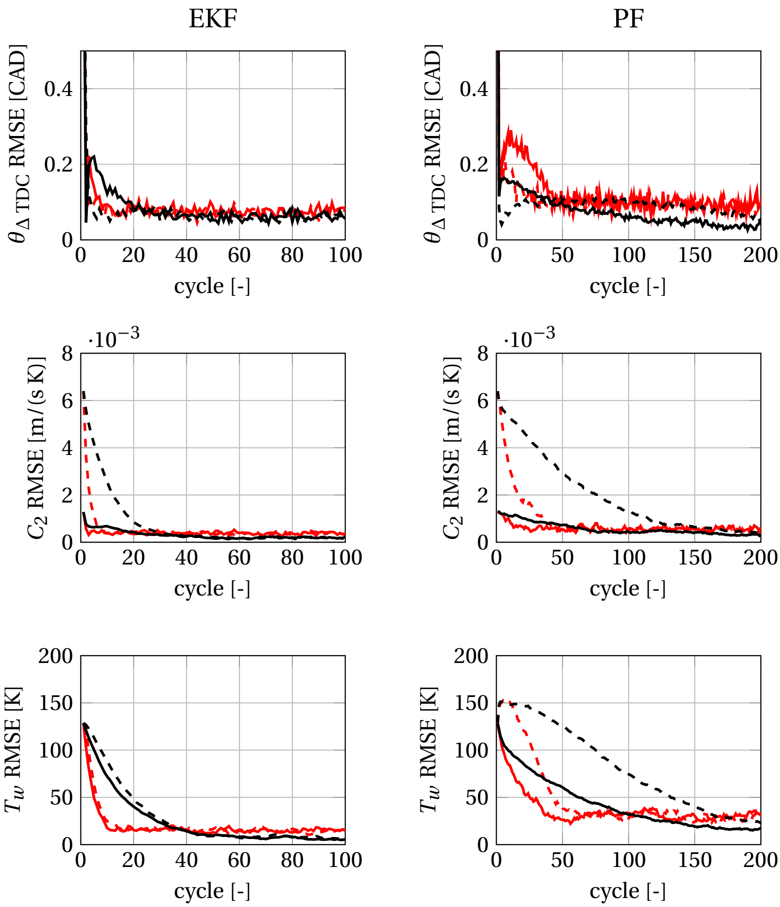

Figure 4.6 Filter RMSE with the true model uncertainty Σ_1 (black) and an increased assumed model uncertainty $16\Sigma_1$ (red). The latter increased the filter convergence rate and steady state RMSE.

ased exploration of the parameter space. This did, however, increase steady-state variation. Filter convergence rates decreased when the assumed Q_c noise levels were increased. This was due to the reduced parameter correction for Q_c deviation from (2.9), since variation in Q_c was more probable. Assumed noise variances essentially functioned as tuning parameters that determined the trade-off between speed of convergence and steady-state variation.

Incorporating the stochastic fuel-energy component d in the filters was shown to be important. This made constant Q_c after combustion more probable and allowed for constant offsets in Q_c after θ_{EOC}, which improved robustness

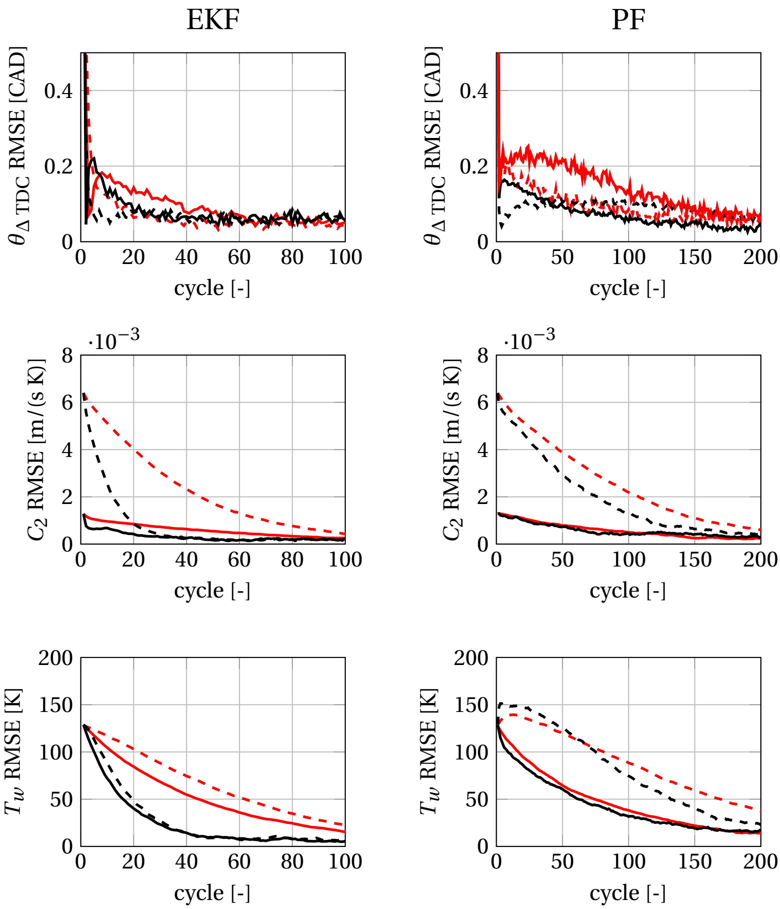

Figure 4.7 Filter RMSE with the correct Q_c noise levels σ_x (black) and increased assumed noise levels, with $4\sigma_x$ (red). An increased assumed Q_c noise level clearly decreased the convergence rates.

to variation in the burned fuel energy. Without d, the filters attempted to fit the mean Q_c to Q_c^{tot} after θ_{EOC}, which resulted in non-physical Q_c appearances.

Sensitivity to Model-Parameter Errors

The sensitivity to erroneous model parameters was investigated by introducing errors to p_{in}, T_{in}, λ, r_c, T_c and Q_c^{tot}. Stationary parameter-estimate bias due to these errors are presented in Table 4.2, together with the model-parameter error magnitude. It can be concluded that the filter estimates are very sensitive to errors in p_{in} and r_c, but not as sensitive to errors in the other parameters. A positive

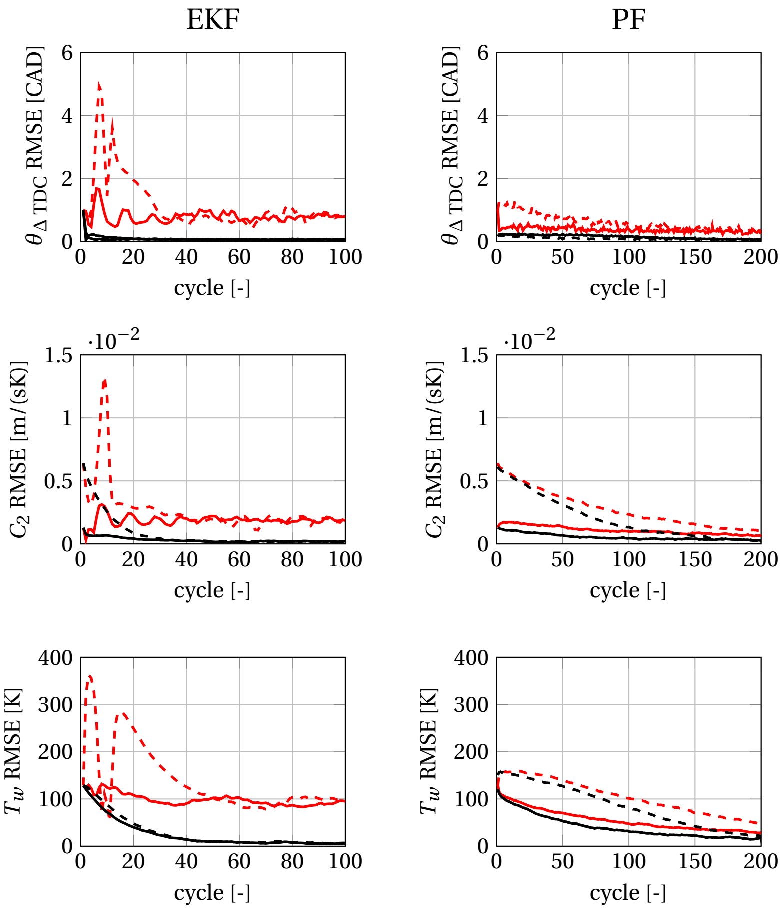

Figure 4.8 Filter RMSE with correct Q_c noise levels (black) and modified assumed Q_c noise levels (red), where $\sigma_d = 0$ and $\sigma_2 = \sqrt{25^2 + 100^2}$. The assumption of Gaussian noise before and after combustion clearly degraded performance when there was a stochastic offset d to the total fuel energy. The EKF oscillated greatly and also had larger steady-state RMSE.

error in p_{in} or r_c gives an increase in the assumed motored pressure curve p_m and a decrease in the computed T, see (2.11) and (2.16). Both effects contribute to a decrease in $dQ_{ht}/d\theta$ and affect estimated C_2 and T_w. The parameter sensitivity could be decreased by increasing the assumed Q_c noise level σ_x. The numbers in parentheses in Table 4.2 correspond to stationary parameter-estimate bias when σ_x was increased a factor of 4. Another observation is that the PF was overall less sensitive to model errors.

4.5 Experimental Results

The filters were also tested against experimental data with a known $\theta_{\Delta\text{TDC}}$ of 1 CAD, obtained from the operating point in Table 4.3. Filter convergence can be seen in Figs 4.9 and 4.10 when initiated with the states in (4.20), and manually tuned noise parameters

$$\sigma_1 = 100,\ \sigma_2 = 100,\ \sigma_d = 400$$

$$\Sigma_0 = \begin{pmatrix} 9/4 & 0 & 0 \\ 0 & 2.5 \times 10^{-7} & 0 \\ 0 & 0 & 625 \end{pmatrix} \tag{4.23}$$

$$\Sigma_1 = \begin{pmatrix} 0.0625 & 0 & 0 \\ 0 & 1 \times 10^{-8} & 0 \\ 0 & 0 & 0.1 \end{pmatrix}$$

which gave an acceptable trade-off between convergence rate and steady-state estimate variance. The T_w noise level was set low, which allowed T_w to follow the dynamic heat-transfer model whilst $\theta_{\Delta\text{TDC}}$ and C_2 were adjusted for probable Q_c output.

The initial Q_c output (black, dashed) is presented in Fig. 4.9, together with the final Q_c outputs (red, black, solid), where the known Q_c^{tot} level (black, dash-dotted) was computed from fuel-flow measurements. It can be seen that the PF converged closer to the estimated final Q_c value in Fig. 4.9. Both filters converged in approximately 200 cycles, and managed to detect the known $\Delta\theta_{\text{TDC}}$, see Fig. 4.10. Moreover, the filters converged to slightly different final states in Fig. 4.10, where the EKF converged to a higher C_2 value.

4.6 Discussion

For the choice of 250 particles, the PF was slower than the EKF (see Fig. 4.5). The EKF is the minimum-variance unbiased state estimator if the system is linear and perturbed with Gaussian noise, which could explain the higher convergence rate in Fig. 4.5. The PF was however less sensitive to model-parameter errors and had comparable RMSE in stationarity. Here, $N_p = 250$ was chosen so that the filters would have comparable computation times, and it is possible that the PF performance would have been improved with an increased N_p. The effects of N_p and the re-sampling criterion on PF performance were not addressed here and is suggested future work.

The suggested parameter-estimation framework could easily be extended or modified to cover other model parameters. It should however be kept in mind that observability or identifiability might be degraded or lost when many

Table 4.2 Sensitivity to model-parameter errors. The filters were more sensitive to errors in p_{in} and r_c and not as sensitive to other parameter errors. The PF was overall less sensitive to model errors compared to the EKF. The units for $\theta_{\Delta\text{TDC}}$, C_2 and T_w are CAD, m/(sK) and K.

EKF	PF
p_{in} error, 1.3 ± 0.065 bar	
$\theta_{\Delta\text{TDC}} = 0 \pm 0.48$ (0.38)	$\theta_{\Delta\text{TDC}} = 0 \pm 0.3$ (0.33)
$C_2 = 0.0032 \pm 0.003$ (0.0024)	$C_2 = 0.0032 \pm 0.0014$ (0.0012)
$T_w = 497 \pm 198$ (151)	$T_w = 497 \pm 100$ (95)
T_{in} error, 303 ± 20 K	
$\theta_{\Delta\text{TDC}} = 0 \pm 0.17$ (0.14)	$\theta_{\Delta\text{TDC}} = 0 \pm 0.12$ (0.12)
$C_2 = 0.0032 \pm 0.0003$ (0.0001)	$C_2 = 0.0032 \pm 0.00015$ (0.0001)
$T_w = 497 \pm 65$ (45)	$T_w = 497 \pm 40$ (25)
λ error, 2 ± 0.2	
$\theta_{\Delta\text{TDC}} = 0 \pm 0.07$ (0.09)	$\theta_{\Delta\text{TDC}} = 0 \pm 0.05$ (0.07)
$C_2 = 0.0032 \pm 0.00045$ (0.0004)	$C_2 = 0.0032 \pm 0.0004$ (0.0003)
$T_w = 497 \pm 12$ (10)	$T_w = 497 \pm 7.5$ (7.5)
r_c error, 1.6 ± 0.8	
$\theta_{\Delta\text{TDC}} = 0 \pm 0.65$ (0.55)	$\theta_{\Delta\text{TDC}} = 0 \pm 0.5$ (0.51)
$C_2 = 0.0032 \pm 0.003$ (0.003)	$C_2 = 0.0032 \pm 0.0017$ (0.0012)
$T_w = 497 \pm 179$ (138)	$T_w = 497 \pm 90$ (70)
T_c error, 333 ± 20 K	
$\theta_{\Delta\text{TDC}} = 0 \pm 0.01$ (0.0)	$\theta_{\Delta\text{TDC}} = 0 \pm 0.02$ (0.025)
$C_2 = 0.0032 \pm 0.00005$ (0)	$C_2 = 0.0032 \pm 0$ (0.0001)
$T_w = 497 \pm 7$ (4)	$T_w = 497 \pm 9$ (10)
Q_c^{tot} error, $4 \times 10^3 \pm 200$ J	
$\theta_{\Delta\text{TDC}} = 0 \pm 0.15$ (0.1)	$\theta_{\Delta\text{TDC}} = 0 \pm 0.13$ (0.12)
$C_2 = 0.0032 \pm 0.001$ (0.0011)	$C_2 = 0.0032 \pm 0.0012$ (0.0013)
$T_w = 497 \pm 30$ (17)	$T_w = 497 \pm 0$ (7)

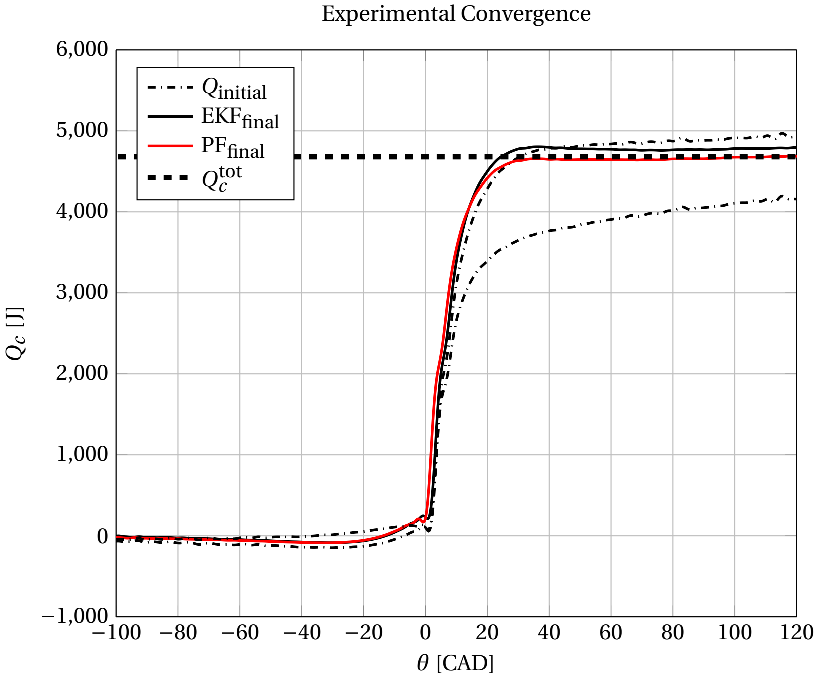

Figure 4.9 Filter Q_c-output convergence for the parameters presented in Fig. 4.10. The EKF (black) and the PF (red) converged to slightly different Q_c when initiated at $\hat{\boldsymbol{x}}_0^{1,2}$ (black, dashed). The black dash-dotted line indicates Q_c^{tot} computed from fuel-flow measurements.

heat-release parameters are to be estimated simultaneously [Eriksson, 1998]. Moreover, it could be beneficial to include additional measurements from wall temperature, rail pressure and λ sensors, along with sensor-uncertainty characteristics. Model assumptions for Q_c could also be developed further. For instance, by making monotonic Q_c more probable or by obtaining a more accurate Q_c noise model from experimental data.

Table 4.3 Operating point for experimental evaluation.

N_{speed} [rpm]	1200	T_{in} [°C]	40
p_{IMEPn} [bar]	10	λ [-]	1.8
p_{rail} [bar]	800	Q_c^{tot} [J]	4680

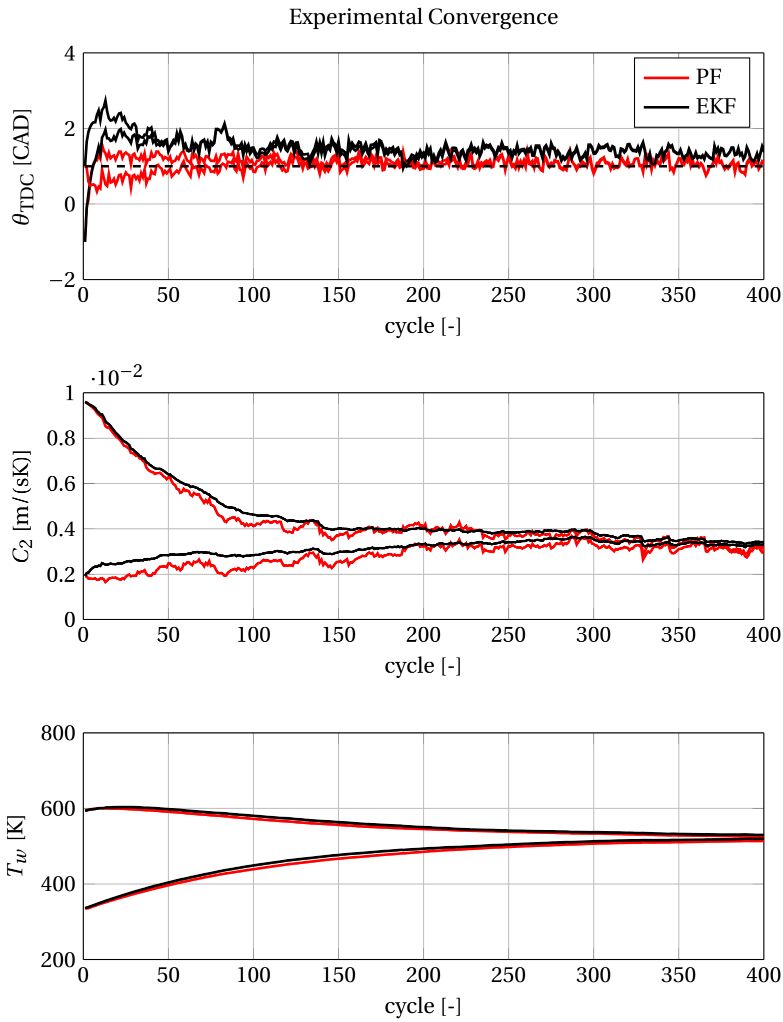

Figure 4.10 Filter convergence with respect to 400 cycles of experimental data from the operating point in Table 4.3. The EKF (black) and the PF (red) have comparable performance but converged to slightly different state estimates. Both filters managed to detect a significant top-dead-center offset close to 1 CAD.

4.7 Conclusions

A statistical framework for estimation of unknown heat-release model parameters was introduced in this chapter. Within this framework, the EKF and the PF both seem to be feasible options for on-line estimation. The simulation results showed that both filters were consistent in converging to the correct parameter values. The relation between assumed model and heat-release noise variance determined a trade-off between convergence rate and steady-state RMSE, and could be used as a tuning parameter. An assumed stochastic accumulated-heat-release offset showed to be crucial when the injected fuel energy varied. In reality, such variations are present due to common-rail pressure fluctuations. The model-error-sensitivity results in Table 4.2 indicated that the filters were more sensitive to intake-pressure and compression-ratio errors, compared to other parameter errors. The model-error sensitivity was also found to be dependent on the assumed heat-release noise variance. Furthermore, both filters showed consistent convergence from different initial states with respect to experimental data and manually tuned filter parameters, see Figs. 4.9 and 4.10.

5

Experimental Setup

5.1 The Scania D13 Engine

All experiments were performed on a Scania D13 six-cylinder heavy-duty diesel engine in the combustion-engine lab at Lund University, see Fig. 5.1. Engine specifications are given in Table 5.1. The original gas-exchange system was extended with an additional water-cooled low-pressure EGR path and a water-cooled air path prior to the intake manifold. The engine was boosted with a fixed-geometry turbocharger.

Fuel

The fuel used was a mixture of 80 volume % gasoline and 20 volume % n-heptane. This ratio was chosen based on previous results showing that a fuel octane number around 80 could be used over a wide range of engine operating points [Manente, 2010b]. The fuel was mixed together with an Infimeum fuel lubricant to increase the lifetime of the fuel-injection system which was developed for conventional diesel fuel.

Table 5.1 Engine Specifications

Total displaced volume	12.74 dm^3
Number of cylinders	6
Stroke	160 mm
Bore	130 mm
Connecting rod length	255 mm
Compression ratio	18:1
Valves per cylinder	4
Maximum Power	360 kW

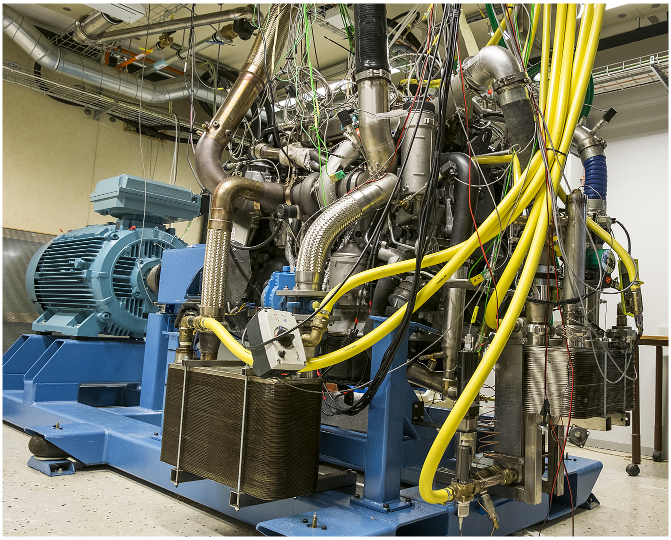

Figure 5.1 Scania D13 engine, located in the combustion-engine lab at Lund University. Figure courtesy of Nhut Lahm.

5.2 Instrumentation

Actuation

Fuel Injection The fuel-injection system was a production extra-high pressure-injection (XPI) common-rail system with solenoid injectors. The common-rail pressure was regulated with an inlet-metering valve, positioned prior to a fuel pump used to elevate the pressure in the common rail volume. Fuel-injection timings and durations were determined by current pulses sent to the injectors. Current-pulse timings and durations were set from the LabVIEW control system and actuated with Drivven direct-injection drivers. A more detailed description of the fuel-injection system is given in [Källkvist, 2011].

Gas Flow The engine was equipped with two cooled EGR loops, located before and after the turbine. EGR flows were regulated with two valves. Two valves positioned prior to the intake manifold were used to regulate the intake temperature by adjusting the flow over an intercooler. A back-pressure valve positioned after the tubine was used to create back pressure for sufficient EGR flow. Servo motors used for valve actuation were controlled from the LabVIEW control system and actuated with Drivven drivers. Valve locations are marked in Fig. 5.2.

Engine Speed The engine speed was controlled with an ABB M2BA electrical motor with a rated power of 355 kW. The motor reference speed was adjusted manually from the engine control room.

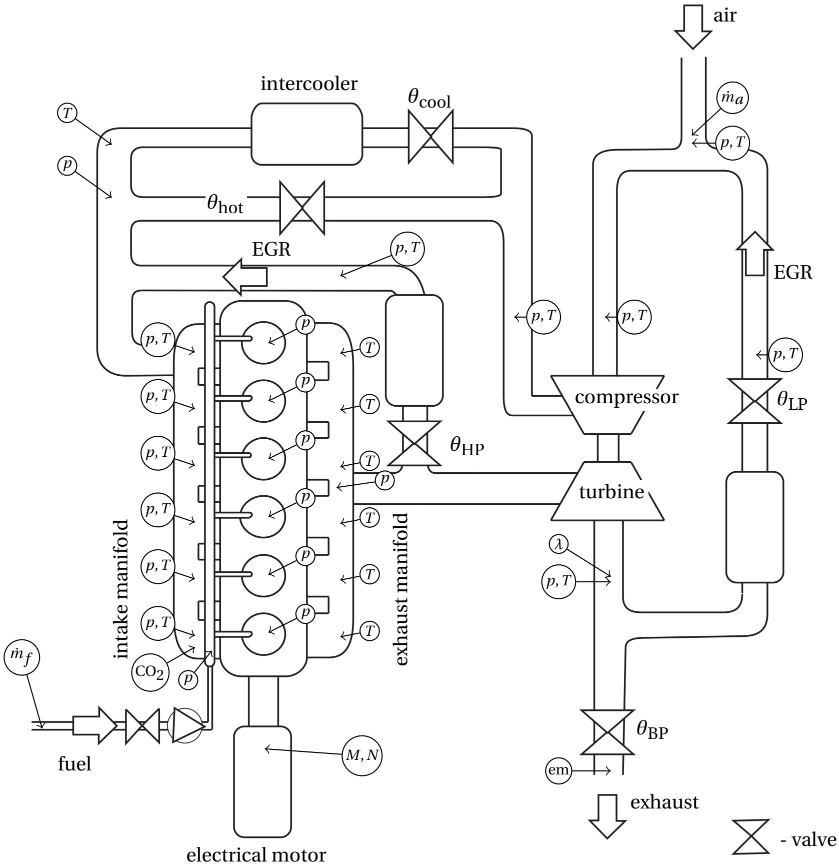

Figure 5.2 A schematic illustration of the engine configuration with locations of sensors and valves. Sensor symbols: p - pressure, T - temperature $\dot{m}_f$ - fuel-mass flow, $\dot{m}_a$ - air-mass flow, λ - air/fuel ratio, M - torque, N - engine speed, em - emissions. Valves are denoted θ_x.

Sensing

Sensor locations are marked in Fig. 5.2.

Sampling Crank-angle based sampling was enabled through a Leine & Linde encoder emitting 5 pulses every CAD which triggered sampling of cylinder pressure, engine torque and injector current. Other sensor signals were sampled every engine cycle.

In-cylinder pressure sensors The in-cylinder pressure was measured with water-cooled Kistler 7061B piezo-electrical pressure tranducers. The cylinder-pressure signal was sampled every 0.2 CAD with the crank-angle encoder.

Common-rail pressure sensor The common-rail pressure was measured with pressure sensor mounted to the common-rail volume.

Pressure and temperature sensors Pressures and temperatures were measured at various locations in the gas-exchange system. Keller PAA-23S absolute pressure sensors with response times of milliseconds were mounted accordingly:

- intake manifold close to the intake valves of cylinders 1-6.
- exhaust manifold.
- after the turbine.
- before and after the compressor.
- after the thermal-management system.
- after the low-pressure EGR valve.
- after the high-pressure EGR valve.

Temperatures were measured with K-type thermocouples with response times of seconds. These sensors were mounted accordingly:

- intake manifold close to the intake valves of cylinders 1-6.
- exhaust manifold at the exhaust valves of cylinders 1-6.
- after the turbine.
- before and after the compressor.
- after the thermal-management system.
- after the low-pressure EGR valve.
- after the high-pressure EGR valve.

Torque sensor A force sensor integrated in the electrical motor was used to measure engine torque.

Engine Speed Engine speed was obtained from the internal speed measurement of the electrical motor.

Fuel flow A Bronkhorst mini CORI-FLOW M15 mass-flow meter mounted prior to the fuel system was used to measure the fuel-mass flow.

Air flow A Bronkhorst hot-film air-mass flow meter mounted prior to the compressor was used to measure the air-mass flow.

λ sensor A broadband λ sensor mounted after the turbine measured the exhaust oxygen concentration.

Emissions Intake and exhaust CO_2 and exhaust NO_x, HC, CO and O_2 levels were measured with an AVL AMA i60 exhaust-measurement system. Soot levels were measured with an AVL micro soot sensor measurement unit.

5.3 Control-System Architecture

Hardware

The engine was controlled with a real-time system, consisting of a NI PXIe-8135 embedded controller with a 2.3 GHz quad-core processor, and NI PXI-7854/7854 R which is a multifunction reconfigurable I/O with Virtex 5-LX110/LX30 FPGAs. The FPGAs were used as configurable hardware for flexible AO / DIO and AD acquisition, triggered by the crank-angle encoder. The ADC sampled analog signals with a 16-bit resolution. A user interface was run on a separate host PC with a Windows 7 operating system which communicated with the real-time system over TCP/IP.

Software

The engine control system was programmed in LabVIEW which is a graphical programming environment developed by National Instruments. The software was originally developed by Borgquist for his thesis work [Borgquist, 2013].

Real-time heat-release analysis and controller computations were executed by the real-time PXI system. Computations were done using floating point arithmetic, and most of them were done in LabVIEW MathScript RT Module nodes inside timed loops, triggered every engine cycle. PI controllers were implemented using the LabVIEW PID advanced VI and QPs were solved using the LabVIEW quadratic programming VI. The quadratic programming VI had functionalities useful for model predictive control implementation such as initialization, warm start of active constraints, various stopping criteria and error flags when feasible solutions were not found. The user interface was also programmed in LabVIEW.

Signal Processing

The in-cylinder pressure was measured with piezo-electric transducers. This measurement technique has high cut-off frequency, good linearity and handling of the environment inside the combustion chamber. The signal given by these sensors is on the form

$$p_{\text{meas}} = kp + \Delta p \tag{5.1}$$

where p_{meas} is the sensor signal, p the actual pressure, k the sensor conversion factor and Δp the sensor offset. Methods for determining k and Δp were presented by Randolph [1990]. In this work, k were known from sensor calibration and Δp was determined by referencing the cylinder pressure at intake valve closing (IVC) to the measured intake-manifold pressure p_{in}. High-frequency content in p_{meas} during combustion and expansion was attenuated using a digital zero-phase filter.

6

Proportional-Integral Combustion-Timing Control

This chapter investigates how a proportional-integral (PI) controller should be designed for robust and noise insensitive combustion-timing control through injection-timing actuation. The aim of the chapter is to provide physical understanding of the combustion-timing control problem and to illustrate how parameters such as fuel reactivity and engine load affect controller performance.

Combustion-timing feedback is motivated by the sensitivity of partially premixed combustion, where the increased importance of autoignition reactions leads to an increased combustion-timing variability. Disturbances in injected fuel amount and EGR flow could either result in a too early combustion timing with excessive in-cylinder temperatures and rapid combustion rates, or a too late combustion timing with incomplete combustion and resulting hydrocarbon emissions. This sensitivity has previously been described in [Ekholm et al., 2008; Yin et al., 2015; Henningsson, 2012; Li et al., 2016]. Additional motives for combustion-timing feedback are hardware variation and aging and the increased variation in fuel properties due to the introduction of different types of biofuels.

In-cylinder pressure measurements allow for detection of the combustion timing, indicated by θ_{50}, as described in Chapter 4. Detected θ_{50} can be regulated cycle-by-cycle by varying the injection timing θ_{SOI} as illustrated in Fig. 6.1, where a controller determines θ_{SOI} from the θ_{50} set-point deviation e. Closed-loop θ_{50} control of this type was previously used in [Shaver et al., 2004; Bengtsson et al., 2004; Willems et al., 2010].

The proportional-integral (PI) controller is the most common solution to practical closed-loop control problems and is attractive because of its simplicity. Furthermore, the problem of designing a PI controller illustrates the inherent limitations and complexities of combustion-timing feedback, which gives valuable insights for other controller-design approaches.

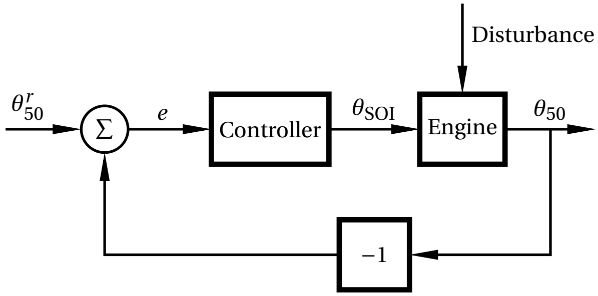

Figure 6.1 The combustion-timing feedback loop. The indicator for combustion timing θ_{50} is obtained from the measured in-cylinder pressure and heat-release analysis. The controller varies θ_{SOI} to counteract the error $e = \theta_{50}^r - \theta_{50}$ caused by, e.g., changes in fuel-amount or intake conditions.

The PI controller considered is given by

$$\begin{aligned} \theta_{\mathrm{SOI}}(k+1) &= k_p e(k) + I(k) \\ I(k) &= I(k-1) + k_I e(k-1) \end{aligned} \tag{6.1}$$

where the injection timing of the following cycle $\theta_{\mathrm{SOI}}(k+1)$ is determined by the previous-cycle error

$$e(k) = \theta_{50}^r(k) - \theta_{50}(k) \tag{6.2}$$

multiplied with the proportional gain k_p, and the integral term $I(k)$, which is the sum of previous errors, scaled with the integral gain k_I. The integral term is introduced to bring e to zero in steady state.

When introducing feedback, the controller has to be robustly designed to ensure closed-loop stability. It is also important that the controller does not enhance stochastic cycle-to-cycle variation. In PI-controller design, this is done by carefully deciding the controller gains k_p and k_I. The problem of deciding k_p and k_I is investigated in this chapter by evaluating controller performance through simulation. Simulation allows for evaluation of a large number of gain combinations at different engine loads.

The effect of fuel reactivity on controller design is addressed by evaluating controller performance for different primary reference fuels (PRF). A PRF is a mixture of n-heptane and iso-octane, where the PRF number indicates the iso-octane volume percentage. Primary reference fuels are commonly used as reference in engine research and are used to determine the octane number of a fuel. The octane number (ON) is a measure of the fuel resistance to autoignition which increases with ON, and is defined by the PRF value needed to provide equivalent autoignition properties.

The presented controller-gain evaluation provides gains that simultaneously maximize attenuation of θ_{50} disturbances and fulfill constraints on robustness and noise sensitivity. The evaluation also investigates the trade-off between these performance requirements. The optimization-based approach to PI controller design was inspired by works presented in [Hast et al., 2013; Garpinger and Hägglund, 2015], where understanding and rules of thumb for PI controller design were found through optimization.

The chapter is outlined as follows: The model used for controller evaluation is introduced in Sec. 6.1. The steady-state relation between θ_{SOI} and θ_{50} is studied in Sec. 6.2. Section 6.3 presents the criteria used for controller evaluation. Robust and noise-insensitive controllers, found through simulation of transient and steady-state operation for different PRFs are presented in Sec. 6.4, together with an analysis of the results. Finally, conclusions are given in Sec. 6.5.

6.1 Modeling

The in-cylinder state and wall-surface temperature were modeled using the zero-dimensional model presented in Sec. 2.2. Constant-volume combustion and static gas-exchange boundary conditions were assumed to speed up computations. A detailed description of this model is given in [Widd et al., 2008] where it was shown to successfully predict experimental θ_{50} and p_{IMEPg}. The ignition-delay τ was computed using the model M4, presented in Sec. 2.4

$$\tau = \phi^{\alpha(T,\text{PRF})} p^{\beta(T,\text{PRF})} x_{O_2}^{\zeta(T,\text{PRF})} e^{\Lambda(T,\text{PRF})} \tag{6.3}$$

This is a PRF correlation, calibrated from constant-volumes simulation data over a wide range of engine-relevant operating conditions. The model was presented in [Delvescovo et al., 2016] and was able to predict θ_{50} in experimental HCCI operation. The start of combustion θ_{SOC} was computed using the Livengood-Wu integration criterion [Livengood and Wu, 1955]

$$\int_{\theta_{\text{SOI}}}^{\theta_{\text{SOC}}} \frac{1}{\tau} dt = 1 \tag{6.4}$$

The model of the closed engine cycle was used in closed-loop simulation experiments, for which the model outputs θ_{50} and p_{IMEPg} were regulated on a cycle-to-cycle basis using θ_{SOI} and the injected fuel energyf Q_c^{tot}. Model parameters used are presented in Table 6.1.

6.2 Steady-State Characteristics

Fuel injection provides direct control of the combustion processes. This means that the combustion timing can be adjusted from one engine cycle to the next. There is also weak cycle-to-cycle dependence due to residual gas and

Table 6.1 Model parameters used in simulation. Three different convection coefficients were used during compression (compr.), expansion (exp.) and gas exchange (gas ex.).

Cylinder Geometry		Heat-Transfer	
Comp. ratio [-]	18	h_c (comp.) [W/(m^{2}K)]	250
V_d [m^3]	2.1×10^3	h_c (exp.) [W/(m^{2}K)]	500
Bore [mm]	130	h_c (gas ex.) [W/(m^{2}K)]	250
Stroke [mm]	160	T_c [K]	333
IVC [CAD]	-151	$m_c c_p$ [J/K]	1150
EVO [CAD]	146	k_c [W/(m^{2}K)]	45
		L_c [m]	0.025

slow wall-temperature dynamics. These effects will be discussed in the following sections. The strong direct effect between θ_{SOI} and θ_{50} makes the system steady-state characteristics important in the controller design.

The model steady-state input-output relation between θ_{SOI} and θ_{50} is presented in Fig. 6.2 for PRF20 (red) and PRF100 (blue). The relation is represented as bands, generated from a range of engine loads. Load was varied by increasing the fuel energy Q_c^{tot} from 2000 to 6000 J, at a relative air-fuel ratio $\lambda = 2$, and intake temperature $T_{\text{in}} = 70$ °C. These values were chosen to resemble typical mid-to-high load conditions in the author's engine lab, with the exception of the high T_{in}.

The system exhibits a nonlinear input/output behavior. For a given Q_c^{tot}, there is a limited interval of obtainable θ_{50}, and an interval of θ_{SOI} for which θ_{50} is controllable. It is within these intervals the PI controller should operate. For late θ_{SOI}, θ_{50} is excessively delayed which indicates that ignition never occurs, i.e., the charge misfires. This happens when insufficient time and reactivity during the expansion stroke result in an unfulfilled ignition condition, see (6.4). For early θ_{SOI}, the system gain approaches zero due to low reactivity during the early compression stroke, which results in poor controllability.

There is a clear difference between the two fuels. The obtainable θ_{50} interval is narrower with a higher PRF value due to the decreased fuel reactivity. With $Q_c^{\text{tot}} = 2000$ J, it is not possible to obtain $\theta_{50} < 6$ CAD for PRF80 due to insufficient reactivity during compression. There is also a visible difference in Q_c^{tot} sensitivity for the two fuels. In order to obtain similar θ_{50} and conduct a comparable controller-evaluation for the different fuels, T_{in} was adjusted as a function of PRF. This adjustment was done to ensure that $\theta_{50} = 5$, an efficient θ_{50} set point, could be obtained from PRF0 to PRF100 at the lowest Q_c^{tot}. Found T_{in} values are presented in Table 6.2. A variable compression ratio or variable valve timings are other possible adjustments for fuel-reactivity compensation. These solutions would,

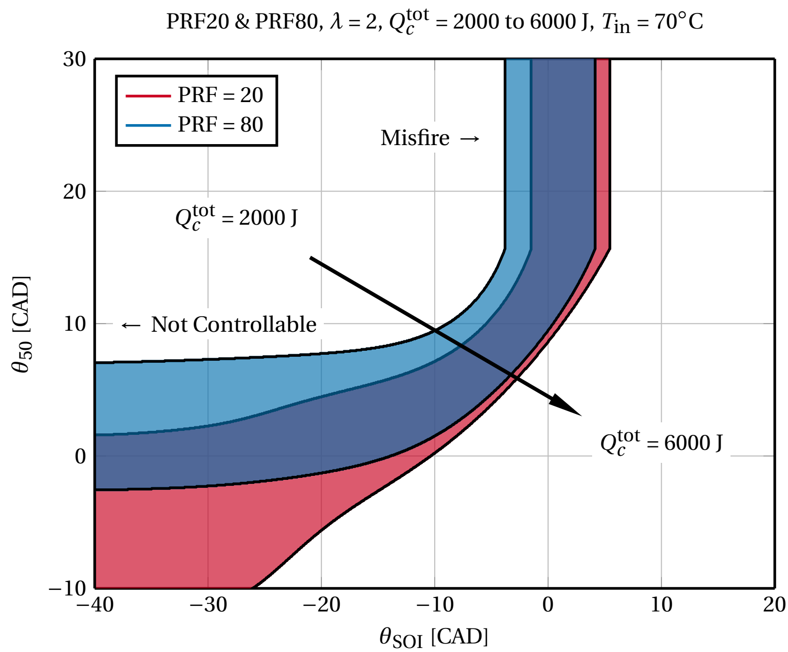

Figure 6.2 Steady-state θ_{50} / θ_{SOI} relation for PRF20 and PRF80 with fuel energies from 2000 to 6000 J. The Q_c^{tot} sweep generates a band of θ_{50} / θ_{SOI} relations. For late θ_{SOI}, θ_{50} is excessively delayed which means that ignition never occurs. Controllability is reduced when θ_{SOI} decreases.

Table 6.2 Relation between PRF and T_{in} in order to obtain $\theta_{50} = 5$ CAD with $\lambda = 2$ and $Q_c^{tot} = 2000$ J.

PRF [-]	0-10	20	30	40	50	60	70	80	90	100
T_{in} [°C]	50	53	58	62	67	70	73	76	78	80

however, be more demanding on engine hardware, as T_{in} could be varied using fast thermal management [Haraldsson, 2005]. The T_{in} adjustment gave the θ_{50} / θ_{SOI} characteristics in Fig. 6.3, where the layered bands represent θ_{50} / θ_{SOI} relations from PRF0 (dark red) to PRF100 (dark blue). Now, $\theta_{50} \in [5, 15]$ are obtainable for all fuels and Q_c^{tot}. There are however still differences in Q_c^{tot} sensitivity, which decreases from PRF0 to PRF100 in the θ_{SOI} interval for which θ_{50} is controllable.

There is also a shape difference between for the different fuels. The gain changes more steeply as θ_{SOI} is delayed prior to the misfire region for higher PRF values, whilst lower PRF values show a more linear trend. Figure 6.4 shows how this

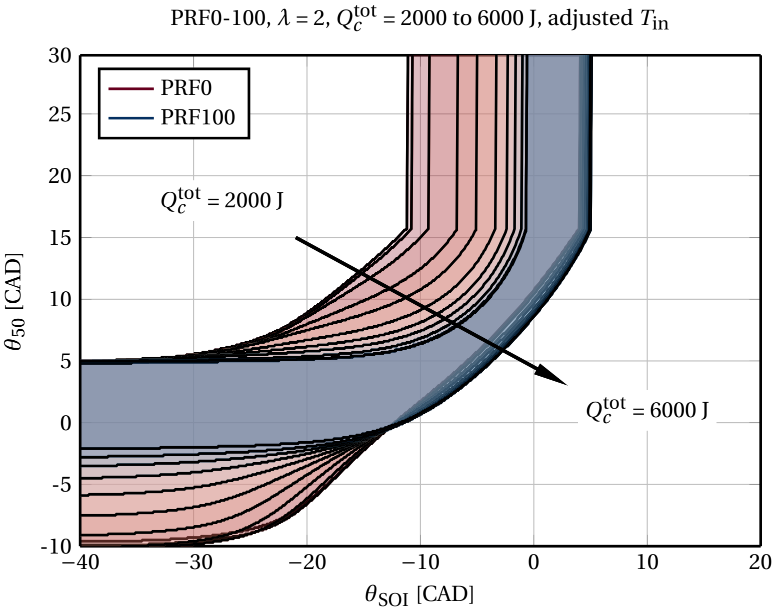

Figure 6.3 Steady-state θ_{50} / θ_{SOI} relation with adjusted T_{in} are presented as layered bands. The lower red band corresponds to PRF0 and the upper blue band to PRF100.

difference can be explained by how τ varies as a function of θ. Higher PRF values have a narrower range with shorter τ, and exhibit a different τ behavior close to TDC.

This difference is caused by the negative-temperature coefficient (NTC) behavior of low-value PRFs. NTC means that the reaction rate decreases with increasing temperature, and is the result of an increase in relative importance of terminating reaction paths over branching reaction paths, which slows down overall reaction rates [Curran et al., 2002]. The ignition delay therefore increases with increasing temperature for certain operating conditions. For the lower value PRFs, τ starts to increase with CAD during the compression stroke, and then decreases again as θ_{SOI} is delayed towards top-dead center. The NTC behavior is then repeated during the expansion stroke and gives an overall more constant τ close to TDC.

In order to ensure adequate PI-controller performance, it is necessary to limit θ_{SOI} in an interval where θ_{50} is controllable whilst avoiding misfire. Misfire leads to irregular power output and greatly increases fuel consumption. Too early injection timings, as a result of infeasible θ_{50}^r, leads to controller wind up. The region where $0.1 < \partial\theta_{50}/\partial\theta_{SOI} < \infty$ is represented by the shaded areas in Fig. 6.5 for PRF0 and PRF100. The region is narrower for low Q_c^{tot} and high PRF values. This

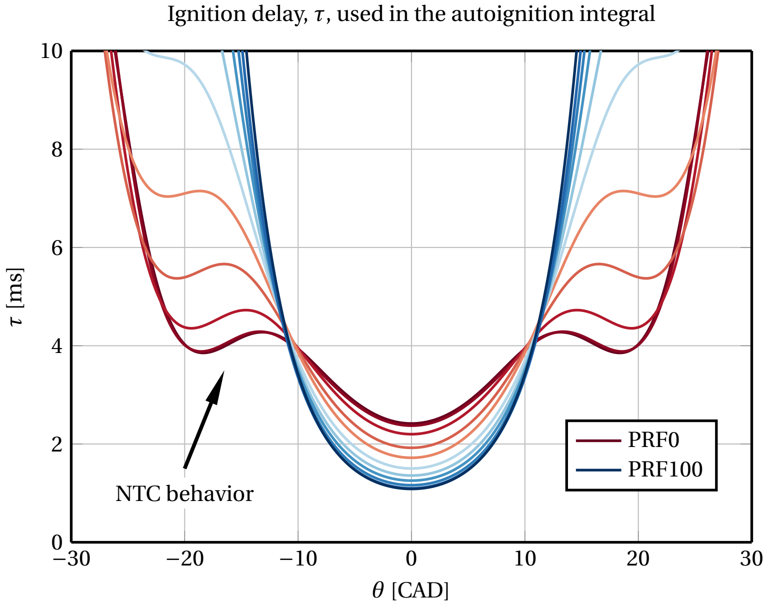

Figure 6.4 Ignition delay τ used in the autoignition criterion in (2.69) as a function of θ with adjusted T_{in} according to Table 6.2. The low-value PRFs exhibit a NTC behavior during compression and expansion. Note that both temperature and PRF value are varied for the different curves, and that the NTC behavior is dependent on both parameters. It was decided to study NTC behavior after T_{in} adjustment since this would be necessary prior to engine operation to get satisfactory operation for the high PRF values.

implies that a PI controller alone is not sufficient. A controller also has to be able to detect misfire, and if θ_{50}^r is infeasible to avoid wind up. The controller should then take action by adjusting θ_{50}^r or limit θ_{SOI}. Design of such a controller is not covered here.

6.3 Controller Evaluation

This section presents the controller-evaluation method used. The approach adopted was to evaluate PI-controller performance over a grid of controller gains. Optimal controller gains were computed by evaluating accumulated tracking error, robustness to instability and θ_{SOI} variation due to stochastic disturbances. Tracking error was computed during a simulated test cycle where changes in θ_{50}^r, T_{in} and p_{IMEPg}^r were made. Cycle-to-cycle variation in θ_{SOI} was evaluated in steady-state where the model was exposed to stochastic disturbances.

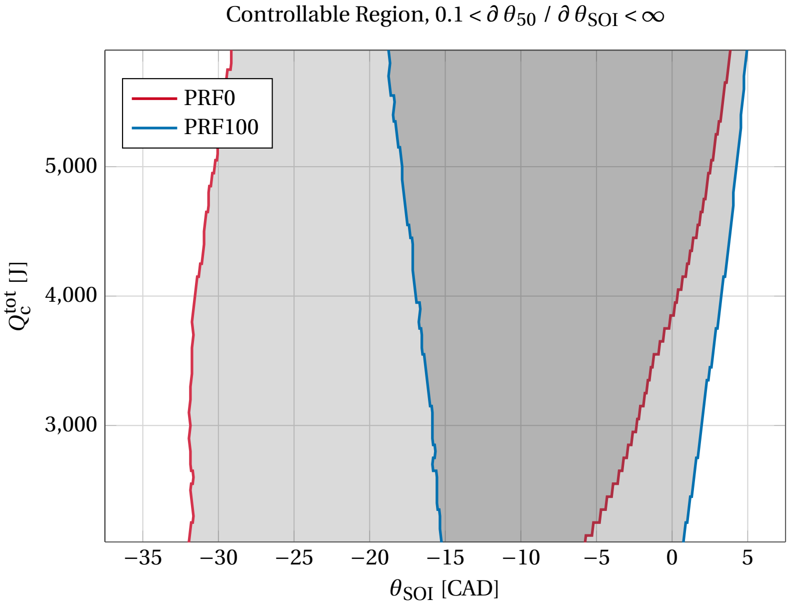

Figure 6.5 The region where $0.1 < \partial\theta_{50}/\partial\theta_{SOI} < \infty$. In order for the controller to perform satisfactorily, θ_{SOI} should be limited within this region. Note that the region is narrower for low load and PRF100.

Load Control

The gross indicated mean effective pressure p_{IMEPg} was also controlled during simulation. This was done using a PI controller that adjusted Q_c^{tot} for tracking of a set point p^r_{IMEPg}. The PI-controller gains were tuned for a response time of 10 cycles. Robustness and measurement-noise sensitivity were therefore evaluated with respect to the resulting multiple input/output system to account for cross coupling from Q_c^{tot} to θ_{50}, and from θ_{SOI} to p_{IMEPg}.

Disturbance Rejection

The θ_{50}-controller objective is to follow θ^r_{50} changes whilst attenuating the effects of disturbances, see Fig. 6.1. The controller ability to fulfill this objective was measured by computing the discrete-time integrated absolute error (IAE)

$$\mathrm{IAE} = \sum_{k=1}^{N} |e(k)| \tag{6.5}$$

during the simulation experiments, where N is the number of cycles. The IAE is a commonly used measure for controller evaluation [Åström and Hägglund, 2006].

Here, it will mainly penalize transient control error since the controllers exhibit error-free tracking in steady state due to integral action.

Robustness

It is important that the controller is stable around the set point. This can be ensured by having sufficient stability margins. For linear discrete-time systems, robustness is captured by the sensitivity function S and the complementary sensitivity function T [Zhou and Doyle, 1998]

$$
\begin{aligned}
S(z) &= (I + P(z)C(z))^{-1} \\
T(z) &= P(z)C(z)(I + P(z)C(z))^{-1}
\end{aligned}
\tag{6.6}
$$

Here, $z \in \mathbb{C}$ and I denotes the identity matrix, P is the pulse-transfer function of the system to be controlled and C is the controller in feedback interconnection. Bounds on the H_∞-norms of S and T can be introduced as guarantees for robustness

$$
\begin{aligned}
M_s &= ||S(e^{i\omega})||_\infty \leq \kappa_{M_s} \\
M_t &= ||T(e^{i\omega})||_\infty \leq \kappa_{M_t} \\
\omega &\in [0, \pi]
\end{aligned}
\tag{6.7}
$$

An elaborate description of robust controller design can be found in [Zhou and Doyle, 1998]. Norm values ranging from 1.2 to 2 correspond to gain margins from 0 to 2 and phase margins between 49° to 29° [Åström and Hägglund, 2006]. Here, $\kappa_{M_s} = \kappa_{M_t} = 1.4$ were introduced as upper bounds.

The norms M_s and M_t were computed through model linearization. Linearization was done with step-response analysis at multiple stationary points along the test-cycle trajectory, indicated by the symbols in Fig. 6.7. The obtained worst-case M_s and M_t were then used in (6.7). The transfer function of the linearized model were on the form

$$
\begin{aligned}
P(z) &= \begin{pmatrix} P_{11}(z) & P_{12}(z) \\ P_{21}(z) & P_{22}(z) \end{pmatrix} \\
P_{ij}(z) &= k_{ij}^{d} + k_{ij}^{\text{res}} z^{-1} + \frac{k_{ij}^{\text{wall}}(1 + a_{\text{wall}})z^{-1}}{1 + a_{\text{wall}} z^{-1}}
\end{aligned}
\tag{6.8}
$$

Here, P_{11} is the transfer function from θ_{SOI} to θ_{50}, P_{22} is the transfer function from Q_c^{tot} to p_{IMEPg} and P_{12}, P_{21} represent the corresponding cross-coupling dynamics. Furthermore, k_{ij}^{d} is a direct gain, k_{ij}^{res} models the one-cycle delayed residual-gas effect, and a_{wall} and k_{ij}^{wall} determine the time constant and gain of the wall-temperature dynamics. Step responses for P are presented in Fig. 6.6, for PRF0 at $p_{\text{IMEPg}} = 6$ and $\theta_{50} = 12$.

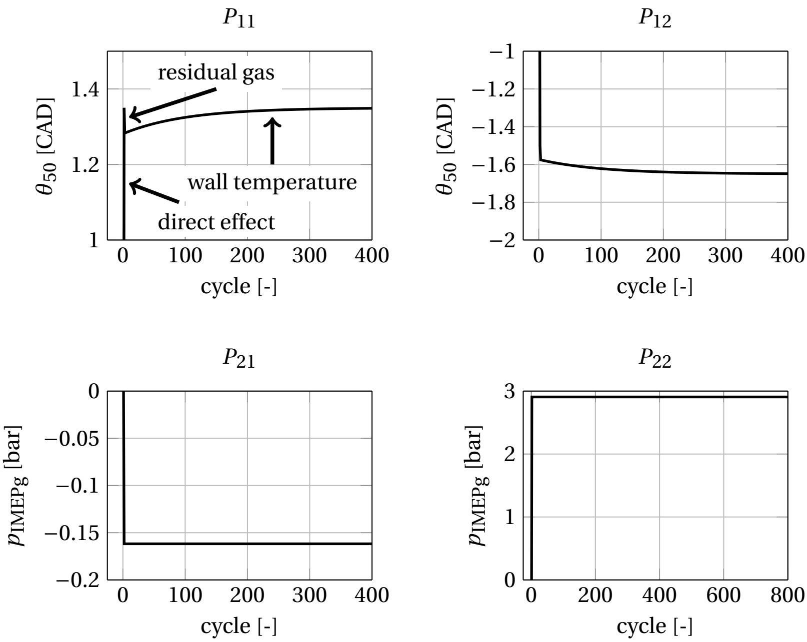

Figure 6.6 Step response for (6.8). Input steps of $\theta_{\mathrm{SOI}} = 1$ CAD and $Q_c^{\mathrm{tot}} = 1000$ J are applied at cycle 1. The P_{11} subdiagram indicates the direct effect, the residual-gas effect and the wall-temperature dynamics, respectively.

The 2×2 controller is given by

$$C = \begin{pmatrix} C_1(z) & 0 \\ 0 & C_2(z) \end{pmatrix} \tag{6.9}$$

where C_1 and C_2 are θ_{50} and p_{IMEPg} PI controllers on the form

$$C_i(z) = z^{-1}(k_p^i + \frac{k_I^i}{z-1}) \tag{6.10}$$

Where z^{-1} is the delay from measurement to actuation. The reason for designing a decoupled controller, and for designing C_2 given C_1, was because of weak coupling (see P_{12} and P_{21} in Fig. 6.6) and the convenience of designing a load controller with respect to other aspects than θ_{50}.

Noise Sensitivity

It is necessary to avoid excessive θ_{SOI} variation due to stochastic cycle-to-cycle variation. This requirement was formulated as a constraint on the steady-state

θ_{SOI} standard deviation

$$\sigma_{\theta_{\mathrm{SOI}}} \leq \kappa_\sigma \tag{6.11}$$

Stochastic cycle-to-cycle variation was evaluated by introducing Gaussian-noise disturbances on Q_c^{tot}, T_{in} and p_{in}. It was decided to set the upper bound $\kappa_\sigma = 0.25$ to maintain θ_{SOI} within ± 1 CAD in steady state.

Optimization Problem

In summary, the design problem is described by the following optimization problem from PRF0 to PRF100

$$\begin{aligned} \underset{k_p, k_I}{\text{minimize}} \quad & \sum_{k=1}^{N} |e(k)| \\ \text{subject to} \quad & M_s \leq 1.4 \\ & M_t \leq 1.4 \\ & \sigma_{\theta_{\mathrm{SOI}}} \leq 0.25 \end{aligned} \tag{6.12}$$

The optimization problem was solved by simulating the system model and evaluating (6.12) over a grid of controller gains. This was not only done to find optimal gains but also to investigate cost function and constraint characteristics as a function of k_I, k_p, Q_c^{tot} and PRF.

6.4 Results

The optimization problem (6.12) was solved by evaluating a grid of gains $k_p,\ k_I \in \{0.05, 0.1, \ldots, 1\}$ and PRFs $\in \{0, 10, \ldots, 100\}$ during two simulation experiments:

1. A transient cycle consisting of 750 engine cycles for which disturbances in T_{in} (±5°C), and changes in θ_{50}^r (±6 CAD) and p_{IMEPg}^r (±10 bar) were made to evaluate M_s, M_t and IAE.

2. A steady-state noise-sensitivity experiment consisting of 8000 engine cycles at p_{IMEPg}^r = 5 and 15 bar with θ_{50}^r = 6 and 12 CAD. Gaussian-noise disturbances were applied to T_{in}, p_{in} and Q_c^{tot}, with standard deviations $\sigma_{T_{\mathrm{in}}} = 1$ °C, $\sigma_{Q_c^{\mathrm{tot}}} = 50$ J and $\sigma_{p_{\mathrm{in}}} = 0.025$ bar.

The relative air-fuel ratio λ was set equal to 2 by adjusting p_{in}, whereas T_{in} was adjusted as a function of PRF according to Table 6.2.

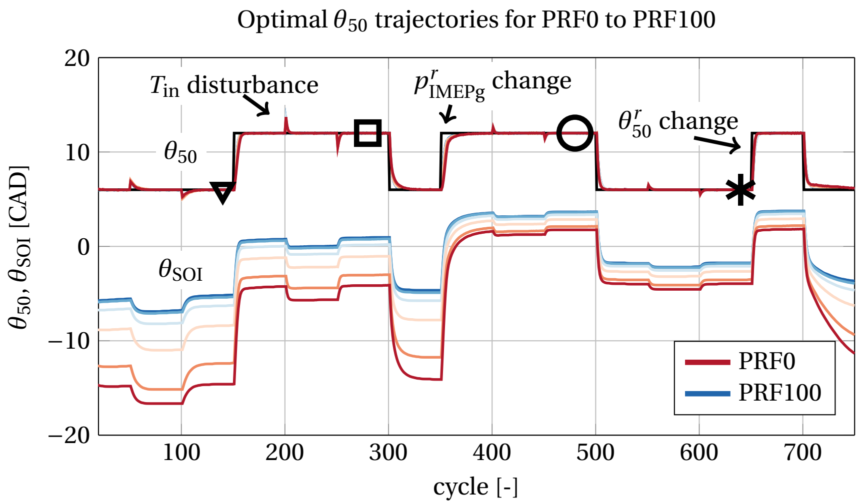

Figure 6.7 Optimal θ_{50} and θ_{SOI} trajectories from PRF0 to PRF100. Changes in T_{in} were applied at cycles 50, 100, 200, 250, 400, 450, 550 and 600, p^r_{IMEPg} changes were applied at cycles 350 (increase) and 700 (decrease), and θ^r_{50} was varied at cycles 150, 300, 350, 500, 650 and 750. During the p^r_{IMEPg} steps, θ^r_{50} was also changed in order to increase θ_{SOI} variation. The symbols indicate the points of linearization where M_s and M_t where computed, see Table 6.3 for static-gain values. When comparing PRF performance, the difference in θ_{50} was not as significant as the difference in θ_{SOI} for the different PRFs. It can be seen that changes in p_{IMEPg} and θ^r_{50} resulted in greater θ_{SOI} variation for lower PRF values, and that the θ_{SOI} response was more comparable during T_{in} changes.

Optimal Gains

Optimal transient θ_{50} and θ_{SOI} trajectories with respect to (6.12) are presented in Fig. 6.7, where optimal time constants of the closed loops are within 10 cycles for all disturbances and set-point changes. When comparing different PRFs, it can be seen that the difference in θ_{50} was not as significant as the difference in θ_{SOI}. Load and θ^r_{50} variation gave greater θ_{SOI} variation for low-value PRFs, whilst θ_{SOI} variation was comparable for different PRFs during T_{in} changes.

Linearization points for which robustness was evaluated are indicated by the symbols $\triangledown$, $\square$, $\bigcirc$ and $*$ in Fig. 6.7. Computed static gains with respect to these points are presented in Table 6.3 for PRF0 and PRF100. It can be seen that the P_{11} gains were higher for late θ_{50} and PRF100, and that the interaction from Q_c^{tot} to θ_{50} (P_{12}) was higher at low p^r_{IMEPg}.

Optimal steady-state performance is presented in Fig. 6.8. The θ_{SOI} standard deviation $\sigma_{\theta_{\text{SOI}}}$ was higher for the low-load operating points (cycles 1-500), $\sigma_{\theta_{\text{SOI}}}$ was also higher for lower PRF values.

Table 6.3 Static gains at the linearization points. Units are given by [-], [CAD/kJ], [bar/CAD] and [bar/J] for P_{11}, P_{12}, P_{21} and P_{22}. Note the following trends: higher P_{11} gains at late θ_{50} and PRF100 and a larger interaction from Q_c^{tot} to θ_{50} at low p_{IMEPg}.

PRF0

$$P_{\triangledown} \qquad p^r_{\text{IMEPg}} = 5 \text{ bar}, \theta^r_{50} = 6 \text{ CAD} \qquad \begin{pmatrix} 0.35 & -0.005 \\ 0.0033 & 0.0029 \end{pmatrix}$$

$$P_{\square} \qquad p^r_{\text{IMEPg}} = 5 \text{ bar}, \theta^r_{50} = 12 \text{ CAD} \qquad \begin{pmatrix} 1.35 & -0.007 \\ -0.07 & 0.003 \end{pmatrix}$$

$$P_{*} \qquad p^r_{\text{IMEPg}} = 15 \text{ bar}, \theta^r_{50} = 6 \text{ CAD} \qquad \begin{pmatrix} 0.9 & -0.001 \\ -0.056 & 0.0029 \end{pmatrix}$$

$$P_{\bigcirc} \qquad p^r_{\text{IMEPg}} = 15 \text{ bar}, \theta^r_{50} = 12 \text{ CAD} \qquad \begin{pmatrix} 1.35 & -0.0015 \\ -0.16 & 0.0029 \end{pmatrix}$$

PRF100

$$P_{\triangledown} \qquad p^r_{\text{IMEPg}} = 5 \text{ bar}, \theta^r_{50} = 6 \text{ CAD} \qquad \begin{pmatrix} 0.7 & -0.0025 \\ -0.0011 & 0.0028 \end{pmatrix}$$

$$P_{\square} \qquad p^r_{\text{IMEPg}} = 5 \text{ bar}, \theta^r_{50} = 12 \text{ CAD} \qquad \begin{pmatrix} 1.85 & -0.004 \\ -0.1 & 0.0029 \end{pmatrix}$$

$$P_{*} \qquad p^r_{\text{IMEPg}} = 15 \text{ bar}, \theta^r_{50} = 6 \text{ CAD} \qquad \begin{pmatrix} 1 & -0.0005 \\ -0.065 & 0.0029 \end{pmatrix}$$

$$P_{\bigcirc} \qquad p^r_{\text{IMEPg}} = 15 \text{ bar}, \theta^r_{50} = 12 \text{ CAD} \qquad \begin{pmatrix} 1.4 & -0.001 \\ -0.16 & 0.0028 \end{pmatrix}$$

Finally, optimal controller gains are presented in Fig. 6.9 as a function of PRF. Both k_p and k_I decreased with PRF and k_p was slightly lower than k_I. The M_s value at the $\square$-linearizing point in Fig. 6.7 was always found to be the constraint limiting controller-gain magnitudes. At this point, the system gain $\partial\theta_{50}/\partial\theta_{\text{SOI}}$ was highest among the linearization points, see Table 6.3. This partial derivative also increased with PRF, which explains the trend in Fig. 6.9. These trends could have been anticipated by studying Fig. 6.3, where $\partial\theta_{50}/\partial\theta_{\text{SOI}}$ increased with θ_{50}, PRF value, and decreased with Q_c^{tot}. The remainder of this chapter investigates how the robustness and noise-sensitivity constraints vary with PRF.

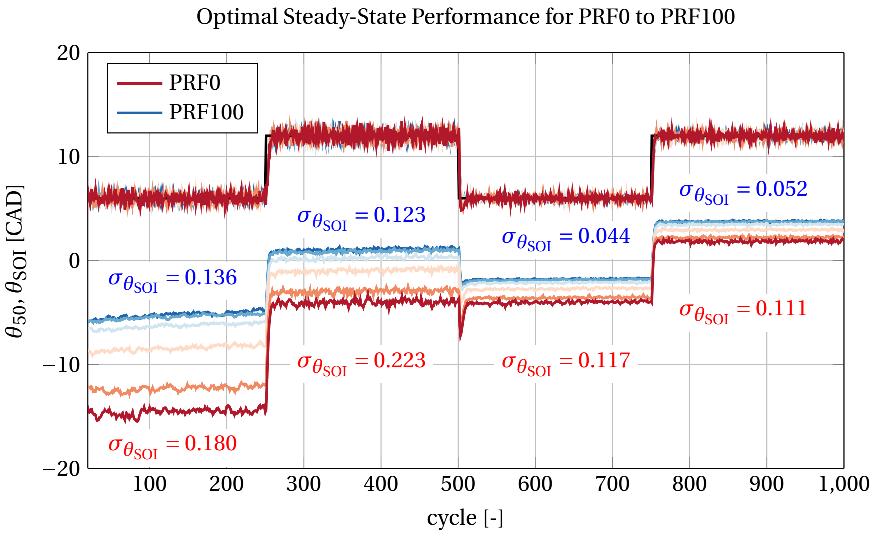

Figure 6.8 Optimal steady-state performance from PRF0 to PRF100. The θ_{SOI} standard deviation $\sigma_{\theta_{\mathrm{SOI}}}$ was higher for the low p_{IMEPg} points (cycles 1-500), and for the lower PRFs. The presented data is a part of the steady-state experiment consisting of 8000 cycles.

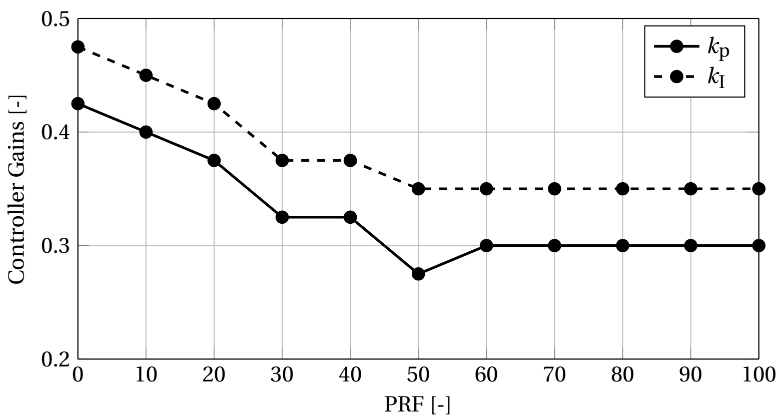

Figure 6.9 Optimal controller gains as a function of PRF. The $M_s < 1.4$ constraint at the □ operating point was consistently limiting the controller gains. The system gain $\partial\theta_{50}/\partial\theta_{\mathrm{SOI}}$ was highest at this point. Furthermore, $\partial\theta_{50}/\partial\theta_{\mathrm{SOI}}$ increased with PRF which explains the trend in this figure.

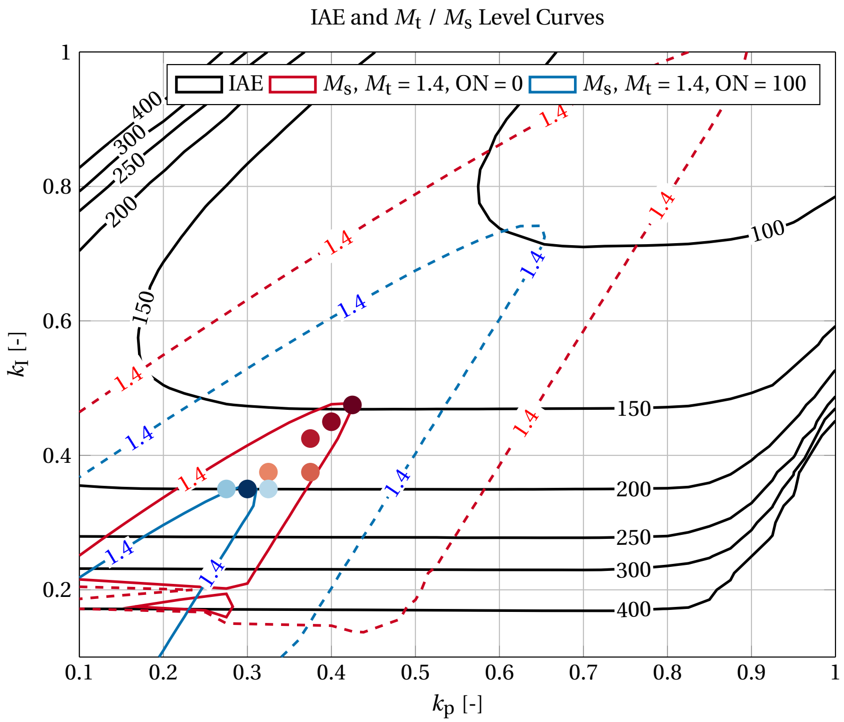

Figure 6.10 IAE (black), M_s = 1.4 (solid) and M_t = 1.4 (dashed) level curves as a function of controller gains k_p and k_I, for PRF0 and PRF100. The IAE score decreased as k_p and k_I increased. The allowed gains for which M_s, M_t < 1.4 are encircled by the colored lines, and optimal gains are indicated by circles.

Robustness

To illustrate robustness-constraint characteristics, IAE level curves (black, solid) are presented in Fig. 6.10, together with level curves of $M_s = 1.4$ (solid) and $M_t = 1.4$ (dashed) as a function of controller gains for PRF0 and PRF100. The IAE score decreased as k_p and k_I were simultaneously increased. The stability limits are indicated by the steep increase in IAE in the upper-left and lower-right regions of the figure. The constraint on M_t was less restrictive than the constraint on M_s, and the M_s and M_t constraints were overall less restrictive for PRF0. The limiting M_s value was computed at the late θ_{50}^r and low p_{IMEPg}^r operating point □. The PRF0 fuel also had visible M_s and M_t constraints for low controller gains due to interaction with the p_{IMEPg} loop. This was a result of the higher P_{12} gain for PRF0.

These results can be explained by linear-systems analysis. With the

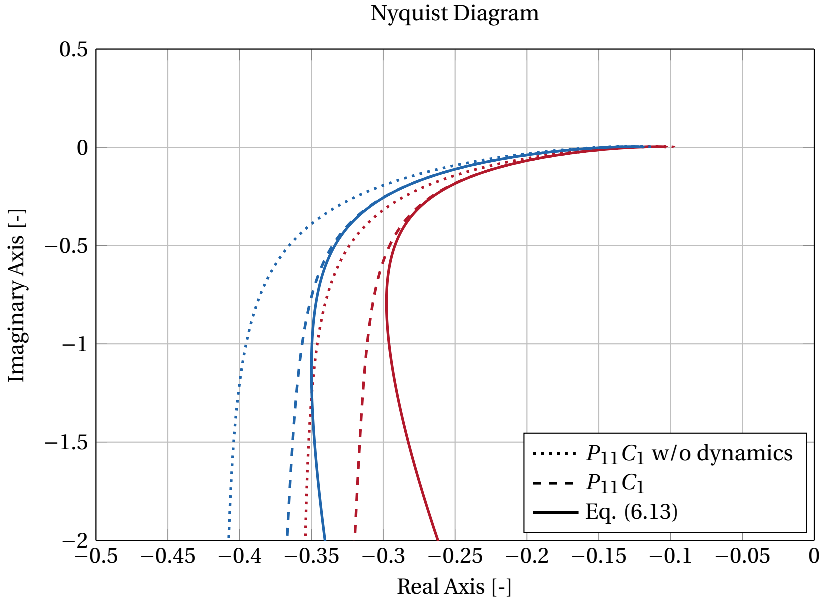

Figure 6.11 Nyquist curves with optimal controller gains for PRF0 (red) and PRF100 (blue), for (6.13) (solid), P_1C_1 (dashed), and P_1C_1 without residual and wall-temperature dynamics (dotted). It can be seen that the simple model has the smallest stability margin.

p_{IMEPg}-loop closed, the θ_{50} open-loop transfer function is given by

$$\left(P_{11} - \frac{P_{12}C_2P_{21}}{1+P_{22}C_2}\right)C_1 \tag{6.13}$$

Nyquist curves with $k_I = 0.35,\ k_p = 0.3$ for PRF0 (red) and PRF100 (blue) are presented in Fig. 6.11. This figure presents Nyquist curves for (6.13) (solid), P_1C_1 (dashed) and P_1C_1 without residual and wall-temperature dynamics (dotted). It can be seen that the simplest open-loop transfer function has the smallest stability margin. The intuition behind this result is that both residual-gas dynamics and the p_{IMEPg} controller counteract the θ_{SOI} effect on θ_{50}, which decreases the open-loop gain. Analysis of the simple system can therefore be used to compute stability margins that are sufficient for the more detailed loops.

When omitting wall-temperature, residual-gas and p_{IMEPg}-loop dynamics, the linearized closed-loop pulse-transfer function, from θ^r_{50} to θ_{50} is given by

$$H_{cl}(z) = \frac{KC_1(z)}{1+KC_1(z)} \tag{6.14}$$

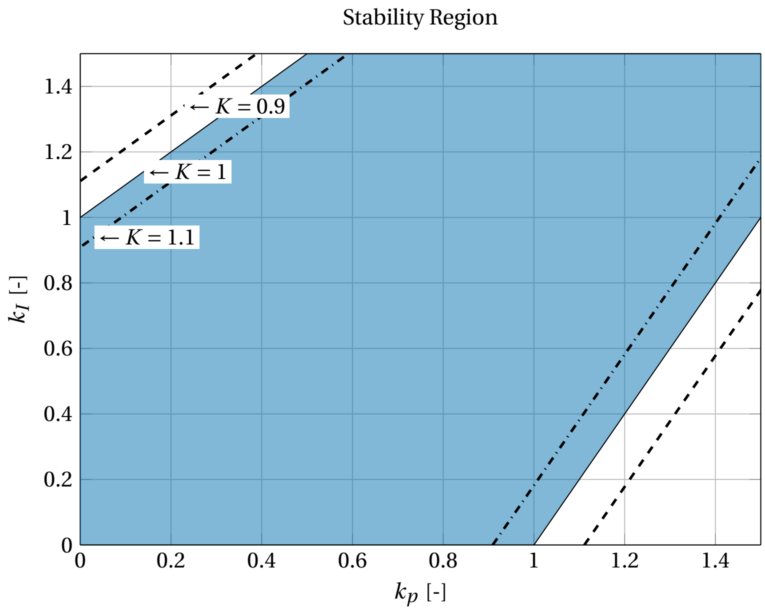

Figure 6.12 PI-gain stability region, computed using the critera in (6.16). The stability region shrinks as K increases. The stability limits are similar to the IAE level curves in Fig. (6.10).

where $K = \partial\theta_{50}/\partial\theta_{\mathrm{SOI}}$. Inserting the pulse transfer function for (6.10) into (6.14) yields the characteristic polynomial for the closed-loop poles

$$z^2 + z(Kk_p - 1) + K(k_I - k_p) \tag{6.15}$$

By applying the Jury stability criterion [Jury, 1964], and assuming positive controller gains, the conditions for stability is obtained

$$\begin{aligned} k_p &< k_I/2 + 1/K \\ k_p &> k_I - 1/K \end{aligned} \tag{6.16}$$

The controller-gain stability region becomes narrower as K increases, see Fig. 6.12.

Noise Sensitivity

Figure 6.13 presents IAE (black) and $\sigma_{\mathrm{SOI}} = 0.25$ level curves for PRF0 and PRF100 as functions of k_p and k_I. Allowed gains for which $\sigma_{\mathrm{SOI}} \leq 0.25$ are within the red and blue lines. The σ_{SOI} constraint was more restrictive for PRF0, and the most restrictive σ_{SOI} constraint was found at late θ_{50} and low p_{IMEPg} for both fuels, see Fig. 6.8.

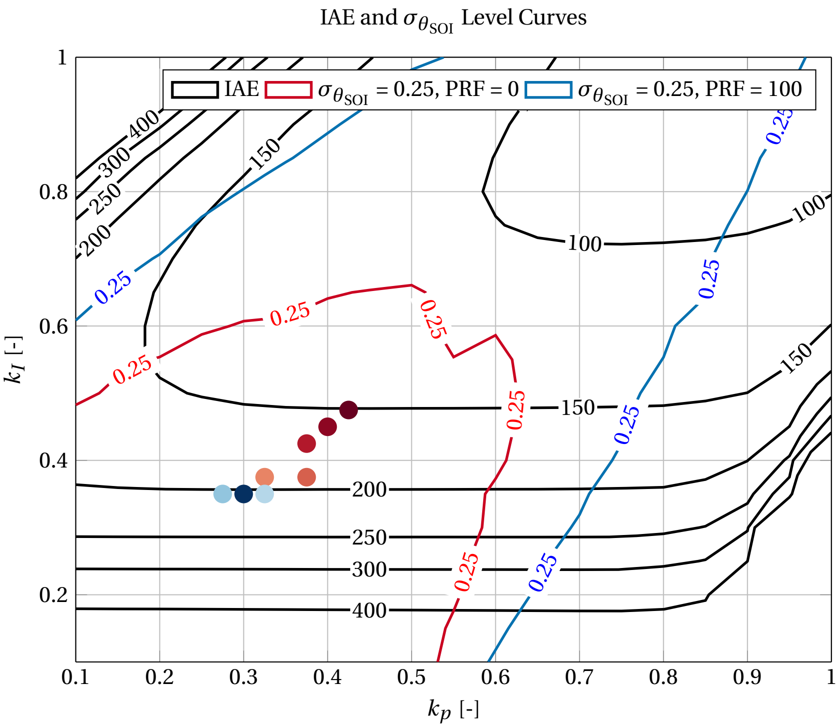

Figure 6.13 IAE (solid, black) and $\sigma_{SOI} = 0.25$ level curves for PRF0 and PRF100 as a function of k_p and k_I. The allowed gains for which $\sigma_{SOI} \leq 0.25$ are within the solid colored lines. The most restrictive $\sigma_{SOI} = 0.25$ constraints, for both fuels were found at the late θ_{50} at the low-load operating points, see Fig. 6.8.

The θ_{SOI} standard deviation can be evaluated by studying the H_2-norm of the transfer function S_c

$$S_c = C(z)(I + P(z)C(z))^{-1} \tag{6.17}$$

which maps $\sigma_{\theta_{50}}$ to σ_{SOI}. The H_2-norm of S_c amplifies $\sigma_{\theta_{50}}$ according to

$$\sigma_{SOI} = ||S_c||_2 \sigma_{\theta_{50}} \tag{6.18}$$

With independent disturbances on T_{in}, Q_c^{tot} and p_{in}, $\sigma_{\theta_{50}}$ can be approximated through linearization, using the expression

$$\sigma_{\theta_{50}} = \sqrt{\left(\frac{\partial \theta_{50}}{\partial T_{in}}\right)^2 \sigma_{T_{in}}^2 + \left(\frac{\partial \theta_{50}}{\partial Q_c}\right)^2 \sigma_{Q_c^{tot}}^2 + \left(\frac{\partial \theta_{50}}{\partial p_{in}}\right)^2 \sigma_{p_{in}}^2}$$

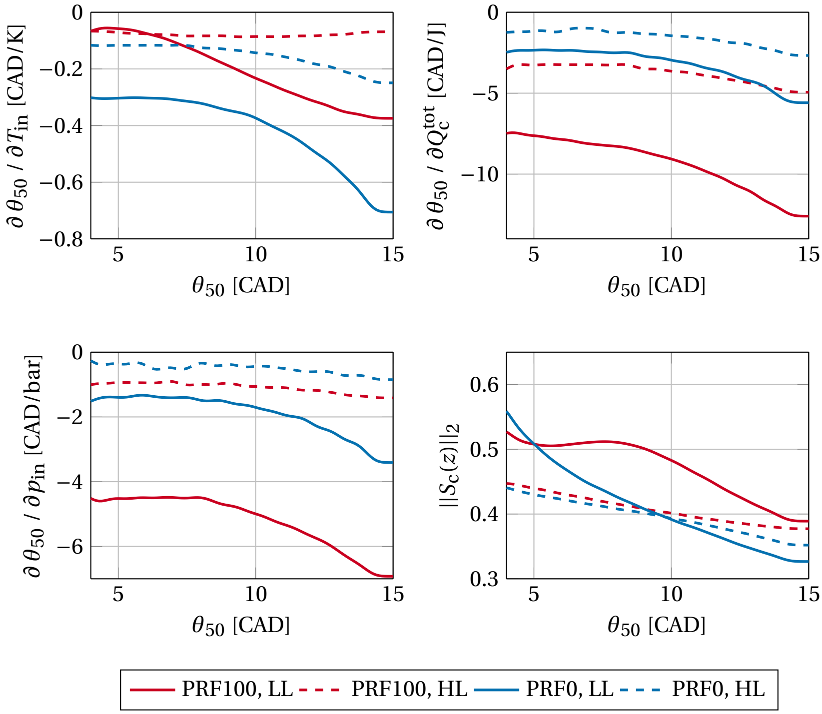

Figure 6.14 The closed-loop noise sensitivity depends on θ_{50} partial derivatives with respect to T_{in}, p_{in}, Q_c^{tot} and the S_c norm. This figure presents these quantities as a function of θ_{50} for PRF0, PRF100 with $p_{\text{IMEPg}} = 5$ bar (LL) and 15 bar (HL).

Partial derivatives of θ_{50} and $||S_c||_2$ with constant controller gains are presented in Fig. 6.14 for $p_{\text{IMEPg}} = 5$ and 15 bar. The partial-derivate magnitudes were clearly larger at low p_{IMEPg} and late θ_{50}. It can also be seen that PRF0 was more sensitive to Q_c^{tot} and p_{in} whilst PRF100 was more sensitive to T_{in}. The closed-loop noise sensitivity $||S_c||_2$ was higher for PRF100 and decreased with θ_{50}. Similar experimental PRF trends were presented in [Sjöberg and Dec, 2005], where T_{in} was adjusted according to PRF.

The standard deviation $\sigma_{\theta_{\text{SOI}}}$, computed using (6.18) is presented in Fig. 6.15. It can be seen that σ_{SOI} decreased with p_{IMEPg} and θ_{50}. Overall, σ_{SOI} was also higher for PRF0 which agrees with the observed trends in Figs. 6.8 and 6.13.

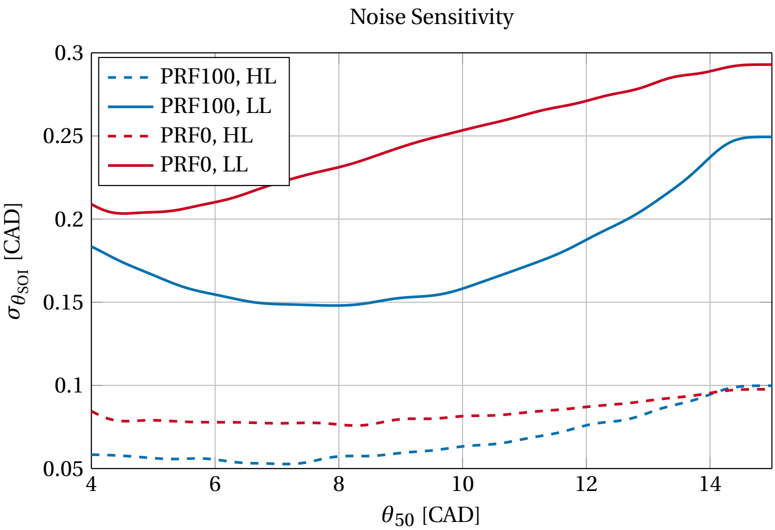

Figure 6.15 Injection-timing standard deviation σ_{SOI} as a function of θ_{50}, computed using (6.18). The standard deviation was altogether higher for PRF0 which agrees with the observed trends in Figs. 6.8 and 6.13.

Rules of Thumb

To summarize, the simulation results provided the following rules of thumb for PI-controller tuning:

1. Robustness was limited by operating points with large $\partial\theta_{50}/\partial\theta_{\mathrm{SOI}}$. These were found at late θ_{50} and low p_{IMEPg}. At these points, $\partial\theta_{50}/\partial\theta_{\mathrm{SOI}}$ increased with PRF value, meaning that robustness constraints became more restrictive for higher PRF values.

2. Noise sensitivity was higher at low loads and late combustion timings where gains from disturbances to θ_{50} were higher. The noise sensitivity was also higher for lower PRF values due to an increased Q_c^{tot} and p_{in} sensitivity.

3. A robust and noise-insensitive controller-gain choice for all fuels and operating points is given by $0.2 < k_p < k_I < 0.35$.

6.5 Conclusions

This chapter showed that the θ_{SOI} interval for which θ_{50} is controllable is limited between a low-gain limit for early θ_{SOI} and a misfire limit for late θ_{SOI}. In order to obtain early combustion timings for higher PRFs, T_{in} had to be adjusted as a function of PRF. Even after T_{in} adjustment, the PRFs have different θ_{50} characteristics, partly due to the varying NTC behavior for the different fuels. The computation of suitable θ_{SOI} limits is a part of the controller design where such limits could be a function of fuel, load and intake conditions.

Optimal PI-controller gains found through simulation were limited by the high system gain at late θ_{50} and low p_{IMEPg}. Controller measurement-noise sensitivity was also found to be higher at this operating point due to an increased θ_{50} sensitivity to load and intake-condition variation. Controller gain requirements also varied with the PRF value: robustness was lower for higher PRFs due to an increased system gain, and noise sensitivity was higher for lower PRFs due to a higher Q_c^{tot} and p_{in} sensitivity.

7

Model-Based Control of Combustion Timing and Ignition Delay

7.1 Introduction

A sufficiently long ignition delay τ is a prerequisite for the fuel / air mixing leading to premixed low-temperature combustion, as described in Sec. 1.3. Meanwhile, it is also important that the combustion timing θ_{50} (4.3) is sufficiently well timed for high thermodynamic efficiency. A too early θ_{50} leads to increased heat-transfer and inefficient pressure build-up during the compression stroke, and a late θ_{50} results in high exhaust losses and a lowered combustion efficiency. Simultaneous control of τ and θ_{50} is an important component for a successful implementation of partially premixed combustion, and when controlling these two variables, one has to pay attention to their coupling through θ_{SOI} and thermodynamic in-cylinder conditions.

This chapter studies model-based multi-cylinder control of τ and θ_{50} with combined actuation of the gas-exchange and fuel-injection systems. The objective is to regulate τ and θ_{50} during load disturbances and set-point changes. This is an under-determined control problem due to more output than input variables for the engine setup used.

A model predictive control (MPC) is suggested, see Sec. 3.1. This is a suitable design choice for multiple input/output systems with actuator constraints. The controller obtains τ and θ_{50} from in-cylinder pressure measurement and heat-release analysis, and the ignition-delay model M1 (see Sec. 2.4) is linearized every engine cycle for model-based prediction. The MPC feedback loop is illustrated in Fig. 7.1, where the multiple cylinders are indicated by the (bold type) vector notation. The MPC computes fuel-injection timings and valve positions of the two EGR paths and the fast thermal-management (FTM) system. Valve po-

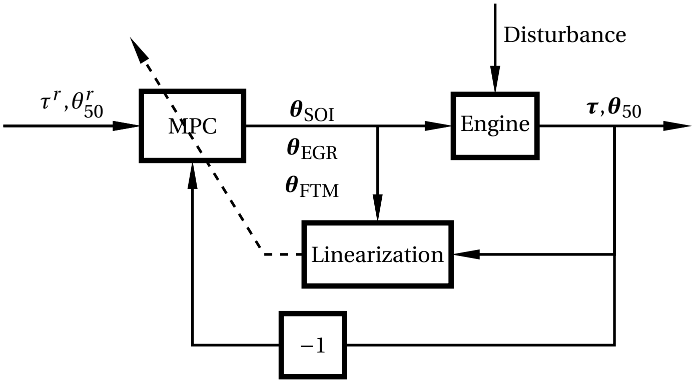

Figure 7.1 This chapter presents and studies the following MPC feedback loop. The controller obtains $\boldsymbol{\tau}$ and $\boldsymbol{\theta}_{50}$ from in-cylinder pressure measurement and heat-release analysis, and then linearizes the ignition-delay model M1, presented in Sec. 2.4. The controller computes fuel-injection timings $\boldsymbol{\theta}_{\mathrm{SOI}}$ and valve positions of the two EGR paths $\boldsymbol{\theta}_{\mathrm{EGR}}$ and the fast thermal-management system $\boldsymbol{\theta}_{\mathrm{FTM}}$. Multiple cylinders are indicated by the (bold type) vector notation.

sitions determine gas-mixture temperature and exhaust-gas recirculation (EGR) ratio, see Fig. 2.3.

Previous research on this subject was presented in [Lewander et al., 2008], where MPC was used to control τ for premixed operation whilst θ_{50} was kept within an acceptable range by injection-timing adjustment. Karlsson et al. [2008] controlled τ and θ_{50} in conventional diesel combustion using a linear-quadratic regulator (LQR) to minimize emissions using the back-pressure valve and θ_{SOI} as system inputs. The main contributions of the work presented in this chapter are the use of a physics-based τ model for MPC, and the use of additional gas-exchange actuators.

The modeling and linearization procedures are introduced in Sec. 7.2, and the controller design is presented in Sec. 7.3. The main part of this chapter covers an experimental controller evaluation, which is presented in Sec. 7.4. Discussion and conclusions are given in Sec. 7.5.

7.2 Modeling

Model M1 (see, Sec. 2.4) was used to model τ, whereas a calibrated static model was used to model the gains from gas-exchange valve positions to intake-manifold composition and temperature. This section describes these models and how they were used in the controller design.

Ignition Delay Model

The ignition-delay model M1, without p dependence showed comparable performance to more detailed models but had a lower computational complexity, see Sec. 2.4. The model is given by

$$\tau = A\overline{[O_2]}^{\alpha} e^{E_a/\tilde{R}\overline{T}} \tag{7.1}$$

where E_a is an apparent activation energy, $\tilde{R}$ is the universal gas constant and $\overline{T}$ and $\overline{[O_2]}$ are the mean cylinder temperature and oxygen concentration between θ_{SOI} and θ_{10}. Here, the in-cylinder temperature was computed using the adiabatic compression relation

$$T = T_{\text{IVC}}\left(\frac{V_{\text{IVC}}}{V}\right)^{\gamma-1} \tag{7.2}$$

where γ was held constant. The oxygen concentration was then given by

$$[O_2] = \frac{[O_2]_{\text{IVC}}}{V} V_{\text{IVC}} \tag{7.3}$$

where $[O_2]_{\text{IVC}}$ is the in-cylinder oxygen concentration at intake-valve closing. It was computed using (2.41) and an estimated EGR mass flow, as described in Sec. 2.3. The following expression for τ

$$\tau = A\exp\left(\frac{E_a}{\frac{\tilde{R}}{\tau}\int_{\theta_{\text{SOI}}}^{\theta_{\text{SOI}}+\tau} T_{\text{IVC}}\left(\frac{V_{\text{IVC}}}{V(\theta)}\right)^{\gamma-1} d\theta}\right)\left(\frac{1}{\tau}\int_{\theta_{\text{SOI}}}^{\theta_{\text{SOI}}+\tau}\frac{[O_2]_{\text{IVC}}}{V(\theta)}V_{\text{IVC}}\,d\theta\right)^{\alpha} \tag{7.4}$$

is obtained when substituting for (7.2) and (7.3), with assumed constant N_{speed}. Model parameters A, E_a and α were found using the identification procedure presented in Sec. 2.4 at $p_{\text{IMEPg}} = 5$ bar and $N_{\text{speed}} = 1200$ rpm.

Gas-Exchange System Model

Simple static models, determined from experimental data, were used to relate changes in gas-system valve positions to changes in T_{IVC} and $[O_2]_{\text{IVC}}$. In Fig. 7.2, T_{IVC} and $[O_2]_{\text{IVC}}$ are displayed as functions of the high and low-pressure EGR valve positions θ_{LP}, θ_{HP}, and the hot-path valve positions θ_{hot}. The cool-path valve position was changed by setting

$$\theta_{\text{cool}} = \cos^{-1}(1-\cos(\theta_{\text{hot}})) \tag{7.5}$$

in order to keep an approximately constant total valve-opening area. This approach was previously used in [Widd et al., 2009].

This modeling approach is of course an oversimplification. One argument for using this model instead of the dynamic gas-exchange model in Sec. 2.3, besides reducing computational complexity, was that the valve-actuator dynamics were slower than the pressure dynamics.

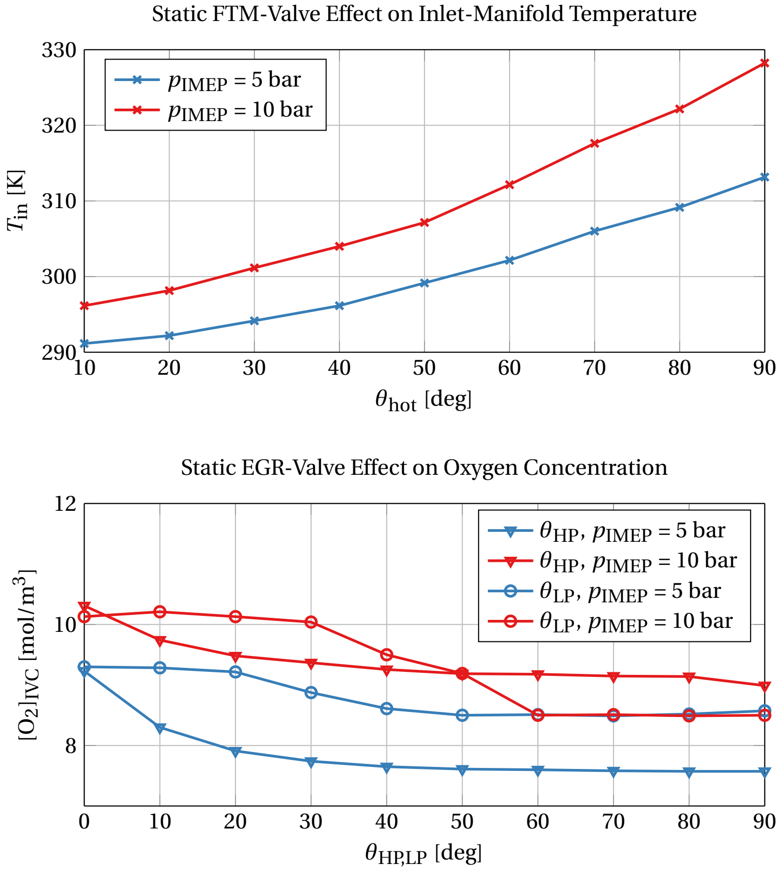

Figure 7.2 T_{IVC} and $[O_2]_{\text{IVC}}$ as functions of θ_{LP}, θ_{HP} and θ_{hot} at two different loads and $N_{\text{speed}} = 1200$ rpm. These experimentally obtained functions were used to model the relation between the gas-exchange valve positions and the intake manifold conditions. Note that the gain from θ_{HP} decreased with load. This was because of the decreased pressure difference over the exhaust and intake manifolds due to increased turbocharger boost.

Differentiation and Linearization

The presented models are not directly applicable for linear MPC. Model linearization was therefore necessary to obtain linear equality constraints. The approach taken was to linearize (7.4) and the trends in Fig. 7.2 numerically every engine cycle to provide a good model approximation. Since (7.4) is an implicit relation in τ, the partial derivatives of τ with respect to θ_{SOI}, T_{IVC} and $[O_2]_{\text{IVC}}$

were approximated by keeping τ constant in the integration limit in (7.4)

$$\begin{aligned}
\frac{\partial \tau}{\partial \theta_{\mathrm{SOI}}} &\approx \frac{\tau(\theta_{\mathrm{SOI}}+\Delta\theta_{\mathrm{SOI}}/2)-\tau(\theta_{\mathrm{SOI}}-\Delta\theta_{\mathrm{SOI}}/2)}{\Delta\theta_{\mathrm{SOI}}}\\
\frac{\partial \tau}{\partial T_{\mathrm{IVC}}} &\approx \frac{\tau(T_{\mathrm{IVC}}+\Delta T_{\mathrm{IVC}}/2)-\tau(T_{\mathrm{IVC}}-\Delta T_{\mathrm{IVC}}/2)}{\Delta T_{\mathrm{IVC}}}\\
\frac{\partial \tau}{\partial [\mathrm{O_2}]_{\mathrm{IVC}}} &\approx \frac{\tau([\mathrm{O_2}]_{\mathrm{IVC}}+\Delta[\mathrm{O_2}]_{\mathrm{IVC}}/2)-\tau([\mathrm{O_2}]_{\mathrm{IVC}}-\Delta[\mathrm{O_2}]_{\mathrm{IVC}}/2)}{\Delta[\mathrm{O_2}]_{\mathrm{IVC}}}
\end{aligned} \tag{7.6}$$

This approximation is motivated by the fact that small increments in $\overline{T}$ and $\overline{[\mathrm{O_2}]}$ do not change τ significantly. The partial derivatives in (7.6) make it possible to relate changes in ΔT_{IVC}, $\Delta\theta_{\mathrm{SOI}}$, $\Delta[\mathrm{O_2}]_{\mathrm{IVC}}$ to changes in τ and θ_{50} on a cycle-to-cycle basis

$$\begin{aligned}
\tau_i(k+1) &= \tau_i(k) + \begin{pmatrix} \frac{\partial \tau_i}{\partial \theta^i_{\mathrm{SOI}}} & \frac{\partial \tau_i}{\partial T_{\mathrm{IVC}}} & \frac{\partial \tau_i}{\partial [\mathrm{O_2}]_{\mathrm{IVC}}} \end{pmatrix} \begin{pmatrix} \Delta\theta_{\mathrm{SOI}_i}(k) \\ \Delta T_{\mathrm{IVC}}(k) \\ \Delta[\mathrm{O_2}]_{\mathrm{IVC}}(k) \end{pmatrix}\\
\theta_{50_i}(k+1) &= \theta_{50_i}(k) + \Delta\theta_{\mathrm{SOI}_i}(k)\\
&\quad + \frac{\partial \theta}{\partial t} \begin{pmatrix} \frac{\partial \tau_i}{\partial \theta^i_{\mathrm{SOI}}} & \frac{\partial \tau_i}{\partial T_{\mathrm{IVC}}} & \frac{\partial \tau_i}{\partial [\mathrm{O_2}]_{\mathrm{IVC}}} \end{pmatrix} \begin{pmatrix} \Delta\theta_{\mathrm{SOI}_i}(k) \\ \Delta T_{\mathrm{IVC}}(k) \\ \Delta[\mathrm{O_2}]_{\mathrm{IVC}}(k) \end{pmatrix}
\end{aligned} \tag{7.7}$$

where k is the cycle index, Δ is the forward-difference operator, i is the cylinder index, and $d\theta/dt$ is crank angles per millisecond at the current N_{speed}, needed here since τ and θ_{50} have different units.

The partial derivatives $\partial T_{\mathrm{IVC}}/\partial\theta_{\mathrm{hot}}$, $\partial[\mathrm{O_2}]_{\mathrm{IVC}}/\partial\theta_{\mathrm{LP}}$ and $\partial[\mathrm{O_2}]_{\mathrm{IVC}}/\partial\theta_{\mathrm{HP}}$, computed from the slopes in Fig. 7.2, relate the gas-system valve positions to the system outputs τ and θ_{50} accordingly

$$\begin{aligned}
\tau_i(k+1) &= \tau_i(k) + \begin{pmatrix} \frac{\partial \tau_i}{\partial \theta^i_{\mathrm{SOI}}} & \frac{\partial \tau_i}{\partial \theta_{\mathrm{hot}}} & \frac{\partial \tau_i}{\partial \theta_{\mathrm{HP}}} & \frac{\partial \tau_i}{\partial \theta_{\mathrm{LP}}} \end{pmatrix} \begin{pmatrix} \Delta\theta_{\mathrm{SOI}i}(k) \\ \Delta\theta_{\mathrm{hot}}(k) \\ \Delta\theta_{\mathrm{HP}}(k) \\ \Delta\theta_{\mathrm{LP}}(k) \end{pmatrix}\\
\theta_{50_i}(k+1) &= \theta_{50_i}(k) + \begin{pmatrix} \frac{\partial \theta_{50_i}}{\partial \theta_{\mathrm{SOI}_i}} & \frac{\partial \theta_{50_i}}{\partial \theta_{\mathrm{hot}}} & \frac{\partial \theta_{50_i}}{\partial \theta_{\mathrm{HP}}} & \frac{\partial \theta_{50_i}}{\partial \theta_{\mathrm{LP}}} \end{pmatrix} \begin{pmatrix} \Delta\theta_{\mathrm{SOI}_i}(k) \\ \Delta\theta_{\mathrm{hot}}(k) \\ \Delta\theta_{\mathrm{HP}}(k) \\ \Delta\theta_{\mathrm{LP}}(k) \end{pmatrix}
\end{aligned} \tag{7.8}$$

The complete linear state-space model can be written on more compact form

$$\begin{pmatrix} \boldsymbol{\theta}_{50}(k+1) \\ \boldsymbol{\tau}(k+1) \end{pmatrix} = \begin{pmatrix} \boldsymbol{\theta}_{50}(k) \\ \boldsymbol{\tau}(k) \end{pmatrix} + B \begin{pmatrix} \Delta\boldsymbol{\theta}_{\mathrm{SOI}}(k) \\ \Delta\theta_{\mathrm{hot}}(k) \\ \Delta\theta_{\mathrm{HP}}(k) \\ \Delta\theta_{\mathrm{LP}}(k) \end{pmatrix} \tag{7.9}$$

where

$$\begin{pmatrix} \boldsymbol{\theta}_{50}(k) \\ \boldsymbol{\tau}(k) \end{pmatrix} = \begin{pmatrix} \theta_{50_1}(k) & \ldots & \theta_{50_6}(k) & \tau_1(k) & \ldots & \tau_6(k) \end{pmatrix}^T$$

$$\Delta\boldsymbol{\theta}_{\mathrm{SOI}}(k) = \begin{pmatrix} \Delta\theta_{\mathrm{SOI},1}(k) & \ldots & \Delta\theta_{\mathrm{SOI},6}(k) \end{pmatrix}^T$$

$$B = \begin{pmatrix} \frac{\partial\theta_{50,1}}{\partial\theta_{\mathrm{SOI},1}} & \cdots & 0 & \frac{\partial\theta_{50,1}}{\partial\theta_{\mathrm{hot}}} & \frac{\partial\theta_{50,1}}{\partial\theta_{\mathrm{HP}}} & \frac{\partial\theta_{50,1}}{\partial\theta_{\mathrm{LP}}} \\ \vdots & \ddots & \vdots & \vdots & \vdots & \vdots \\ 0 & \cdots & \frac{\partial\theta_{50,6}}{\partial\theta_{\mathrm{SOI},6}} & \frac{\partial\theta_{50,6}}{\partial\theta_{\mathrm{hot}}} & \frac{\partial\theta_{50,6}}{\partial\theta_{\mathrm{HP}}} & \frac{\partial\theta_{50,6}}{\partial\theta_{\mathrm{LP}}} \\ \frac{\partial\tau_1}{\partial\theta_{\mathrm{SOI},1}} & \ldots & 0 & \frac{\partial\tau_1}{\partial\theta_{\mathrm{hot}}} & \frac{\partial\tau_1}{\partial\theta_{\mathrm{HP}}} & \frac{\partial\tau_1}{\partial\theta_{\mathrm{LP}}} \\ \vdots & \ddots & \vdots & \vdots & \vdots & \vdots \\ 0 & \cdots & \frac{\partial\tau_6}{\partial\theta_{\mathrm{SOI},6}} & \frac{\partial\tau_6}{\partial\theta_{\mathrm{hot}}} & \frac{\partial\tau_6}{\partial\theta_{\mathrm{HP}}} & \frac{\partial\tau_6}{\partial\theta_{\mathrm{LP}}} \end{pmatrix} \tag{7.10}$$

The system is not controllable due to more outputs than inputs, which is indicated by the fact that the controllability matrix $\mathscr{C}$

$$\mathscr{C} = \begin{pmatrix} B & \ldots & B \end{pmatrix} \tag{7.11}$$

has less than 12 independent columns. The system outputs $\boldsymbol{\tau}$ and $\boldsymbol{\theta}_{50}$ can therefore not be controlled independently and we are left with two options. Combustion timings $\boldsymbol{\theta}_{50}$ can either be controlled cylinder individually by varying $\boldsymbol{\theta}_{\mathrm{SOI}}$ and then letting gas-exchange actuators control $\boldsymbol{\tau}$. The other option is to control $\boldsymbol{\tau}$ cylinder individually and let the gas-exchange actuators control $\boldsymbol{\theta}_{50}$. The first of the two approaches was taken here. The reason for this choice was the nonlinear relationship between $\boldsymbol{\theta}_{\mathrm{SOI}}$ and $\boldsymbol{\tau}$ (see Fig. 6.4), and the monotone relationship between $\boldsymbol{\tau}$ and T_{IVC}, $[\mathrm{O}_2]_{\mathrm{IVC}}$. It was also shown in Sec. 2.4 that it is difficult to accurately model the sign of $\partial\tau/\partial\theta_{\mathrm{SOI}}$ when θ_{SOI} is close to TDC. Such model errors could lead to unwanted closed-loop behavior if $\boldsymbol{\theta}_{\mathrm{SOI}}$ is set to control $\boldsymbol{\tau}$.

The desired controller can be obtained by MPC-weight tuning, which is covered in the following sections.

7.3 Model Predictive Control Formulation

The MPC problem was formulated accordingly

$$\begin{aligned}
\underset{\substack{\Delta\boldsymbol{\theta}_{\mathrm{SOI}},\Delta\theta_{\mathrm{HP}},\\ \Delta\theta_{\mathrm{LP}},\Delta\theta_{\mathrm{hot}}}}{\text{minimize}} \quad & \sum_{k=1}^{H_p}\Big(\omega_1||\theta_{50}^r(k)-\boldsymbol{\theta}_{50}(k)||_2^2+\omega_2||\tau^r(k)-\boldsymbol{\tau}(k)||_2^2 \\
& \qquad +\omega_3\theta_{\mathrm{HP}}(k)^2+\omega_4\theta_{\mathrm{LP}}(k)^2\Big) \\
& +\sum_{k\in k_{H_c}}\Big(\omega_5||\Delta\boldsymbol{\theta}_{\mathrm{SOI}}(k)||_2^2+\omega_6\Delta\theta_{\mathrm{hot}}(k)^2 \\
& \qquad +\omega_7\Delta\theta_{\mathrm{HP}}(k)^2+\omega_8\Delta\theta_{\mathrm{LP}}(k)^2\Big)
\end{aligned} \tag{7.12}$$

$$\text{subject to} \quad \theta^l \le \begin{pmatrix}\boldsymbol{\theta}_{\mathrm{SOI}}\\ \theta_{\mathrm{hot}}\\ \theta_{\mathrm{HP}}\\ \theta_{\mathrm{LP}}\end{pmatrix} \le \theta^u$$

$$\text{and. (7.9) for } k=0,\ldots,H_p-1$$

Here, k is the cycle index, and $||\cdot||_2$ is the Euclidian norm in $\mathbb{R}^6$. Initial conditions at the current cycle $k=0$ are obtained from measurements. The first sum penalizes θ_{50} and τ set-point error, and the usage of EGR over the prediction horizon H_p. Set points θ_{50}^r and τ^r are considered to be precomputed as a function of the engine operating point. It was decided to penalize EGR-valve opening area to favor flow over the turbine and to not use more EGR than needed. The terms in the second sum penalize control action over the control horizon H_c. The cost function should be minimized subject to absolute constraints on actuators and the linearized system dynamics in (7.9).

MPC Design and Implementation

In order for the controller to overlook the slow valve actuators, H_p was set equal to 50 engine cycles. Moreover, the inputs were allowed to change nonequidistantly at samples $k \in k_{Hc}$ over the control horizon to decrease the number of variables in the optimization problem, and allow for shorter computation times, see Fig. 7.3.

The relation between the weights ω_{1-2} and ω_{5-8} determines the trade-off between tracking performance and controller sensitivity to cycle-to-cycle variation and model error. The weights ω_{6-8} determine how fast the valve positions are allowed to change, and were chosen to conform with physical limitations. The choice of ω_{3-4} is a trade-off between the ability to supply EGR to increase $\boldsymbol{\tau}$ and gas-exchange efficiency. Input bounds for EGR-valve positions were chosen so that the controller would operate in intervals where the $[O_2]_{\mathrm{IVC}}$-gains were non-

Table 7.1 Weights and constraints for (7.12).

ω_1	ω_2	ω_3	ω_4
10^2	10^4	5000	3000
ω_5	ω_6	ω_7	ω_8
0.1	10^{-2}	400	800
$3 \le \theta_{\text{HP}} \le 40$	$20 \le \theta_{\text{LP}} \le 50$	$5 \le \theta_{\text{hot}} \le 85$	$-40 \le \theta_{\text{SOI}} \le 10$

zero, see Fig. 7.2. Other actuator bounds were chosen to fulfill physical limitations, and θ_{SOI} was limited to avoid misfire, see Fig 6.2.

The weights and constraints used are presented in Table 7.1. Solution trajectories with these weights are presented in Fig. 7.3 for an arbitrary initial condition. The dashed black lines in the upper part of Fig. 7.3 are set points τ^r and θ_{50}^r. The cylinder numbers are indicated by different colors, cylinder 1 being the upper cylinder in Fig. 2.3.

The weights were tuned to obtain the desired behavior where $\boldsymbol{\theta}_{\text{SOI}}$ controls cylinder-individual $\boldsymbol{\theta}_{50}$. This was done by prioritizing $\boldsymbol{\theta}_{50}$ tracking, and let the slow gas-system actuators control the mean $\boldsymbol{\tau}$. Note that the grid over which $\boldsymbol{\theta}_{\text{SOI}}$ is allowed to change is denser initially than for the gas system valves. This is because the actuation of $\boldsymbol{\theta}_{\text{SOI}}$ is much faster than for the valve positions.

Solving (7.12) is a quadratic program (QP) and was solved in LabVIEW using the QP-solver VI. The solver used the previous-cycle solution and active set as initial guesses for the next cycle to shorten computation times. Early termination was also used for the solver to finish within one engine cycle. These are well known methods for speeding up MPC execution, see [Wang and Boyd, 2010]. The average computation time for differentiating Eqs. (7.6) and constructing the QP matrices was 10 ms, while it took 25 ms on average to solve (7.12). These computations were repeated every engine cycle after sampling of the previous-cycle cylinder pressure.

7.4 Experimental Results

Controller experiments were conducted in steady-state and during load and speed changes. In steady state, the objective was to track step changes in θ_{50}^r and τ^r, whereas the objective during load and speed changes was to regulate $\boldsymbol{\theta}_{50}$ and $\boldsymbol{\tau}$ at constant set points. The engine load p_{IMEPn} was changed by varying the injection durations, whilst the common-rail pressure p_{rail} was held constant at 800 bar. Both p_{IMEPn} and p_{rail} were controlled using PI controllers with feedforward. Engine-speed ramps were performed by manually changing the engine-brake speed set point.

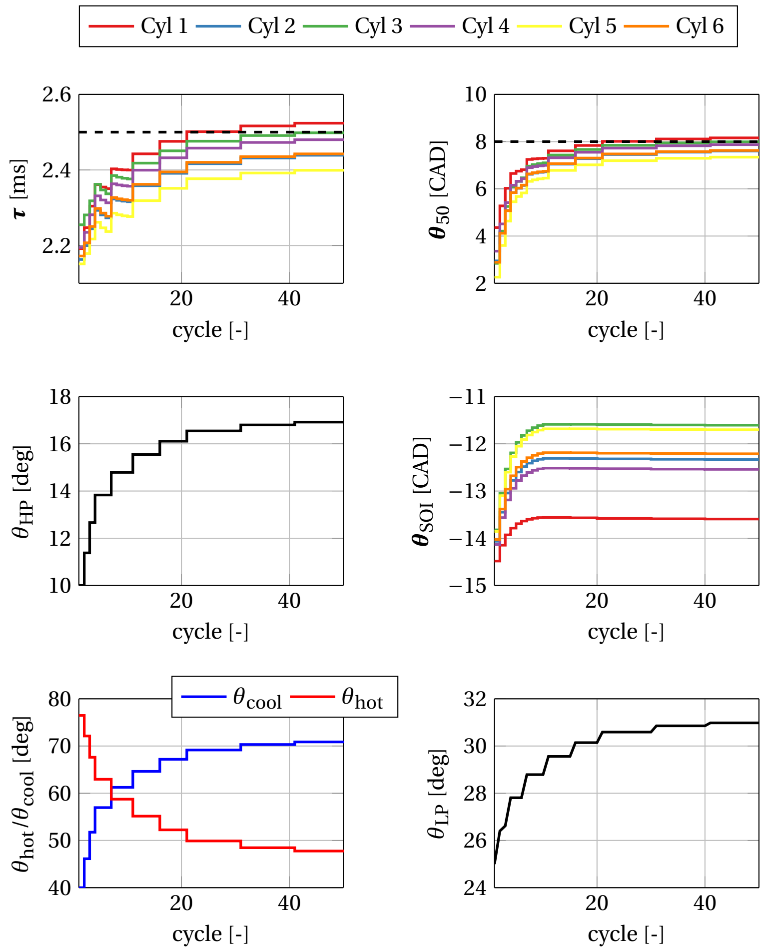

Figure 7.3 Solution trajectories of (7.12) using the weights and constraints in Table 7.1 and an arbitrary initial condition. The inputs were allowed to change at predefined cycle indices over H_c. The weights were chosen to prioritize $\boldsymbol{\theta}_{50}$ tracking, and let the slower gas-system actuators control the mean $\boldsymbol{\tau}$. Note that the samples for which $\boldsymbol{\theta}_{\mathrm{SOI}}$ was allowed to change was denser initially than for the gas-system valves. This was because control action of $\boldsymbol{\theta}_{\mathrm{SOI}}$ was much faster than for the valve positions.

Set-Point Tracking

Set-point tracking performance was evaluated by keeping p_{IMEPn} and N_{speed} constant and varying θ_{50}^r and τ^r. System inputs and outputs during 800 cycles of θ_{50}^r step changes are presented in Fig. 7.4. The controller weights ω_i (see Table

3) were set so that tracking of $\boldsymbol{\theta}_{50}$ was done by changing $\boldsymbol{\theta}_{\text{SOI}}$, $\boldsymbol{\tau}$ was then jointly controlled by the gas-exchange system actuators. This tuning resulted in regulation of the mean cylinder $\boldsymbol{\tau}$.

As $\boldsymbol{\theta}_{50}$ was delayed at cycle 950 in Fig. 7.4, $\boldsymbol{\tau}$ decreased due to the increased temperature at $\boldsymbol{\theta}_{\text{SOI}}$. This forced θ_{hot} to close while $\theta_{\text{HP,LP}}$ opened. The controller tried to find the lowest possible θ_{HP} in stationarity for higher turbine mass flows. Some chattering is visible in the gas-exchange actuators. This was due to stochastic cycle-to-cycle variation in $\boldsymbol{\theta}_{50}$ and $\boldsymbol{\tau}$ which could have been reduced by introducing filtering or increasing ω_{6-8}.

A zoom-in around cycle 950 is presented in Fig. 7.5. Here, it can be seen that $\boldsymbol{\theta}_{50}$ reached the new set point in 5 cycles. There was an internal delay of 5 cycles from set point to the controller, caused by the communication from the user interface and the real-time system. The gas system managed to adjust for the $\boldsymbol{\tau}$ decrease in 50 cycles where cylinder-to-cylinder variation created a τ-distribution among the cylinders. This variation could be caused by non-uniform EGR distribution to the different cylinders or different cylinder-wall temperatures. It can be seen that τ_6 was consistently shorter whilst τ_1 was the longest. A hypothetical explanation for this is that cylinder 1 is closer to the high-pressure EGR path, see Fig. 2.3.

In Fig. 7.6, system inputs and outputs are displayed during 1400 cycles for which step changes in τ^r were made. The tracking of τ^r was realized by varying θ_{hot} and $\theta_{\text{HP,LP}}$ whilst $\boldsymbol{\theta}_{\text{SOI}}$ was varied to keep $\boldsymbol{\theta}_{50}$ constant. The high-pressure EGR valve opened too much initially which gave a slight overshoot in $\boldsymbol{\tau}$. A zoom-in around cycle 550 is presented in Fig. 7.7. Here, it can be seen that $\boldsymbol{\theta}_{\text{SOI}}$ was varied to keep $\boldsymbol{\theta}_{50}$ within 0.6 CAD whilst $\boldsymbol{\tau}$ reached the new set point in 50 cycles.

Load Changes

In Fig. 7.8, system inputs and outputs are displayed during 1000 cycles for which p^r_{IMEPn} steps were made between 6 and 10 bar, and p_{IMEPn} reached its new set point in 20 cycles. The ignition delays decreased as p_{IMEPn} was increased due to increased cylinder temperature and richer cylinder mixtures. This forced $\theta_{\text{HP,LP}}$ to increase. The FTM system was limited to the cold-flow upper limit during the higher p_{IMEPn} values. Adjustments in $\boldsymbol{\theta}_{\text{SOI}}$ managed to keep $\boldsymbol{\theta}_{50}$ within 1 CAD.

In-cylinder data at $p_{\text{IMEPn}} = 6$ (dashed) and $p_{\text{IMEPn}} = 10$ bar (solid) are presented in Fig. 7.9. The figure shows pressure and heat-release rates for the different cylinders, and the injection current from cylinder 1. The controller manages to maintain constant $\boldsymbol{\theta}_{50}$ and $\boldsymbol{\tau}$ despite the p_{IMEPn} difference.

Speed Changes

In Fig. 7.10, system inputs and outputs are displayed during 2000 cycles for which the engine speed N_{speed} was varied between 1200 and 1500 rpm. The igni-

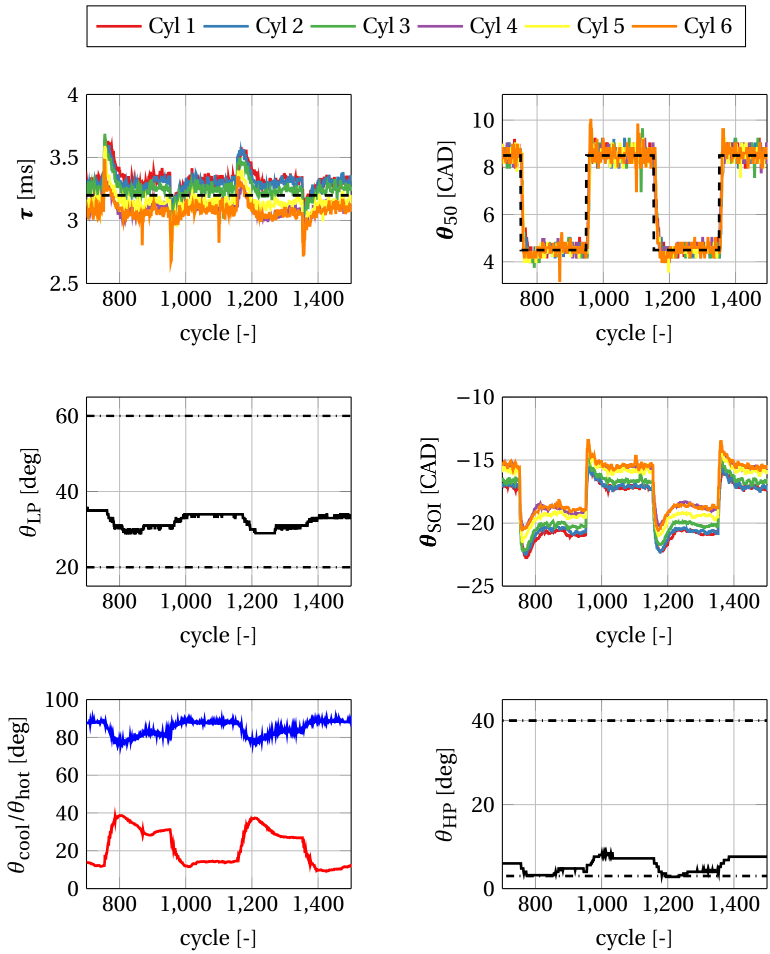

Figure 7.4 System inputs and outputs during step changes in θ^r_{50}. θ_{hot} is indicated in red and θ_{cool} in blue. The black dashed lines in the upper diagrams are θ^r_{50} and τ^r, whilst the dash-dotted lines are constraints on θ_{LP} and θ_{HP}.

tion delays decreased as N_{speed} was increased. Probably due to increased engine temperatures and cylinder-gas turbulence levels [Heywood, 1988]. This forced $\theta_{HP,LP}$ and θ_{cool} to open. The FTM system was limited to the cold-flow limit at $N_{speed} = 1500$ rpm, and $\boldsymbol{\theta}_{SOI}$ managed to keep $\boldsymbol{\theta}_{50}$ within 1 CAD from θ^r_{50}.

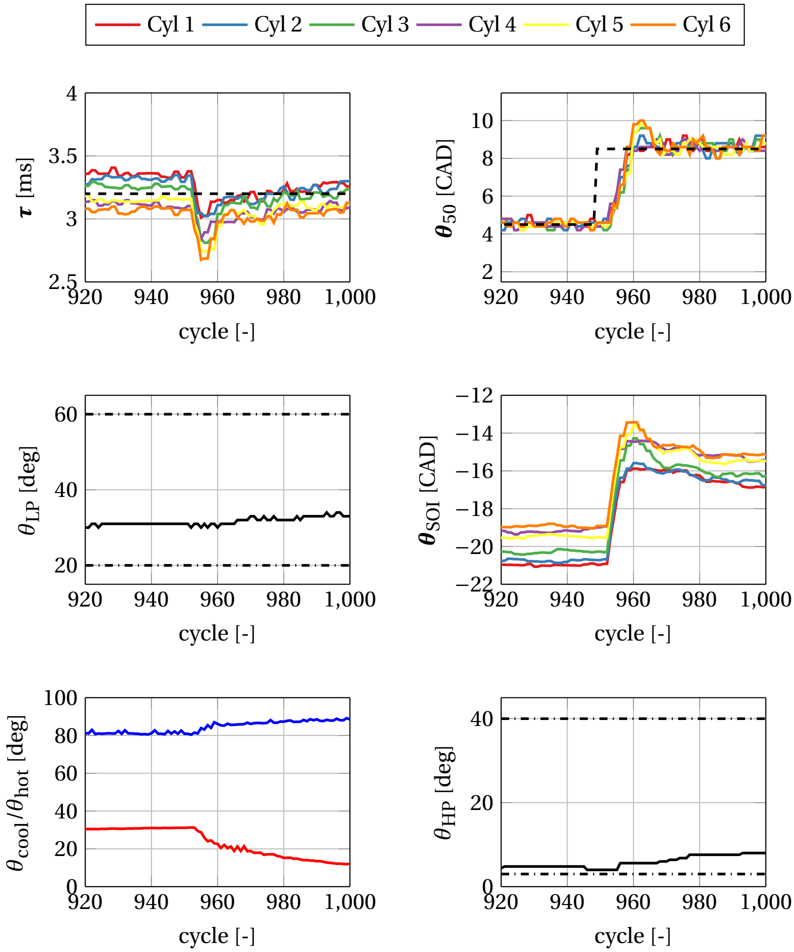

Figure 7.5 A zoom in around cycle 960 in Fig. 7.4 where $\boldsymbol{\theta}_{50}$ reached a new set point in 5 cycles. There is a visible internal delay from the set point to the controller of about 5 cycles. The gas system managed to adjust for the $\boldsymbol{\tau}$ decrease in 50 cycles.

7.5 Discussion and Conclusions

This chapter presented a physics-based MPC for control of θ_{50} and τ in a multi-cylinder engine. The controller was tuned for fast control of θ_{50} compared to τ, which resulted in a controller behavior where θ_{SOI} controlled cylinder-individual θ_{50} and the cylinder-averaged τ was controlled by gas-exchange system actuation. The motivation for this design was the simp-

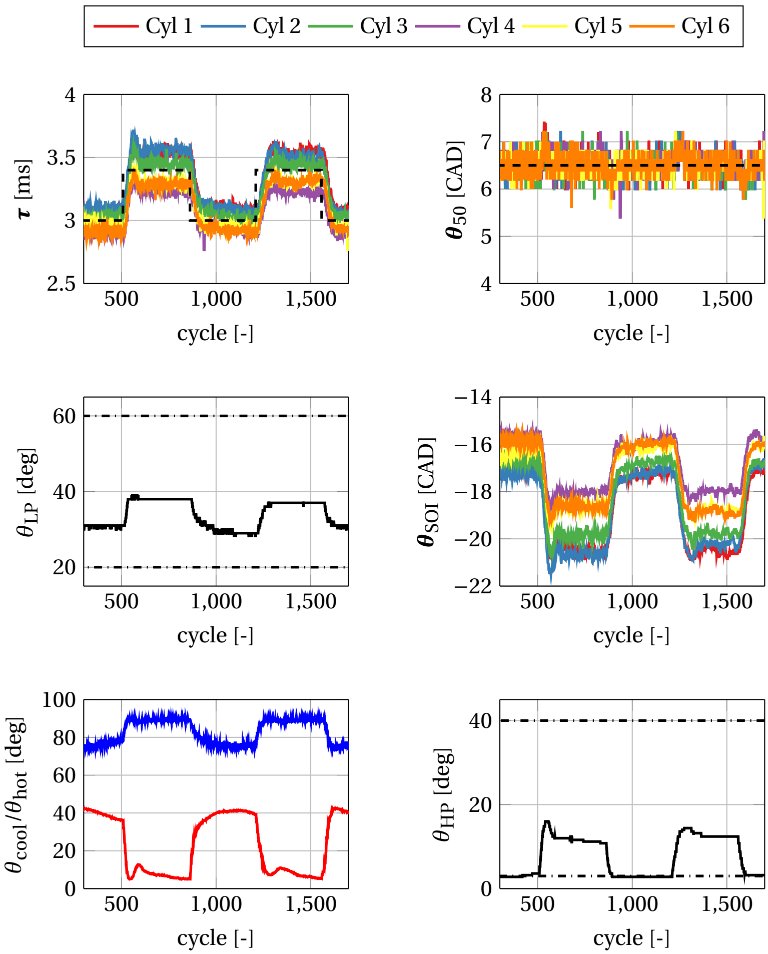

Figure 7.6 System inputs and outputs during 1400 cycles for which steps in τ^r were made. The tracking of τ^r was realized by varying θ_{hot} and $\theta_{\text{HP,LP}}$ whilst $\boldsymbol{\theta}_{\text{SOI}}$ kept $\boldsymbol{\theta}_{50}$ constant.

ler relation between intake conditions and τ, compared to the relation between θ_{SOI} and τ. Additional actuation techniques such as variable valve timings, variable compression ratio or spark ignition could be applied to control both θ_{50} and τ cylinder individually

The suggested controller was successful in tracking τ and θ_{50} set points with response times of 50 and 5 cycles, respectively. Both in stationarity and during load and speed changes. A general observation was that MPC-weight tuning was a trade-off between short response times and closed-loop robustness

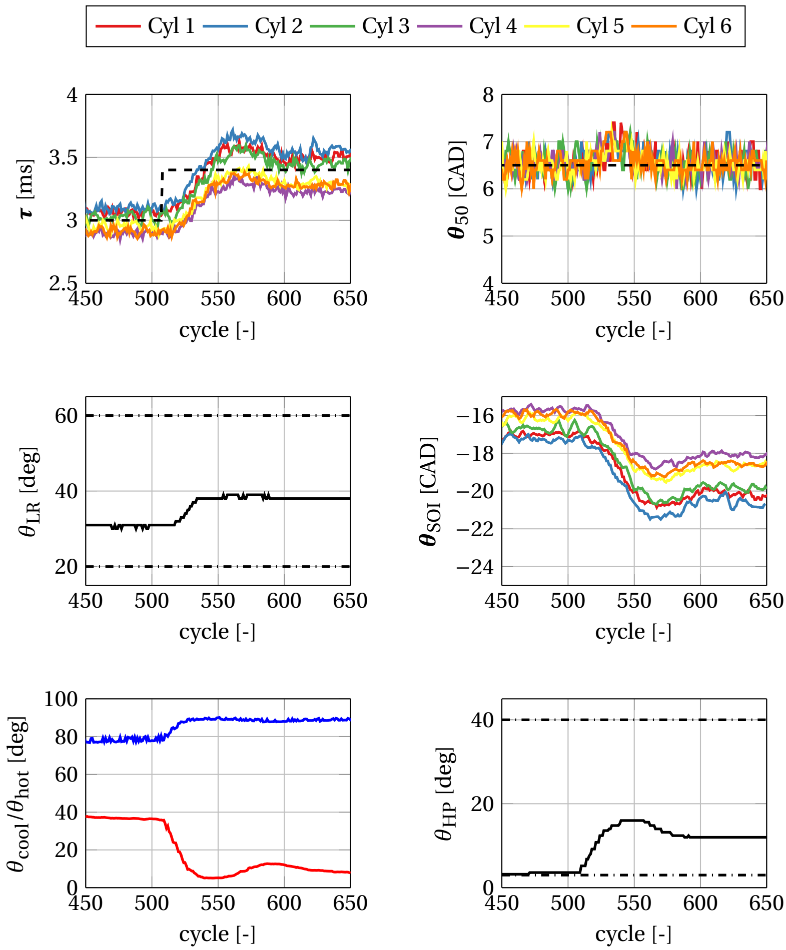

Figure 7.7 A zoom in around cycle 550 in Fig. 7.6. The ignition delay reached its new set point after 50 cycles and $\boldsymbol{\theta}_{SOI}$ kept $\boldsymbol{\theta}_{50}$ within 0.6 CAD during the step change.

to model-errors and cycle-to-cycle variation. Control action would increase if the control-action weights were to be decreased. This could however lead to system-output overshoot during set-point changes and increased actuator chattering in steady state, partly as result of insufficient model accuracy. As a result, the controller was tuned to give slow but robust performance. The gas-system model used in this work was limited to the static relation between valve positions and the intake manifold gas state in a small operating range. It is, however, possible that a dynamic model of valve actuators and the gas-system dynamics could

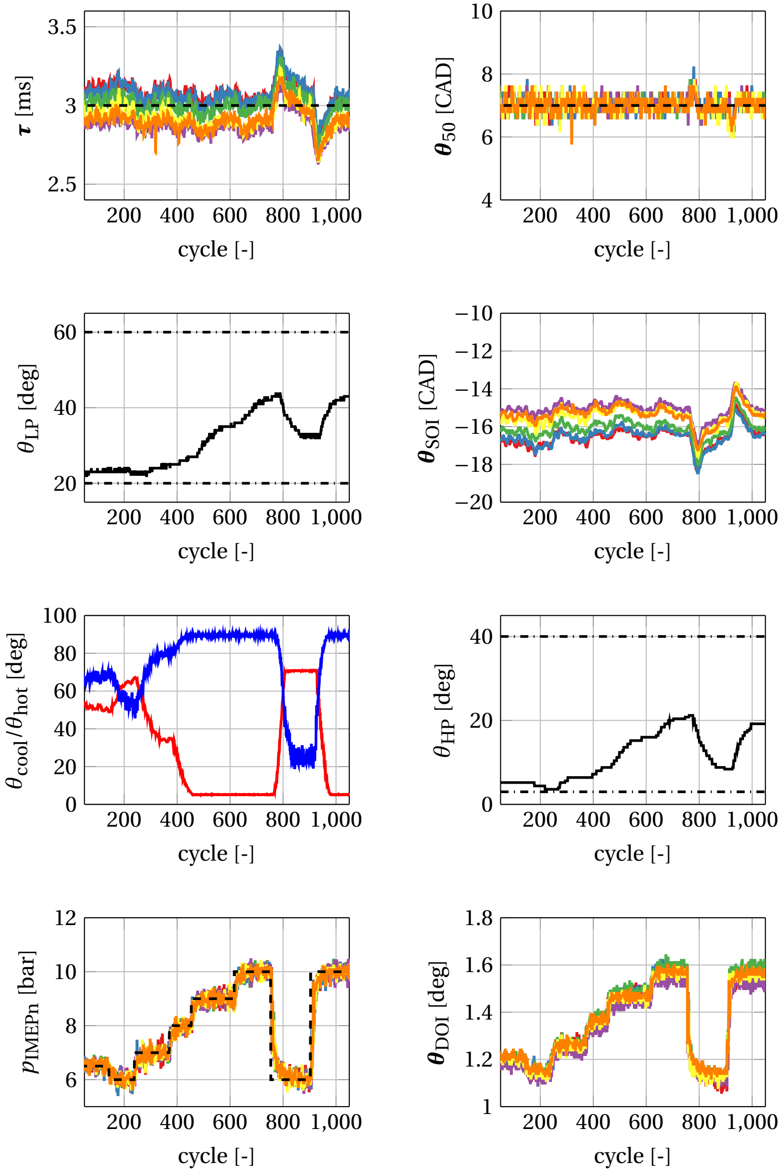

Figure 7.8 System inputs and outputs during 1000 cycles for which steps in p^r_{IMEPn} were made. In addition to the signals displayed in the previous figures, p_{IMEPn} is plotted together with its set point in the lower left figure. Injection durations θ_{DOI} are presented in the lower-right subdiagram. In-cylinder data from this experiment are presented in Fig. 7.9.

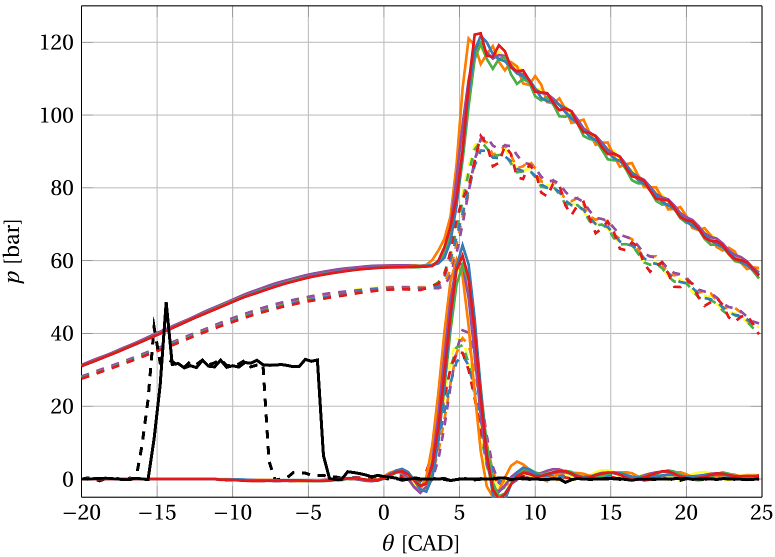

Figure 7.9 In-cylinder data from the experiment in Fig. 7.8 at p_{IMEPn} = 6 (dashed) and p_{IMEPn} = 10 bar (solid). The figure shows pressures and heat-release rates for the different cylinders and the injection current from cylinder 1. The controller maintains constant $\boldsymbol{\theta}_{50}$ and $\boldsymbol{\tau}$ despite the p_{IMEPn} difference.

improve performance. This would also allow for the gas-exchange efficiency to be included in the MPC cost function.

The MPC framework provided a simple way of prioritizing system output behavior. It also took interaction effects into account. Input constraints and the cost of using EGR were also incorporated. Comparable controller performance could probably be obtained by adopting an approach where θ_{50} is controlled with θ_{SOI} and cylinder-individual controllers, and then let the mean τ be controlled by the gas-system valve positions, see [Karlsson et al., 2008]. This approach demands less on-line computations but is less general compared to the framework presented here, where input and output constraints can be incorporated. The MPC could also be extended to cover p_{IMEPn} control by adding the injected fuel amount and its effect on τ to the model. Variation in fuel amount could in this way also be included in the prediction to reduce set-point deviation during load transients.

A sufficient τ was here considered to be an indicator for low temperature combustion with favorable emission properties. An assumption that was shown to be accurate in [Karlsson et al., 2008; Lewander et al., 2008]. In future work, this controller could be evaluated with emission measurements to conclude if this hypothesis holds or if supplementary control actions need to be taken.

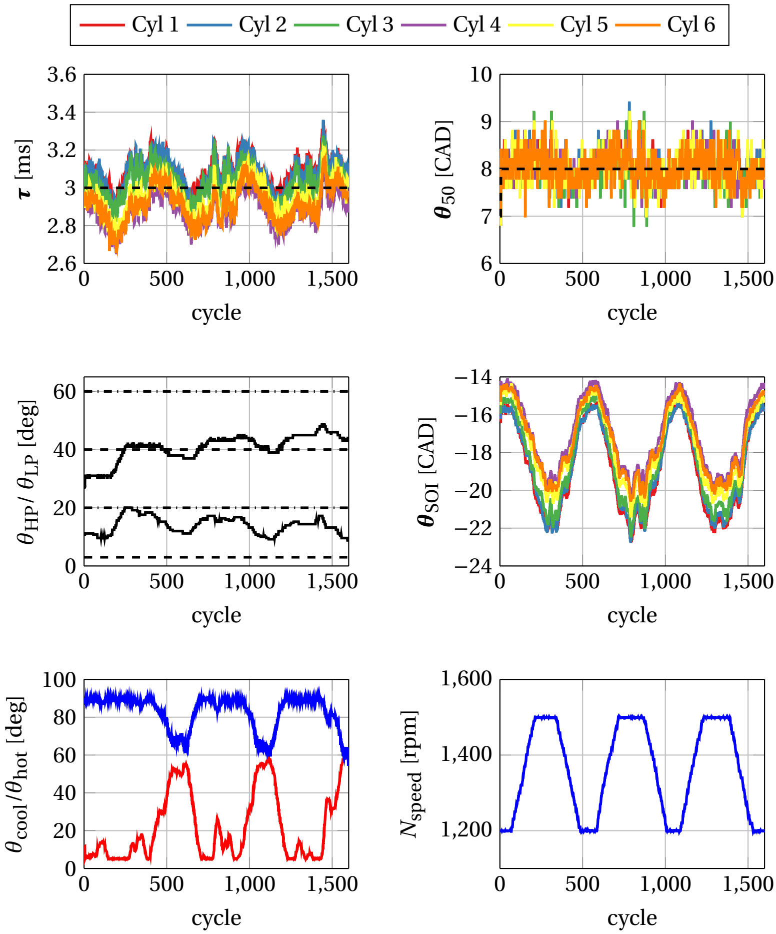

Figure 7.10 System inputs and outputs during 2000 cycles for which N_{speed} was varied, see the lower-right subdiagram. Both EGR-valve positions are now plotted together in the mid-left figure.

8

Pilot Injection

8.1 Introduction

It was discovered in [Manente et al., 2009] that long ignition delays in single-injection PPC give rise to high pressure-rises rate due to violent HCCI-like combustion. A long ignition delay creates in-cylinder mixtures where the majority of the injected fuel reaches high-temperature reactions simultaneously, which result in high heat-release and pressure-rise rates. An example of this can be seen at the higher-load operating point in Fig. 7.9. A high pressure-rise rate is an indicator for high audible noise levels and could also lead to mechanical engine damage. The pressure-rise rate therefore has to be kept below certain levels in order to ensure silent and safe engine operation. Previous research by Tsurushima et al. [2009] implies that pressure oscillations resulting from violent combustion rates are able to break insulating gas boundary layers in the cylinder. High pressure-rise rates could therefore result in increased heat-transfer flux to the cylinder walls. The issue of having high pressure-rise rates is not as severe in conventional diesel engines where the heat-release rate is limited by the rates of fuel-injection and fuel-air mixing.

A means of counteracting the pressure-rise rate problem is to introduce a pilot injection, e.g., by having a smaller fuel injection earlier during the compression stroke and then inject the majority of the fuel amount closer to TDC in a main injection. Optical OH chemiluminescence experiments and computational fluid dynamics (CFD) simulations suggest that the pilot injection provides a background mixture whose reactions increase in-cylinder temperature and assist autoignition of the the main injection [Tanov et al., 2014; Solsjö, 2014]. The reduced ignition delay of the main injection increases in-cylinder stratification during combustion with decreased combustion rates as a result.

In-cylinder data showing the effect of introducing a pilot injection is presented in Fig. 8.1. The two fuel-injection configurations produce the same load, $p_{\text{IMEP}} = 5$ bar, and the same combustion timing $\theta_{50} = 6$ CAD, but with different pressure-rise rates $dp_{\max} = 11$ bar/CAD (blue) and $dp_{\max} = 30$ bar/CAD. Pilot injections are also used in conventional diesel engines, both to improve low-load

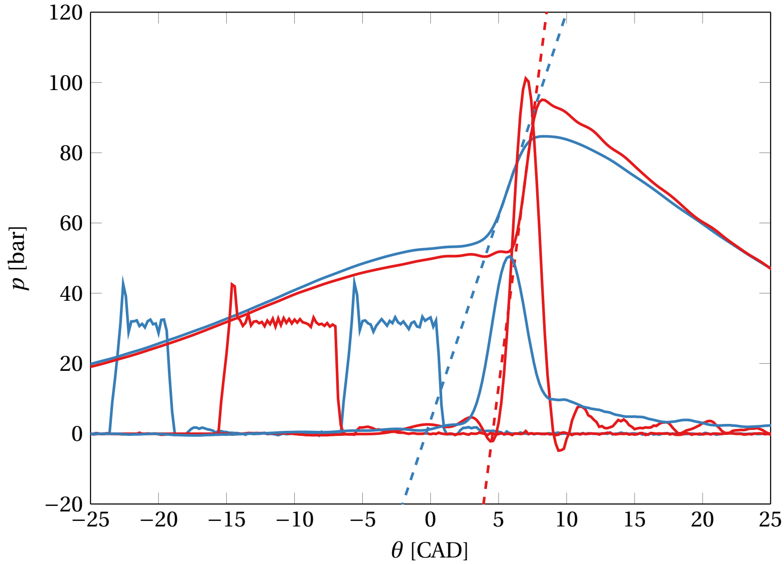

Figure 8.1 In-cylinder data showing the effect of introducing a pilot injection. The two fuel-injection configurations produce the same load, $p_{\mathrm{IMEP}} = 5$ bar, and the same combustion timing $\theta_{50} = 6$ CAD, with different maximum pressure-rise rates $dp_{\max} = 11$ bar/CAD (blue) and $dp_{\max} = 30$ bar/CAD (red). Pressure-rise rates are indicated by the dashed tangent lines.

performance [MacMillan et al., 2009; Osuka et al., 1994] and to decrease emissions and engine-noise levels [Kiencke and Nielsen, 2000].

With additional injections, the amount of calibration work for optimized engine performance at different operating points grows exponentially [Meyer, 2011]. It would therefore be advantageous to have a fuel-injection controller that automatically adjusts injection timings and the fuel distribution among the injections depending on the engine operating point. Previous work on pilot-injection combustion control in low-temperature combustion concepts has been investigated in [Ott et al., 2013; Eichmeier et al., 2012; Ekholm et al., 2008; Kokjohn et al., 2009]. Whereas previous works have focused either on calibration and control in open-loop, or on decentralized PI control of θ_{50} and $dp_{\max}$, this chapter introduces an MPC that aims to decouple control of θ_{50} and $dp_{\max}$, where control of $dp_{\max}$ is formulated as an output constraint. The suggested feedback loop is presented in Fig. 8.2, where a Kalman filter is used to attenuate stochastic output variation.

This chapter begins with a presentation of experimental engine-performance characteristics in terms of efficiency, emissions and maximum pressure-rise rate controllability, with respect to pilot-injection parameters in the low-to-mid load

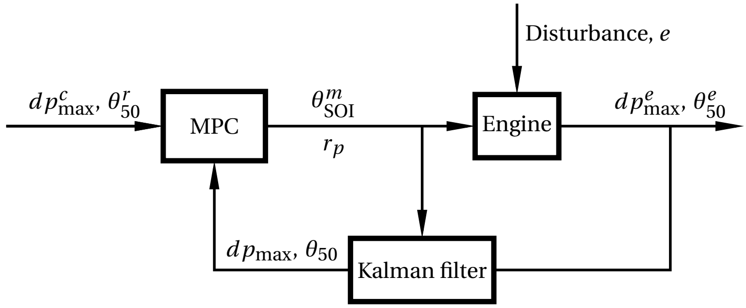

Figure 8.2 This chapter studies the following feedback loop where the ratio of pilot-fuel injected r_p and main-injection timing θ^m_{SOI} are adjusted to keep the pressure-rise rate $dp_{\max}$ below an upper limit $dp^c_{\max}$, while the combustion timing θ_{50} should follow a set point θ^r_{50}. A Kalman filter was used to attenuate stochastic output variation.

range of the engine. The experimental results are then used to design the controller in Fig. 8.2. An experimental controller evaluation during engine load and speed changes is also presented in this chapter.

Controlled Outputs

The maximum pressure rise rate $dp_{\max}$ is here defined as

$$dp_{\max} = \max_{\theta} \frac{dp}{d\theta} \tag{8.1}$$

Due to the high cycle-to-cycle variation in $dp_{\max}$, filtering is necessary for $dp_{\max}$ to be used as a feedback variable. The computed $dp^e_{\max}$ was therefore modeled as the cycle mean $dp_{\max}$, corrupted with additive Gaussian noise e with standard deviation $\sigma_{dp_{\max}}$

$$dp^e_{\max} = dp_{\max} + e_{dp_{\max}}, \quad e_{dp_{\max}} \sim N(0, \sigma^2_{dp_{\max}}) \tag{8.2}$$

Stochastic variation in θ_{50} was also modeled as additive Gaussian noise according to

$$\theta^e_{50} = \theta_{50} + e_{\theta_{50}}, \quad e_{\theta_{50}} \sim N(0, \sigma^2_{\theta_{50}}) \tag{8.3}$$

A Kalman filter was then used to recover $dp_{\max}$ and θ_{50} from $dp^e_{\max}$ and θ^e_{50}. The Kalman filter will be presented in Sec. 8.3.

Input Variables

The input variables considered are the fuel-injection timings and durations defined by the current pulses sent to the injector, see Fig. 8.3. The injector-current rising flanks indicate the start of the main and pilot injections $\theta^m_{\mathrm{SOI}}, \theta^p_{\mathrm{SOI}}$, that occur

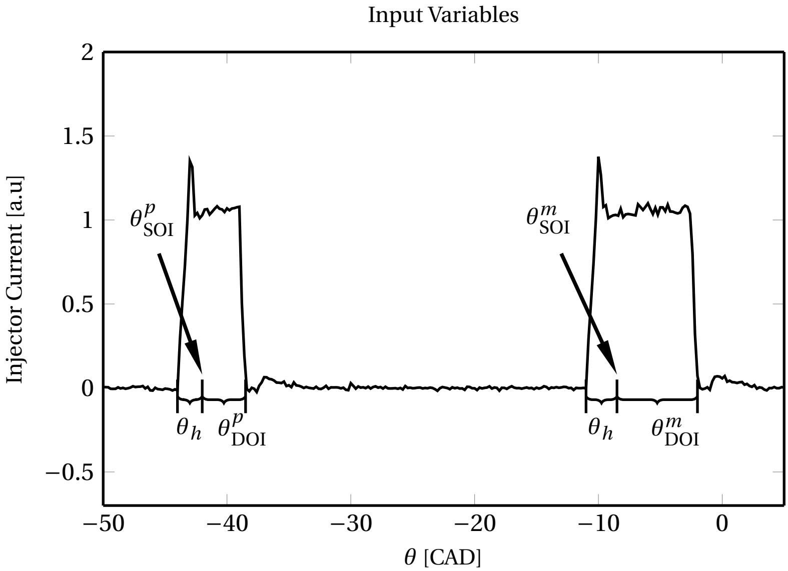

Figure 8.3 Injector-current signal with a pilot (p) and a main (m) injection together with definitions of θ^x_{SOI}, θ^x_{DOI}, and θ_h.

after an hydraulic injector delay, θ_h. The fuel-injection durations θ^m_{DOI} and θ^p_{DOI} are defined as the difference between the injector-current pulse width and θ_h. The delay therefore determines the minimum current-pulse duration for which fuel is injected into the cylinder. It was here assumed to be constant at 0.25 ms.

Instead of studying the effects of θ^m_{SOI}, θ^p_{SOI}, θ^m_{DOI} and θ^p_{DOI} explicitly, the pilot ratio r_p

$$r_p = \frac{\theta^p_{\text{DOI}}}{\theta^p_{\text{DOI}} + \theta^m_{\text{DOI}}} \tag{8.4}$$

the injection separation d_{SOI}

$$d_{\text{SOI}} = \theta^m_{\text{SOI}} - \theta^p_{\text{SOI}} \tag{8.5}$$

the main-injection timing θ^m_{SOI}, and the total injection duration

$$\theta^{\text{tot}}_{\text{DOI}} = \theta^m_{\text{DOI}} + \theta^p_{\text{DOI}} \tag{8.6}$$

were considered.

These variables were chosen because $\theta^{\text{tot}}_{\text{DOI}}$ and θ^m_{SOI} are determined by the desired load and θ_{50} at a given operating point. The objective is then to determine the pilot-injection variables r_p and d_{SOI}. The influence of r_p and d_{SOI} on engine performance is studied in the following sections.

Table 8.1 The investigated operating points. The notion $x : y : z$ indicates that the corresponding parameter was swept from x to z in steps of y. Every combination of r_p and d_{SOI} was tested.

	OP 1	OP 2
p_{IMEPg} [bar]	5	10
N_{speed} [rpm]	1200	1200
λ [-]	2.5	1.8
r_{EGR} [-]	0.15	0.25
θ_{50} [CAD]	6	10
r_p [-]	0 : 0.125 : 0.5	0 : 0.075 : 0.3
d_{SOI} [CAD]	12.5 : 12.5 : 50	12.5 : 12.5 : 50
p_{rail} [bar]	800	800

It would have been more convenient to use the injected fuel masses as input variables as opposed to injection durations. Both for increased physical understanding and the more direct connection between the injected fuel amount and the combustion processes. The reason for not doing so was due to the lack of injector characteristics to compute the injection duration for a given demanded fuel amount at the time of this study.

8.2 Experimental Characterization

Engine-output characteristics with respect to different pilot-injection configurations were investigated by varying r_p and d_{SOI} whilst θ_{50} and p_{IMEPg} were kept constant using θ_{SOI}^m and $\theta_{\mathrm{DOI}}^{\mathrm{tot}}$, at the operating points (OP) presented in Table 8.1. The reason for keeping θ_{50} and p_{IMEPg} constant was to exclude the pilot effect on these variables, and to be able to answer the question of how the controller should adjust a pilot injection for given θ_{50} and p_{IMEPg} set points.

At each operating point, dp_{max}, the gross indicated efficiency η_{GIE}, NO_x, unburned hydrocarbons (HC) and soot emission levels were measured in steady state during 1000 cycles. The partial derivatives of θ_{50} with respect to θ_{SOI}^m and θ_{SOI}^p were also investigated. The data obtained from these experiments and their implications for controller design are presented and discussed in the following sections.

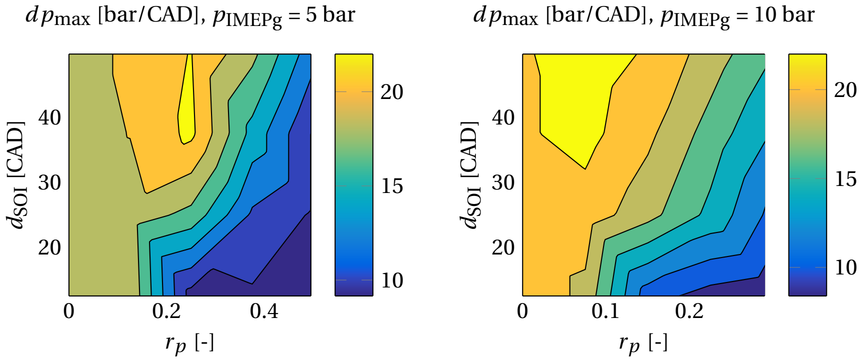

Figure 8.4 The relation between the pilot-injection variables and dp_{max} at $p_{IMEPg} = 5, 10$ bar. It is clear that r_p can be used to control dp_{max} since dp_{max} decreased with r_p. The dp_{max} controllability increased when d_{SOI} was reduced.

Maximum Pressure-Rise Rate dp_{max}

The measured influence of r_p and d_{SOI} on dp_{max} is presented in Fig. 8.4. It can be seen that dp_{max} decreased with r_p which makes r_p a candidate for controlling dp_{max}. At a certain r_p, however, additional pilot fuel does not affect the main-injection combustion rate, and the effect of r_p saturates. The dp_{max} controllability varied with d_{SOI} and was higher for small d_{SOI}.

These results agree with previous research which states that the reactions of the injected pilot fuel decrease the ignition delay of the main-injection, which in turn decreases the heat-release rate. This effect is enhanced for larger pilot-fuel amounts. This explanation is supported by the computed main-injection ignition delay

$$\tau^m = \theta_{10} - \theta^m_{SOI} \text{ [ms]} \tag{8.7}$$

which is presented in Fig. 8.5, where it can be seen that τ^m and dp_{max} correlate.

The pilot effect weakened with increased d_{SOI}. This could be explained by a more dilute pilot mixture at θ^m_{SOI}, with a lowered temperature increase as a result. An increased d_{SOI} would also result in more diverse fuel-spray targets for the two injections. Early pilot injections put more fuel in the crevice volume outside of the piston bowl where the main-injection is targeted. The resulting spatial separation of the injections could explain the observed trends. This was suggested by optical engine data obtained from a similar heavy-duty engine setup, see [Lönn et al., 2017]. Furthermore, the results in Figs. 8.4 and 8.5 indicate a significant trade-off between obtainable τ and dp_{max}, which could be problematic if a long τ is required.

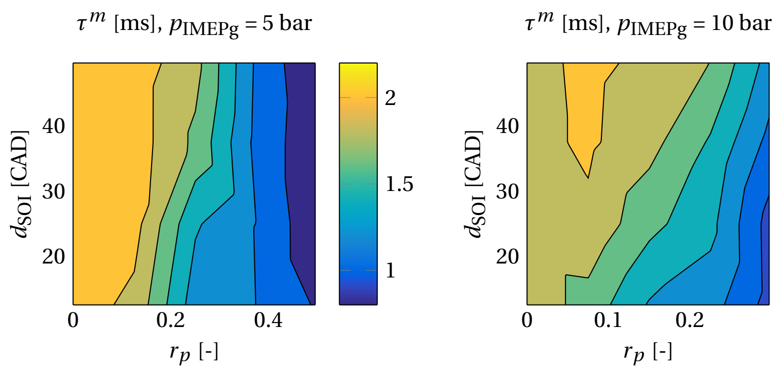

Figure 8.5 The relation between the pilot-injection variables and τ^m at $p_{\text{IMEPg}} = 5, 10$ bar. The main-injection ignition delay correlated with $dp_{\max}$ in Fig. 8.4.

Indicated Efficiency

The pilot-injection impact on efficiency was evaluated by computing the gross indicated efficiency

$$\eta_{\text{GIE}} = \frac{p_{\text{IMEPg}} V_d}{m_f Q_{\text{LHV}}} \tag{8.8}$$

where m_f is the injected fuel amount, computed from the average fuel-flow during the experiment. The results presented in Fig. 8.6 show that η_{GIE} had a shallow maximum when d_{SOI} was short. This trend was more significant for OP 1, where η_{GIE} was more sensitive to the pilot configuration. Another visible trend is that η_{GIE} decreased when d_{SOI} increased, and that this effect was stronger when r_p was higher. These results show that it could be efficient to have a pilot injection but that this effect is reversed for very early θ^p_{SOI}.

HC

The measured unburned hydrocarbon (HC) emission levels are presented in Fig. 8.7. HC emissions increased steeply as d_{SOI} and r_p were simultaneously increased. The explanation for this could be that the pilot fuel was injected into the crevice regions outside of the piston bowl and did not burn completely due to wall-cooling effects and too lean conditions. This effect is clearer at $p_{\text{IMEP}} = 5$ bar where in-cylinder temperatures were lower. The decrease in combustion efficiency indicated by the HC-emission increase could explain the η_{GIE} decrease observed in Fig. 8.6.

NO$_x$

The measured NO$_x$ emission levels are presented in Fig. 8.8, where it can be seen that NO$_x$ emissions mainly depended on r_p and decreased with an in-

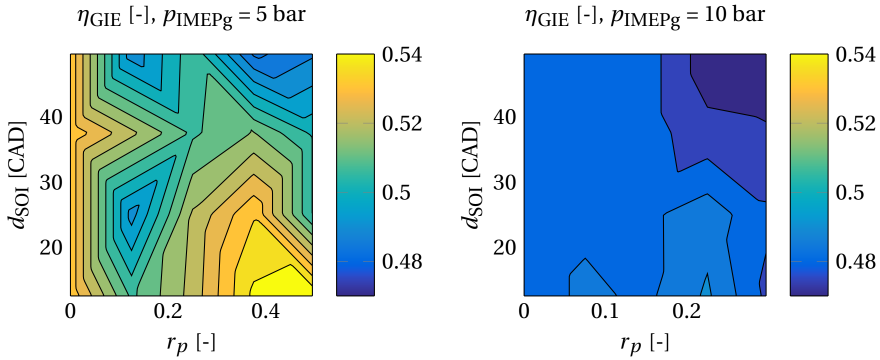

Figure 8.6 The relation between the pilot-injection variables and η_{GIE} at $p_{IMEPg} = 5, 10$ bar. The results show that η_{GIE} had a shallow maximum when the pilot was close to the main injection. Another visible trend is that η_{GIE} decreased when d_{SOI} increased, and that this effect was stronger for larger r_p.

creased r_p. A hypothetical explanation for the decrease in NO_x is the decrease in τ^m with r_p. The decrease in τ^m resulted in a decrease in heat-release rate and in-cylinder pressure, which indicates lowered peak temperatures and decreased NO_x-formation rates. Lower peak temperatures also results in reduced heat-transfer losses, which could explain the η_{GIE} increase with r_p in Fig. 8.6.

Soot

Figure 8.9 shows that measured soot levels increased with r_p and more so when d_{SOI} was small. An explanation for this is that the ignition delays for the fuel injections were minimized at these operating points. A decreased air/fuel mixing time results in richer combustion and increased soot formation. The increase in soot emissions was not as large for longer d_{SOI}, which means that dp_{max} could be reduced with a lower soot-emission penalty. Similar NO_x and soot-emission trends were presented in [Manente et al., 2009, 2010b].

Combustion-Timing Controllability

The θ_{50} controllability was investigated by varying θ^m_{SOI} and θ^p_{SOI} in open loop at the operating points in Table 8.1. For each operating point, θ^m_{SOI} and θ^p_{SOI} were varied individually in square-wave sequences with an amplitudes of 1 CAD and a period of 25 cycles during 500 cycles. The partial derivatives $\partial\theta_{50}/\partial\theta^{m,p}_{SOI}$ were then computed.

Computed partial derivatives in Figs. 8.10 and 8.11 indicate that θ_{50} is controlled by θ^m_{SOI}, and that the controllability decreased slightly with r_p. The θ^p_{SOI} effect was an order of magnitude smaller, where θ^p_{SOI} affected θ_{50} more when r_p

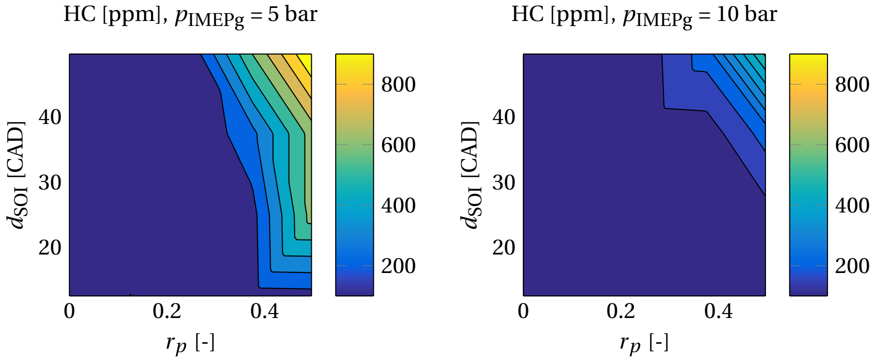

Figure 8.7 The relation between the pilot-injection variables and HC at $p_{\text{IMEPg}} = 5, 10$ bar. The HC emission levels increased steeply as d_{SOI} and r_p were simultaneously increased. The explanation for this could be that the pilot fuel was injected into the crevice regions outside of the piston bowl, resulting in incomplete combustion. The decrease in combustion efficiency indicated by the HC emission-level increase explains the η_{GIE} decrease observed in Fig. 8.6.

was increased. A hypothetical explanation is that the main injection initiated the high-temperature reactions with corresponding heat-release rate. Similar trends were shown in [Hasegawa and Yanagihara, 2003; Manente et al., 2009].

Another observation is that the pilot injection linearizes the relation between θ^m_{SOI} and θ_{50}, due to its reduction of τ. This argument is supported by the findings in Chapter 6, where τ contributed to a nonlinear relation between θ^m_{SOI} and θ_{50}. A pilot injection therefore increases the controllable region in Fig. 6.2, which facilitates θ_{50} control.

Summary

The experimental findings show that r_p can be used to control $dp_{\max}$. The choice of r_p gives a trade off between obtainable τ and $dp_{\max}$ and a trade off between soot and NO_x emissions. A controller-design approach would be to let a fast cycle-to-cycle controller decide r_p to obtain acceptable $dp_{\max}$, and then let the gas-exchange system set suitable boundary conditions in terms of EGR ratio and intake temperature that simultaneously allow for low $dp_{\max}$ and high τ.

The efficiency η_{GIE} was shown to vary slightly with r_p where η_{GIE} decreased or increased depending on d_{SOI}. This is believed to be linked to the observed trends in NO_x and HC-emission levels as discussed previously. This hypothesis should be confirmed with optical experiments.

The injection separation d_{SOI} was shown to be a trade-off between high $dp_{\max}$ controllability and η_{GIE} with shorter d_{SOI}, and simultaneously low NO_x

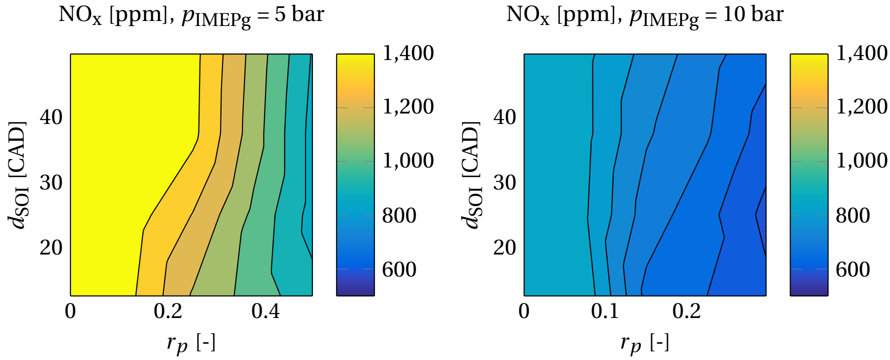

Figure 8.8 The relation between the pilot-injection variables and NO_x at $p_{\mathrm{IMEPg}} = 5, 10$ bar. It can be seen that NO_x mainly depended on r_p and decreased with an increased r_p. A hypothetical explanation for this is the decrease in τ^m with r_p. The resulting decrease in heat-release rate and in-cylinder pressure with τ^m indicate lowered peak temperatures and decreased NO_x-formation rates.

and soot emissions with increased d_{SOI}. The experiments also showed that θ^m_{SOI} should be used to control θ_{50}.

8.3 Controller Design

The controller-design objective was to keep θ_{50} at a predefined value, and maintain $dp_{\max}$ below an upper bound. The experimental results above showed that $dp_{\max}$ can be controlled with r_p while θ_{50} is mainly affected by θ^m_{SOI}. The injection separation was chosen to be constant and low, $d_{\mathrm{SOI}} = 20$ CAD, to maintain high η_{GIE} and high $dp_{\max}$ controllability. In order to keep the ignition delay τ^m as long as possible under these circumstances, it was decided to keep r_p low. The engine load was controlled with $\theta^{\mathrm{tot}}_{\mathrm{DOI}}$ in a separate closed loop using feedforward and PI control with constant p_{rail}.

The model-complexity needed to physically model the relation between pilot injection and pressure-rise rate is fairly involved. An empirical modeling approach was therefore adopted, where experimental data provided an approximate linear cycle-to-cycle model. The state $\boldsymbol{x}$ and input $\boldsymbol{u}$ are introduced accordingly

$$\begin{aligned} \boldsymbol{x}(k) &= \begin{pmatrix} \theta_{50}(k) & dp_{\max}(k) & r_p(k) \end{pmatrix}^T \\ \boldsymbol{u}(k) &= \begin{pmatrix} \Delta\theta^m_{\mathrm{SOI}}(k) & \Delta r_p(k) \end{pmatrix}^T \end{aligned} \tag{8.9}$$

where k denotes the cycle index, and Δ is the forward-difference operator. The pilot ratio was introduced as a state to keep track of its absolute value.

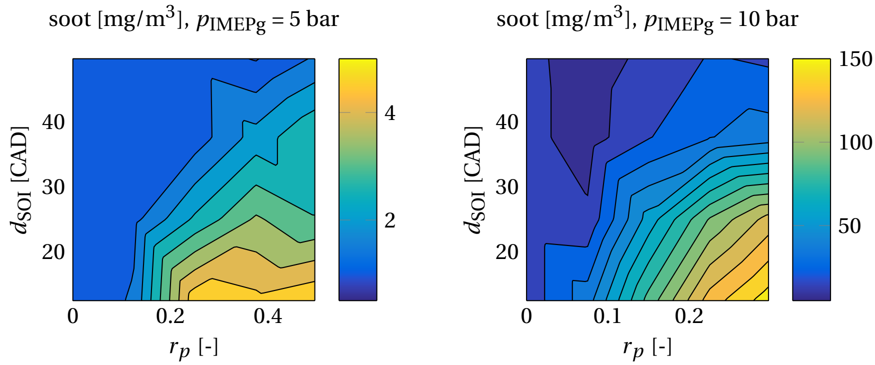

Figure 8.9 The relation between the pilot-injection variables and soot at $p_{\mathrm{IMEPg}} = 5, 10$ bar. Note the difference in z-axis scale. Soot levels increased with r_p and more so when d_{SOI} was small. An explanation for this is that the ignition delays for the fuel injections were minimized at these operating points which decreased air/fuel mixing time and resulted in richer combustion with increased soot formation.

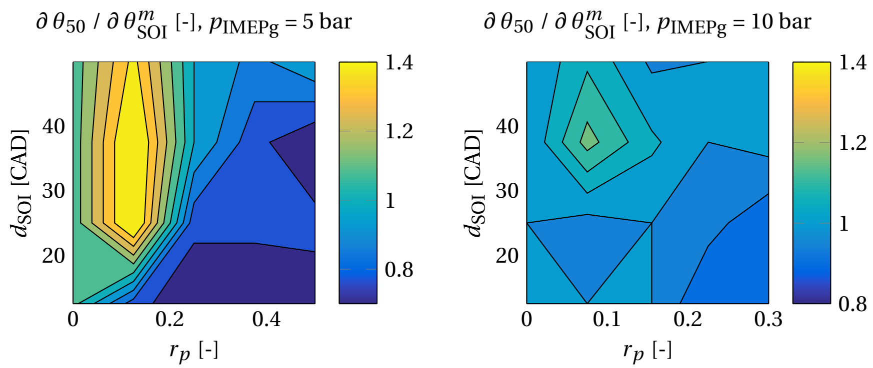

Figure 8.10 The computed gain from θ^m_{SOI} to θ_{50} at $p_{\mathrm{IMEPg}} = 5, 10$ bar. The gain from θ^m_{SOI} was high for all injection configuration and decreased as r_p was increased.

The cycle-to-cycle model

$$\begin{aligned} \boldsymbol{x}(k+1) &= A\boldsymbol{x}(k) + B\boldsymbol{u}(k) + \boldsymbol{v}(k) \\ \boldsymbol{y}(k) &= C\boldsymbol{x}(k) + \boldsymbol{e}(k) \end{aligned} \tag{8.10}$$

was then formulated, where the assumption of a static relation between $\boldsymbol{u}$ and $\boldsymbol{x}$

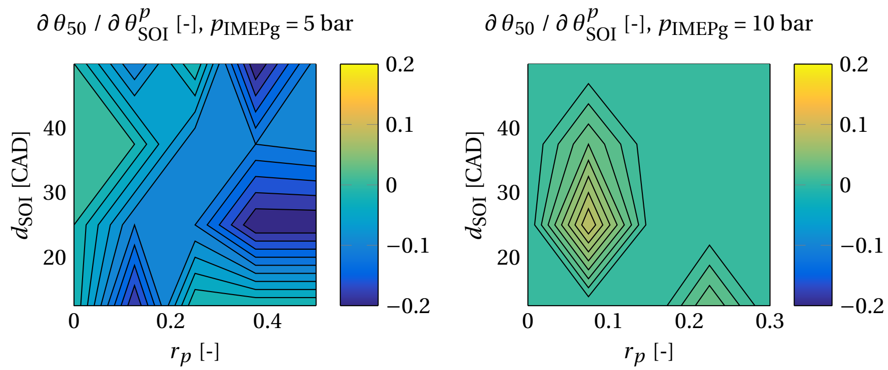

Figure 8.11 The computed gain from θ^{p}_{SOI} to θ_{50} at $p_{\text{IMEPg}} = 5, 10$ bar. The gain was low for all injection configurations. When comparing these trends with Fig. 8.10, it is clear that θ^{m}_{SOI} should be used to control θ_{50}.

gives $A = I_{3x3}$, and B contains the partial derivatives of $\boldsymbol{x}$ with respect to $\boldsymbol{u}$

$$B = \begin{pmatrix} \dfrac{\partial\theta_{50}}{\partial\theta_{\text{SOI}}} & \dfrac{\partial\theta_{50}}{\partial r_p} \\ \dfrac{\partial dp_{\max}}{\partial\theta_{\text{SOI}}} & \dfrac{\partial dp_{\max}}{\partial r_p} \\ 0 & 1 \end{pmatrix} = \begin{pmatrix} 1 & -3 \\ -0.5 & -25 \\ 0 & 1 \end{pmatrix} \tag{8.11}$$

From the experimental results in figures 8.10 and 8.11, it was found that $\partial\theta_{50}/\partial\theta_{\text{SOI}} = 1$. The partial derivative $\partial\theta_{50}/\partial r_p = -3$ was extracted from Fig. 8.5. A decrease in θ_{SOI} resulted in an increased τ^m which in turn increased $dp_{\max}$, which explains $\partial dp_{\max}/\partial\theta_{\text{SOI}} = -0.5$. The $dp_{\max}$ data in Fig. 8.4 gave $\partial dp_{\max}/\partial r_p = -25$. The matrix C in (8.10) is given by I_{3x3}, since the first two states can be computed directly using in-cylinder pressure measurements and heat-release analysis. In order to incorporate model uncertainty and stochastic cycle-to-cycle variation, zero-mean Gaussian processes $\boldsymbol{v}(k)$ and $\boldsymbol{e}(k)$ were introduced with covariance matrices Q_v and Q_e

$$\begin{aligned} Q_v &= E\big(\boldsymbol{v}(k)\boldsymbol{v}(k)^T\big) \\ Q_e &= E\big(\boldsymbol{e}(k)\boldsymbol{e}(k)^T\big) \end{aligned} \tag{8.12}$$

Table 8.2 The chosen MPC weights.

ω_1	ω_2	ω_3	ω_4	ω_5	ρ
100	0.01	25	6000	8000	1

Model Predictive Control

A linear-system model allows for linear MPC, which is suitable design choice for output-constraint handling. The MPC problem was formulated according to

$$\begin{aligned}
\underset{\theta_{\mathrm{SOI}}^m,\ r_p}{\text{minimize}} \quad & \sum_{k=1}^{H_p} \omega_1 ||\theta_{50}^r(k) - \theta_{50}(k)||_2^2 + \omega_2 ||\theta_{\mathrm{SOI}}^m(k)||_2^2 + \omega_3 ||r_p(k)||_2^2 \\
& \quad + \sum_{k=0}^{H_c-1} \omega_4 ||\Delta\theta_{\mathrm{SOI}}(k)||_2^2 + \omega_5 ||\Delta r_p(k)||_2^2 + \rho\epsilon^2 \qquad (8.13)\\
\text{subject to} \quad & \boldsymbol{x}(k+1) = A\boldsymbol{x}(k) + B\boldsymbol{u}(k) \quad \text{for } k = 0, \ldots, H_c - 1 \\
& \boldsymbol{x}(k+1) = A\boldsymbol{x}(k) \quad \text{for } k = H_c, \ldots, H_p - 1 \\
& \boldsymbol{x}(0) = \boldsymbol{x}_0 \\
& 0 \le r_p(k) \le r_p^c \\
& dp_{\max}(k) \le dp_{\max}^c + \epsilon \\
& \epsilon \ge 0
\end{aligned}$$

where r_p^c and $dp_{\max}^c$ are upper bounds for r_p and $dp_{\max}$. These were set to 0.3 and 8 bar/CAD, respectively. The variable ϵ is a cost variable that penalizes violation of the $dp_{\max}$ inequality constraint, and was introduced to ensure existence of feasible solutions. The positive weights ω_i and ρ determine the controller priority and were tuned to obtain adequate closed-loop response times subject to overshoot and enhanced cycle-to-cycle variation. The weights used are presented in Table 8.2. The horizons were chosen according to $H_p = 16$ and $H_c = 8$. Average computation times for solving (8.13) were 3 ms for one cylinder.

Kalman Filter

State estimation was used to handle cycle-to-cycle variation in $dp_{\max}$ and θ_{50}. In order to estimate x from y, u and (8.10), a stationary Kalman filter was used. The Kalman-filter state estimate $\hat{x}$ was updated recursively according to

$$\hat{\boldsymbol{x}}(k+1) = A\hat{\boldsymbol{x}}(k) + B\boldsymbol{u}(k) + K(\boldsymbol{y}(k) - C\hat{\boldsymbol{y}}(k)) \qquad (8.14)$$

where the Kalman-filter gain K was given by the steady-state solution to Algorithm 1 in Chapter 3

$$\begin{aligned}
K &= APC^T(Q_e + CPC^T)^{-1} \\
P &= APA^T + Q_v - APC^T(Q_e + CPC^T)^{-1}CPA^T
\end{aligned} \qquad (8.15)$$

The covariance matrices used

$$Q_e = \begin{pmatrix} 25 & 0 \\ 0 & 800 \end{pmatrix}, \; Q_v = \begin{pmatrix} 10 & 0 \\ 0 & 50 \end{pmatrix} \tag{8.16}$$

were chosen to get sufficient measurement-noise attenuation. The choice $Q_v^{2,2} > Q_v^{1,1}$ reflects an increased model uncertainty in $dp_{\max}$. The Kalman filter only considered the first two state equations in (8.10).

8.4 Controller Evaluation

Controller performance was evaluated experimentally during set-point changes in θ_{50} and p_{IMEPg}, as well as during changes in $dp_{\max}^c$ and N_{speed}. Indicated mean-effective pressure and p_{rail} were controlled using PI controllers and feedforward, whilst N_{speed} was changed by adjusting the engine-brake speed set point.

Input and output data for one cylinder are presented during a sequence of θ_{50}^r step changes in Fig. 8.12, where the θ_{50} response time was in the range of 3 cycles. In the upper diagrams, $\hat{\boldsymbol{x}}$ is indicated in black together with $\boldsymbol{y}$, which is indicated in gray. The ignition delay and $dp_{\max}$ increased as θ_{50} was advanced. This forced r_p to increase for $dp_{\max}^c$ = 8 bar/CAD to be fulfilled. This controller behavior allows for a more advanced θ_{50}^r for a given $dp_{\max}^c$. The pilot ratio was then decreased when θ_{50}^r was delayed due to its absolute-value cost.

In Fig. 8.13, input and output data are presented during step changes in $dp_{\max}^c$. The response time of $dp_{\max}$ during a negative $dp_{\max}^c$ step change was approximately 2 cycles, while the response time of $dp_{\max}$ during a positive $dp_{\max}^c$ step change was approximately 10 cycles. This was due to the high penalty of violating $dp_{\max}^c$. The main-injection timing θ_{SOI}^m adjusted for variation in θ_{50} caused by changes in τ^m.

The closed-loop response during p_{IMEPg}^r changes are presented in Fig. 8.14, where the p_{IMEPg} response time was approximately 20 cycles. As $\theta_{\mathrm{DOI}}^{\mathrm{tot}}$ varied, θ_{SOI}^m was adjusted to keep θ_{50} constant. The pilot ratio made minor adjustments to keep $dp_{\max}$ below $dp_{\max}^c$. The small variation in r_p indicates that $dp_{\max}$ was not very sensitive to changes in $\theta_{\mathrm{DOI}}^{\mathrm{tot}}$ at this operating point. Input-signal oscillation can be observed at cycles 200 and 500 in Fig. 8.14, indicating that the control-action weights could be increased for more robust performance.

System response to N_{speed} changes are presented in Fig. 8.15. Here, the controller had to increase r_p and advance θ_{SOI}^m in order to fulfill $dp_{\max}^c$ and θ_{50}^r when N_{speed} was increased. It can also be seen that the $dp_{\max}$ noise level decreased with N_{speed}, which indicates a reduced cycle-to-cycle variation with N_{speed}.

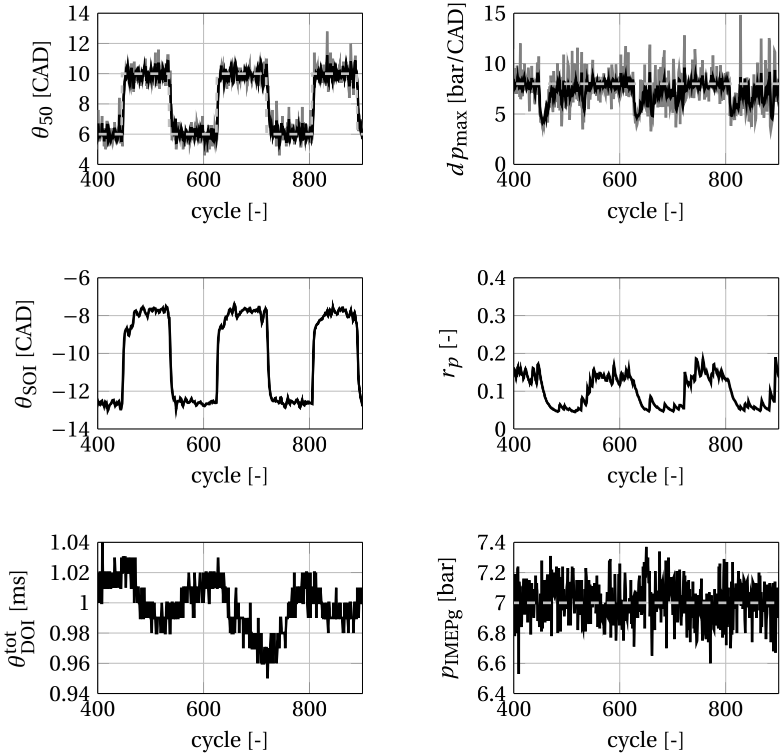

Figure 8.12 Input and output data during a sequence of θ_{50}^r step changes. In the upper diagrams, $\hat{\boldsymbol{x}}$ is presented in black together with $\boldsymbol{y}$ which is presented in gray. The pilot ratio was forced to increase as θ_{50} was advanced to fulfill $dp_{\max}^c = 8$ bar/CAD. As θ_{50} was delayed, r_p was decreased due to its absolute-value cost.

8.5 Discussion and Conclusions

The results indicate that the designed controller was successful in maintaining an upper bound for $dp_{\max}$ whilst θ_{50} was kept at a predefined value. Both in steady state and during load and speed transients. The response time to changes in θ_{50}^r was 3 cycles, and 2 cycles for a negative change in $dp_{\max}^c$. There were cases of significant cycle-to-cycle variation in $\boldsymbol{u}$ for some of the experiments, see Figs. 8.14 and 8.15. This variation could be decreased by increasing the control-action weights in (8.13).

The pressure-rise rate $dp_{\max}$ was in this chapter treated as a stochastic signal whose mean value was to be controlled below an upper limit. The validity of this treatment could of course be questioned since $dp_{\max}$ levels above $dp_{\max}^c$ will occur even if the mean $dp_{\max}$ level is kept below $dp_{\max}^c$. A more sophisticated de-

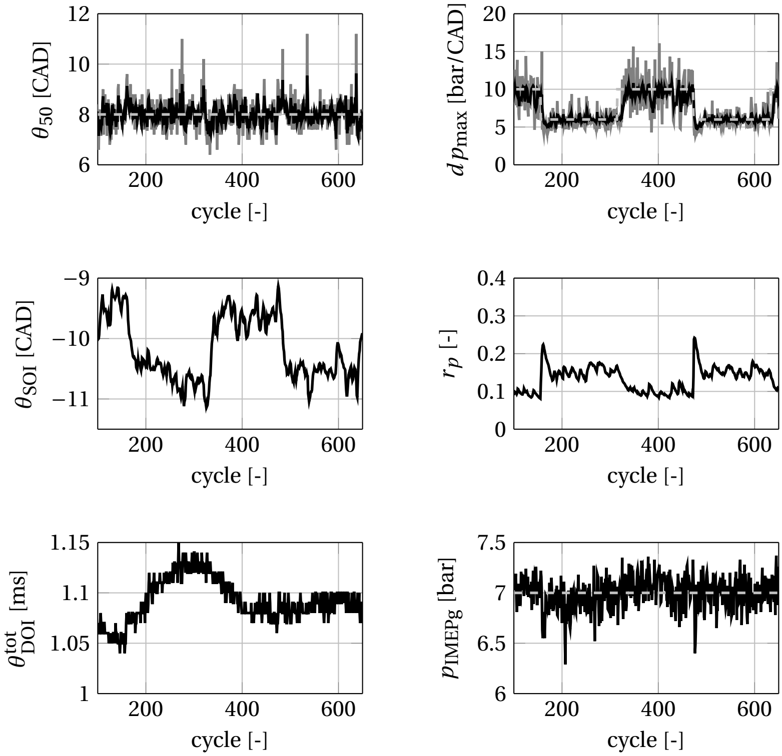

Figure 8.13 Input and output data during step changes in $dp^c_{\max}$. The response time of $dp_{\max}$ during a negative $dp^c_{\max}$ step change was 2 cycles, while the response time of $dp_{\max}$ during a positive $dp^c_{\max}$ step change was 10 cycles. The main-injection timing $\theta^m_{\rm SOI}$ adjusted for variations in θ_{50} caused by changes in r_p.

sign approach would be to incorporate the statistical distribution of $dp_{\max}$ in the controller design, and in this way control the frequency or probability of $dp^c_{\max}$ violation as presented in [Jones and Frey, 2015].

It is possible that comparable performance could be obtained with a simpler controller structure. For instance by handling the $dp_{\max}$ limit as a set-point problem as presented in [Ott et al., 2013]. This would however demand additional heuristic logic, and the framework would not be as general and easily expandable if more states and inputs were to be added to the control problem.

Suggested future work consists of investigating higher engine loads and the controller compatibility with a gas-system controller that adjusts the engine intake conditions to maximize τ for a given $dp^c_{\max}$. It would also be interesting to generalize the control problem to incorporate more than two injections.

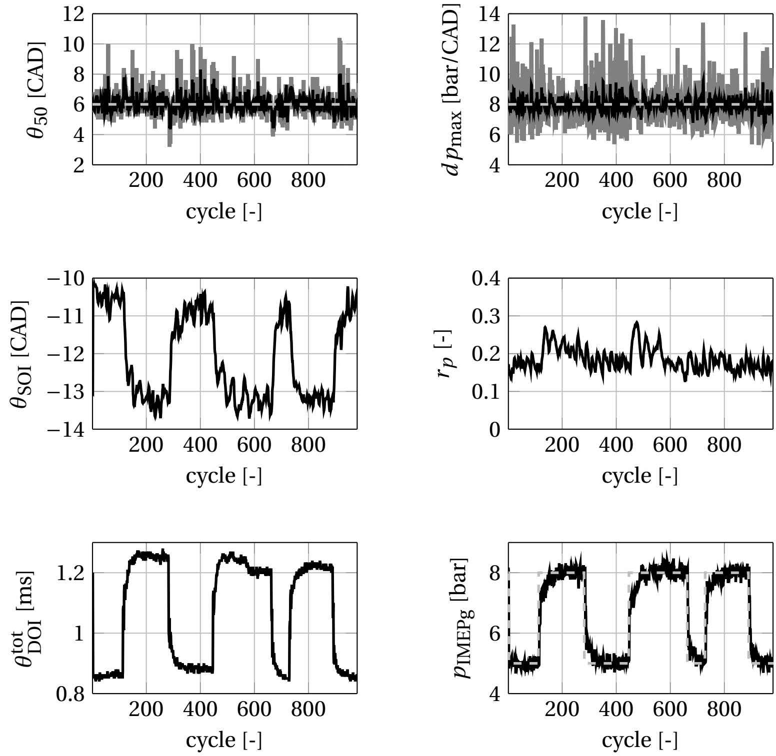

Figure 8.14 Input and output data during p_{IMEPg} set-point changes. The response time for p_{IMEPg} was approximately 20 cycles. The pilot ratio was only doing minor adjustments in order to keep $dp_{\max}$ below the upper limit. This indicates that $dp_{\max}$ was not very sensitive to changes in $\theta_{\mathrm{DOI}}^{\mathrm{tot}}$ at this operating point.

Triple-injection strategies has previously been suggested for PPC operation [Manente et al., 2010a].

The injection separation d_{SOI} was shown to impact both emissions and efficiency, but was in this work held constant for simplicity. A suggested extension of the controller presented here is therefore to incorporate d_{SOI} as an input variable in the controller design. This was for instance done in [Yang et al., 2017] to control soot-emission levels.

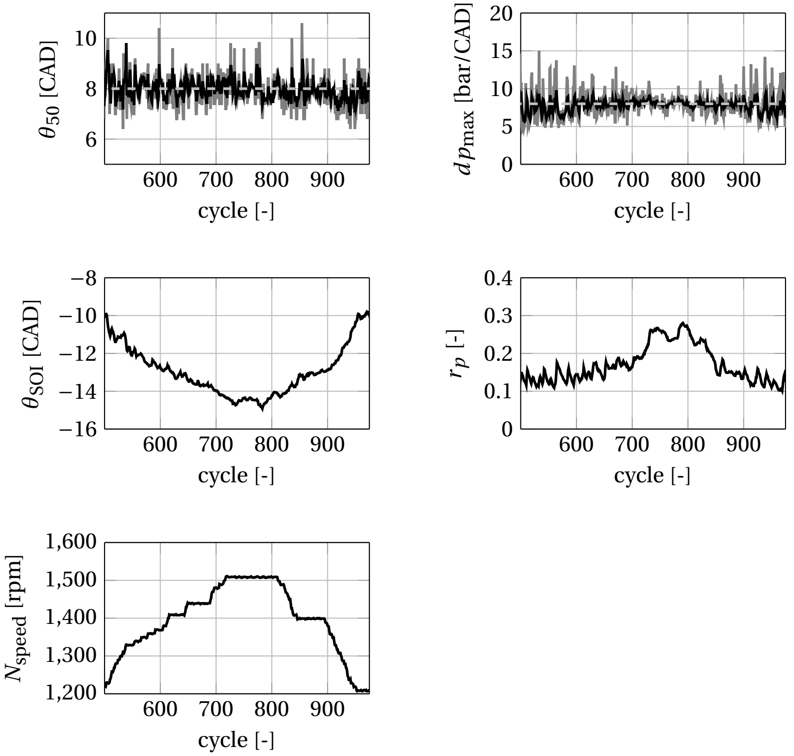

Figure 8.15 Input and output data during N_{speed} set-point changes. The controller increased r_p and decreased θ_{SOI}^m in order to fulfill $dp_{\max}^c$ and track θ_{50}^r when N_{speed} was increased. It can also be seen that the $dp_{\max}$-noise level decreased with N_{speed}.

9

Low-Load Control

9.1 Introduction

To obtain reliable low-load operation is one of the major challenges with gasoline PPC, both due to high cycle-to-cycle variation and low combustion efficiency. Advantages with a high octane number (ON) have mainly been observed at mid-to-high engine load. With a high ON, the in-cylinder conditions at low-load operation result in too long ignition delays for combustion to complete during the closed part of the engine cycle [Fieweger et al., 1997]. The issue of having too long ignition delays was discussed in Chapter 6, where elevated intake temperatures were needed to achieve θ_{50} close to TDC, see Fig. 6.2.

Incomplete combustion and misfire result in reduced engine efficiency and increased HC and CO emission levels. Homogeneous-reactor simulations have shown that high levels of HC and CO are a result of lean mixtures at too low temperature [Kim et al., 2008]. Fuel reactivity is also an important factor. Manente et al. [2010a] showed that as the fuel ON increased from 70 to 100, the PPC low-load limit, defined as the p_{IMEP} at the fuel-ignitability limit, increased from 3 to 15 bar at atmospheric intake conditions.

Results in [Kalghatgi et al., 2006] and [Weall and Collings, 2009] showed that a remedy to the PPC low-load issue is to increase in-cylinder temperature and equivalence-ratio stratification levels, since combustion initiated in rich regions with high temperature aids combustion of the overall cylinder charge. Previous studies presented in [Borgqvist et al., 2012; 2013] aimed to improve the gasoline PPC low-load efficiency using variable-valve actuation. These results showed that negative valve overlap and re-breathing in combination with a split-main injection strategy were able to increase the low-load performance by increasing the temperature of trapped residual gases. In [Solaka et al., 2012], the low-load limit of a single-cylinder light-duty engine was extended down to $p_{\mathrm{IMEPg}} = 2$ bar, using boosted intake air. The absolute intake pressure needed at this load was approximately 2 bar for the fuels with the highest ON (88.6 and 87.1). Other actuator options for improved low-load operation include variable compression ratio [Haraldsson et al., 2002] and fast thermal management [Martinez-Frias et al., 2000].

This chapter investigates how fuel injection and intake conditions should be chosen for improved PPC efficiency, with the objective of extending the operation range towards lower loads. Section 9.2 presents experimental data for $p_{\mathrm{IMEPn}} \in [1, 5]$ bar. This data were then used to suggest a simple controller that acts to minimize the ignition delay τ during low-load operation, see Sec. 9.3.

Section 9.4 shows how the controller-design choices affect fuel consumption during transient operation.

9.2 Low-Load Experiments

This section presents experimental data for $p_{\mathrm{IMEPn}} \in [1, 5]$ bar. The data describe combustion sensitivity to injection timing, pilot injection and intake conditions.

Injection Timing

The combustion timing θ_{50} has to be phased shortly after TDC for work ouput to be maximized and temperatures to be sufficient for the chemical reactions to complete. Experimental θ_{50} data are presented in Fig. 9.1 as a function of θ_{SOI} for three different fuel-injection durations θ_{DOI} and $p_{\mathrm{rail}} = 800$ bar.

The gain from θ_{SOI} to θ_{50} was positive for $\theta_{\mathrm{SOI}} > -20$ CAD. As θ_{SOI} decreased from this point, the increase in τ with θ_{SOI} became more significant, and the gain from θ_{SOI} to θ_{50} decreased. The gain even became slightly negative for very early θ_{SOI}, as the increase in τ exceeded the decrease in θ_{SOI}. Similar θ_{50} / θ_{SOI} characteristics were observed in Chapter 6, Fig. 6.2, with the difference that the τ model in Chapter 6 was unable to capture the negative-gain region for early θ_{SOI}. A physical explanation for a negative gain was given in [Kalghatgi et al., 2006], where similar experimental results were presented: An increase in τ gives more time for fuel-air mixing, which in turn gives leaner mixtures and even longer τ. The model in Chapter 6 did not include the time-resolved equivalence ratio history of the fuel/air mixture when computing the accumulated reactivity, and was therefore not able to capture the negative-gain effect.

The data in Fig. 9.1 provide a lower bound for which θ_{SOI} can be used to effectively control θ_{50} with a linear controller. With integral action and a too low infeasible set point, the controller would keep advancing θ_{SOI} and instead increase set-point deviation. It was therefore decided to saturate θ_{SOI} at -20 CAD to maintain a positive gain. In this way, the controller could obtain the wanted set-point or the earliest obtainable θ_{50}, without risking unnecessarily long τ.

Pilot Injection

It was previously shown in Chapter 8 that a pilot injection reduces τ of the main injection. A decrease in main-injection τ makes it possible to obtain a more advanced θ_{50}. This pilot-injection effect has previously been observed for conventional diesel combustion [Osuka et al., 1994; Macmillan et al., 2009].

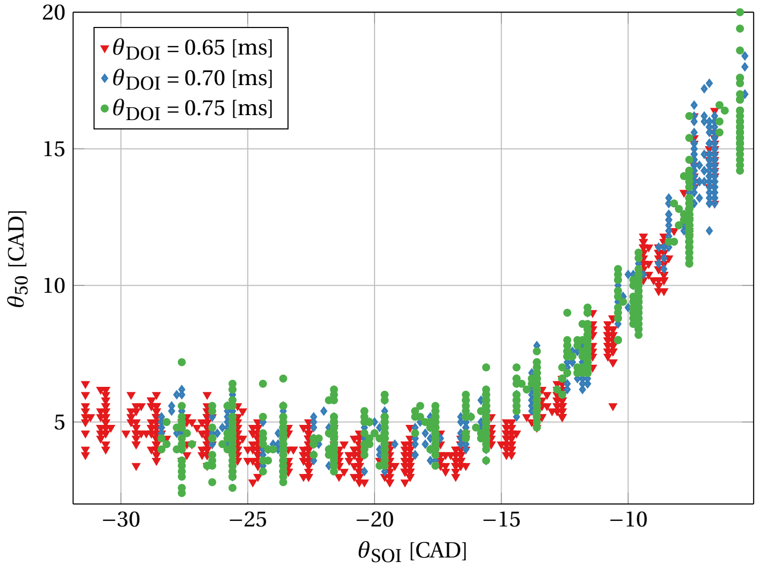

Figure 9.1 Combustion timing θ_{50} as a function of fuel-injection timing θ_{SOI} for three different fuel-injection durations θ_{DOI}. For injections closer to TDC, the gain between θ_{SOI} and θ_{50} was positive. As θ_{SOI} was advanced, the gain decreased and became slightly negative. The negative gain was more significant for the shorter injection durations.

Experiments with different pilot- and main-fuel injection durations, $\theta^{p}_{\mathrm{DOI}}$ and $\theta^{m}_{\mathrm{DOI}}$, were conducted to investigate the $\theta^{p}_{\mathrm{DOI}}$ effect on the gross indicated efficiency

$$\eta_{\mathrm{GIE}} = \frac{p_{\mathrm{IMEPg}} V_d}{m_f Q_{\mathrm{LHV}}} \tag{9.1}$$

The combustion timing θ_{50} was kept as close to TDC as possible, whilst the pilot injection was positioned 10 CAD prior to the main injection. A small separation between pilot and main was previously shown to minimize τ, see Fig. 8.5. Level curves of p_{IMEPn} (blue, dashed) and η_{GIE} (red, solid) as a function of $\theta^{m}_{\mathrm{DOI}}$ and $\theta^{p}_{\mathrm{DOI}}$ are presented in Fig. 9.2. Figure 9.2 shows that for a given p_{IMEPn}, η_{GIE} could be increased by having a longer $\theta^{p}_{\mathrm{DOI}}$. This effect became less significant for higher p_{IMEPn}. The pilot-injection effect on heat-release rate is presented in Fig. 9.3, where it can be seen that the pilot injection both reduced τ and increased the heat-release rate. From these results it was concluded that a pilot injection should be used to aid main-injection ignition and allow for a more advanced θ_{50}.

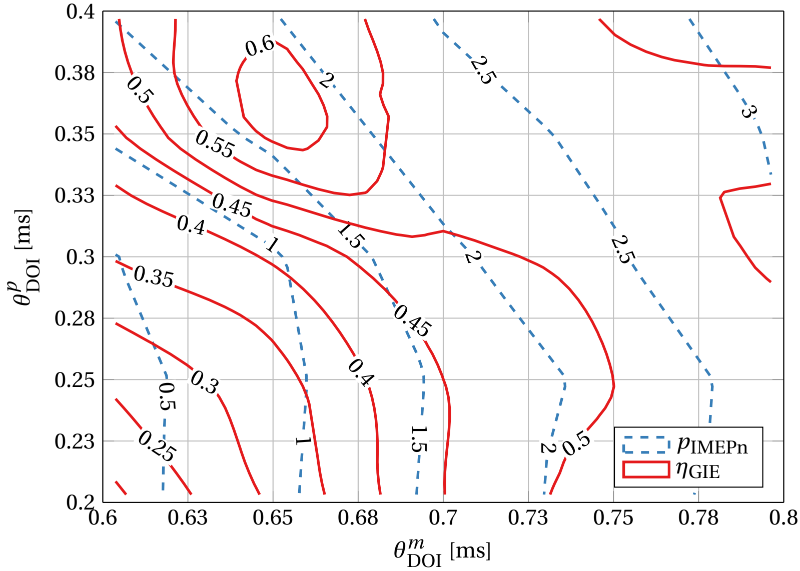

Figure 9.2 Level curves of p_{IMEPn} (blue, dashed) and η_{GIE} (red, solid) as a function of θ^m_{DOI} and θ^p_{DOI}. For a low p_{IMEPn}, η_{GIE} could be increased by having a longer θ^p_{DOI}. This effect became less significant for higher p_{IMEPn}.

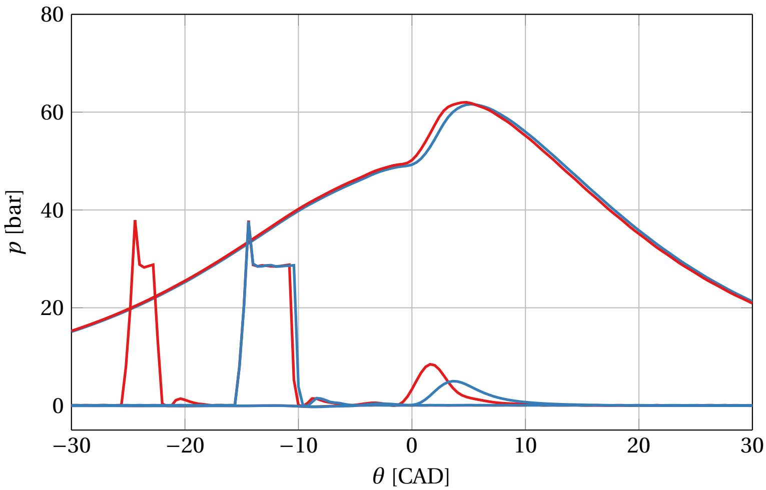

Figure 9.3 In-cylinder data comparing heat-release and pressure with and without a pilot injection. With the same main-injection timing, τ was reduced by the pilot injection, which gave an advanced θ_{50} and an increased heat-release rate.

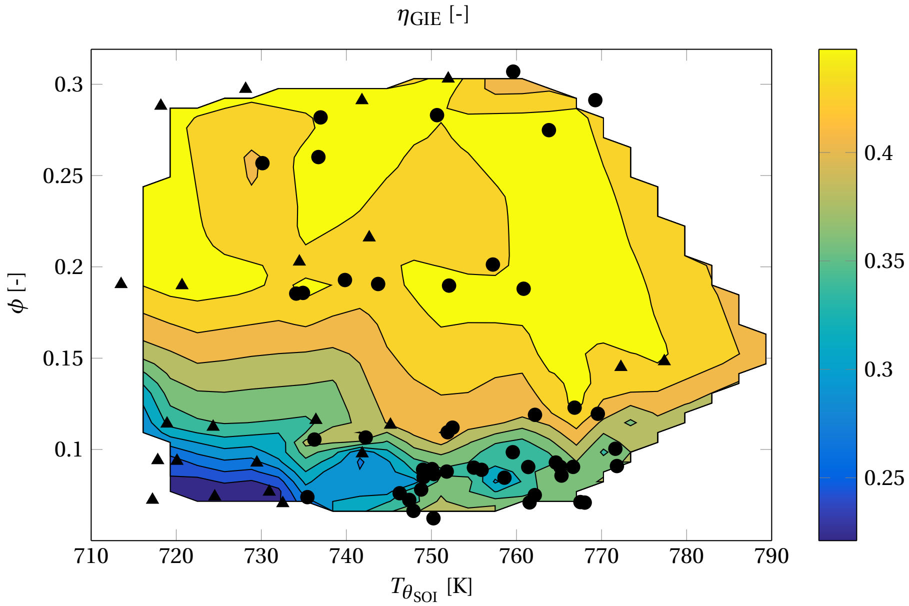

Figure 9.4 Experimental η_{GIE} as a function of equivalence ratio ϕ and temperature at θ_{SOI}. For low ϕ, η_{GIE} increased with temperature. These data were used to model η_{NIE} in the MPC simulations.

Intake Conditions

The gas-system valve positions θ_{HP} and θ_{cool} were varied at the following injection durations

$$\theta_{\mathrm{DOI}}^{m} = \{0.65,\ 0.7,\ 0.75,\ 0.85,\ 1.05\}\ \ [\mathrm{ms}] \tag{9.2}$$

to investigate how the intake conditions affect η_{GIE}. The combustion timing was kept in the interval 0-5 CAD and no pilot injection was used. Computed η_{GIE} during these experiments are presented as a function of global equivalence ratio ϕ and temperature at θ_{SOI}, $T_{\theta_{\mathrm{SOI}}}$ in Fig. 9.4. The temperature $T_{\theta_{\mathrm{SOI}}}$ was computed by assuming adiabatic compression

$$T_{\theta_{\mathrm{SOI}}} = T_{\mathrm{in}} \left(\frac{V(\theta_{\mathrm{IVC}})}{V(\theta_{\mathrm{SOI}})} \right)^{\gamma - 1} \tag{9.3}$$

In Fig. 9.4, the efficiency η_{GIE} decreased steeply when ϕ and $T_{\theta_{\mathrm{SOI}}}$ were simultaneously reduced. It can also be seen that η_{GIE} was more sensitive to $T_{\theta_{\mathrm{SOI}}}$ at low ϕ, and could be increased significantly by increasing $T_{\theta_{\mathrm{SOI}}}$. The effect of increasing T_{in} can also be seen in Fig. 9.5, where the increase in T_{in} decreased τ and increased the heat-release rate.

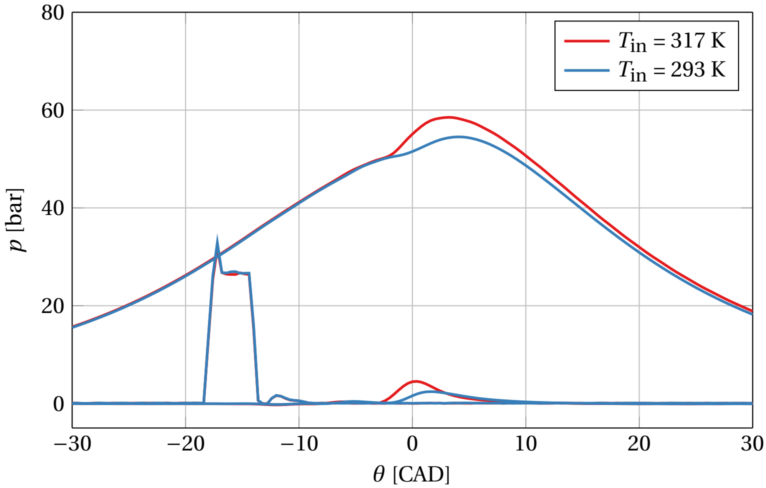

Figure 9.5 The effect of elevating the intake temperature. This was done by opening the high-pressure EGR valve and closing the cool thermal-management valve. An increased temperature gave a decrease in τ as well as an increased heat-release rate, which indicates an improved combustion efficiency since $\theta^{m}_{\mathrm{DOI}}$ was kept constant.

Varying θ_{HP} and θ_{cool} also affected pumping losses p_{PMEP}, which is the indicated mean-effective pressure during the gas-exchange strokes. The relation between p_{PMEP} and the intake and exhaust manifold pressures, p_{in}, p_{ex}, is presented in Fig. 9.6, where the symbols ○ and △ relate the data in Figs. 9.4 and 9.6. Pumping losses correlated with $p_{\mathrm{in}} - p_{\mathrm{ex}}$ as expected. Moreover, the symbols indicate that p_{PMEP} in Fig. 9.6 correlated with T_{SOI} in Fig. 9.4. This was because opening θ_{HP} not only heated the intake charge, it also elevated the intake-manifold pressure, and in that way reduced pumping losses. The data presented in Figs. 9.4 and 9.6 were used for efficiency optimization through simulation in the following section.

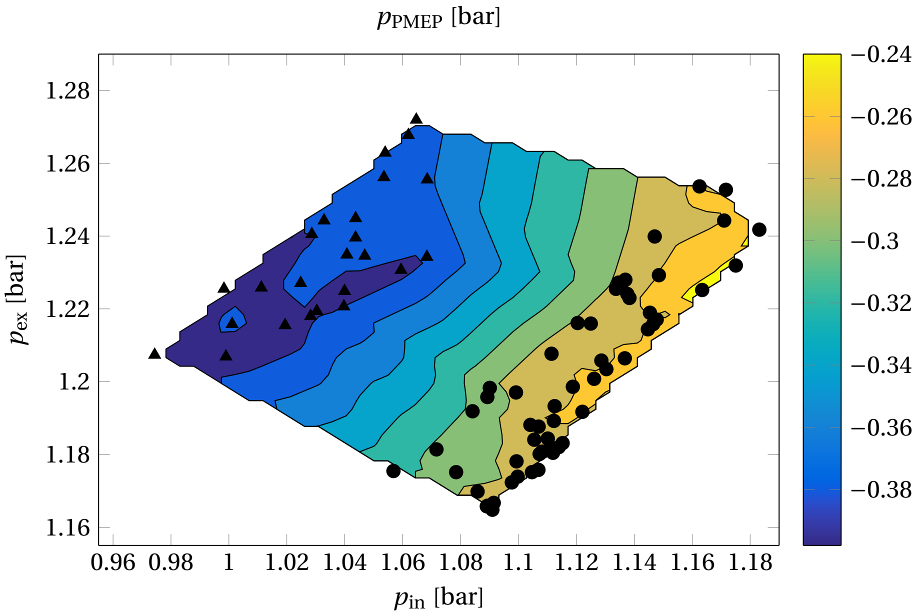

Figure 9.6 Experimental p_{PMEP} as a function of intake and exhaust-manifold pressures, p_{in}, p_{ex}. These data were used to model η_{NIE} in model predictive control simulations.

Optimal Gas-Exchange Actuation

The efficiency data in Figs. 9.4 and 9.6 were used together with the calibrated gas-exchange-system model, presented in Sec. 2.3, to find efficiency-optimal θ_{cool} and θ_{HP} actuation during p_{IMEPn} set-point changes.

A model predictive control problem was formulated for this purpose

$$\begin{aligned}
&\underset{\theta_{\mathrm{cool}},\,\theta_{\mathrm{HP}}}{\text{minimize}} && \sum_{k=1}^{H_p} \omega_1|m_f(k)| + \omega_2||1-\theta_{\mathrm{cool}}(k)||_2^2 + \omega_3||\theta_{\mathrm{HP}}(k)||_2^2 && (9.4)\\
&\text{subject to} && \theta^l \leq \begin{pmatrix} \theta_{\mathrm{HP}} \\ \theta_{\mathrm{cool}} \\ \Delta\theta_{\mathrm{HP}} \\ \Delta\theta_{\mathrm{cool}} \end{pmatrix} \leq \theta^u \\
& && \dot{\boldsymbol{x}} = f(\boldsymbol{x}, \theta_{\mathrm{cool}}, \theta_{\mathrm{HP}}), \quad (2.22)-(2.37)\\
& && \eta_{\mathrm{GIE}} = g_1(\phi, T_{\theta_{\mathrm{SOI}}})\\
& && p_{\mathrm{PMEP}} = g_2(p_1, p_2)
\end{aligned}$$

The objective of this controller is to minimize fuel consumption. This is represented by the first cost term in (9.4). The other two terms penalize deviation from suitable valve positions at mid-to-high engine load where intake-manifold temperature should be kept low to reduce heat-transfer losses and the low-pressure EGR path is preferred over the high-pressure EGR path. Valve positions θ_{cool} and θ_{HP} are here normalized from 0 to 1, where 1 denotes fully open. The cost function is defined over a prediction horizon of H_p engine cycles, where k denotes cycle index. The cost function was minimized subject to the dynamics of the gas-exchange system model in Sec. 2.3. Here, the state $\boldsymbol{x}$ include the pressures and temperatures of the volumes in Fig. 2.3. The functions g_1 and g_2 were obtained by interpolating the data in Figs. 9.4 and 9.6.

The gas-exchange model in Sec. 2.3 was then used to simulate the MPC in (9.4). During this experiment, p_{IMEPn} was set to follow a set-point trajectory using a PI controller. Combustion timing θ_{50} was also regulated through θ_{SOI} adjustments. No combustion model was used since p_{IMEPn} was given directly by g_1 and g_2. An ignition-delay model was however used to compute $T_{\theta_{\text{SOI}}}$. The nonlinear MPC problem (9.4) was solved every simulated engine cycle using the MATLAB nonlinear-optimization toolbox together with the ode23s solver to compute the gas-system model output. Global solutions of (9.4) can not be guaranteed due to the nonlinearity of the optimization problem. Solutions obtained were however justified by confirming that they were consistent for different initial guesses.

Simulation results for three MPCs with different fuel-consumption weights $\omega_1 = 0, 1, 5$, $\omega_2 = \omega_3 = 10$ and $H_p = 10$ are presented in Fig. 9.7. As the cost for fuel consumption was increased, the controller increased gas-exchange actuation by closing θ_{cool} and opening θ_{HP} when p_{IMEPn} was reduced. The controller was in this way able to avoid the low-efficiency region in the $\phi - T$ diagram (see the lower right subdiagram in Fig. 9.7). This lowered the injected fuel amount m_f needed at low load. Overshoot in p_{IMEPn} was also slightly reduced.

Fuel efficient actuation of θ_{cool} and θ_{HP} in Fig. 9.7 was approximated with a static ϕ-feedback law $K(\phi)$

$$\begin{pmatrix}\theta_{\text{cool}}\\ \theta_{\text{HP}}\end{pmatrix} = \begin{pmatrix}K_1(\phi)\\ K_2(\phi)\end{pmatrix} \tag{9.5}$$

Figure 9.8 shows K coincidence with the actuated valve positions in Fig. 9.7. There is some deviation between data and K_1 for higher ϕ. This deviation was deliberately chosen to utilize the full range of θ_{cool} for reduced intake-manifold temperatures at higher engine loads. The reason for approximating the MPC behavior was due to the inhibiting computation times needed to solve (9.4) online.

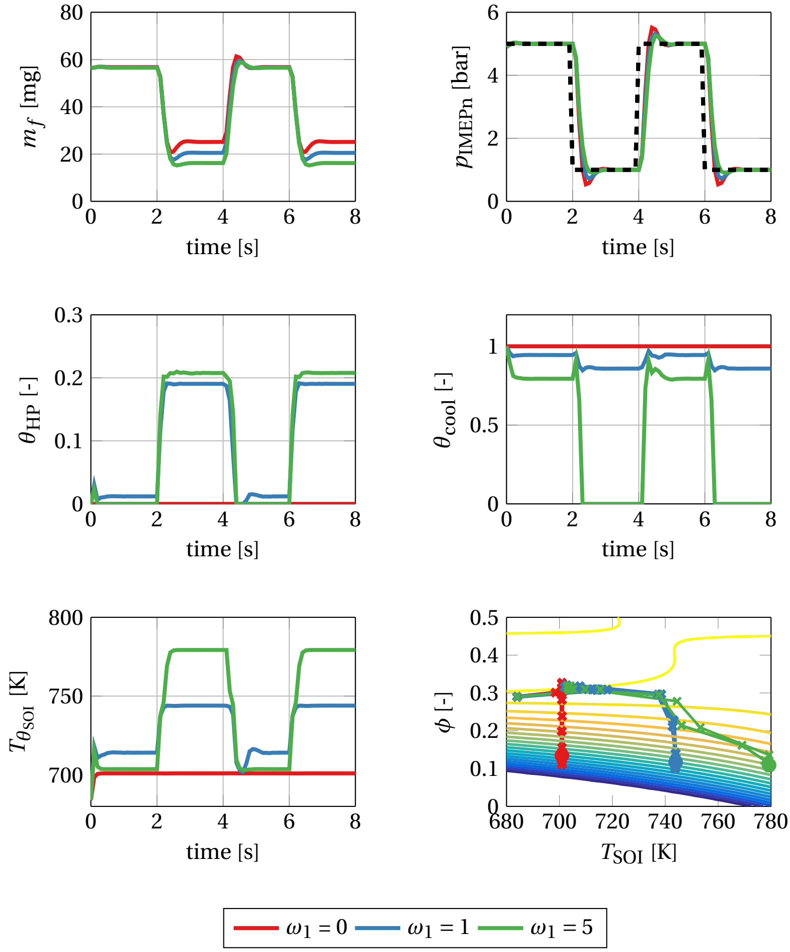

Figure 9.7 Simulated MPC output for different fuel-consumption weights ω_1. With a larger weight, the controller avoids the low efficiency region in the $\phi - T$ diagram. This behavior is indicated by the lower right subdiagram where the level curves represent η_{GIE} obtained from the data in Fig. 9.4.

9.3 Suggested Controller

The results presented suggest the following controller design:

- The combustion timing θ_{50} can be controlled by adjusting θ_{SOI} with a PI controller. The set point θ_{50}^r should then be located close TDC in order to avoid misfire. Furthermore, θ_{SOI} should be limited to the positive-gain region in Fig. 9.1, to ensure θ_{50} controllability and closed-loop stability.

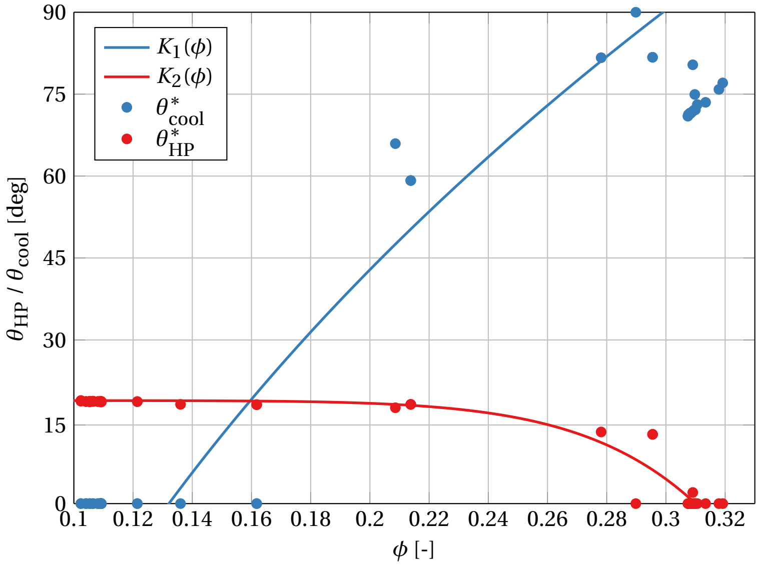

Figure 9.8 The static feedback law K was used to approximate efficient MPC valve positions in Fig. 9.7. It was decided to use the full range of θ_{cool} which gave a deviation between θ^*_{cool} and K_1 for higher ϕ.

- A pilot injection should be used to reduce τ for advanced θ_{50} and increased heat-release rates. It was here decided to use a small pilot, located 10 CAD prior to the main-injection. The reason the short separation time was to minimize τ, see Fig. 8.5.

- Gas-exchange valve positions should be set according to the feedback law $K(\phi)$ in Fig. 9.8 to increase intake temperature at low load. In this work, ϕ was computed from intake-manifold conditions (2.27) and fuel-mass flows from a calibrated injection-duration map.

The suggested feedback loop is presented in Fig. 9.9. The controller is fairly simple, and the decentralized controller design is easy to implement. The controller would nevertheless be able to maximize efficiency according to the presented experimental results. The design of a centralized controller structure, that for example utilizes ignition-delay and gas-exchange models, as presented in Chapter 7, is suggested future work. Another possible extension to the controller in Fig. 9.9 is a method that experimentally identifies the θ_{50} gain, in order to adapt the θ_{SOI} saturation limit.

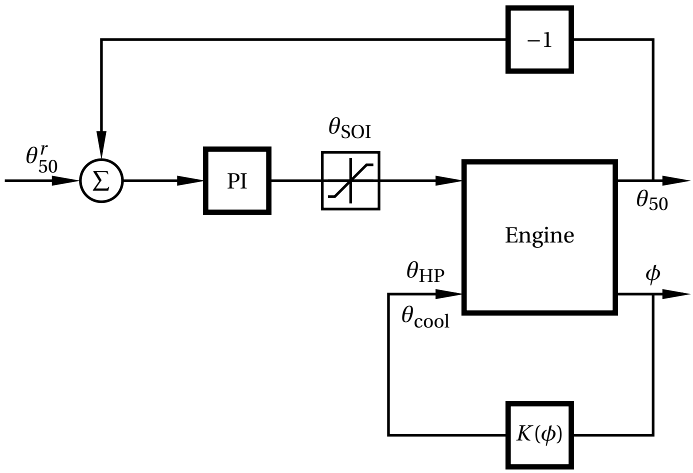

Figure 9.9 The experimental results suggested the following low-load control strategy: A range-limited θ_{50} PI controller in combination with a static gas-exchange controller with global ϕ as feedback variable. Load and rail pressure are controlled separately using PI controllers with feedforward.

9.4 Controller Evaluation

The suggested controller was evaluated experimentally during a test cycle where p_{IMEPn} was set to follow set-point changes from 1 to 5 bar at $N_{\mathrm{speed}} = 1200$ rpm. Four different controller-design cases were evaluated in order to compare controller performance:

1. Cylinder-individual θ_{50} PI controllers.

2. Cylinder-individual θ_{50} PI controllers with θ_{SOI} saturation (> -20 CAD).

3. Case (2) with a pilot injection.

4. Case (3) with the gas-system feedback law $K(\phi)$.

For all cases, p_{IMEPn} was controlled by keeping the rail pressure constant and varying the main-injection duration with PI controllers and feedforward.

Experimental test-cycle results from one cylinder are presented in Fig. 9.10 for cases (1-4). Differences between the cases are more noticeable at low engine load. The injection timing was not limited in case (1). This led to very early injection timings when the earliest obtainable θ_{50} was larger than θ_{50}^r. The early injection timing in case (1) resulted in a τ increase and a delayed θ_{50} as a result. When limiting θ_{SOI}, as in case (2), θ_{50} was advanced and the deviation from θ_{50}^r was reduced.

When a pilot injection was introduced in case (3), τ decreased, see the θ_{SOI} and θ_{50} subdiagrams in Fig. 9.10. The reduction in τ allowed the controller to keep θ_{50} closer to θ_{50}^r. In case (4), τ was further decreased as T_{in} and $T_{\theta_{\text{SOI}}}$ increased due to valve-position actuation. This resulted in smaller θ_{50} error at low load.

In-cylinder data showing these trends more clearly are presented in Fig. 9.11 where in-cylinder pressure, injection current and heat-release rate are presented at cycle 250. It can be seen that the gradual controller adjustments led to decreased τ. The heat-release rate also differed for the different cases where case 1, with the longest ignition delay had the lowest heat-release rate.

Accumulated fuel consumption, computed from injection durations is presented in Fig. 9.12. The fuel-consumption rates differed more clearly at the low-load operating points. Figure 9.12 shows that fuel consumption decreased from case (1-4), with reductions from 2 to 9 %. The greatest reduction resulted from the introduction of a pilot injection.

9.5 Conclusions

This chapter presented a control strategy for improved PPC performance at low load. The combustion timing θ_{50} was only controllable with respect to θ_{SOI} in a specific interval, see Fig. 9.1. It was therefore important keep θ_{SOI} in this interval to maintain closed-loop stability with a θ_{50}-feedback controller.

A pilot injection was shown to increase the combustion efficiency at low load, see Figs. 9.2 and 9.12. This was due to the decrease in τ, which led to an increased heat-release rate and the possibility to further advance θ_{50}.

The problem of maximizing η_{GIE} was formulated as an optimization problem in the ϕ-T diagram, where η_{GIE} could be increased by heating the inducted air charge, see Fig. 9.4. Control of the intake conditions was achieved by varying θ_{HP} and θ_{cool} according to a feedback law $K(\phi)$, obtained from MPC simulations.

An experimental controller evaluation showed that these findings could reduce fuel consumption from 2 to 9 %, see Fig. 9.12.

Summary of PPC Control

This chapter concludes the results related to PPC control. The following three chapters of this thesis cover controller designs applicable to conventional compression-ignition operation. A summary of the PPC results presented in chapters 6 to 9 will be given in Chapter 13.

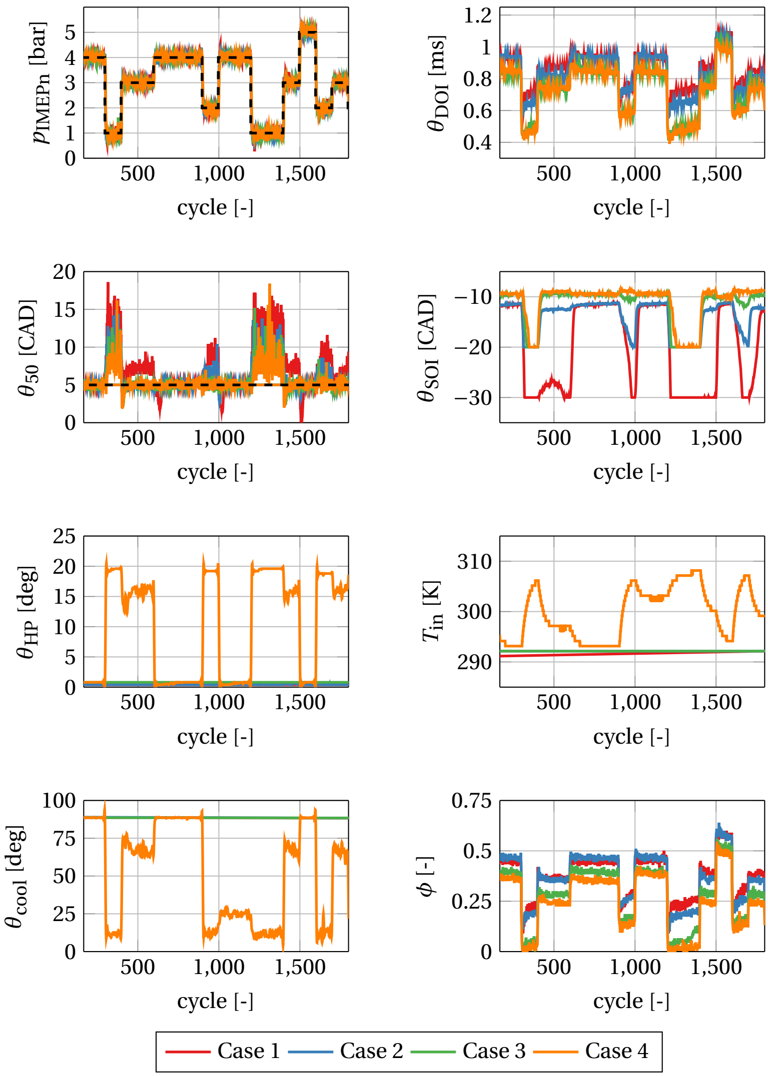

Figure 9.10 Experimental results for the four different controller cases. In case 1, θ_{SOI} was not limited to the positive-gain region. This led to very early θ_{SOI}, and as a result, a delayed θ_{50} (compare case 1 and case 2). With a pilot injection in case 3, τ decreased, see the θ_{SOI} and θ_{50} subdiagrams. Finally, in case 4, τ decreased further as θ_{HP} was opened and θ_{cool} was closed.

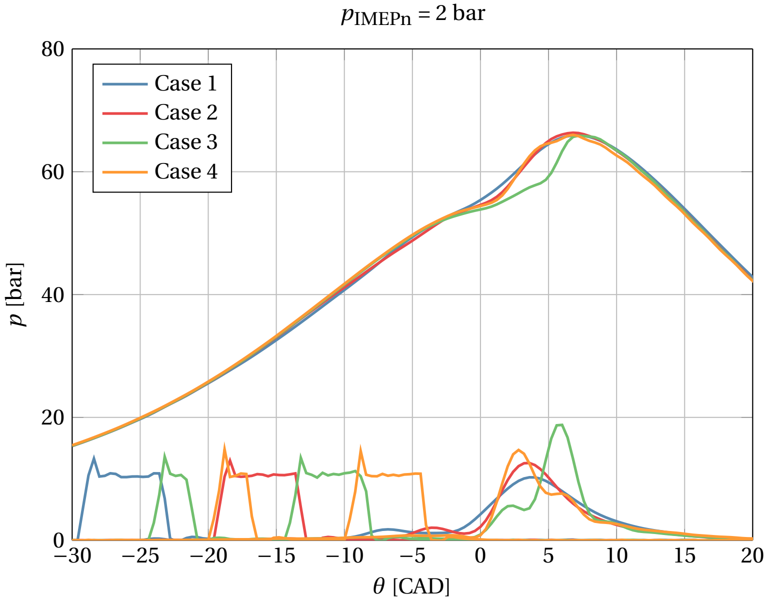

Figure 9.11 In-cylinder data from cycle 950 in Fig. 9.10. The gradual controller adjustments from case 1 to case 4 resulted in a decreased τ. It can also be seen that the advanced θ_{SOI} in case (1) gave a reduced heat-release rate.

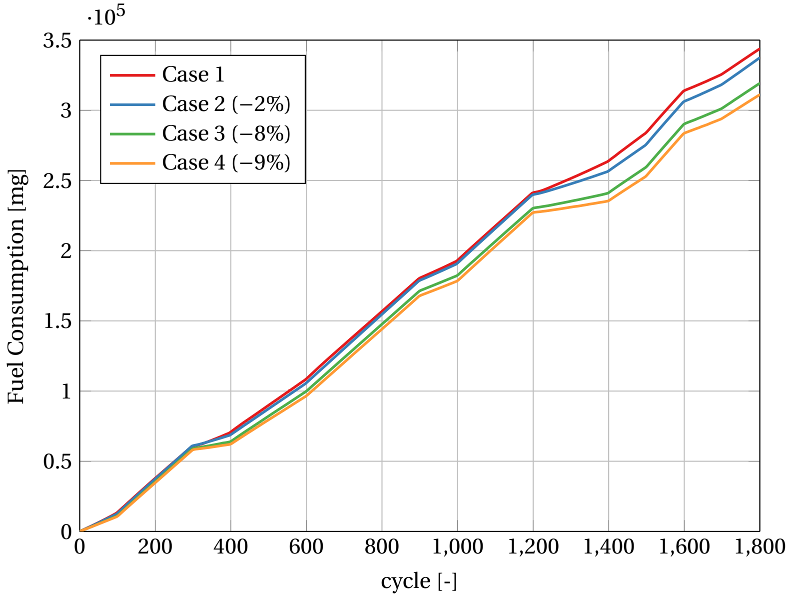

Figure 9.12 Accumulated fuel consumption for the four controller cases in Fig. 9.10 where the fuel-consumption rate differed more at low load. Fuel consumption decreased from case (1-4), with reductions from 2 to 9 % where the greatest reduction came with the introduction of a pilot injection. Here, the injected fuel mass was computed from fuel-injection durations. The reason for not using the fuel-mass-flow meter was that the meter was mounted far from the engine, and was therefore not reliable in transient operation.

10

Constraint Handling with Multiple Injections

10.1 Introduction

Despite its lack of spatial information, the heat-release rate as a function of crank-angle degree is an important variable when maximizing the thermodynamic engine efficiency. When assuming a zero-dimensional, adiabatic model with constant γ, the thermodynamic efficiency is maximized when heat is released instantaneously at TDC. This heat-release rate minimizes exhaust losses without generating counterproductive pressure during the compression stroke, and is equivalent to the ideal Otto cycle with constant-volume combustion at TDC.

The optimal combustion timing is delayed to after TDC when heat-transfer to cylinder walls is also accounted for. A delayed combustion timing reduces in-cylinder temperature and heat-transfer losses. It also reduces peak in-cylinder pressure which in turn reduces engine friction and heat-losses to crevice volumes. A drawback with delaying the combustion timing is the resulting increase in exhaust-gas energy. The optimal combustion timing is therefore a compromise between these losses.

The optimal heat-release rate becomes more involved when constraint fulfillment is required. With constraints on maximum cylinder pressure and NO_x formation, motivated by mechanical tolerances and emission regulations, combustion has to be delayed during the expansion stroke to reduce the in-cylinder pressure and temperature. Furthermore, efficient aftertreatment-system performance requires sufficient exhaust-gas temperature, which in turn demands increased exhaust losses [Gieshoff et al., 2000; Katare et al., 2009]. As suggested by these examples, there are also compromises between constraint fulfillment and the thermodynamic efficiency.

Optimal heat-release rates with respect to constraints on in-cylinder pressure, NO_x formation and knock intensity were computed in [Eriksson and Sivertsson, 2016; Guardiola et al., 2017]. In these studies, optimal heat-release rates were found to be multimodal to reduce in-cylinder pressure and temperature. With a single fuel injection and a production heavy-duty fuel-injection system, however, the heat-release rate controllability is limited. The combustion timing can be controlled more or less freely by varying the injection timing, but the heat-release shape depends on rates of fuel injection, mixing and chemical reactions. These rates can only be controlled partially by adjusting cylinder-mixture properties and the fuel-injection pressure.

The degrees of freedom increase when multiple injections are used. It was found in [Han et al., 1996] that two injections can be used to provide a more distributed heat-release rate with reduced peak temperature and NO_x formation. This allows for a more advanced effective combustion timing without NO_x-constraint violation. Okamoto and Uchida [2016] presented a multiple-injector strategy for heat-release shaping. Experimental results showed that heat-release shaping could provide a 75 % reduction of NO_x emissions due to suppressed peak average temperature and pressure with maintained indicated efficiency. An indicated specific-fuel consumption reduction of 12 % was reported in [Dober et al., 2008] with maintained NO_x emissions, using a novel fuel-injection system and multiple injections. The use of post injections for control of exhaust-gas temperature was demonstrated in [Zheng et al., 2005; Castellano et al., 2013] among others.

Some insight to the potential efficiency benefit with multiple injections can be gained by studying the simulated pressure curves in Fig. 10.1. Here, the different heat-release rates and injection configurations generate the same work output, $p_{\mathrm{IMEPn}} = 15$ bar. Without a constraint on maximum pressure $p_{\max}$, the optimal combustion timing is close to TDC with the gross indicated efficiency $\eta_{\mathrm{GIE}} = 0.5$, see the upper subdiagram. When a $p_{\max}$ constraint is imposed (lower subdiagram), the combustion timing has to be delayed for constraint fulfillment. This results in a 4.8 % η_{GIE} decrease with one injection (blue). With two injections (red), however, the combustion timing is allowed to be advanced, and the decrease in η_{GIE} is only 0.8 %.

An extensive calibration effort is demanded in order to find efficiency-optimal fuel-injection configurations that fulfill pressure, NO_x and exhaust-temperature constraints over the engine operating range. Optimal configurations are also sensitive to hardware aging, fuel properties and variation in operating conditions. Moreover, the engine should operate as close to the constraint as possible for maximized engine efficiency.

This chapter therefore investigates the use of feedback control for automatic fuel-injection adjustment and increased engine efficiency subject to specified constraints. The suggested controller is a hybrid, multiple-input multiple-output PI controller that utilizes feedback from in-cylinder pressure-sensor measurements, an NO_x-emission model functioning as a virtual sensor, and measured exhaust temperature. The controller varies the number of injections and adjusts

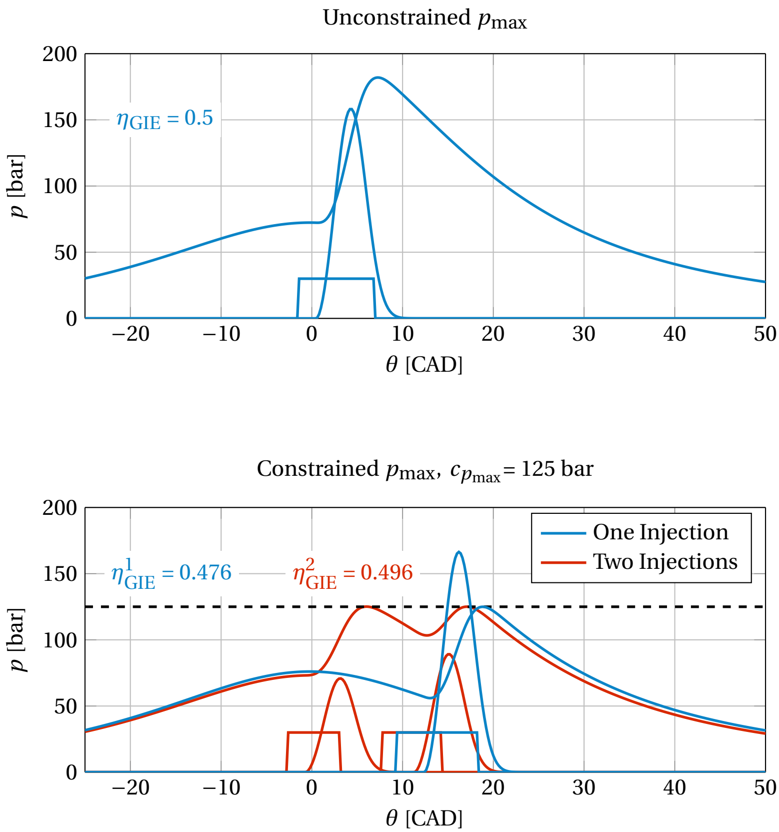

Figure 10.1 Simulated pressure curves with and without constraints on p_{max}. Without a constraint on p_{max}, the optimal combustion timing is close to TDC with the gross indicated efficiency $\eta_{GIE} = 0.5$, see the upper subdiagram. When a p_{max} constraint at 125 bar is imposed, the combustion timing has to be delayed (see lower subdiagram). This results in a 4.8 % η_{GIE} decrease, with one injection (1). With two injections (2), the combustion timing can be advanced, and the decrease in η_{GIE} is only 0.8 %.

injection timings and durations depending on operating conditions. Moreover, the presented controller uses the heat-release detection method presented in Chapter 4 to distinguish heat-release rates from different injections. The designed controller behavior was motivated by zero-dimensional simulation experiments that are also presented in this chapter. These simulation results show how optimal combustion timings vary as a function of constraint limits.

The chapter is outlined as follows: The problem formulation is given in Sec. 10.2. The zero-dimensional model used in simulation is presented together with simulation results in Sec. 10.3. The proposed controller design is then introduced in Sec. 10.4. Experimental evaluation results are presented in Sec. 10.5, where both transient and steady-state operation are evaluated. Controller performance is also compared to that of a simpler single-injection controller. Finally, discussion and conclusions are given in Secs. 10.6 and 10.7.

10.2 Problem Description

The objective of this chapter is to maximize the gross indicated efficiency

$$\eta_{\mathrm{GIE}} = \frac{p_{\mathrm{IMEPg}} V_d}{m_f Q_{\mathrm{LHV}}} \tag{10.1}$$

The efficiency η_{GIE} should be maximized whilst p_{max}, formed NO_x emissions and the exhaust temperature T_{ex} fulfill upper and lower bounds

$$\begin{aligned} p_{\mathrm{max}} &\leq p_{\mathrm{max}}^c \\ \mathrm{NO}_x &\leq \mathrm{NO}_x^c \\ T_{\mathrm{ex}} &\geq T_{\mathrm{ex}}^c \end{aligned} \tag{10.2}$$

Upper bounds on p, $dp/d\theta$ and NO_x are motivated by mechanical engine tolerances and legislated emission limits. The lower limit for T_{ex} is introduced to guarantee after-treatment system performance. The demanded work output p_{IMEPn}^r should also be delivered

$$p_{\mathrm{IMEPn}} = p_{\mathrm{IMEPn}}^r \tag{10.3}$$

The case with up to two fuel injections is first considered. The optimization variables are the injection timings, denoted $\theta_{\mathrm{SOI}}^1, \theta_{\mathrm{SOI}}^2$, and injected fuel masses, m_f^1 and m_f^2. The optimization problem can be simplified by assuming that the total fuel mass m_f^{tot} is determined by p_{IMEPn}^r. The ratio

$$r = \frac{m_f^1}{m_f^{\mathrm{tot}}} \tag{10.4}$$

can then be optimized instead of m_f^1 and m_f^2. This ratio was here limited to

$$0.5 \leq r \leq 1 \tag{10.5}$$

to exclude redundant configurations. Injection durations θ_{DOI}^1 and θ_{DOI}^2 are determined by r, m_f^{tot} and p_{rail}, with the use of an injector map M_{inj}

$$\begin{pmatrix}\theta_{\mathrm{DOI}}^1 & \theta_{\mathrm{DOI}}^2\end{pmatrix}^T = M_{\mathrm{inj}}(r, m_f^{\mathrm{tot}}, p_{\mathrm{rail}}) \tag{10.6}$$

The injection pulses are not allowed to overlap in order to ensure that the injector needle closes in-between injections. This imposes constraints on possible fuel-injection timings and durations.

The optimization variable

$$\boldsymbol{u} = \begin{pmatrix}\theta_{\text{SOI}}^{m} & \theta_{\text{SOI}}^{p} & r & Q_{\text{tot}}\end{pmatrix}^T \tag{10.7}$$

is related to the system output variables

$$\boldsymbol{y} = \begin{pmatrix}\eta_{\text{GIE}} & p_{\text{IMEPn}} & p_{\text{max}} & \text{NO}_x & T_{\text{ex}}\end{pmatrix}^T \tag{10.8}$$

through a non-trivial relation

$$\boldsymbol{y} = f(\boldsymbol{u}) \tag{10.9}$$

We can now formulate the optimization problem as

$$\begin{aligned} \underset{\boldsymbol{u}}{\text{maximize}} \quad & \eta_{\text{GIE}}(\boldsymbol{u}) \\ \text{subject to} \quad & p_{\text{max}}(\boldsymbol{u}) \le p_{\text{max}}^{c} \\ & \text{NO}_x(\boldsymbol{u}) \le \text{NO}_x^{c} \\ & T_{\text{ex}}(\boldsymbol{u}) \ge T_{\text{ex}}^{c} \\ & p_{\text{IMEPn}}(\boldsymbol{u}) = p_{\text{IMEPn}}^{r} \\ & \boldsymbol{y} = f(\boldsymbol{u}) \\ & \boldsymbol{u} \in \mathbb{U} \end{aligned} \tag{10.10}$$

where the set $\mathbb{U}$ denotes feasible fuel-injection configurations.

The most difficult part of solving (10.10) is to evaluate f for a given $\boldsymbol{u}$. In reality, f is determined by injector dynamics, turbulent combustion and thermodynamic processes. The approach taken here was to model f with the zero-dimensional model presented in Chapter 2, and then evaluate f over a grid of inputs $\boldsymbol{u}$. This was done both to find optimal system inputs $\boldsymbol{u}^*$ and to find trends for how $\boldsymbol{u}^*$ depend on different constraints x^c. Simulation results showing $\boldsymbol{u}^*$ for different x^c are presented in the following section. These results provide a foundation for controller design in subsequent sections.

10.3 Simulation

Simulation experiments with two combustion timings were conducted to find optimal $\boldsymbol{u}$ with respect to (10.10). The objective was to investigate when multiple injections are beneficial and how optimal combustion timings are configured as a function of imposed constraints. This section presents the model used, and simulation results showing trends for p_{max}, NO_x, temperature at exhaust-valve opening, T_{EVO}, and η_{GIE} as $\boldsymbol{u}$ is varied.

Model

The model used was the zero-dimensional model presented in Chapter 2

$$\frac{dp}{d\theta} = -\frac{\gamma}{V}\frac{dV}{d\theta}p + \frac{\gamma - 1}{V}\left(\frac{dQ_c}{d\theta} - \frac{dQ_{ht}}{d\theta}\right), \quad p(\theta_{\text{IVC}}) = p_{\text{in}} \tag{10.11}$$

where γ was dependent on in-cylinder temperature and composition. The heat-transfer rate $dQ_{ht}/d\theta$ was computed with a Woschni-type convective heat-transfer coefficient [Woschni, 1976], and the heat-release rate was modeled with the Wiebe expression [Wiebe, 1970]

$$\frac{Q_c(\theta)}{Q_c^{\text{tot}}} = \begin{cases} 1 - \exp\left(-a\left(\dfrac{\theta - \theta_{\text{SOC}}}{\Delta\theta}\right)^{b+1}\right) & \text{for } \theta \geq \theta_{\text{SOC}} \\ 0 & \text{otherwise} \end{cases} \tag{10.12}$$

Here, θ_{SOC} was related to the i:th injection timing θ^i_{SOI} with the use of an Arrhenius ignition-delay expression

$$\begin{aligned} \theta^i_{\text{ign}} &= \theta^i_{\text{SOI}} + \tau^i \\ \tau^i &= Ap^{-n}_{\text{SOI}^i}e^{E_a/\tilde{R}T_{\text{SOI}^i}} \end{aligned} \tag{10.13}$$

where ignition delay τ^i was omitted in (10.13) if combustion had started prior to injection.

NO_x formation was computed with the two-zone, Zeldovich-mechanism model presented in [Egnell, 2001]. A more detailed description of this model is given in Chapter 2.

Instead of modeling T_{ex}, it was decided to study the in-cylinder temperature at exhaust-valve opening T_{EVO}, which correlates with T_{ex}.

Simulated Conditions

Simulation experiments were conducted with two injections and the corresponding accumulated heat-release

$$Q_c(\theta) = rQ^1_c(\theta) + (1-r)Q^2_c(\theta), \qquad r \in [0.5, 1] \tag{10.14}$$

where Q^1_c and Q^2_c are Wiebe expressions on the form of (10.12) and r is defined by (10.5). The combustion timings of Q^1_c and Q^2_c, θ^1_{CT} and θ^2_{CT} were swept for different r and constant total fuel energy. The reason for limiting the study to two injections and not considering a more general heat-release was that this would resemble a realistic scenario that could be realized in the experimental setup used. Constraints on p_{max} and NO_x were evaluated at a higher load compared to T_{EVO}, since lower bounds on T_{EVO} are more likely to become active at low load. Model parameters used are presented in Table. 10.1.

Table 10.1 Model parameters used in simulation. Constraints on $p_{\max}$ and NO_x were evaluated at a higher load compared to T_{EVO}.

$p_{\max}$ and NO_x constraints			
Intake Conditions		Wiebe Parameters	
p_{in} [bar]	0.98	Q_c^{tot} [J]	5×10^3
T_{in} [K]	293	a [-]	2.3
λ [-]	2.5	$\Delta\theta$ [CAD]	6
r_{EGR} [-]	0	b [-]	1.8
T_{EVO} constraints			
Intake Conditions		Wiebe Parameters	
p_{in} [bar]	1.6	Q_c^{tot} [J]	3×10^3
T_{in} [K]	293	a [-]	2.3
λ [-]	2.5	$\Delta\theta$ [CAD]	7.5
r_{EGR} [-]	0	b [-]	1.8
All constraints			
Cylinder Geometry		Heat-Transfer	
r_c [-]	18	C_1 [-]	2.28
V_d [m^3]	2.1×10^3	C_2 [m/(sK)]	0.0032
B [mm]	130	T_c [K]	333
L [mm]	160	$m_c c_p$ [J/K]	1150
IVC [CAD]	-151	k_c [J/(mK)]	45
EVC [CAD]	146	L_c [m]	0.025
Ignition Delay [Spadaccini and TeVelde, 1982]			
A [CAD]	1.7496×10^{-8}		
n [-]	2		
$E_a/\tilde{R}$ [K]	20926		

Simulation Results

Level curves for $p_{\max}$, NO_x, T_{EVO} and η_{GIE} as a function of θ^1_{CT} and θ^2_{CT} are presented in Figs. 10.2, 10.3 and 10.4. Results with $r = 0.5$, 0.625, 0.75 and 0.875 are presented in Fig 10.2, whereas results with $r = 0.5$ are presented in Figs. 10.3 and 10.4. In these figures, the black lines are η_{GIE} level curves, with the most efficient combustion timing, marked ×, found close to TDC. The efficiency then decreases with delayed θ^1_{CT} and θ^2_{CT}. The colored lines indicate $p_{\max}$ [bar], NO_x [ppm] and T_{EVO} [K] level curves, where the colored symbols indicate η_{GIE}-optimal combustion timings with respect to the different level curves as constraints, for both $\theta^1_{\mathrm{CT}} > \theta^2_{\mathrm{CT}}$ ($*$) and $\theta^1_{\mathrm{CT}} < \theta^2_{\mathrm{CT}}$ ($\diamond$). The gray regions indicate combustion-timings where fuel-injection pulses overlap, i.e., $u \notin \mathbb{U}$.

Figures 10.2-10.4 show that it is more efficient with two combustion timings when subject to $p_{\max}$, NO_x and T_{EVO} constraints. This is recognized by observing that optimal timings occur away from the $\theta^1_{\mathrm{CT}} = \theta^2_{\mathrm{CT}}$ line which indicate a unimodal, single-injection heat release rate. This holds even if $u \notin \mathbb{U}$ would have been allowed.

The symmetry with respect to $\theta^1_{\mathrm{CT}} = \theta^2_{\mathrm{CT}}$ in Figs. 10.3 and 10.4 is due to the heat-release rates being identical with $r = 0.5$. The symmetry was altered as r was varied in Fig. 10.2. In this figure, it can be seen that η_{GIE} was maximized for both $\theta^1_{\mathrm{CT}} > \theta^2_{\mathrm{CT}}$ and $\theta^1_{\mathrm{CT}} < \theta^2_{\mathrm{CT}}$. In general, there was no trend favoring any of these two configurations.

Trade-offs between η_{GIE} and x^c for different r are presented in Fig. 10.5. The $p_{\max}$ and NO_x trade-offs can be improved by up to 4 % when using two combustion timings instead of one ($r = 1$), whereas the T_{EVO} trade-off can be improved by up to 2 %. The potential η_{GIE} advantage with two injections increases as $p^c_{\max}$ and NO^c_x become more conservative. This does not hold for T^c_{EVO}. The trade-offs in Fig. 10.5 do not distinguish any clear choice for $r < 1$.

An attempt to explain the observed trends is made in Fig. 10.6. This figure presents efficiency-optimal combustion timings for one and two injections with arbitrary $p^c_{\max}$ (upper), NO^c_x (middle) and T^c_{EVO} (lower). For $p_{\max}$ and NO_x constraints, two injections give a more distributed heat-release. This lowers the peak pressure and temperature which gives a slower NO_x-formation rate. Similar trends were observed experimentally in [Han et al., 1996]. For the T_{EVO} constraint in the lower subdiagram, the late injection gives a sufficient contribution to T_{EVO} for the first combustion timing to be timed optimally. To summarize: the overall trend in Fig. 10.6 is that two injections allow for an effective or mean combustion timing closer to TDC, which increases the indicated efficiency $\eta^2_{\mathrm{GIE}} > \eta^1_{\mathrm{GIE}}$.

10.4 Controller Design

The optimization problem (10.10) was solved through simulation and by evaluating a grid over $\boldsymbol{u}$ in the previous section. With the simulation results obtained, the objective is to design a controller that automatically finds optimal $\boldsymbol{u}$ depending on operating conditions. The simulation results suggested that a single fuel injection should be used to obtain the efficiency optimal point $\times$ when no constraints are active. A constraint is here said to be active if the constrained output variable is equal to the constraint limit at optimal fuel injection.

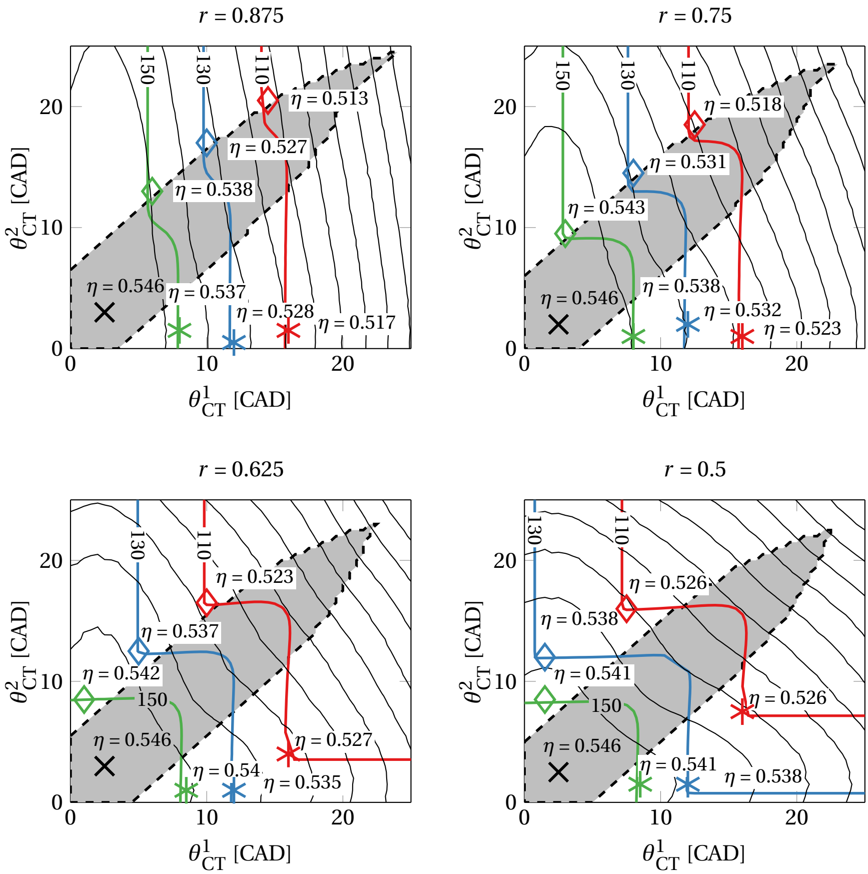

Figure 10.2 Level curves of η_{GIE} (black) for different combustion timings θ^1_{CT}, θ^2_{CT}, and ratios r. Level curves for $p_{\max}$ are presented in red (110 bar), blue (130 bar) and green (150 bar). The shaded gray areas correspond to infeasible injection timings where the injection pulses overlap. For each r, the most efficient timings are marked ×. The colored marks indicate the most efficient feasible points, given the different $p_{\max}$ constraints for the feasible regions where $\theta^1_{\mathrm{CT}} > \theta^2_{\mathrm{CT}}$ and $\theta^1_{\mathrm{CT}} < \theta^2_{\mathrm{CT}}$. The figure shows that two combustion timings are optimal when subject to $p_{\max}$ constraints. This is recognized by observing that optimal timings occur away from the $\theta^1_{\mathrm{CT}} = \theta^2_{\mathrm{CT}}$ line which indicate a unimodal, single-injection heat release rate. Pressure curves corresponding to the marked high-efficiency points for $r = 0.5$ are presented in Fig. 10.7.

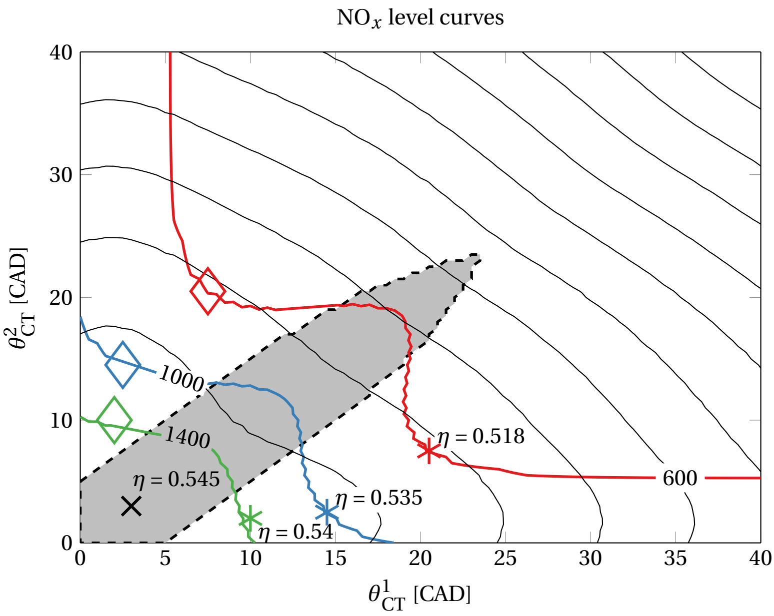

Figure 10.3 Simulated η_{GIE} level curves (black) as a function of θ^1_{CT} and θ^2_{CT}. Level curves for NO$_x$ are presented in red (600 ppm), blue (1000 ppm) and green (1400 ppm). The colored marks indicate η_{GIE}-optimal combustion timings with respect to the different NO$_x$ constraints. NO$_x$-formation curves corresponding to the marked high-efficiency points are presented in Fig. 10.8.

As constraints become active, additional injections should be introduced. One injection should be kept close to TDC and the second should be delayed in order to fulfill the constraint. The controller should also keep the constrained output as close to the limit as possible. This behavior is more clearly illustrated in Figs. 10.7, 10.8 and 10.9 where crank-angle resolved heat-release rates are presented together with p, NO$_x$ and T for the optimal timings in Figs. 10.2-10.4. The dashed horizontal lines in Figs. 10.2-10.4 indicate x^c.

It was decided to handle the different constraints separately: $p^c_{\max}$ and NO^c_x by introducing an early pilot injection and delaying both injections, and T^c_{ex} by introducing and adjusting a late post injection. This choice was motivated by the trends in Fig. 10.9, where a late combustion timing was found to be optimal. The system input was therefore redefined as

$$\boldsymbol{u} = \begin{pmatrix}\theta^1_{\mathrm{SOI}} & \theta^2_{\mathrm{SOI}} & \theta^3_{\mathrm{SOI}} & r^1 & r^3\end{pmatrix}^T \tag{10.15}$$

where r^1 and r^3 are given by

$$r^x = \frac{m^x}{m^x + m^2} \tag{10.16}$$

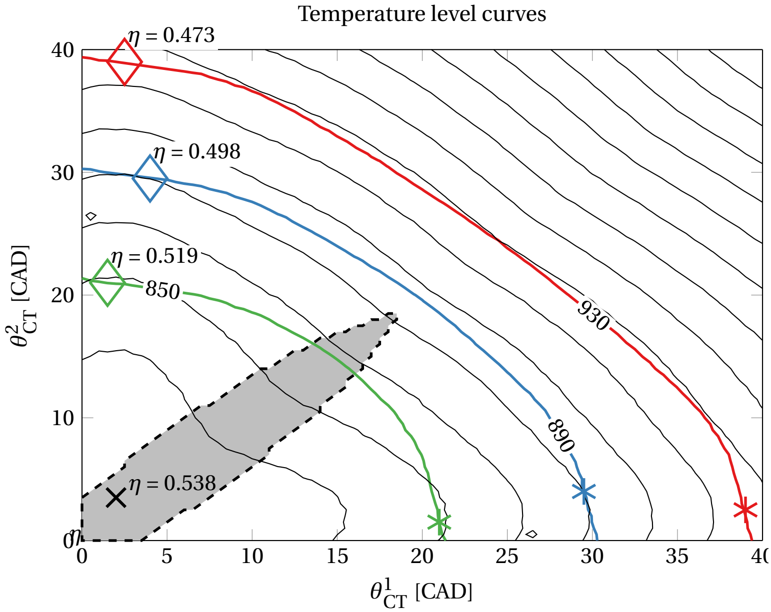

Figure 10.4 Simulated η_{GIE} level curves as a function of θ^1_{CT} and θ^2_{CT}. Level curves for T_{EVO} are presented in red (930 K), blue (890 K) and green (850 K). It is optimal to keep one injection close the optimal point ×, and then delay the latter to fulfill the constraint. Temperature curves corresponding to the marked high-efficiency points are presented in Fig. 10.9.

The indices 1, 2 and 3 represent the pilot, main and post injection, respectively. The controller should also deliver the desired load output, which was handled by adjusting the total fuel mass m_f^{tot}.

A simple controller design is attractive from an implementation perspective. Therefore, a hybrid multiple-input multiple-output PI controller

$$\boldsymbol{u}(k+1) = \boldsymbol{u}(k) + k_p(\boldsymbol{e}(k) - \boldsymbol{e}(k-1)) + k_I(\boldsymbol{e}(k-1)) \tag{10.17}$$

with gains k_p and k_I was designed to achieve the desired system behavior. The suggested controller used combustion timings, peak pressure levels, the modeled NO_x-emission level and measured exhaust temperature as feedback signals. This controller is presented in the remainder of this section.

Combustion Detection

When controlling multiple combustion timings, it is no longer sufficient to use the crank-angle of 50 % burnt as feedback variable. This quantity might not be related to a physical combustion timing with a multimodal heat-release rate. The

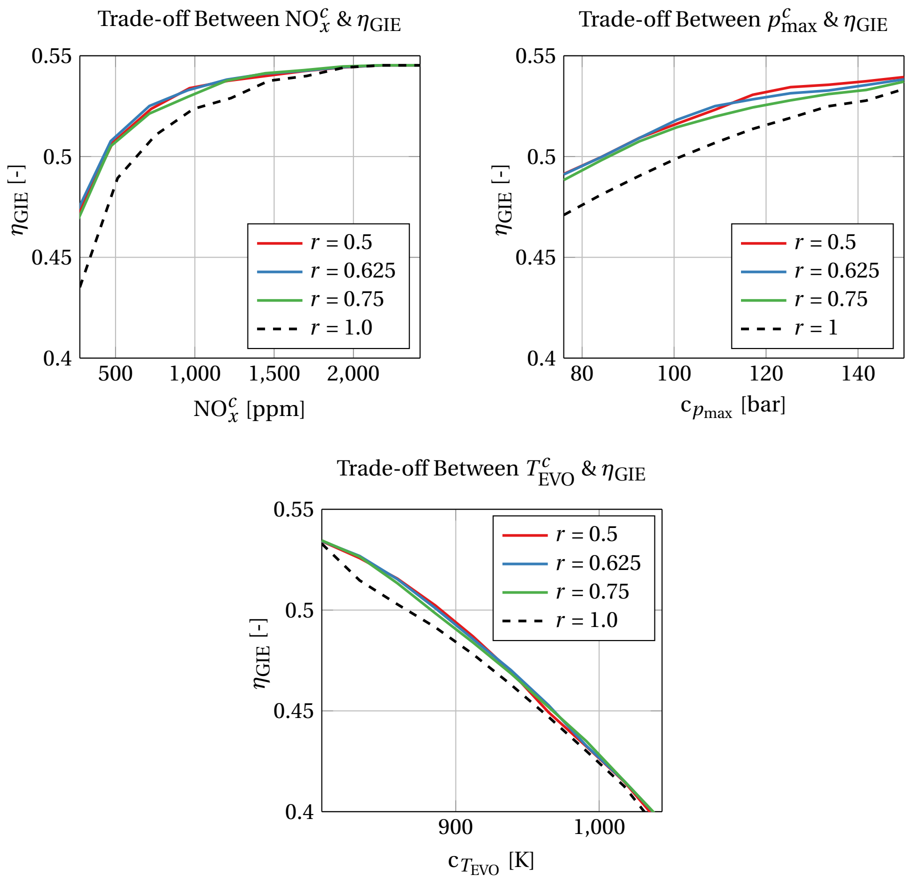

Figure 10.5 Simulated x_c / η_{GIE} efficiency trade-offs for different r. Multiple combustion timings can increase η_{GIE} by up to 4 % with respect to NO_x^c and p_{max}^c, and 2 % with respect to T_{EVO}^c.

approach taken was to instead use the combustion-detection method presented in Chapter 4 to detect θ_{CT}^x from the pilot, main and post injections. In this method, the heat-release rate $dQ_c/d\theta$ is first computed. Then, the M most significant peaks above a threshold level are detected, where M is the number of injections used. The crank angles at the detected peaks then constitute the combustion timings θ_{CT}. A minimum distance between detected peaks was introduced in order to not detect multiple peaks from one injection. This could otherwise occur if a single-injection heat-release rate has multiple peaks, which is common for conventional diesel combustion.

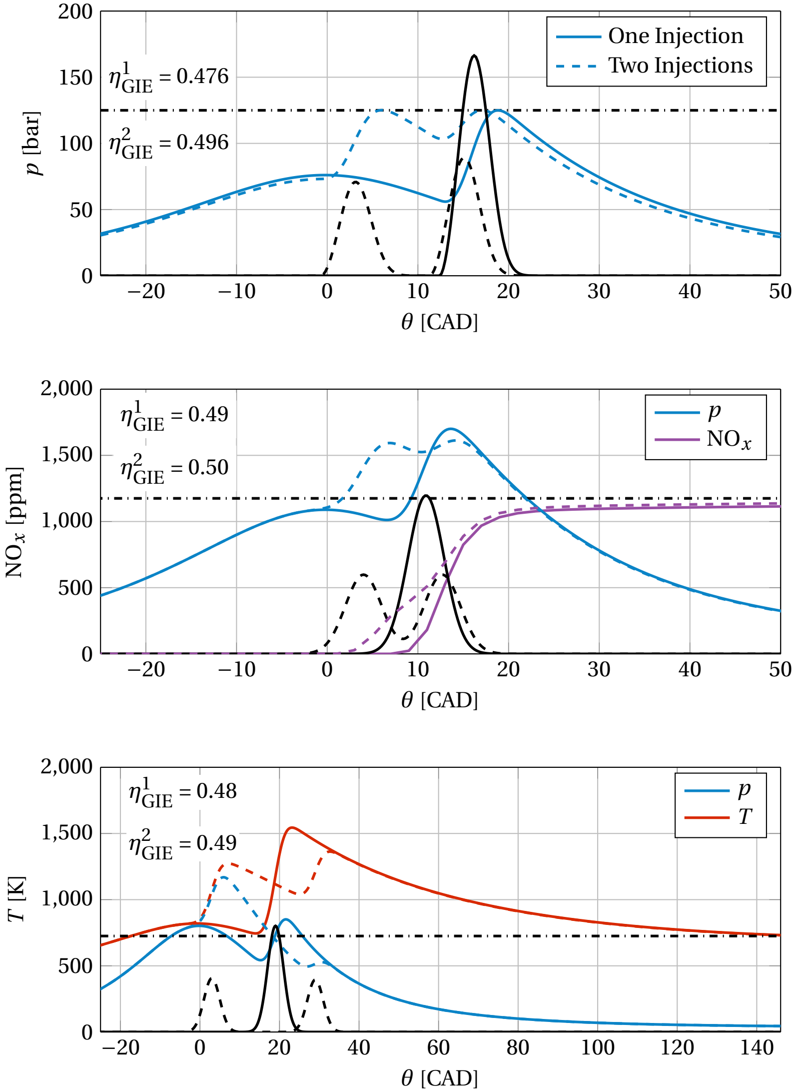

Figure 10.6 A physical explanation for the difference between one (1) and two (2) injections with arbitrary p^c_{max} (upper), NO^c_x (middle) and T^c_{EVO} (lower). For p_{max} and NO_x constraints, two injections give a more distributed heat-release. A distributed heat release lowers the peak pressure and gives a slower NO_x-formation rate, which allows for an effective or mean combustion timing closer to TDC. For the T_{EVO} constraint, the late injection provides a sufficient T_{EVO} increase for the first injection to be timed optimally.

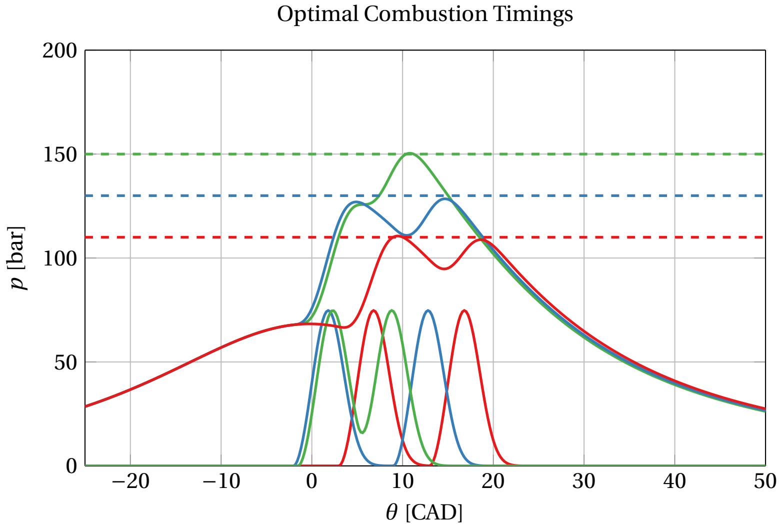

Figure 10.7 Efficiency-optimal combustion timings with respect to $p_{\max}$ constraints and $r = 0.5$ in Fig. 10.2. When the constraint becomes increasingly stringent, it is optimal to keep one combustion timing close to TDC and then delay the latter. For a very stringent constraint the early combustion timing is also delayed.

Small fuel quantities are not always sufficient to generate heat-release. For instance, in Chapter 8, a small pilot was only used to enhance the reactivity of the main-injection and did not generate a separate heat-release impulse. The detection method therefore only allocated detected θ_{CT}^{x} to injections with sufficient fuel mass. Values in the range of 15-30 mg were used as lower limits in the engine experiments presented below. When a single combustion timing was expected, θ_{50} was used instead of θ_{CT} as a combustion-timing indicator. A similar procedure was applied for detecting the peak pressure levels generated by the pilot and main injection $p_{\max}^{1}$, $p_{\max}^{2}$ which are necessary quantities for the controller to fulfill $p_{\max}^{c}$. The motored pressure curve was first subtracted from p before detecting $p_{\max}^{1,2}$, to not detect the pressure peak generated by compression.

Without Active Constraints

Without active constraints, the main combustion timing θ_{CT}^{2} was set to follow an efficient set point θ_{CT}^{r} through $\theta_{\mathrm{SOI}}^{2}$ adjustment. The engine load p_{IMEPn} was controlled with m_f^{tot} for tracking of a set point p_{IMEPn}^{r}. This controller behavior

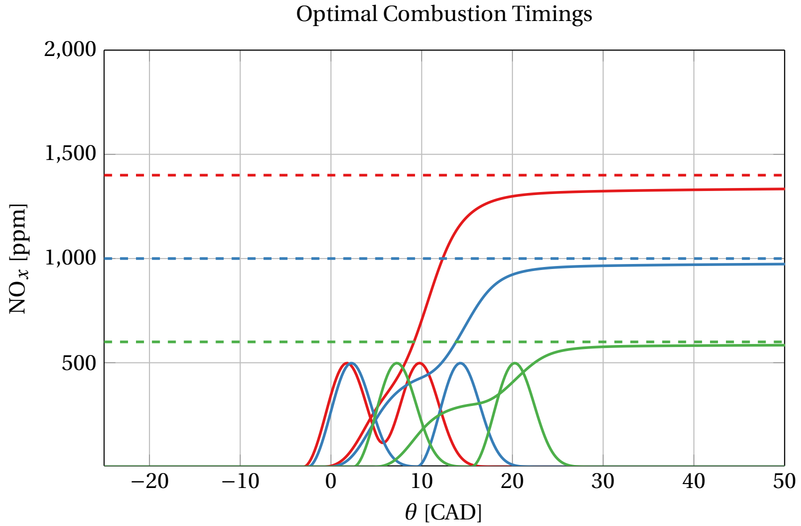

Figure 10.8 Efficiency-optimal combustion timings with respect to the NO_x-emission constraints in Fig. 10.3. When NO_x^c becomes increasingly stringent, it is optimal to keep the early combustion timing close to TDC and then delay the latter. For a very restrictive constraint, the early combustion timing is also delayed.

was obtained by the following cycle-to-cycle PI controller

$$\begin{aligned}\theta^2_{\mathrm{SOI}}(k+1) &= \theta^2_{\mathrm{SOI}}(k) + k_p^{\theta_{\mathrm{CT}}}(e_{\theta^2_{\mathrm{CT}}}(k) - e_{\theta^2_{\mathrm{CT}}}(k-1)) + k_I^{\theta_{\mathrm{CT}}} e_{\theta^2_{\mathrm{CT}}}(k-1)\\ m_f^{\mathrm{tot}}(k+1) &= m_f^{\mathrm{tot}}(k) + k_p^{p_{\mathrm{IMEPn}}}(e_{p_{\mathrm{IMEPn}}}(k) - e_{p_{\mathrm{IMEPn}}}(k-1))\\ &\quad + k_I^{p_{\mathrm{IMEPn}}} e_{p_{\mathrm{IMEPn}}}(k-1)\end{aligned} \tag{10.18}$$

where k is cycle index, $e_{p_{\mathrm{IMEPn}}}$ and $e_{\theta^2_{\mathrm{CT}}}$ are p_{IMEPn} and θ_{CT} errors

$$\begin{aligned}e_{\theta^2_{\mathrm{CT}}}(k) &= \theta^r_{\mathrm{CT}}(k) - \theta_{\theta^2_{\mathrm{CT}}}(k)\\ e_{p_{\mathrm{IMEPn}}}(k) &= p^r_{\mathrm{IMEPn}}(k) - p_{\mathrm{IMEPn}}(k)\end{aligned} \tag{10.19}$$

Pressure Constraint

The main-injection timing θ^2_{SOI} was adjusted if $p^c_{\max}$ was violated to keep the pressure peak corresponding to the main injection, $p^2_{\max}$, below $p^c_{\max}$. This behavior was obtained by the following controller

$$\theta^2_{\mathrm{SOI}}(k+1) = \begin{cases}\theta^2_{\mathrm{SOI}}(k) + \Delta\mathrm{PI}_{\mathrm{CT}}(e_{\theta^2_{\mathrm{CT}}}(k)) & \text{if } p^2_{\max}(k) < p^c_{\max}\\ \theta^2_{\mathrm{SOI}}(k) + \Delta\mathrm{PI}_{p_{\max}}(e_{p^2_{\max}}(k)) & \text{otherwise}\end{cases} \tag{10.20}$$

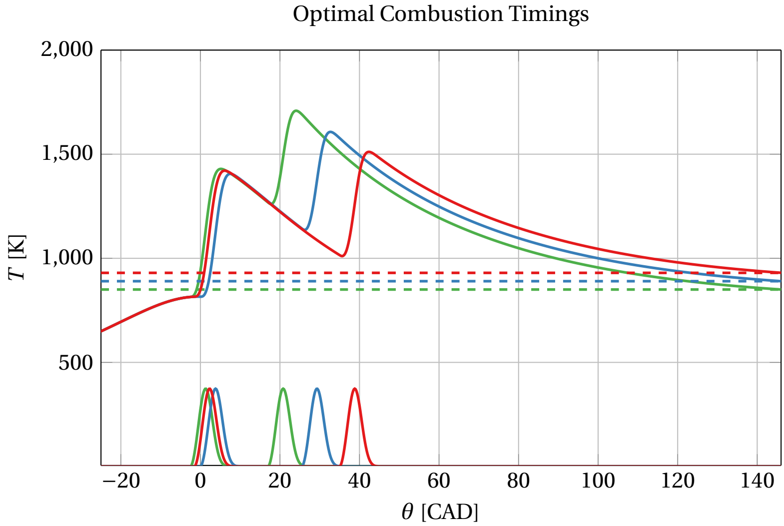

Figure 10.9 Efficiency-optimal combustion timings with respect to the T_{EVO}-emission constraints presented in Fig. 10.9. When the T_{EVO} constraint becomes increasingly stringent, it is optimal to keep the first injection timing combustion close to TDC and then delay the latter.

where

$$e_{p^2_{\max}}(k) = p^2_{\max}(k) - p^c_{\max} \tag{10.21}$$

and $\Delta\mathrm{PI}_x$ are combustion timing updates from two separate PI controllers on the form of (10.17). A pilot injection was also introduced if $p_{\max} > p^c_{\max}$, in order to obtain a distributed heat-release rate, see Fig. 10.7. This was done by varying r^1 according to

$$r^1(k+1) = \begin{cases} r^1(k) + k_r(r^1_* - r^1(k)) & \text{if } p_{\max}(k) > p^c_{\max} \\ r^1(k) - k_r r^1(k) & \text{otherwise} \end{cases} \tag{10.22}$$

where r^1_* is a predefined set point. Furthermore, once the pilot injection was introduced, a pilot-injection controller was used to keep $p^1_{\max}$ below $p^c_{\max}$

$$\theta^1_{\mathrm{SOI}}(k+1) = \begin{cases} \theta^1_{\mathrm{SOI}}(k) + \Delta\mathrm{PI}_{\mathrm{CT}}(e_{\theta^1_{\mathrm{CT}}}(k)) & \text{if } p^1_{\max}(k) < p^c_{\max} \\ \theta^1_{\mathrm{SOI}}(k) + \Delta\mathrm{PI}_{p_{\max}}(e_{p^1_{\max}}(k)) & \text{otherwise} \end{cases} \tag{10.23}$$

where

$$\begin{aligned} e_{\theta^1_{\mathrm{CT}}}(k) &= \theta^r_{\mathrm{CT}}(k) - \theta^1_{\mathrm{CT}}(k) \\ e_{p^1_{\max}} &= p^1_{\max} - p^c_{\max} \end{aligned} \tag{10.24}$$

NO_x Constraint

NO_x-constraint fulfillment was handled similarly

$$\theta^2_{\mathrm{SOI}}(k+1) = \begin{cases} \theta^2_{\mathrm{SOI}}(k) + \Delta \mathrm{PI}_{\mathrm{CT}}(e_{\theta^2_{\mathrm{CT}}}(k)) & \text{if } \mathrm{NO}_x(k) < \mathrm{NO}_x^c \\ \theta^2_{\mathrm{SOI}}(k) + \Delta \mathrm{PI}_{\mathrm{NO}_x}(e_{\mathrm{NO}_x}(k)) & \text{otherwise} \end{cases} \tag{10.25}$$

where

$$e_{\mathrm{NO}_x}(k) = \mathrm{NO}_x(k) - \mathrm{NO}_x^c \tag{10.26}$$

A pilot injection was also introduced if $\mathrm{NO}_x(k) > \mathrm{NO}_x^c$ to obtain a distributed heat-release rate according to Fig. 10.8

$$r^1(k+1) = \begin{cases} r^1(k) + k_r(r^1_* - r^1(k)) & \text{if } \mathrm{NO}_x(k) > \mathrm{NO}_x^c \\ r^1(k) - k_r r^1(k) & \text{otherwise} \end{cases} \tag{10.27}$$

Furthermore, as the pilot injection was introduced, the pilot-injection controller

$$\theta^1_{\mathrm{SOI}}(k+1) = \begin{cases} \theta^1_{\mathrm{SOI}}(k) + \Delta \mathrm{PI}_{\mathrm{CT}}(e_{\theta^1_{\mathrm{CT}}}(k)) & \text{if } \mathrm{NO}_x(k) < \mathrm{NO}_x^c \\ \theta^1_{\mathrm{SOI}}(k) + \Delta \mathrm{PI}_{\mathrm{NO}_x}(e_{\mathrm{NO}_x}(k)) & \text{otherwise} \end{cases} \tag{10.28}$$

was used to adjust θ^1_{SOI} for constraint fulfillment.

Temperature Constraint

The exhaust temperature T_{ex} was controlled by adjusting the post injection to obtain the configurations presented in Fig 10.9

$$\begin{aligned} r^3(k+1) &= \begin{cases} r^3(k) + k_r(r^3_* - r^3(k)) & \text{if } T_{\mathrm{ex}}(k) < T_{\mathrm{ex}}^c \\ r^3(k) - k_r r^3(k) & \text{otherwise} \end{cases} \\ \theta^3_{\mathrm{SOI}}(k+1) &= \begin{cases} \theta^3_{\mathrm{SOI}}(k) + \Delta \mathrm{PI}_{\mathrm{CT}}(e_{\theta^3_{\mathrm{CT}}}(k)) & \text{if } T_{\mathrm{ex}}(k) > T_{\mathrm{ex}}^c \\ \theta^3_{\mathrm{SOI}}(k) + \Delta \mathrm{PI}_{T_{\mathrm{ex}}}(e_{T_{\mathrm{ex}}}(k)) & \text{otherwise} \end{cases} \end{aligned} \tag{10.29}$$

where

$$\begin{aligned} e_{\theta^3_{\mathrm{CT}}}(k) &= \theta^r_{\mathrm{CT}}(k) - \theta^3_{\mathrm{CT}}(k) \\ e_{T_{\mathrm{ex}}} &= T_{\mathrm{ex}}^c - T_{\mathrm{ex}} \end{aligned} \tag{10.30}$$

p_{IMEPn} Control

The engine load was controlled by adjusting the total injected fuel mass using the controller

$$m_f^{\mathrm{tot}}(k+1) = m_f^{\mathrm{tot}}(k) + \Delta \mathrm{PI}_{p_{\mathrm{IMEPn}}}(e_{p_{\mathrm{IMEPn}}}(k)) \tag{10.31}$$

The commanded fuel was then distributed according m_f^{tot}, r^1 and r^3, and fuel-injection durations were computed using the injector map in (10.6).

Saturation

Saturation limits were introduced to enforce

$$\boldsymbol{u} \in \mathbb{U} \tag{10.32}$$

This was done by saturating the pilot and post injection timings θ_{SOI}^1, θ_{SOI}^3 to avoid overlap with the main injection. Unfortunately, this could lead to deadlock and constraint violation for $p_{\mathrm{max}}^1(k)$ when regulating $p_{\mathrm{max}}^{1,2}$. A remedy to this problem was to reduce r^1 when $p_{\mathrm{max}}^1(k) > p_{\mathrm{max}}^2(k)$

$$r^1(k+1) = r^1(k) - k_r r^1(k) \quad \text{if } p_{\mathrm{max}}^1(k) > p_{\mathrm{max}}^2(k) \tag{10.33}$$

Additional minimum and maximum limits on $\theta_{\mathrm{SOI}}^{1,2,3}$, m_f^{tot} and $r^{1,3}$ were introduced as safety margins to ensure feasible injection timings and durations.

Slack Variables

Slack variables ϵ_x were added to the constraint conditions above

$$\begin{aligned} p_{\mathrm{max}}(k) &> p_{\mathrm{max}}^c - \epsilon_{p_{\mathrm{max}}} \\ \mathrm{NO}_x(k) &> \mathrm{NO}_x^c - \epsilon_{\mathrm{NO}_x} \\ T_{\mathrm{ex}}(k) &< T_{\mathrm{ex}}^c + \epsilon_{T_{\mathrm{ex}}} \end{aligned} \tag{10.34}$$

to avoid limit cycles around the constraint limits.

Summary

The controllers presented above are summarized in Algorithm 4. Here, p_{max}- and NO_x -constraint handling were merged using the max function. In this way, the controller would adjust for the constraint demanding the latest θ_{SOI}, since both p_{max} and NO_x decrease with θ_{SOI}. The notation

$$\tilde{x}_c = x^c \pm \epsilon_x \tag{10.35}$$

was introduced in Algorithm 4 to ease notation.

10.5 Experimental Evaluation

The controller in Algorithm 4 was evaluated experimentally, both in transient and steady-state operation. The different constraints were investigated separately in both cases. The controller was also compared to the single-injection controller presented in Algorithm 5. This controller delayed a single injection timing to fulfill the constraints. Controller parameters used are presented in Table 10.2, where the parameters were tuned in favor of robustness over convergence rate.

Algorithm 4 Merged Constraint Controller

Pilot-Injection Controller

if $p_{\max}(k) > \tilde{p}^{c}_{\max} \vee \mathrm{NO}_x(k) > \tilde{\mathrm{NO}}^{c}_{x}$ **then**

  $\theta^{1}_{\mathrm{SOI}}(k+1) = \theta^{1}_{\mathrm{SOI}}(k) + \max\big(\Delta\mathrm{PI}_{p_{\max}}(e_{p^{1}_{\max}}(k)),\ \Delta\mathrm{PI}_{\mathrm{NO}_x}(e_{\mathrm{NO}_x}(k))\big)$

  if $p_{\max}(k) > \tilde{p}^{c}_{\max} \wedge p^{1}_{\max}(k) > p^{2}_{\max}(k)$ **then**

    $r^{1}(k+1) = r^{1}(k) - k_r r^{1}(k)$

  else

    $r^{1}(k+1) = r^{1}(k) + k_r(r^{1}_{*} - r^{1}(k))$

  end if

else

  $\theta^{1}_{\mathrm{SOI}}(k+1) = \theta^{1}_{\mathrm{SOI}}(k) + \Delta\mathrm{PI}_{\mathrm{CT}}(e_{\theta^{1}_{\mathrm{CT}}}(k))$

  $r^{1}(k+1) = r^{1}(k) - k_r r^{1}(k)$

end if

Main-Injection Controller

if $p_{\max}(k) > \tilde{p}^{c}_{\max} \vee \mathrm{NO}_x(k) > \tilde{\mathrm{NO}}^{c}_{x}$ **then**

  $\theta^{2}_{\mathrm{SOI}}(k+1) = \theta^{2}_{\mathrm{SOI}}(k) + \max\big(\Delta\mathrm{PI}_{p_{\max}}(e_{p^{2}_{\max}}(k)),\ \Delta\mathrm{PI}_{\mathrm{NO}_x}(e_{\mathrm{NO}_x}(k))\big)$

else

  $\theta^{2}_{\mathrm{SOI}}(k+1) = \theta^{2}_{\mathrm{SOI}}(k) + \Delta\mathrm{PI}_{\mathrm{CT}}(e_{\theta^{2}_{\mathrm{CT}}}(k))$

end if

Post-Injection Controller

if $T_{\mathrm{ex}}(k) < \tilde{T}_{\mathrm{ex}}$ **then**

  $\theta^{3}_{\mathrm{SOI}}(k+1) = \theta^{3}_{\mathrm{SOI}}(k) + \Delta\mathrm{PI}_{T_{\mathrm{ex}}}(e_{T_{\mathrm{ex}}}(k))$

  $r^{3}(k+1) = r^{3}(k) + k_r(r^{3}_{*} - r^{3}(k))$

else

  $\theta^{3}_{\mathrm{SOI}}(k+1) = \theta^{3}_{\mathrm{SOI}}(k) + \Delta\mathrm{PI}_{\mathrm{CT}}(e_{\theta^{3}_{\mathrm{CT}}}(k))$

  $r^{3}(k+1) = r^{3}(k) - k_r r^{3}(k)$

end if

Algorithm 5 Single Injection Controller

Main-Injection Controller

if $p_{\max}(k) > \tilde{p}^c_{\max} \lor \mathrm{NO}_x(k) > \tilde{\mathrm{NO}}^c_x \lor T_{\mathrm{ex}}(k) < \tilde{T}^c_{\mathrm{ex}}$ **then**

$\quad \Delta\theta^2_{\mathrm{SOI}}(k) = \max\Big(\Delta\mathrm{PI}_{p_{\max}}(e_{p^2_{\max}}(k)),\ \Delta\mathrm{PI}_{\mathrm{NO}_x}(e_{\mathrm{NO}_x}(k)),\ \Delta\mathrm{PI}_{T_{\mathrm{ex}}}(e_{T_{\mathrm{ex}}}(k))\Big)$

$\quad \theta^2_{\mathrm{SOI}}(k+1) = \theta^2_{\mathrm{SOI}}(k) + \Delta\theta^2_{\mathrm{SOI}}(k)$

else

$\quad \theta^2_{\mathrm{SOI}}(k+1) = \theta^2_{\mathrm{SOI}}(k) + \Delta\mathrm{PI}_{\mathrm{CT}}(e_{\theta^2_{\mathrm{CT}}}(k))$

end if

Transient Operation

$\boldsymbol{p^c_{\max}}$ The ability to handle $p_{\max}$ constraints was evaluated with $p^c_{\max} = 75$. Experimental results with p^r_{IMEPn} step changes are presented in Fig. 10.10, where p_{IMEPn} increased from 4 to 10 bar in 10 cycles as p^r_{IMEPn} was increased.

At $p_{\mathrm{IMEPn}} = 10$ bar with $\theta^2_{\mathrm{CT}} = \theta^r_{\mathrm{CT}}$, $p_{\max}$ violated $p^c_{\max}$. To fulfill $p^c_{\max}$, the controller increased r^1 and delayed θ^2_{CT}, and reached a new injection configuration in 50 cycles. The controller converged to the initial conditions once p^r_{IMEPn} was decreased.

Cycle-resolved data at cycles 1250 and 1450 are presented in Fig. 10.11. At cycle 1250, a single injection was used where $p_{\mathrm{IMEPn}} = 4$ bar, and $\theta^2_{\mathrm{CT}} = \theta^r_{\mathrm{CT}} = 8$ CAD. At cycle 1450, with $r^1 = 0.5$, the injection timings were adjusted to fulfill $p^c_{\max}$. The red and blue vertical lines indicate detected θ^1_{CT} and θ^2_{CT}, and θ^r_{CT} is indicated by the horizontal dashed line.

$\boldsymbol{NO_x{}^c}$ Fulfillment of $\mathrm{NO}^c_x = 800$ ppm is presented in Fig. 10.12. In this figure, the controller was compared to the single-injection controller in Algorithm 5, which is indicated in purple. The combustion timings were delayed when NO_x was increased due to positive p^r_{IMEPn} step changes. The double-injection controller introduced a pilot injection when NO^c_x was violated, and an additional com-

Table 10.2 Controller parameters used in experiment.

$k_p^{\theta_{\mathrm{CT}}}$ [-]	0.1	$k_I^{\theta_{\mathrm{CT}}}$ [-]	0.15
$k_p^{\mathrm{NO}_x}$ [CAD/ppm]	10	$k_I^{\mathrm{NO}_x}$ [CAD/ppm]	15
$k_p^{p_{\max}}$ [CAD/bar]	0.04	$k_I^{p_{\max}}$ [CAD/bar]	0.05
$k_p^{T_{\mathrm{ex}}}$ [CAD/K]	0.3	$k_I^{T_{\mathrm{ex}}}$ [CAD/K]	0.35
$k_p^{m_f}$ [mg/bar]	1.5	$k_I^{m_f}$ [mg/bar]	2

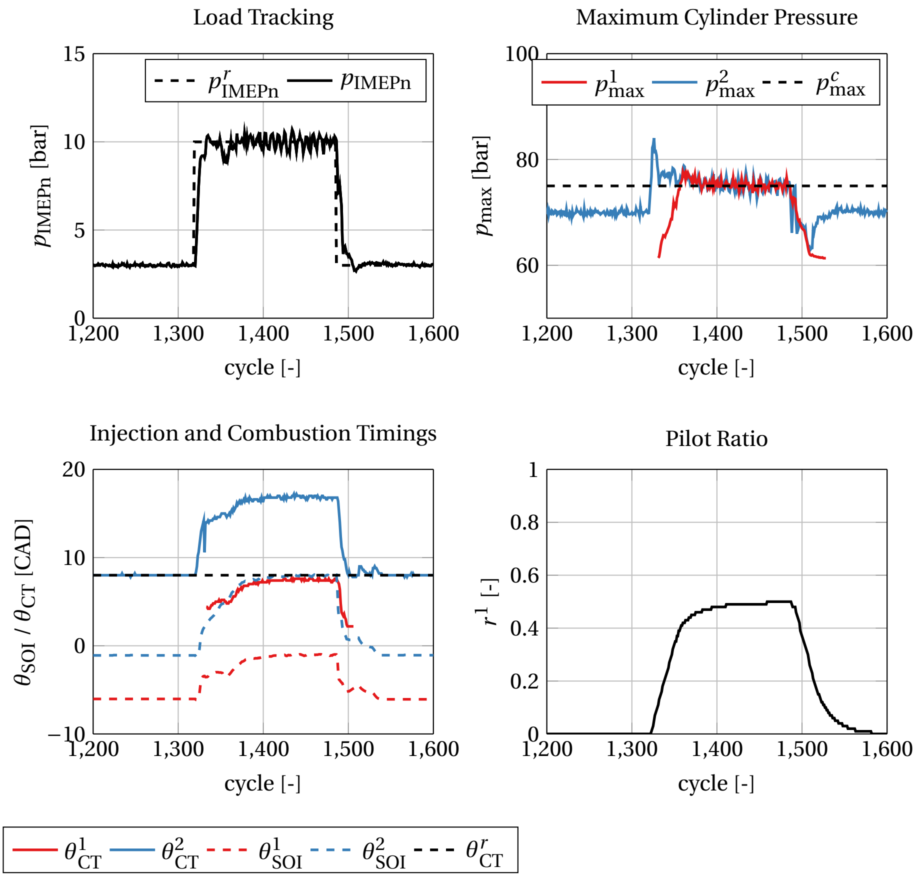

Figure 10.10 Experimental results showing $p_{\max}$ constraint handling. As p^r_{IMEPn} was increased from 4 to 10 bar, $p_{\max}$ with $\theta_{50} = 8$ violated $p^c_{\max}$. Constraint violation forced r^1 to increase and θ^2_{CT} to be delayed. The controller converged to the initial conditions once p^r_{IMEPn} was decreased.

bustion timing (red) was detected. The fuel-masses presented are the fuel masses demanded by the controllers, and not the actual injected fuel mass. Both controllers had comparable p_{IMEPn} response times of 10 cycles and injection-timing settling times of 25 cycles. The double-injection controller had a slightly larger NO_x overshoot.

T^c_{ex} Fulfillment of $T^c_{\mathrm{ex}} = 240°\mathrm{C}$ is presented in Fig. 10.13. The combustion timing was delayed for the single-injection controller in order to fulfill the constraint when T_{ex} was decreased due to negative p^r_{IMEPn} step changes. A post in-

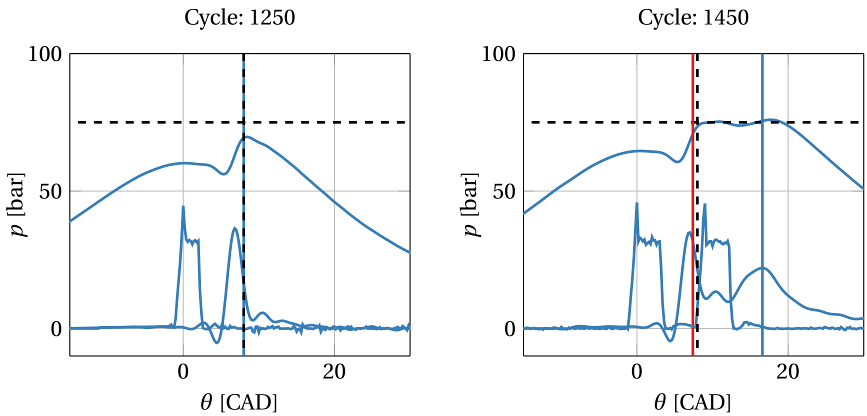

Figure 10.11 Cycle-resolved data belonging to cycle 1250 and 1450 in Fig. 10.10. The vertical lines indicate $\theta_{\text{CT}}^{1,2}$ and θ_{CT}^{r}. The dashed horizontal lines indicate $p_{\max}^{c}$.

jection was introduced by the double-injection controller and two combustion timings were detected. The T_{ex} increase caused by the post injection allowed θ_{CT}^{2} to follow θ_{CT}^{r}. The T_{ex} loop was considerably slower than the other loops due to heat-transfer dynamics in the exhaust system with T_{ex} settling times of approximately 100-200 cycles.

Steady-State Operation and Trade-offs

The controller-design effect on emission and efficiency trade-offs was evaluated in steady-state. An efficiency improvement with respect to $p_{\max}^{c} = 95$ bar is presented in Fig. 10.14 where the constraint was fulfilled with one (blue) and two (red) injections. Two injections allowed for a combustion timing closer to TDC which increased η_{GIE} with 5 %. A drawback with the double-injection strategy was the significant increase in soot emissions.

More detailed NO_x^c and T_{ex}^c trade-offs with respect to η_{NIE}, NO_x, soot and HC emissions are presented in Figs. 10.15 and 10.16. Pressure and heat-release rates for the different x^c sweeps are presented in Fig. 10.17. The results in Fig. 10.15 show that the suggested controller improved the NO_x trade-offs with η_{NIE} and HC, and worsened the trade off with respect to soot and also partly with T_{ex}. Figure 10.16 shows that the suggested controller partly worsened the T_{ex} trade-off with respect to η_{NIE} and NO_x for high T_{ex}^c, but improved the HC trade-off. The worsened trade-off with η_{NIE} contradicts the simulation results presented in Fig. 10.4.

The overall soot increase with two injections is believed to be caused by shortened mixing times and fuel injection during combustion. The improved HC

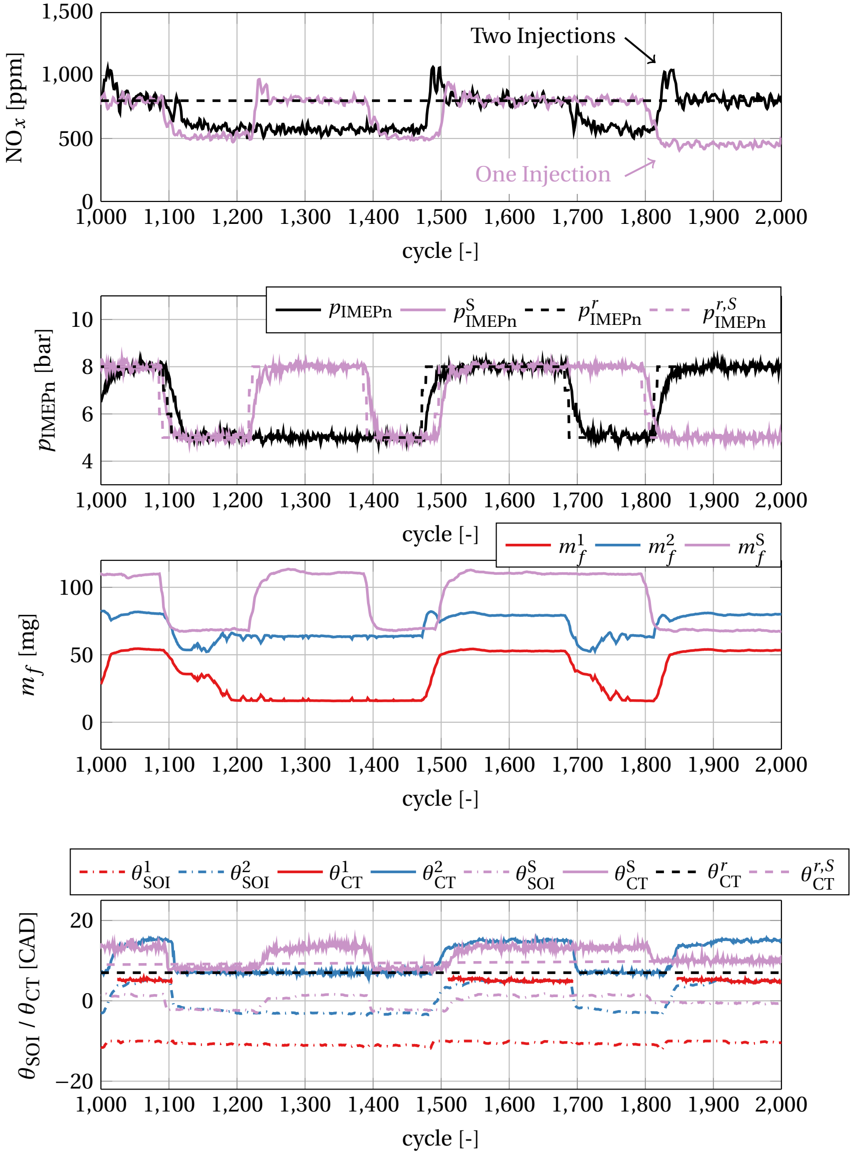

Figure 10.12 A transient NO$_x$-control experiment with a comparison between the single- (purple, S) and double-injection controller. The combustion timings were delayed when NO$_x$ increased due to positive p^{r}_{IMEPn} step changes. A pilot injection was introduced (red) and two combustion timings were detected by the double-injection controller.

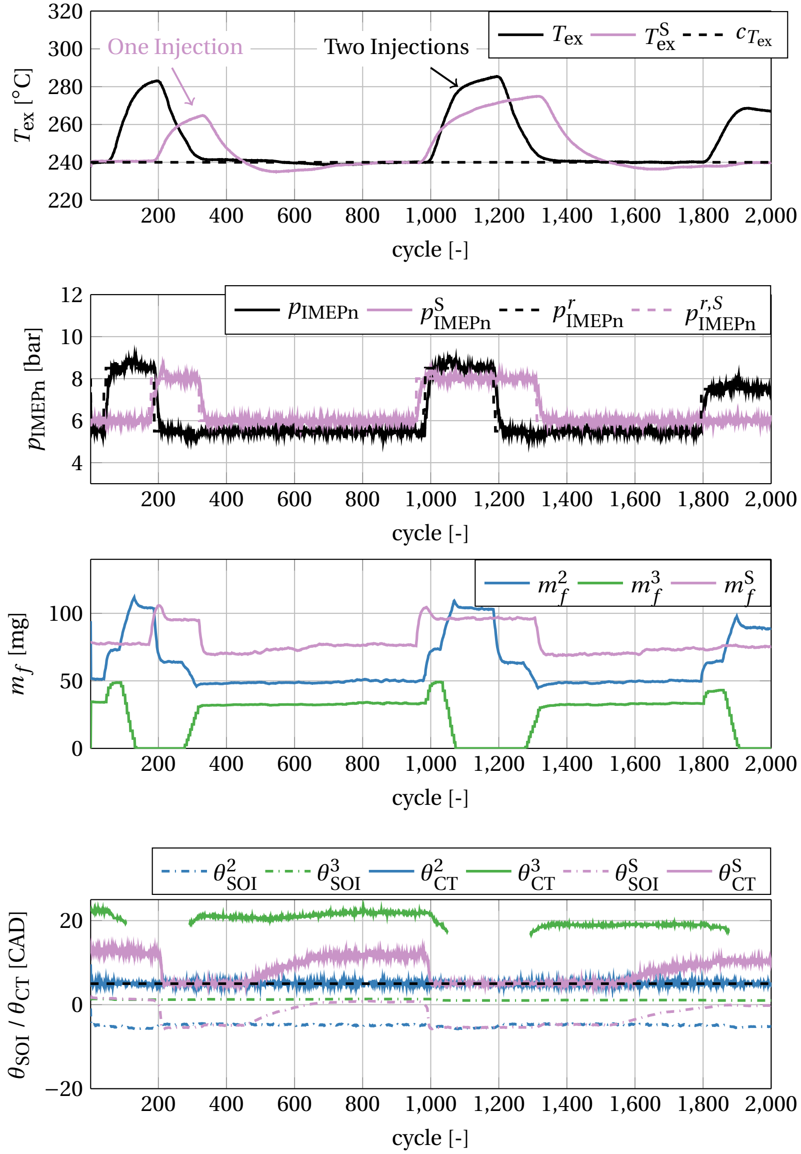

Figure 10.13 A transient T_{ex}-controller experiment with a comparison between the single- (purple) and double-injection controller. A post injection was introduced (green) and two combustion timings were detected by the double-injection controller. This enabled θ_{CT}^2 to follow θ_{CT}^r.

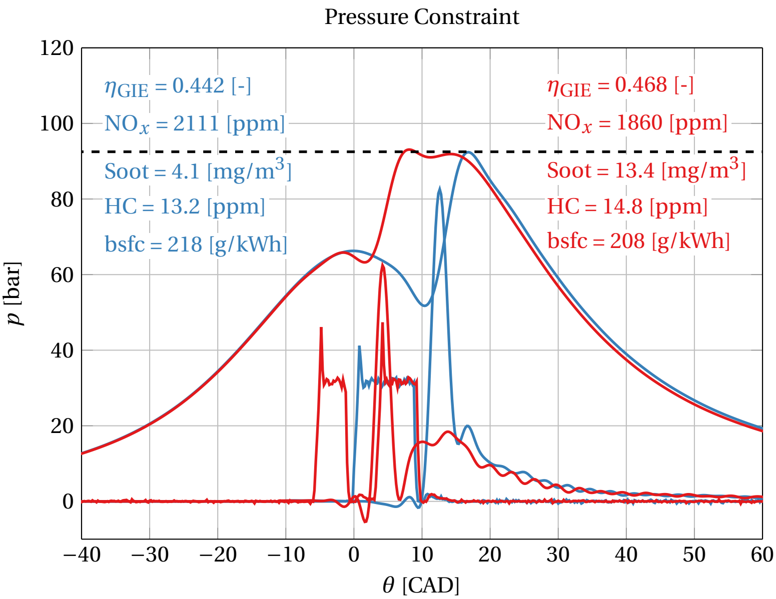

Figure 10.14 Fulfillment of $p^c_{max} = 95$ bar with one (blue) and two (red) injections. Two injections allowed for a combustion timing closer to TDC, which increased gross-indicated efficiency with 5 %. A disadvantage with the double-injection strategy was the significant increase in soot emissions.

trade-offs with two injection could be explained by the advanced combustion timing. It has also been shown that post injections can be used to aid oxidation of HC [Chartier et al., 2011].

10.6 Discussion

From the experimental results in Sec. 10.5, it can be concluded that multiple injections can increase the indicated efficiency when stringent constraints on p_{max} and NO_x are imposed. The efficiency increase was a result of the distributed heat-release rate with reduced peak in-cylinder pressure and temperature, which allowed for a more advanced effective combustion timing, see Fig. 10.6. These results agree with previous simulation and experimental work on optimal heat-release rates [Eriksson and Sivertsson, 2016; Okamoto and Uchida, 2016; Guardiola et al., 2017].

The problem of optimally calibrating multiple injection timings and durations for different engine operating points is both demanding and sensitive to disturbances. The contribution of the work presented in this chapter is a

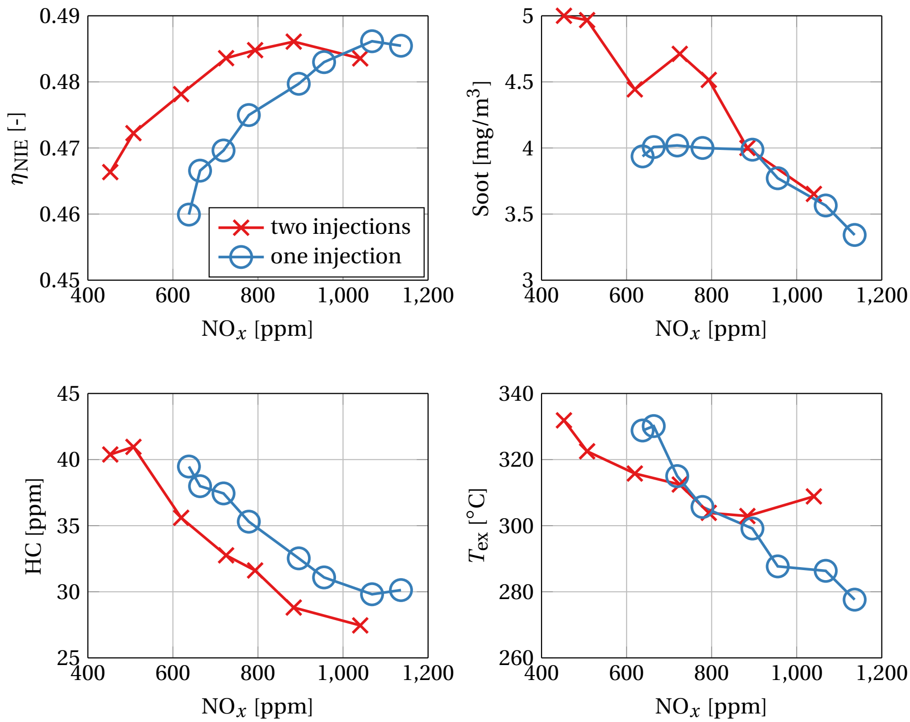

Figure 10.15 Steady-state NO_x trade-offs with the single and double-injection controller. The double-injection controller improved the NO_x trade-off with η_{NIE} by 4 %. It also improved the trade-off with HC. The double-injection controller had a worsened trade off with respect to soot, and a partly worsened trade-off with T_{ex}.

feedback controller that automatically sets the number of injections, timings and durations with pressure-sensor measurements. This allows for operation close to the constraint limits, which increases efficiency. This work differs from previous research, which have, to the author's knowledge, mainly discussed optimal heat-release rates in open loop.

The controller design was motivated by simulation results obtained from a 0D model with a bimodal heat-release rate, which showed a 2-4 % efficiency increase with respect to constraints on p, NO_x and T_{EVO}. The model was mainly chosen for its simplicity. This study should be redone with respect to more detailed fuel-injection, mixing and combustion models to determine if the observed trends still hold when additional effects are considered. This study could also be extended to cover a larger engine operating range, to evaluate how constraint

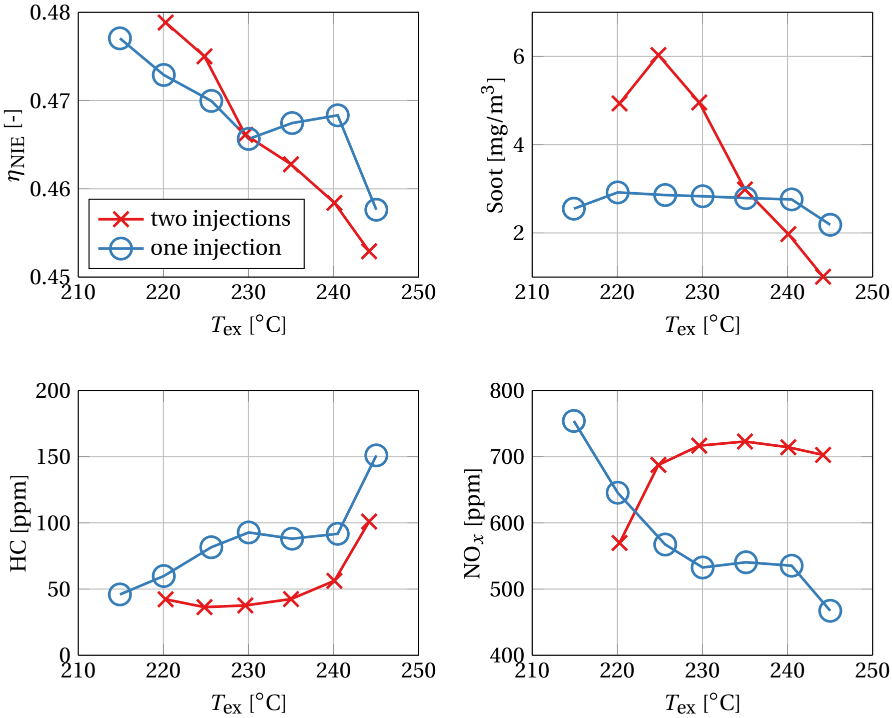

Figure 10.16 Steady-state T_{ex} trade-offs with the single and double-injection controller. The results show that the double-injection controller worsened the T_{ex} trade-off with η_{NIE} and NO_x for high T_{ex}^c, but improved the trade-off with HC emissions.

trade-offs vary with engine load and speed.

A hybrid PI controller was designed with the objective of finding the optimal injection configurations computed in simulation. The controller design was motivated by its simplicity, where tuning parameters were PI controller gains and constraint thresholds for varying the number of injections. A drawback with a hybrid controller design of this kind is however the difficulty of finding conditions for stability, which in this work, was obtained through manual tuning. Constraint limits were chosen arbitrarily in the experimental evaluation to demonstrate that the desired controller behavior was achieved. Suggested future work is to set these limits according to actual engine constraints.

The experimental controller evaluation showed injection-timing settling times of 25-50 cycles with respect to constraints on $p_{\max}$ and NO_x during p_{IMEPn} changes of 10 cycles. Injection-timing settling times during T_{ex} constraint ful-

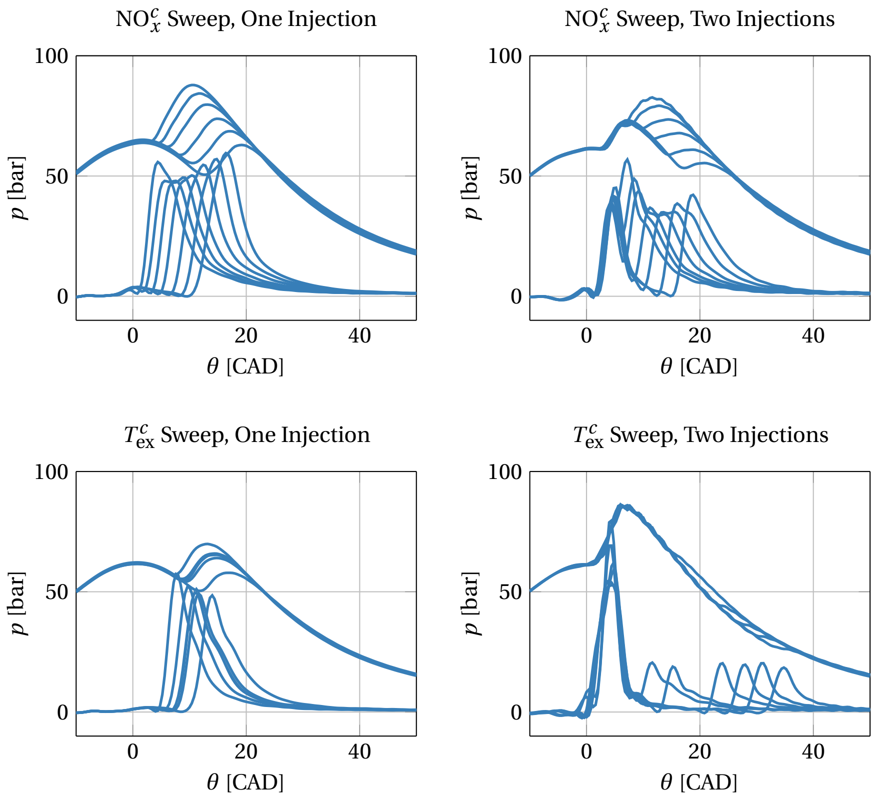

Figure 10.17 Pressure and heat-release rates for the constraint sweeps presented in Figs. 10.15 and 10.16.

fillment were 100-200 cycles. These settling times were comparable to those of the single-injection controller, that adjusted one injection timing to fulfill constraints.

Steady-state experiments showed a 4-5 % efficiency increase with respect to $p_{\max}$ and NO_x constraints, and a 1.7 % efficiency decrease with respect to T_{ex} constraints. The decrease in efficiency with T_{ex}^c contradicted the simulation results in Sec. 10.3. One possible explanation for the efficiency decrease could be the assumption of a constant heat-release shape with combustion timing. In reality, heat-release rates and combustion efficiency decrease with combustion timing, which penalize the efficiency of late post injections. It was however not easy to verify this from the heat-release rates in Fig. 10.17. Despite this fact, the controller suggested provides a framework for how to introduce post injections when favorable. Results presented in [Honardar et al., 2011] showed that a post injection could provide a small fuel-consumption reduction compared to that of a delayed main injection when increasing the exhaust temperature.

Although the controller design was motivated for its simplicity, the controller complexity became rather involved, see Algorithm 4. An alternative approach would be to design a model predictive controller that solves (10.10) on-line. The MPC framework could then provide an increased flexibility when adding and removing constraints and injections in (10.10). Such a controller design is considered in Chapter 12.

10.7 Conclusions

A controller was designed and implemented for increased thermodynamic efficiency when constraints on p_{max}, NO_x and T_{ex} are imposed. The controller design was motivated by previous research on multiple injections and a presented 0D-simulation study that showed a 2-4 % efficiency increase when introducing an additional injection. These results suggested that the controller should adjust the number of injections for efficient constraint fulfillment. This was done by introducing a pilot injection when encountering active p_{max} and NO_x constraints, whilst exhaust-temperature constraints were handled with a post injection. A single injection was found optimal when no constraints were active.

The desired controller behavior was obtained with a hybrid, multiple-input multiple-output PI controller that utilized feedback from in-cylinder pressure measurements, a NO_x-emission model that functioned as a virtual sensor, and measured exhaust temperature. The suggested controller was experimentally evaluated, where it showed comparable transient performance to that of a single-injection controller. The controller exhibited improved p_{max} / η_{NIE} and NO_x / η_{NIE} trade-offs with a 4-5 % increase in η_{NIE}. The controller also showed a worsened T_{ex} / η_{NIE} trade-off with a 1.7 % decrease in η_{NIE}. Increased soot emissions levels with two injections were also observed.

11

Pressure Prediction and Efficiency Optimization

11.1 Introduction

Combustion timing has traditionally been controlled in open loop by means of experimentally calibrated injection-timing maps [Guzella and Onder, 2009]. This approach requires a considerable calibration effort and can be sensitive to variations in hardware and fuel properties, especially in low-temperature combustion modes. Experimental results in the previous chapters of this thesis have shown that closed-loop combustion-timing control can be used to accurately track combustion-timing set points and make the combustion timing robust to disturbances.

Closed-loop combustion-timing controllers can be divided into two subgroups, one where the controller tracks a predefined combustion-timing set point, where set-point optimization is considered to be a separate task. Examples of such controllers were discussed in chapters 6, 7 and 9, where PI control and MPC were used for set-point tracking. Then, there are controllers that instead adjust the combustion timing to directly fulfill higher-level performance targets, such as emission-limit fulfillment and efficiency maximization. An example of a high-level performance controller was presented in [Karlsson et al., 2010], where a dynamical black-box model related the injection timing to p_{IMEPg}, $dp_{\max}$ and NO_x emissions to minimize fuel consumption subject to specified output constraints. Similar data-driven approaches were presented in [Hafner et al., 2000; Atkinson et al., 2009]. Extremum-seeking control is another example of a data-driven controller design that aims to fulfill higher-level specifications. Extremum-seeking control has previously been used to find efficiency-optimal combustion timings through set-point perturbation, see [Lewander et al. 2012]. This technique was also investigated by Killingsworth et al. [2009] and Hellström et al. [2013], in HCCI- and spark-ignition engines, respectively.

A desirable controller feature would be to utilize physical knowledge in the combustion-timing optimization. However, the model complexity needed to describe the steps from fuel injection to heat-release and cylinder pressure makes the design and implementation of such a controller difficult. Approximate modeling approaches are therefore needed to simplify the controller design.

This chapter introduces a physics-based cylinder-pressure controller that takes advantage of the estimated heat-release rate to predict how the cylinder pressure varies with fuel-injection timing. This method allows for high-level combustion-timing control, and keeps modeling complexity at a manageable level. Predicted pressure variation is computed with a linearized 0D model, where the linearization is conducted with respect to the previous engine-cycle pressure and heat-release rate. The predicted cylinder-pressure variation is then used by the controller to maximize indicated efficiency without violating cylinder-pressure constraints.

The controller algorithm is described in Sec. 11.2. The prediction method and closed-loop performance is then experimentally evaluated in Sec. 11.3, together with a parameter-sensitivity analysis. Discussion and conclusions are given in Secs. 11.4 and 11.5.

11.2 Controller Description

The cycle-to-cycle controller can be summarized in three steps:

1. First, the heat-release rate $dQ_c/d\theta$ is estimated from the previous-cycle pressure signal using (4.1).

2. Then, the predicted pressure variation with respect to a crank-angle shift $\Delta\theta$ in $dQ_c/d\theta$ is computed. The pressure variation is computed by linearizing the cylinder-pressure model in (2.9), with respect to the previous-cycle cylinder pressure and $dQ_c/d\theta$.

3. Finally, the desired shift in injection timing $\Delta\theta_{\mathrm{SOI}}$ is obtained by solving an optimization problem. The optimization problem is based on the predicted cylinder pressure obtained in step 2 and aims to optimize the indicated efficiency η_{GIE}, subject to constraints on maximum cylinder pressure $p_{\max}$ and pressure-rise rate $dp_{\max}$.

Steps 1 to 3 are explained in the following sections.

Pressure Prediction

First, the controller obtains the previous-cycle cylinder pressure p^0 and computes the corresponding heat-release rate $dQ_c^0/d\theta$ using (4.1).

After computing $dQ_c^0/d\theta$, the objective is to predict how the pressure changes with combustion timing. A pressure change due to a change in combustion timing was here assumed to be equivalent to the effect of shifting $dQ_c^0/d\theta$ as a function of θ. This assumption relies on weak cycle-to-cycle dynamics and small $dQ_c^0/d\theta$-shape variations with smaller changes in combustion timing. The computed $dQ_c^0/d\theta$ is therefore shifted a crank angle $\Delta\theta$

$$\begin{aligned} \frac{dQ_c^+}{d\theta} &= \frac{dQ_c^0(\theta+\Delta\theta)}{d\theta} \\ \frac{dQ_c^-}{d\theta} &= \frac{dQ_c^0(\theta-\Delta\theta)}{d\theta} \end{aligned} \tag{11.1}$$

In-cylinder pressure curves p^+ and p^-, corresponding to $dQ_c^+/d\theta$ and $dQ_c^-/d\theta$ are then computed by linearizing the model

$$\frac{dp}{d\theta} = -\frac{\gamma}{V}\frac{dV}{d\theta}p + \frac{\gamma-1}{V}\left(\frac{dQ_c}{d\theta} - h_c A\left(\frac{pVT_{\text{IVC}}}{p_{\text{IVC}}V_{\text{IVC}}} - T_w\right)\right) \tag{11.2}$$

with respect to p at the previous-cycle pressure p^0. Constant γ and T_w were assumed to simplify computations. The linearized pressure dynamics are given by

$$\frac{d\Delta p}{d\theta} = -\left(\frac{\gamma}{V}\frac{dV}{d\theta} + \frac{\partial\mu(p^0,\theta)}{\partial p}\right)\Delta p + \frac{\gamma-1}{V}\frac{d\Delta Q_c}{d\theta} \tag{11.3}$$

where Δp is the first order deviation from p^0, $d\Delta Q_c/d\theta$ is the deviation from $dQ_c^0/d\theta$, and the nonlinear term in the heat-transfer model is denoted

$$\mu(p,\theta) = (\gamma-1)\frac{h_c A T_{\text{IVC}}}{p_{\text{IVC}}V_{\text{IVC}}}p \tag{11.4}$$

The convective heat-transfer coefficient used here is given by

$$h_c = \alpha B^{0.2} p^{0.8} T^{-0.55} \omega^{0.8} \tag{11.5}$$

(see, (2.15)), where α was introduced as a heat-transfer tuning parameter. The reason for linearizing (11.2) is that Δp can be computed from the solution to (11.3)

$$\Delta p(\theta) = \int_{\theta_{\text{IVC}}}^{\theta} \Phi(\theta,\vartheta)\Gamma(\vartheta)\frac{d\Delta Q_c(\vartheta)}{d\vartheta}d\vartheta \tag{11.6}$$

where

$$\begin{aligned} \Phi(\theta,\vartheta) &= \exp\left(-\int_{\vartheta}^{\theta}\frac{\partial\mu(p^0,\tau)}{\partial p}d\tau\right)\left(\frac{V(\vartheta)}{V(\theta)}\right)^{\gamma} \\ \Gamma(\vartheta) &= \frac{\gamma-1}{V(\vartheta)} \end{aligned} \tag{11.7}$$

The pressure deviation Δp is therefore computationally cheap to generate, which allows for on-line computations. Another motivation for the linearization is the linear relation between $d\Delta Q_c/d\theta$ and Δp, which is suitable for optimization and linear MPC. The pressure trajectories p^+ and p^- are given by $p^0 + \Delta p$, where Δp is the solution to (11.3) with the inputs

$$\begin{aligned}\frac{d\Delta Q_c^+}{d\theta} &= \frac{dQ_c^+}{d\theta} - \frac{dQ_c^0}{d\theta}\\ \frac{d\Delta Q_c^-}{d\theta} &= \frac{dQ_c^-}{d\theta} - \frac{dQ_c^0}{d\theta}\end{aligned} \tag{11.8}$$

Injection-Timing Optimization

With p^+ and p^-, variations in quantities such as p_{IMEPg}, $p_{\max}$ and $dp_{\max}$ can be computed

$$\begin{aligned}p^+_{\text{IMEPg}} &= \frac{1}{V_d}\int_{V_{\text{IVC}}}^{V_{\text{EVO}}} p^+\,dV & p^-_{\text{IMEPg}} &= \frac{1}{V_d}\int_{V_{\text{IVC}}}^{V_{\text{EVO}}} p^-\,dV\\ p^+_{\max} &= \max_\theta p^+ & p^-_{\max} &= \max_\theta p^-\\ dp^+_{\max} &= \max_\theta dp^+ & dp^-_{\max} &= \max_\theta dp^-\end{aligned} \tag{11.9}$$

Furthermore, approximate numerical derivatives of these quantities with respect to $\Delta\theta$ are given by

$$\begin{aligned}\frac{\partial p_{\text{IMEPg}}}{\partial\Delta\theta} &\approx \frac{p^+_{\text{IMEPg}} - p^-_{\text{IMEPg}}}{2\Delta\theta}\\ \frac{\partial p_{\max}}{\partial\Delta\theta} &\approx \frac{p^+_{\max} - p^-_{\max}}{2\Delta\theta}\\ \frac{\partial(dp_{\max})}{\partial\Delta\theta} &\approx \frac{dp^+_{\max} - dp^-_{\max}}{2\Delta\theta}\end{aligned} \tag{11.10}$$

A simple model for p_{IMEPg}, $p_{\max}$ and $dp_{\max}$ in the subsequent engine cycle can then be formulated with the partial derivatives in (11.10)

$$\begin{pmatrix} p_{\text{IMEPg}}\\ p_{\max}\\ dp_{\max}\end{pmatrix} = \begin{pmatrix} p^0_{\text{IMEPg}}\\ p^0_{\max}\\ dp^0_{\max}\end{pmatrix} + \begin{pmatrix} \dfrac{\partial p_{\text{IMEPg}}}{\partial\Delta\theta}\\ \dfrac{\partial p_{\max}}{\partial\Delta\theta}\\ \dfrac{\partial(dp_{\max})}{\partial\Delta\theta}\end{pmatrix}\Delta\theta \tag{11.11}$$

An optimization problem in $\Delta\theta$ was then constructed with the objective of maximizing work output whilst fulfilling constraints on $p_{\max}$ and $dp_{\max}$

$$\begin{aligned} \underset{\Delta\theta}{\text{minimize}} \quad & -p_{\text{IMEPg}} + \beta(\Delta\theta)^2 \\ \text{subject to} \quad & \begin{pmatrix} p_{\text{IMEPg}} \\ p_{\max} \\ dp_{\max} \end{pmatrix} = \begin{pmatrix} p^0_{\text{IMEPg}} \\ p^0_{\max} \\ dp^0_{\max} \end{pmatrix} + \begin{pmatrix} \dfrac{\partial p_{\text{IMEPg}}}{\partial \Delta\theta} \\ \dfrac{\partial p_{\max}}{\partial \Delta\theta} \\ \dfrac{\partial (dp_{\max})}{\partial \Delta\theta} \end{pmatrix} \Delta\theta \\ & \begin{pmatrix} p_{\max} \\ dp_{\max} \\ |\Delta\theta| \end{pmatrix} \le \begin{pmatrix} p^c_{\max} \\ dp^c_{\max} \\ \Delta\theta^c \end{pmatrix} \end{aligned} \tag{11.12}$$

Here, β is a positive cost weight that penalizes combustion-timing changes, and $p^c_{\max}$, $dp^c_{\max}$ and $\Delta\theta^c$ are upper limits on $p_{\max}$, $dp_{\max}$ and the absolute value of $\Delta\theta$.

The solution to (11.12) without constraints is given by

$$\Delta\theta^*_{uc} = \frac{1}{2\beta} \frac{dp_{\text{IMEPg}}}{d\Delta\theta} \tag{11.13}$$

Combustion-timing shifts $\Delta\theta$ that reach the constraint limits $p^c_{\max}$ and $dp^c_{\max}$ are given by

$$\begin{aligned} \Delta\theta_{p^c_{\max}} &= \frac{p^c_{\max} - p^0_{\max}}{\partial p_{\max}/\partial\Delta\theta} \\ \Delta\theta_{dp^c_{\max}} &= \frac{dp^c_{\max} - dp^0_{\max}}{\partial(dp_{\max})/\partial\Delta\theta} \end{aligned} \tag{11.14}$$

Now, if one assumes that $p_{\max}$ and $dp_{\max}$ are monotonically decreasing with $\Delta\theta$, the solution to (11.12), $\Delta\theta^*$, is simply given by the largest value among $\Delta\theta^*_{uc}$, $\Delta\theta_{p^c_{\max}}$ and $\Delta\theta_{dp^c_{\max}}$, saturated within the limits of $\Delta\theta^c$. Furthermore, the optimization problem can be rephrased as a problem in injection timing $\Delta\theta_{\text{SOI}}$ if $\partial\Delta\theta/\partial\theta_{\text{SOI}}$ is known. This partial derivative was here assumed to be equal to 1 for simplicity.

The steps of the cycle-to-cycle controller have now been defined and are summarized in Algorithm 6 where k denotes cycle index.

11.3 Results

This section presents experimental controller results. Open-loop experiments are first presented for the purpose of evaluating how well the controller predicts

Algorithm 6 Cylinder-Pressure Controller

while true **do**
  Estimate $dQ_c^0/d\theta$ with the measured p^0 at cycle k and (4.1)
  Shift $dQ_c^0/d\theta$ according to (11.1)
  Compute p^+ and p^- with (11.6)
  Compute the partial derivatives in (11.10), and solve (11.12)
  Set $\theta_{\mathrm{SOI}}(k+1) = \theta_{\mathrm{SOI}}(k) + \Delta\theta^*(k)$
end while

changes in cylinder pressure with $\Delta\theta_{\mathrm{SOI}}$. Closed-loop performance is then presented, where convergence, parameter sensitivity and constraint fulfillment are evaluated.

Open-loop Experiments

The injection timing θ_{SOI} was swept with a single injection for three different speed/load combinations to evaluate the pressure-prediction method. Conditions at these three operating points are presented in Table 11.1. Each sweep consisted of 2000 cycles where θ_{SOI} was incremented in steps of one from approximately -25 to 5 CAD after TDC.

Table 11.1 The data used in the prediction- and controller evaluation were obtained from the following operating points.

Operating Point	1	2	3
N_{speed} [rpm]	1200	1200	1500
θ_{DOI} [ms]	1.0	1.6	1.0
p_{rail} [bar]	800	800	800
p_{in} [bar]	1.0	1.5	1.2
T_{in} [°C]	15	45	35
λ [-]	2.5	1.5	2.2
r_{EGR} [-]	0	0	0

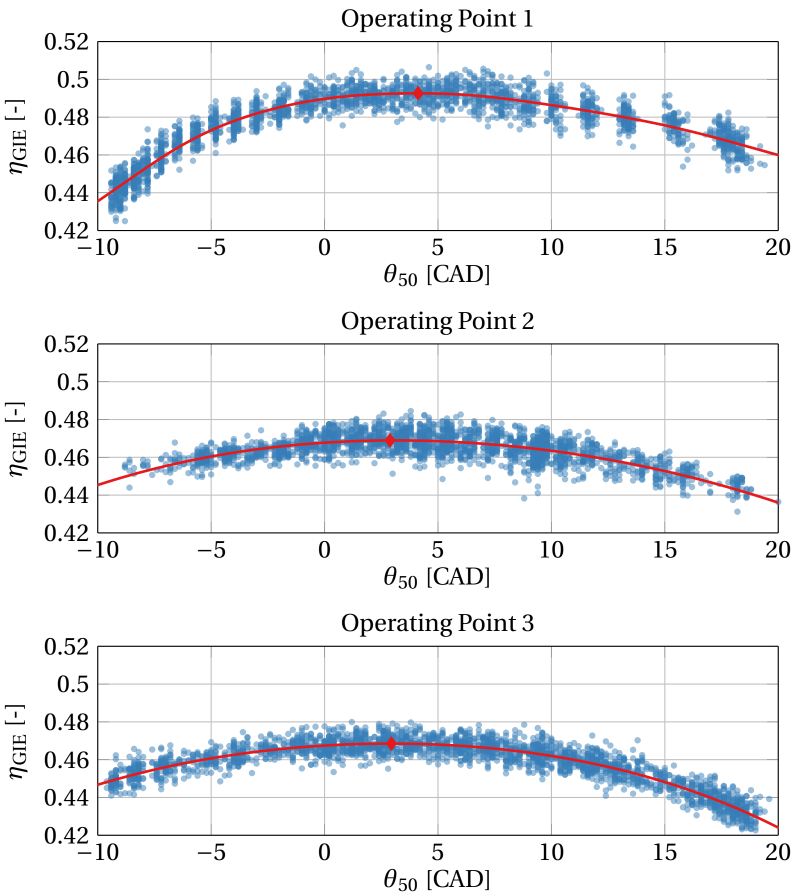

Figure 11.1 Gross indicated efficiency η_{GIE} as a function of θ_{50} at operating points 1-3. The $\circ$-markers are sampled η_{GIE} data, and the solid red line indicates the estimated η_{GIE} sample mean as a function of θ_{50}. The found most efficient θ_{50} are indicated by $\diamond$.

Indicated Efficiency Figure 11.1 shows the gross indicated efficiency

$$\eta_{\mathrm{GIE}} = \frac{p_{\mathrm{IMEPg}} V_d}{m_f Q_{\mathrm{LHV}}} \tag{11.15}$$

as a function of θ_{50} for the three operating points. In Fig. 11.1, the $\circ$-markers are sampled η_{GIE} data, and the solid red line is the estimated η_{GIE} sample mean as a function of θ_{50}. The spread in η_{GIE} was due to cycle-to-cycle variation.

Figure 11.1 shows that the measured η_{GIE} had a shallow maximum in $\theta_{50} \in [0, 5]$ CAD for all operating points. The indicated efficiency then decreased

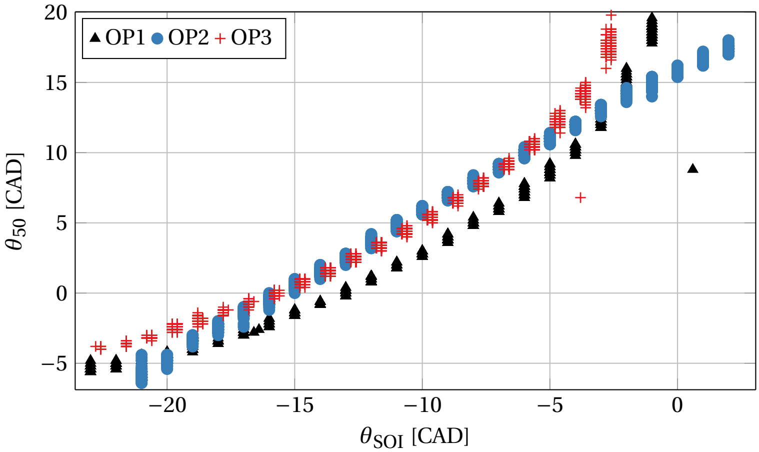

Figure 11.2 The relation between θ_{50} and θ_{SOI} for the θ_{SOI} sweeps in Fig. 11.1

as θ_{50} was increased or decreased outside this interval. The efficiency was slightly higher at operating point 1. This is believed to be a result of the difference in intake temperature T_{in}, which was due to engine warm up and the order of which the experiments were conducted.

$\partial\theta_{50}/\partial\theta_{\mathrm{SOI}}$ Figure 11.2 shows θ_{50} as a function of θ_{SOI} for the three θ_{SOI} sweeps in Fig. 11.1. The assumption of a constant partial derivative $\partial\theta_{50}/\partial\theta_{\mathrm{SOI}}$ was accurate close to $\theta_{50} = 5$. However, at the lower-load operating points, $\partial\theta_{50}/\partial\theta_{\mathrm{SOI}}$ decreased at early θ_{SOI} and increased at late θ_{SOI}. This can be explained by the increase in ignition delay τ when θ_{SOI} was decreased or increased. This effect was then stronger at low load where τ was longer. Similar trends for $\partial\theta_{50}/\partial\theta_{\mathrm{SOI}}$ with engine load was observed in Chapter 6 and Fig. 6.3.

Pressure Prediction The pressure-prediction performance was evaluated by comparing how well the predicted pressure agreed with measured pressure data.

The black solid pressure curve in Fig. 11.3 is the cycle-averaged cylinder pressure p^0 for an arbitrary injection timing θ^0_{SOI}. The red and blue pressure curves to the left and right of this curve are measured pressure curves p^- and p^+ for θ_{SOI} shifted ± 1 CAD relative to θ^0_{SOI}. The dashed red and blue curves are the predicted pressures $\hat{p}^-$ and $\hat{p}^+$, computed with (11.6) and the same θ_{SOI} shifts. It can be seen that the predicted pressure curves $\hat{p}^-$ and $\hat{p}^+$ agree fairly well with p^- and p^+.

Figure 11.4 compares the pressure differences $p^+ - p^0$ and $p^- - p^0$ in Fig. 11.3 with the prediction errors $p^+ - \hat{p}^+$ (dashed, blue) and $p^- - \hat{p}^-$ (dashed, red). The relative error increased with θ, which indicates that the model was unable to predict pressure changes related to the heat release during end of combustion. Inte-

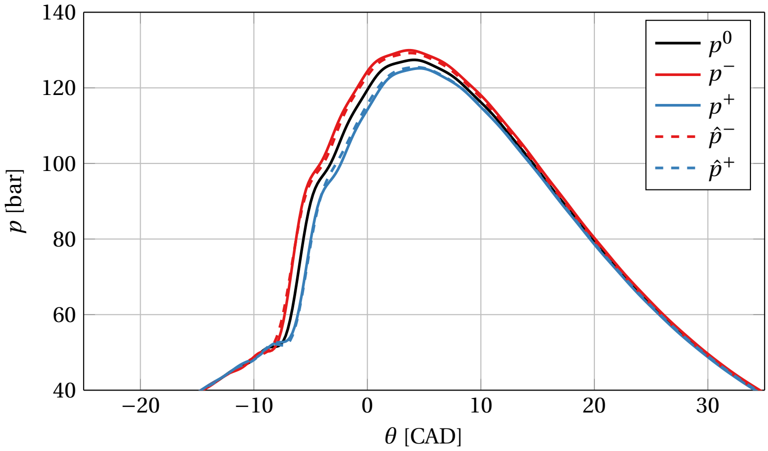

Figure 11.3 The black solid pressure curve is the cycle-averaged pressure p^0 for θ^0_{SOI}. The red and blue pressure curves to the left and right of this curve are the cycle-averaged pressures p^+ and p^- for θ_{SOI} shifted ± 1 CAD relative to θ^0_{SOI}. The dashed red and blue curves are the predicted pressures $\hat{p}^-$ and $\hat{p}^+$, computed with (11.6) and the same θ_{SOI} shifts.

restingly, it can also be seen that the pressure deviation resulting from a θ_{SOI} shift closely resembled a heat-release rate.

Figures 11.5-11.7 presents cycle-averaged pressure changes $p^\pm - p^0$ together with the prediction errors $p^\pm - \hat{p}^\pm$ (as in Fig. 11.4) for all θ_{SOI} at operating points 1-3. Just as in Fig. 11.4, the blue (red) color indicate a pressure change $p^+ - p^0$ ($p^- - p^0$) due to a delayed (advanced) θ_{SOI}. It can be seen that the prediction error was smaller for θ_{SOI} close to TDC for all operating points and that the error gradually increased when θ_{SOI} was advanced or delayed. The prediction error also changed sign somewhere around TDC. For the red lines, indicating a delayed θ_{SOI}, this meant that $\hat{p}^- < p^-$ for late θ_{SOI}, and $\hat{p}^- > p^-$ for early θ_{SOI}. The opposite trend was found for $\hat{p}^+$ and p^+.

The pressure-prediction performance was also evaluated by computing the coefficient of determination R^2

$$R^2 = 1 - \frac{||p^+ - \hat{p}^+||_2^2 + ||p^- - \hat{p}^-||_2^2}{||p^+ - p^0||_2^2 + ||p^- - p^0||_2^2} \tag{11.16}$$

which is a common model-evaluation statistic. The R^2 score describes the fraction of variance in the data explained by the model [Casella and Berger, 2002]. Figure 11.8 presents the R^2 score as a function of θ_{50} for the three θ_{SOI} sweeps in Figs. 11.5-11.7. The pressure-prediction method worked well for $\theta_{50} \in [0, 6]$ where $R^2 \geq 0.9$. The performance then started to degrade outside this interval,

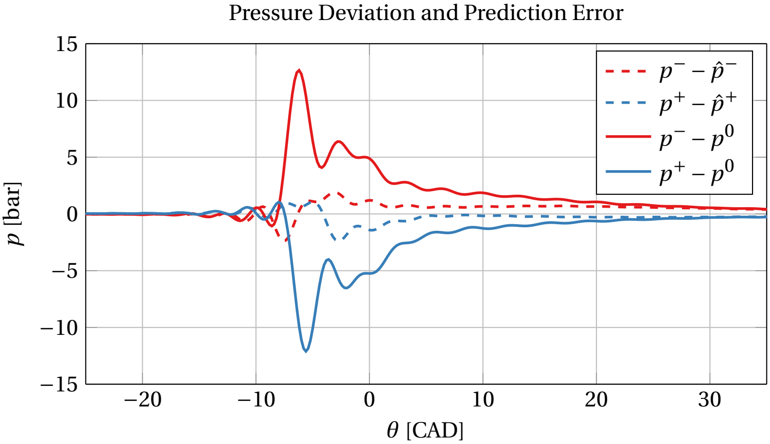

Figure 11.4 The pressure differences $p^+ - p^0$ (blue, solid) and $p^- - p^0$ (red, solid), together with the prediction errors $p^+ - \hat{p}^+$ (blue, dashed) and $p^- - \hat{p}^-$ (red, dashed) for the pressure curves in Fig. 11.3. Interestingly, the pressure deviation closely resembled a heat-release rate.

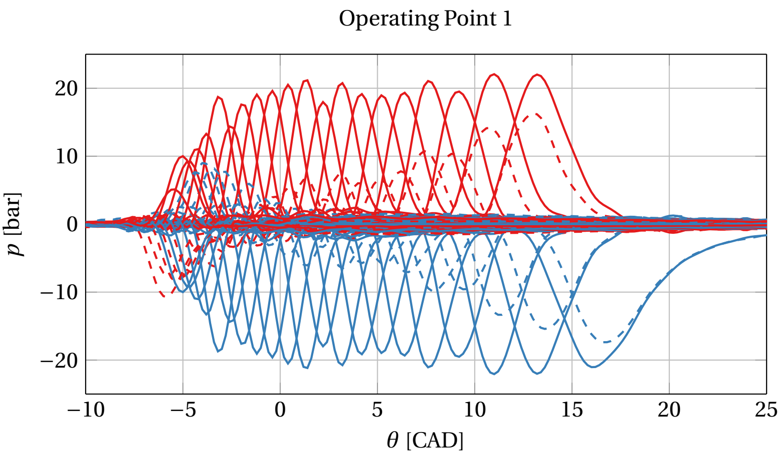

Figure 11.5 Pressure-prediction performance at operating point 1. The solid blue (red) pressure curves correspond to the measured cycle-averaged pressure change $p^+ - p^0$ ($p^- - p^0$) due to a positive (negative) θ_{SOI} shift of 1 CAD. The dashed blue (red) lines correspond to the pressure prediction error for the same θ_{SOI} change.

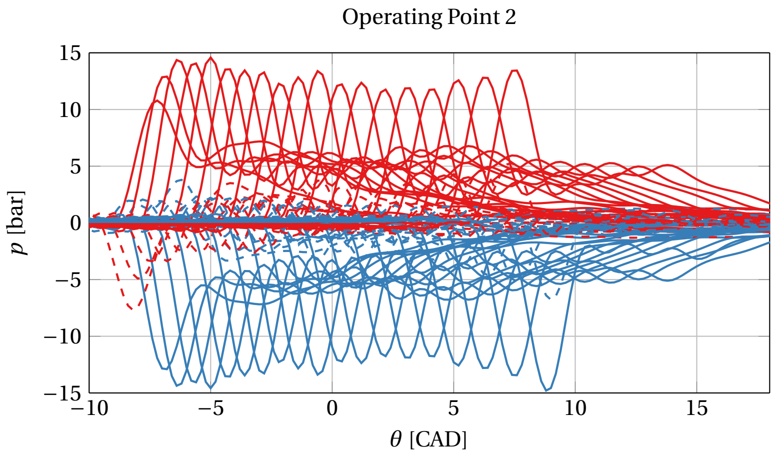

Figure 11.6 Pressure-prediction performance at operating point 2. See the figure caption of Fig. 11.5 for a more detailed description.

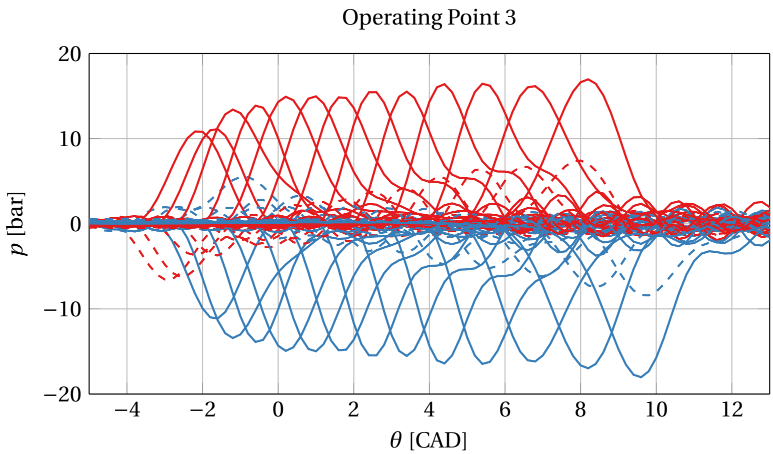

Figure 11.7 Pressure-prediction performance at operating point 3. See the figure caption of Fig. 11.5 for a more detailed description.

and more steeply for the low-load operating points.

It was here assumed that $\partial\Delta\theta/\partial\theta_{\mathrm{SOI}} = 1$, but when θ_{SOI} was decreased (≈ -25), τ increased, which gave $\partial\Delta\theta/\partial\theta_{\mathrm{SOI}} < 1$. This resulted in an overestimated predicted p change. For late θ_{SOI} (≈ -5), τ also increased which gave $\partial\Delta\theta/\partial\theta_{\mathrm{SOI}} > 1$, and resulted in an underestimated p change. This explains the trends in Figs. 11.5-11.7. It also explains why the R^2 curve was higher for the high

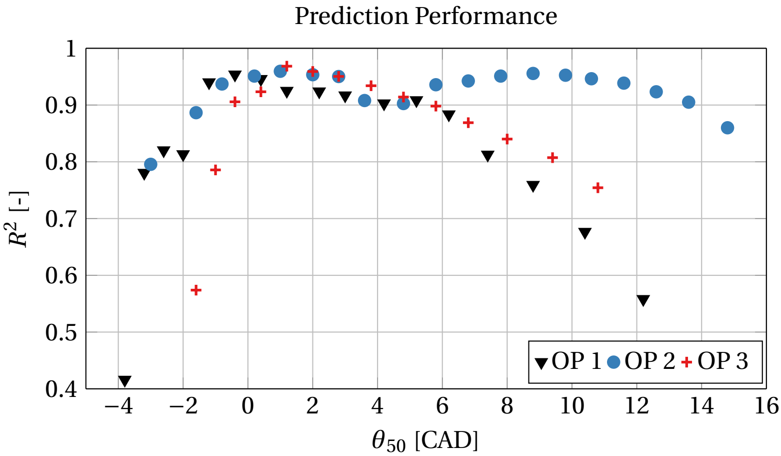

Figure 11.8 R^2 score as a function of θ_{50} for the three sweeps in Figs. 11.5-11.7. The pressure-prediction method worked satisfactorily for $\theta_{50} \in [0,\ 6]$, where $R^2 \geq 0.9$. The performance then started to degrade outside this interval, and more steeply at the low-load operating points.

load experiment in Fig. 11.8, where τ did not change significantly with an almost constant $\partial\Delta\theta/\partial\theta_{\text{SOI}}$, see Fig. 11.2.

Closed-loop Experiments

This section demonstrates closed-loop performance. Tuning for best performance was not carried out as the experiments were focused on convergence and parameter sensitivity.

Convergence and β - Sensitivity The controller in Algorithm 6 was evaluated at the investigated operating points. The parameter β and the initial injection timing θ_{SOI}^0 were varied to investigate controller convergence. Convergence results are presented in Figs. 11.9-11.11, where $\theta_{\text{SOI}}^0 = \{20, 10, 0\}$ [CAD] and $\beta = \{0.05, 0.2\}$.

The controller consistently converged to the same θ_{50}^*, independently of the starting point in Figs. 11.9-11.11. The parameter β clearly influenced the convergence rate, where a larger β gave slower convergence. In Fig. 11.10, the controller behavior in stationarity became oscillatory for $\beta = 0.05$. In the same figure, it also seems as if the controller converged faster for $\beta = 0.2$ and $\theta_{50}^0 = -2$. This was caused by an unintended active p_{max} constraint. The constraint did not affect the stationary behavior since the estimated $dp_{\text{IMEPg}}/d\Delta\theta$ was zero in the convergence point.

Figures 11.9-11.11 show that $1/\beta$ can be viewed as a controller gain, where the choice of β is a trade-off between convergence speed and stationary cycle-to-cycle variation. If β was chosen too small, the derivative $dp_{\text{IMEPg}}/d\Delta\theta$

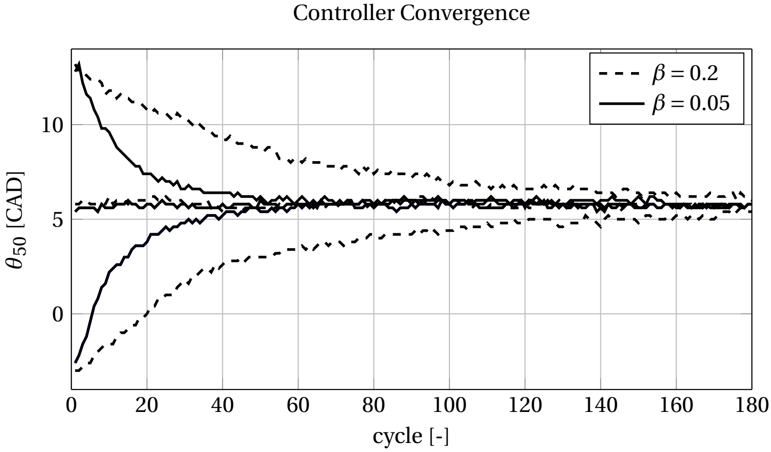

Figure 11.9 Controller convergence at operating point 1 where the solid lines correspond to $\beta = 0.05$ and the dashed lines to $\beta = 0.2$. The controller converged to $\theta_{50}^* = 5.8$, $\theta_{SOI}^* = -7$, in 50 and 150 cycles, depending on β.

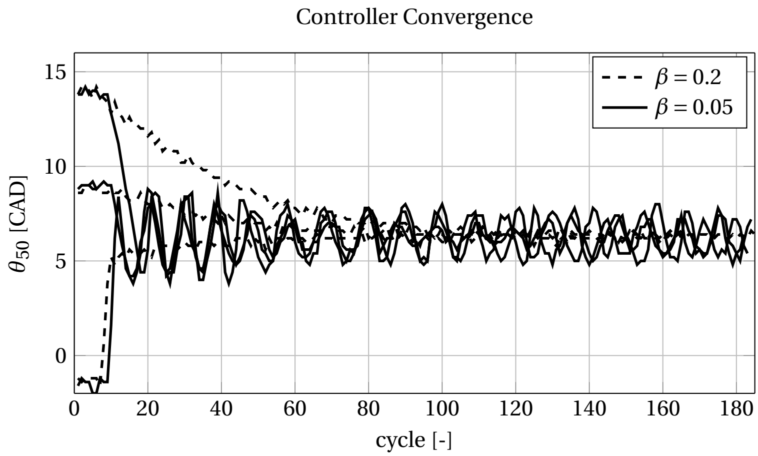

Figure 11.10 Controller convergence at operating point 2, where the solid lines correspond to $\beta = 0.05$ and the dashed lines to $\beta = 0.2$. Here, the point of convergence is $\theta_{50}^* = 6.4$, $\theta_{SOI}^* = -9.5$. In the lower dashed θ_{50} trajectory, the fast convergence was due to an unintended active $p_{\max}$ constraint. This did however not affect the point of convergence, since the computed $\partial p_{\mathrm{IMEPg}}/\partial \Delta\theta$ was zero in the convergence point.

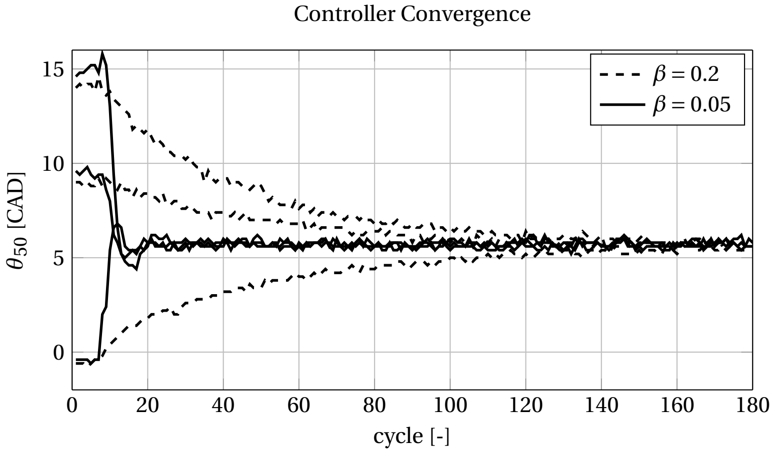

Figure 11.11 Controller convergence at operating point 3, where the solid lines correspond to $\beta = 0.05$ and the dashed lines to $\beta = 0.2$. Here, the point of convergence is $\theta_{50}^* = 5.6$, $\theta_{\text{SOI}}^* = -9.6$, where the controller converged in 5 cycles for $\beta = 0.05$.

caused large controller steps $\Delta\theta_{\text{SOI}}$ which led to an oscillatory controller behavior. For best performance, β should be increased with load as $dp_{\text{IMEPg}}/d\Delta\theta$ increases. The point of convergence in Figs. 11.9-11.11 occurred later than the experimentally found most efficient points in Fig. 11.1. The reason for this will be discussed in the following section.

Parameter Sensitivity The point of convergence θ_{50}^* depends on the parameter values in (11.2), and especially on the parameters of the heat-transfer model. In order to investigate θ_{50}^* sensitivity, the model parameter α (see (11.5)) and the TDC offset $\Delta\theta_{\text{TDC}}$ were varied. These parameters were previously set to $\alpha = 5$ and $\Delta\theta_{\text{TDC}} = 0$. Convergence results can be viewed in Figs. 11.12 and 11.13 where α and $\Delta\theta_{\text{TDC}}$ were varied stepwise from 1 to 6, and from 2 to -2 CAD, respectively. Figure 11.12 shows that the magnitude of α affected the convergence point. With an increased α, θ_{50}^* was delayed and the converse was true for a decreased α. One could view α as a trade-off parameter that weighs efficiency effects from heat-transfer and exhaust losses, and in that way determines an efficiency optimal θ_{50}^*.

In Fig. 11.13, it can be seen that a $\Delta\theta_{\text{TDC}}$ of 2 CAD gave a θ_{50}^* offset of approximately 2 CAD. This indicates that the controller accuracy is limited by the precision of the measured θ, and its synchronization with p.

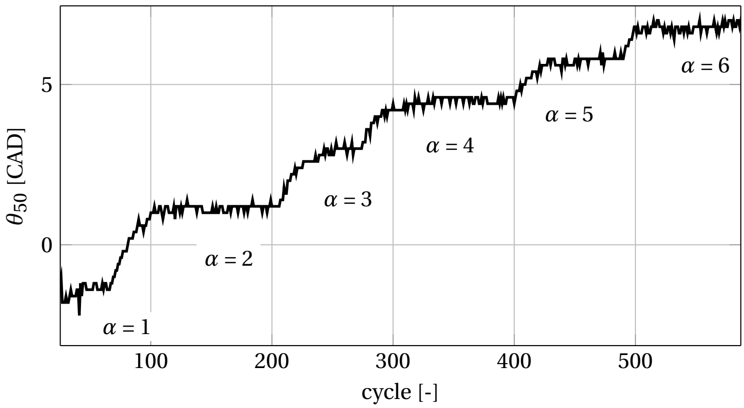

Figure 11.12 Heat-transfer sensitivity at operating point 1. Here the scaling factor α was varied stepwise from 1 to 6, which changed the point of convergence. An α between 3 and 4 would have maximized efficiency according to the data in Fig. 11.1. In Figs. 11.9-11.11, $\alpha = 5$ was used.

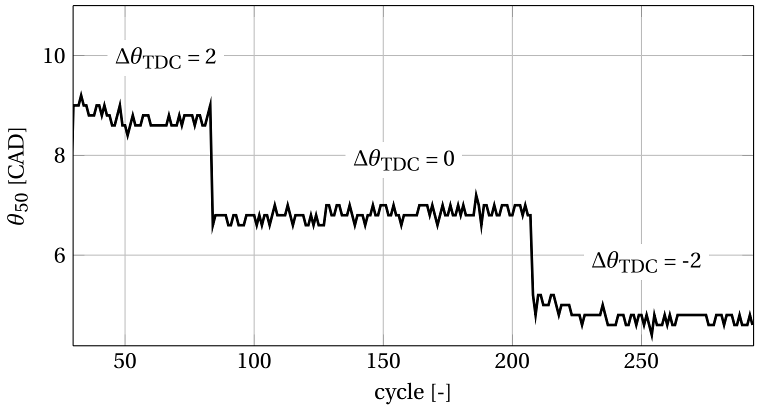

Figure 11.13 TDC-offset sensitivity at operating point 1. Here, $\Delta\theta_{\mathrm{TDC}}$ was changed stepwise from 2 to -2 CAD, which indicates that the controller accuracy is limited by the precision of the measured θ and its synchronization with p.

Pressure-Constraint Handling

Controller performance with respect to constraint fulfillment was also investigated by varying the constraint limits p^c_{max} and dp^c_{max}. Result are presented in Figs. 11.14 and 11.15, where p^c_{max} was varied between 80 to 120 bar and dp^c_{max} was varied between 20 to 40 bar/CAD. The controller managed to fulfill the constraints by initially taking a larger positive step in θ_{SOI} and then slowly advancing θ_{50} to reach the constraint level from below.

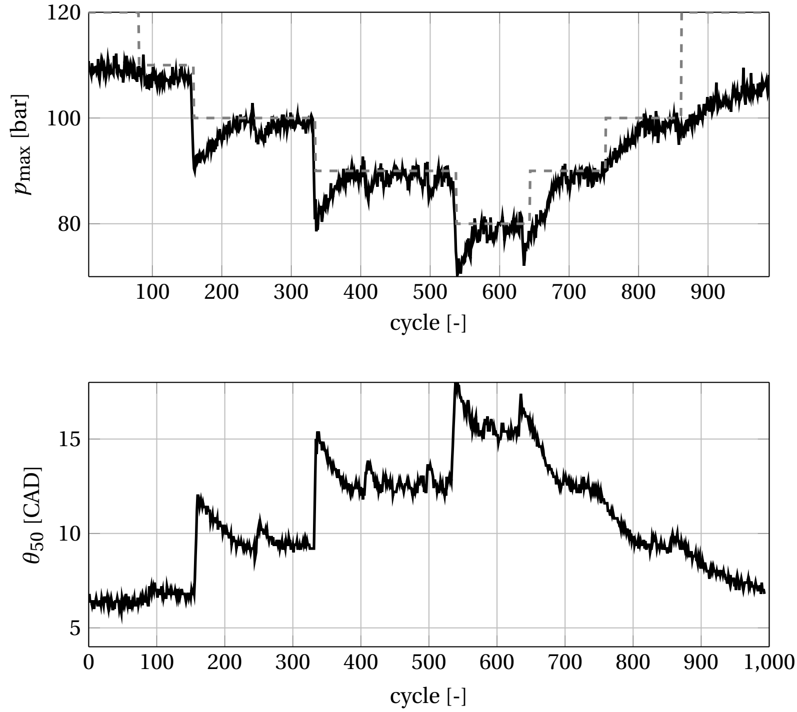

Figure 11.14 In the upper part of the figure, $p_{\max}$ (solid) is displayed together with $p^c_{\max}$ (dashed), The corresponding θ_{50} is displayed in the lower subdiagram.

With active constraints, the controller was found to enhance cycle-to-cycle variation. It would therefore be wise to increase β for decreased cycle-to-cycle variation, if active constraints are expected. The controller also had a specific behavior when a constraint was violated, as seen in Fig. 11.14. At cycle 340, the controller delayed θ_{SOI} greatly and then slowly advanced combustion timing until it reached the allowed $p_{\max}$ limit. This was because the controller was forced to delay θ_{SOI} due to a decrease in $p^c_{\max}$. The partial derivative $\partial p_{\max}/\partial\theta_{\mathrm{SOI}}$ was underestimated due to an increase in τ, which explains why the controller took a too large step to fulfill the constraint.

11.4 Discussion

A desirable combustion timing is a trade-off between exhaust losses, heat transfer, and constraint fulfillment. This chapter introduced a high-level model-based combustion-timing controller that finds the efficiency-optimal combustion

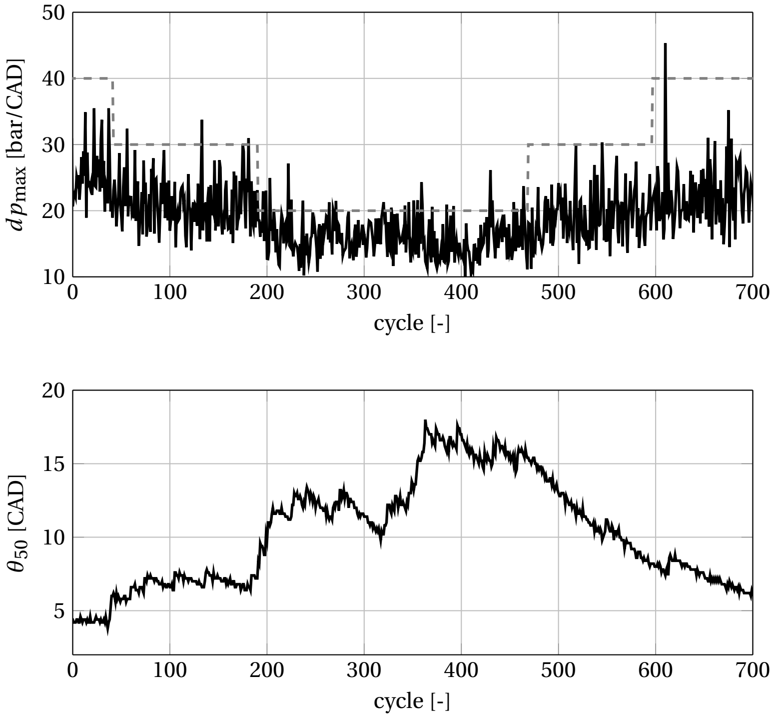

Figure 11.15 In the upper part of the figure, $dp_{\max}$ (solid) is displayed together with $dp^{c}_{\max}$ (dashed). The corresponding θ_{50} is displayed in the lower subdiagram.

timing online. In this way, the controller solves the problem of deciding a combustion-timing set point, which is necessary for most combustion-feedback controllers, see for instance Chapter 6 and [Bengtsson et al., 2004; Chiang and Stefanopoulou, 2005; Widd et al., 2008]. Furthermore, the model-based approach presented here allows for faster convergence (5 cycles) than data-based extremum seeking controllers that search for efficiency-optimal θ_{50} using the computed p_{IMEPg}, see [Killingsworth et al. 2009; Lewander et al. 2012]. The method presented in this chapter could speed up convergence of such methods by providing an initial guess.

Feedback was introduced through the estimated heat-release rate, which was utilized by the controller, together with a linearized 0D model, to predict how the cylinder pressure varies with injection timing. This is a computationally efficient alternative to that of modeling the relation between fuel injection and heat-release rate.

The point of convergence was found to be sensitive to TDC offset and heat-transfer parameters. The controller should therefore be combined with methods capable of computing these parameters. Examples of such methods were introduced in Chapter 4. In addition to model parameters, the controller had one tuning parameter, β. The choice of β was found to be a trade-off between convergence speed and steady-state cycle-to-cycle variation.

It was also found that the pressure prediction performance was dependent on the assumption of $\partial\Delta\theta/\partial\theta_{\mathrm{SOI}}$ as a function of θ_{SOI}. In this chapter, $\partial\Delta\theta/\partial\theta_{\mathrm{SOI}}$ was set constant equal to 1. The results indicate that controller performance would improve if $\partial\Delta\theta/\partial\theta_{\mathrm{SOI}}$ were known. An adaptive method could therefore be used to estimate $\partial\Delta\theta/\partial\theta_{\mathrm{SOI}}$ online with θ_{50} data. A model-based alternative would be to use a τ model.

The prediction method studied in this chapter will be used in the following chapter to solve the optimization-problem studied in Chapter 10 with MPC. The method will also be used to track cycle-resolved pressure set-point trajectories.

11.5 Conclusions

A model-based combustion-timing controller was introduced. The controller utilized the estimated heat-release rate to predict how the in-cylinder pressure varies with injection timing. The controller converged close to experimentally found most efficient combustion timing, and was capable of fulfilling constraints with respect to p_{max} and dp_{max}.

12

Predictive Constraint Handling and Pressure Tracking

This chapter investigates how the pressure-prediction method described in the previous chapter can be used to efficiently fulfill constraints with multiple injections. This optimal-control problem, defined by (10.10), was previously studied and solved with a hybrid PI controller in Chapter 10. The approach taken in this chapter is to instead solve (10.10) on-line with the use of a pressure model and model predictive control (MPC). An advantage with this approach is that physical system knowledge is explicitly included in the controller design. The MPC representation also has the advantage of being able to handle multiple constraints and objectives simultaneously, which reduces the controller-design complexity.

A pressure-tracking problem is also considered where the objective is to follow a cycle-resolved pressure-reference trajectory. The pressure-tracking problem was previously studied and solved in simulation with iterative learning control and CFD-based feedforward control for the same purpose [Jörg et al., 2015; Zweigel et al., 2015]. In contrast to these works, this chapter presents a model-based pressure tracking controller that does not require a fuel-injection model.

These two controllers work by the MPC principle, which means that fuel injections are repeatedly optimized with respect to a receding horizon of future engine cycles. The computations done by the controllers every cycle involves formulating and then solving a quadratic program (QP). The QPs are obtained by approximating the original optimization problems to obtain real-time compatible solution times. A heat-release method that separates the estimated heat-release rate in order to distinguish contributions from different injections was also used, together with model-based criteria for deciding when to add and remove injections.

The chapter is outlined as follows: The optimal-control problems are presented and approximated by QPs in Sec. 12.1. In Sec. 12.2, heat-release separation is used, together with a linearized pressure model to compute expressions needed to solve the QPs. Additional considerations for changing the number of injections and avoiding stochastic constraint violation are covered in Secs. 12.3 and 12.4. Experimental results are presented in Sec. 12.5, and discussion and conclusions are given in Secs. 12.6 and 12.7.

Data presented in Secs. 12.1 to 12.4 were generated from simulation for illustration purposes whilst the data presented in Fig. 12.5 and Sec. 12.5 were obtained from engine experiments.

12.1 Model Predictive Control Formulation

The following two optimal-control problems are considered:

1. To efficiently track load and combustion-timing set points subject to constraints on peak pressure, pressure-rise rate, NO_x and exhaust temperature.

2. To track a predefined cycle-resolved pressure-reference trajectory.

In both problems, the optimization variable is defined as

$$\boldsymbol{u} = \begin{pmatrix} \theta_{\mathrm{SOI}}^1 & m_f^1 & \dots & \theta_{\mathrm{SOI}}^M & m_f^M \end{pmatrix}^T \tag{12.1}$$

where m_f denotes the fuel mass, θ_{SOI} denotes injection timing, and M is the number of injections. Injector-current pulse durations θ_{DOI} are computed from m_f and the common-rail pressure p_{rail} using an injector map

$$\theta_{\mathrm{DOI}}^i = M_{\mathrm{inj}}(m_f^i, p_{\mathrm{rail}}) \tag{12.2}$$

The first optimization problem was introduced and motivated in Chapter 10. In the second problem, the controller aims to obtain a predefined pressure-reference trajectory. This is an alternative control-problem formulation to combustion-timing and work-output regulation, which is more commonly used when utilizing pressure-sensor feedback. In both cases, the optimization problems were reformulated as MPC problems. This procedure will now be presented in the following sections.

Constraint Fulfillment

The first MPC problem concerns optimization problem (10.10), which was studied in Chapter 10. Here, (10.10) is reformulated as an MPC problem with a prediction horizon and additional costs on control action and load-tracking error.

A constraint on pressure-rise rate is also included

$$
\begin{aligned}
\underset{\boldsymbol{u}(1),\dots,\boldsymbol{u}(H_p)}{\text{minimize}} \quad & \sum_{k=1}^{H_p} J_{m_f}(k) + J_{p_{\mathrm{IMEP}}}(k) + J_{\Delta u}(k) && \qquad (12.3)\\
\text{subject to} \quad & p(\theta_j,k) \le p^c_{\max} && \theta_j = \theta_0,\dots,\theta_f,\ k=1,\dots,H_p\\
& dp(\theta_j,k)/d\theta \le dp^c_{\max} && \theta_j = \theta_0,\dots,\theta_f,\ k=1,\dots,H_p\\
& \mathrm{NO}_x(k) \le \mathrm{NO}_x^c && k=1,\dots,H_p\\
& T_{\mathrm{ex}}(k) \ge T^c_{\mathrm{ex}} && k=n_{T_{\mathrm{ex}}},\dots,H_p^{T_{\mathrm{ex}}}\\
& \boldsymbol{u}(k) \in \mathbb{U} && k=1,\dots,H_p
\end{aligned}
$$

The objective of (12.3) is to minimize a sum of cost functions that penalize fuel-consumption, load-tracking error and control action: J_{m_f}, $J_{p_{\mathrm{IMEP}}}$, and $J_{\Delta u}$, with respect to $\boldsymbol{u}$, over a horizon of H_p future engine cycles. The control-action cost is introduced to obtain robustness by suppressing large changes in $\boldsymbol{u}$. The index k denotes engine cycle where $k = 0$ is the previous engine cycle, H_p and $H_p^{T_{\mathrm{ex}}}$ are prediction-horizon lengths in engine cycles.

Constraint limits x^c should be fulfilled with respect to pressure p and pressure-rise rate $dp/d\theta$ at sampled crank angles θ_j, as well as cylinder-out NO_x emissions and exhaust temperature T_{ex}. Upper bounds on p, $dp/d\theta$ and NO_x were motivated by mechanical engine tolerances, engine noise and legislated emission limits. The lower limit for T_{ex} was introduced as a guarantee for after-treatment system performance. The feasible input set $\mathbb{U}$ is described below. Moreover, the argument $\boldsymbol{u}$ is omitted for the different output variables for ease of notation.

Cost Functions The fuel-consumption penalty $J_{m_f}(k)$ in (12.3) is represented as a cost on combustion-timing deviation from efficient set points $\theta^{r,i}_{\mathrm{CT}}$, for the different injections $i = 1,\dots,M$

$$J_{m_f}(k) = \alpha \sum_{i=1}^{M} m^i_f(k)(\theta^{r,i}_{\mathrm{CT}} - \theta^i_{\mathrm{CT}}(k))^2 \qquad (12.4)$$

which allows for control of a multimodal heat-release rate. An efficiency-optimal combustion timing is located somewhere after TDC, and it is here assumed that $\theta^{r,i}_{\mathrm{CT}}$ is obtained from engine experiments or computed using the method presented in Chapter 11. The penalty terms in (12.4) are weighted with m^i_f to prioritize efficient combustion timings for heavier injections. The fuel-mass weights also introduce the controller behavior of moving fuel from a less efficient injection to a more efficient injection.

The engine load p_{IMEP} should follow a set point p^r_{IMEP}. This objective is represented by the quadratic cost

$$J_{p_{\mathrm{IMEP}}}(k) = \beta(p^r_{\mathrm{IMEP}} - p_{\mathrm{IMEP}}(k))^2 \qquad (12.5)$$

where p_{IMEP} is used to denote p_{IMEPg} in this chapter. The control-action cost term in (12.3) is given by

$$J_{\Delta u}(k) = (\boldsymbol{u}(k) - \boldsymbol{u}(k-1))^T R(\boldsymbol{u}(k) - \boldsymbol{u}(k-1)) \tag{12.6}$$

where $\boldsymbol{u}(0)$ is the previous-cycle injection configuration.

Pressure Tracking

The MPC for pressure tracking is given by

$$\begin{aligned} \underset{\boldsymbol{u}(1),\dots,\boldsymbol{u}(H_p)}{\text{minimize}} \quad & \sum_{k=1}^{H_p} J_p(k) + J_{\Delta u}(k) \\ \text{subject to} \quad & \boldsymbol{u}(k) \in \mathbb{U},\ k = 1,\dots,H_p \end{aligned} \tag{12.7}$$

where the cost J_p penalizes in-cylinder pressure deviation from a predefined pressure-reference trajectory.

Cost Functions The first cost term in (12.7) is given by

$$J_p(k) = \alpha_{tr} \sum_{\theta_j=\theta_0}^{\theta_f} \left(p^r(\theta_j) - p(\theta_j, k)\right)^2 \tag{12.8}$$

which is the sum of squared p deviations from p^r at sampled crank angles θ_j. The summation interval was set to only penalize pressure deviation close to TDC and during the expansion stroke, since this is the part which is directly controlled by fuel injection. The control-action cost term in (12.7) is given by (12.6).

Pressure Reference The pressure reference p^r in (12.8) is parameterized as an ideal limited-pressure cycle, where a portion of the fuel α_v is burned with constant cylinder volume at the start of combustion θ^r_{SOC}. The remainder of the fuel α_p is then burned at constant cylinder pressure. Examples of p^r are presented in Fig. 12.1 for different α_v. The start of combustion θ^r_{SOC}, α_v, and the desired total fuel-energy burned Q^r_c are considered to be tuning parameters that determine p^r. A more detailed description of ideal engine cycles can be found in [Heywood, 1988].

Input Constraints

Input constraints were enforced through saturation in Chapter 10. Here, the input constraints are instead included in the optimization problem, where constraints on $\boldsymbol{u}$ are imposed in order for the solution to be realizable. Injected fuel masses have to be positive

$$m_f^i \geq 0,\ i = 1,\dots,M \tag{12.9}$$

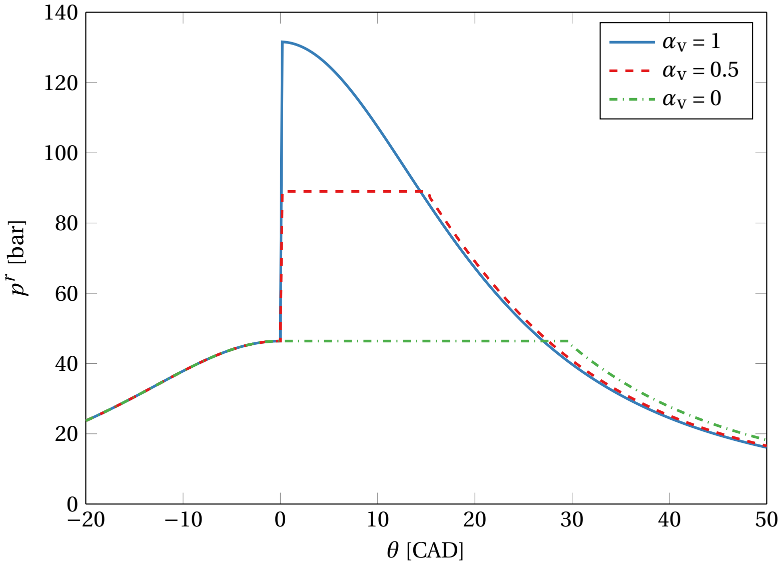

Figure 12.1 The pressure reference signal p^r is an ideal limited-pressure cycle, where a portion of the fuel α_v is burned at constant cylinder volume at the start of combustion θ^r_{SOC}, and the remainder of the fuel α_p is burned at constant cylinder pressure. The constant-volume fraction α_v is here varied from 0 to 1, with $\theta^r_{\text{SOC}} = 0$ and $Q^r_c = 5000$ J.

Furthermore, the fuel-injection pulses have to be positioned so that they do not overlap. This imposes the following constraint

$$\theta^{i-1}_{\text{SOI}} + \theta^{i-1}_{\text{DOI}} + \theta_h \leq \theta^{i}_{\text{SOI}}, \quad i = 2, \ldots, M \tag{12.10}$$

where θ_{DOI} is computed with (12.2) and θ_h is a margin related to the hydraulic delay of the injector, allowing the injector to close in-between injections. Additional absolute and relative constraints on $\boldsymbol{u}$

$$\begin{aligned} \boldsymbol{u}_l \leq \boldsymbol{u}(k) \leq \boldsymbol{u}_u,\ k = 1, \ldots, H_p \\ \Delta\boldsymbol{u}_l \leq \boldsymbol{u}(k) - \boldsymbol{u}(k-1) \leq \Delta\boldsymbol{u}_u,\ k = 1, \ldots, H_p \end{aligned} \tag{12.11}$$

were added to provide robustness and limit the controller operating range. The set of injection configurations fulfilling (12.9)-(12.11) are denoted $\mathbb{U}$ in (12.3) and (12.7).

Cost-Function Weights

The cost-function weights α, α_{tr}, β and the diagonal matrix

$$R = \text{diag}\begin{pmatrix} R^1_{m_f} & R^1_{\text{SOI}} & \cdots & R^M_{m_f} & R^M_{\text{SOI}} \end{pmatrix} > 0 \tag{12.12}$$

are parameters that determine the trade-off between control action and fulfillment of the different tracking objectives. Suitable values will be presented together with experimental results in Sec. 12.5.

Problem Approximation

We have now obtained two nonlinear-programming problems on the form

$$\begin{aligned} \underset{U}{\text{minimize}} \quad & J(U) \\ \text{subject to} \quad & f(U) \le c \\ & U \in \mathbb{U} \end{aligned} \tag{12.13}$$

where

$$U = \begin{pmatrix} \boldsymbol{u}(1) & \dots & \boldsymbol{u}(H_p) \end{pmatrix}^T \tag{12.14}$$

The two functions $f(U)$ and $J(U)$ are non-linear in U, and f demands extensive modeling. Numerical methods could of course be used to search for local optima of (12.13). However, this would require multiple evaluations of J and f which is computationally expensive, since it involves solving differential equations. To allow for shorter computational times, necessary for on-line applications, it was decided to approximate (12.13) by a QP, at the current input $\boldsymbol{u}_0$

$$\begin{aligned} \underset{\Delta U}{\text{minimize}} \quad & J(\boldsymbol{u}_0) + \nabla J(\boldsymbol{u}_0)^T \Delta U + \frac{1}{2}\Delta U^T \nabla^2 J(\boldsymbol{u}_0)\Delta U \\ \text{subject to} \quad & f(\boldsymbol{u}_0) + \nabla f(\boldsymbol{u}_0)^T \Delta U \le c \\ & \boldsymbol{u}_0 + \Delta U \in \hat{\mathbb{U}} \end{aligned} \tag{12.15}$$

where ΔU is the deviation from $\boldsymbol{u}_0$

$$\Delta U = \begin{pmatrix} \boldsymbol{u}(1) & \dots & \boldsymbol{u}(H_p) \end{pmatrix}^T - \boldsymbol{u}_0 = \begin{pmatrix} \Delta\boldsymbol{u}(1) & \dots & \Delta\boldsymbol{u}(H_p) \end{pmatrix}^T \tag{12.16}$$

Another motivation for approximating (12.13) was that gradients and Hessians can be computed using simpler physical models, valid for smaller variations in $\boldsymbol{u}$. The optimization problem can then be re-approximated on a cycle-to-cycle basis when new measurements have been obtained. This means that the gradients $\nabla f(\boldsymbol{u}_0)$, $\nabla J(\boldsymbol{u}_0)$ and Hessian $\nabla^2 J(\boldsymbol{u}_0)$ have to be recomputed as $\boldsymbol{u}_0$ changes. The following section presents how to obtain gradients and Hessians with the use of physical models. A linear approximation of $\hat{\mathbb{U}}$ was obtained by linearizing M_{inj}

$$\theta_{\text{SOI}}^{i-1}(0) + \Delta\theta_{\text{SOI}}^{i-1} + \theta_{\text{DOI}}^{i-1}(0) + \frac{\partial M_{\text{inj}}(\boldsymbol{u}_0)}{\partial m_f}\Delta m_f^{i-1} + \theta_h \le \theta_{\text{SOI}}^{i}(0) + \Delta\theta_{\text{SOI}}^{i} \tag{12.17}$$

12.2 Modeling and Heat-Release Detection

The proposed method for computing the gradients and Hessian in (12.15) is to first establish a relationship between $\Delta\boldsymbol{u}$ and variations in $dQ_c/d\theta$. For this purpose, the estimated $dQ_c/d\theta$ at the previous engine cycle $k=0$ is utilized. The resulting effects of $\Delta\boldsymbol{u}$ on p, NO_x and T_{ex} are then computed using the pressure-linearization method presented in Chapter 11.

From $\Delta\boldsymbol{u}$ to $d\Delta Q_c/d\theta$

First, the previous cycle $dQ_c/d\theta$ is obtained from

$$\frac{dQ_c}{d\theta} = \frac{\gamma}{\gamma-1}p\frac{dV}{d\theta} + \frac{1}{\gamma-1}V\frac{dp}{d\theta} + \frac{dQ_{ht}}{d\theta} \tag{12.18}$$

If multiple injections are used, we have to separate $dQ_c/d\theta$ among the injections. It is assumed that $dQ_c/d\theta$ consists of the heat-release generated from the different injections according to

$$\frac{dQ_c}{d\theta} = \sum_{i=1}^{M}\frac{dQ_c^i}{d\theta} \tag{12.19}$$

The procedure for obtaining $dQ_c^i/d\theta$ from $dQ_c/d\theta$ with M injections was presented in Chapter 4. It is now briefly recaptured for clarity. First, the M most significant peaks are located, where detected peaks have to be larger than a threshold dQ_t and separated with a minimum distance θ_d. The detected peaks constitute the combustion timings θ^i_{CT} in (12.4).

With the peaks detected, $dQ_c/d\theta$ can be separated in different intervals

$$\frac{d\hat{Q}_c^i}{d\theta} = \begin{cases} \dfrac{dQ_c}{d\theta} & \text{if } l_i \le \theta \le d_i \\ 0 & \text{otherwise} \end{cases} \tag{12.20}$$

where the bounds l_i and d_i are determined by the minima between the detected peaks. The obtained heat-release rates $d\hat{Q}_c^i/d\theta$ are then smoothed with a zero-phase filter to obtain more physical heat-release shapes. Finally, $d\hat{Q}_c^i/d\theta$ have to be normalized so that (12.19) is fulfilled

$$\frac{dQ_c^i}{d\theta} = \left(\sum_{i=1}^{M}\frac{d\hat{Q}_c^i}{d\theta}\right)^{-1}\frac{d\hat{Q}_c^i}{d\theta}\frac{dQ_c}{d\theta} \tag{12.21}$$

The four steps of the detection procedure are illustrated in Fig. 12.2. In the case of detecting less than M peaks, which is possible for small injections or if combustion from different injections overlap, the detected peaks are allocated to the largest injections. Furthermore, the detection procedure accounts for the ordering of injections when allocating combustion timings to injections.

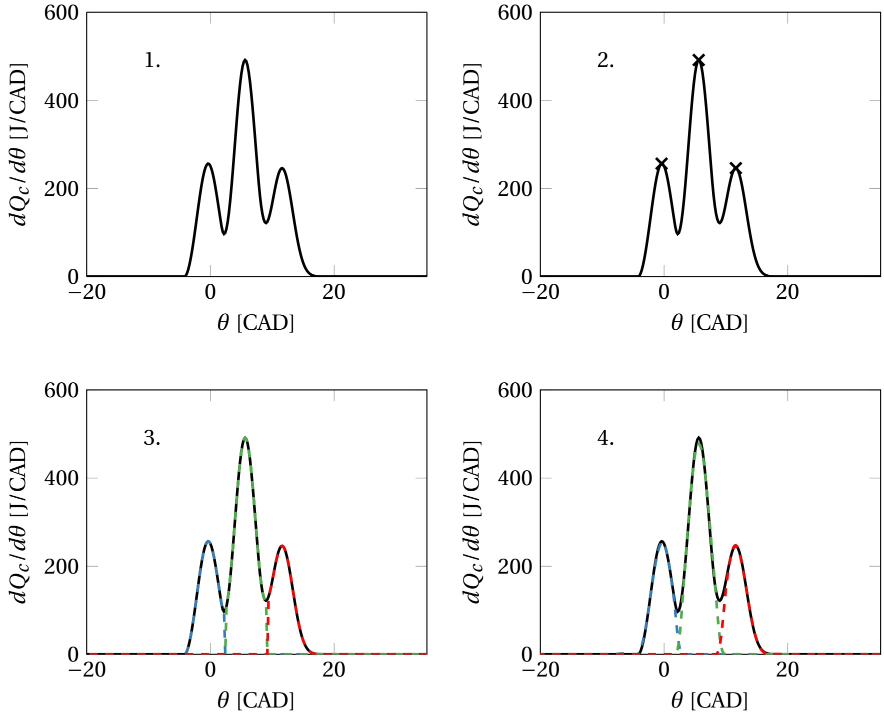

Figure 12.2 The method used for separating $dQ_c/d\theta$ among the different injections (from 1 to 4). First, the heat-release rate is obtained from the measured pressure signal (1) and the most significant M peaks are detected (2). $dQ_c/d\theta$ is then separated in different intervals according to the peak locations (3). The heat-release rates $d\hat{Q}_c^i/d\theta$ in the different intervals are then filtered and normalized (4).

We can now relate a change in $\boldsymbol{u}$, $\Delta\boldsymbol{u}$, to a change in $dQ_c/d\theta$, $d\Delta Q_c/d\theta$. A change in θ_{SOI}^i is assumed to give a crank-angle shift in the part of $dQ_c/d\theta$ that is affected by injection i, $dQ_c^i/d\theta$. This gives the partial derivatives

$$\begin{aligned} \frac{\partial}{\partial\theta_{\mathrm{SOI}}^i}\frac{dQ_c}{d\theta} &= -\frac{d^2Q_c^i}{d\theta^2} \\ \frac{\partial\theta_{\mathrm{CT}}^i}{\partial\theta_{\mathrm{SOI}}^i} &= 1 \end{aligned} \tag{12.22}$$

A change in m_f^i is assumed to only affect the accumulated heat-released in

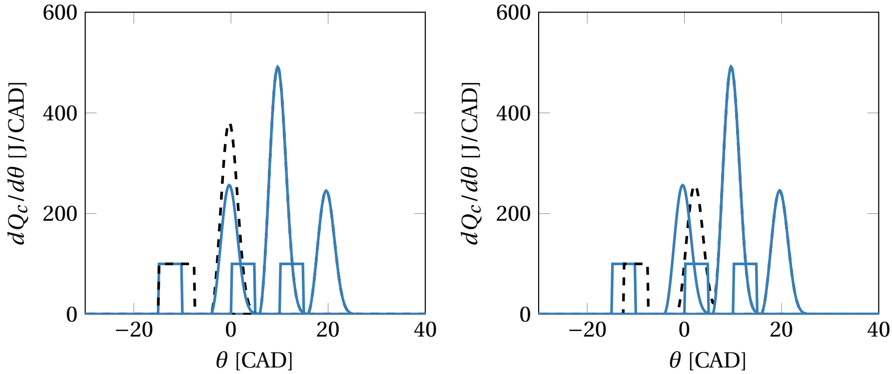

Figure 12.3 The assumed relation between changes in m_f^i (left) and θ_{SOI}^i (right) to changes in $dQ_c/d\theta$. An increase in m_f^i results in an increase in accumulated $dQ_c^i/d\theta$, and a shift in θ_{SOI}^i results in a shift in $dQ_c^i/d\theta$.

$dQ_c^i/d\theta$, which gives

$$\frac{\partial}{\partial m_f^i}\frac{dQ_c}{d\theta} = \frac{Q_{\mathrm{LHV}}}{\int dQ_c^i}\frac{dQ_c^i}{d\theta} \tag{12.23}$$

These assumptions are illustrated in Fig. 12.3. In both cases, the shape of $dQ_c/d\theta$ is preserved. It is also assumed that $\Delta \boldsymbol{u}^j$ and $dQ_c^i/d\theta$ are decoupled when $i \neq j$ and that ignition delays remain constant. These are approximations since subsequent injections are coupled both through ignition delay and rail pressure. The shape of $dQ_c/d\theta$ is also known to change slightly with m_f and θ_{SOI}. If more accurate combustion models are available, those could be incorporated for potential controller-performance improvement. The approximations made could still be motivated for small changes in $\Delta \boldsymbol{u}$, since feedback from subsequent engine cycles corrects for unmodeled effects. Second derivatives, necessary for computing the Hessians in (12.15) are given by

$$\begin{aligned}
\frac{\partial^2}{\partial(\theta_{\mathrm{SOI}}^i)^2}\frac{dQ_c}{d\theta} &= \frac{d^3Q_c^i}{d\theta^3} \\
\frac{\partial^2}{\partial\theta_{\mathrm{SOI}}^i\partial m_f^i}\frac{dQ_c}{d\theta} &= -\frac{Q_{\mathrm{LHV}}}{\int dQ_c^i}\frac{d^2Q_c^i}{d\theta^2} \\
\frac{\partial^2}{\partial(\partial m_f^i)^2}\frac{dQ_c}{d\theta} &= 0
\end{aligned} \tag{12.24}$$

To summarize, we have derived the following quantities relating $\Delta \boldsymbol{u}$ to $\Delta dQ_c/d\theta$

$$\nabla \frac{dQ_c}{d\theta} = \left(\frac{Q_{\text{LHV}}}{\int dQ_c^1} \frac{dQ_c^1}{d\theta} \quad \frac{d^2 Q_c^1}{d\theta^2} \quad \cdots \quad \frac{Q_{\text{LHV}}}{\int dQ_c^M} \frac{dQ_c^M}{d\theta} \quad \frac{d^2 Q_c^M}{d\theta^2} \right)^T$$

$$\nabla^2 \frac{dQ_c}{d\theta} = \text{diag} \left\{ \begin{pmatrix} 0 & -\frac{Q_{\text{LHV}}}{\int dQ_c^i} \frac{d^2 Q_c^i}{d\theta^2} \\ -\frac{Q_{\text{LHV}}}{\int dQ_c^i} \frac{d^2 Q_c^i}{d\theta^2} & \frac{d^3 Q_c^i}{d\theta^3} \end{pmatrix} \right\} \tag{12.25}$$

where $\nabla^2 dQ_c/d\theta$ is a block-diagonal matrix.

From $d\Delta Q_c/d\theta$ to Δp

The relation between $d\Delta Q_c/d\theta$ and Δp can now be established with the linearized pressure model introduced in Chapter 11

$$\frac{d\Delta p}{d\theta} = -\left(\frac{\gamma}{V} \frac{dV}{d\theta} + \frac{d\mu(p_0, \theta)}{dp} \right) \Delta p + \frac{\gamma - 1}{V} \frac{d\Delta Q_c}{d\theta} \tag{12.26}$$

where Δp is the first-order deviation from the initial pressure p_0 due to $d\Delta Q_c/d\theta$, which is related to $\Delta \boldsymbol{u}$ through

$$\frac{d\Delta Q_c}{d\theta} = \left(\nabla \frac{dQ_c}{d\theta} \right)^T \Delta \boldsymbol{u} \tag{12.27}$$

The pressure deviation Δp is given by the solution to (12.26)

$$\Delta p(\theta) = \int_{\theta_{\text{IVC}}}^{\theta} \Phi(\theta, \vartheta) \Gamma(\vartheta) \frac{d\Delta Q_c(\vartheta)}{d\vartheta} d\vartheta \tag{12.28}$$

where

$$\Phi(\theta, \vartheta) = \exp\left(-\int_{\vartheta}^{\theta} \frac{d\mu(p_0, \tau)}{dp} d\tau \right) \left(\frac{V(\vartheta)}{V(\theta)} \right)^{\gamma}$$

$$\Gamma(\vartheta) = \frac{\gamma - 1}{V(\vartheta)} \tag{12.29}$$

Figure 12.4 shows how Δp is related to $\Delta \boldsymbol{u}$ (dashed), together with p_0 (solid, black), and p at $\boldsymbol{u}_0 + \Delta \boldsymbol{u}$ (solid, blue), obtained by solving the nonlinear model (11.2). Note that there is a deviation between the linear approximation and the solution to (11.2).

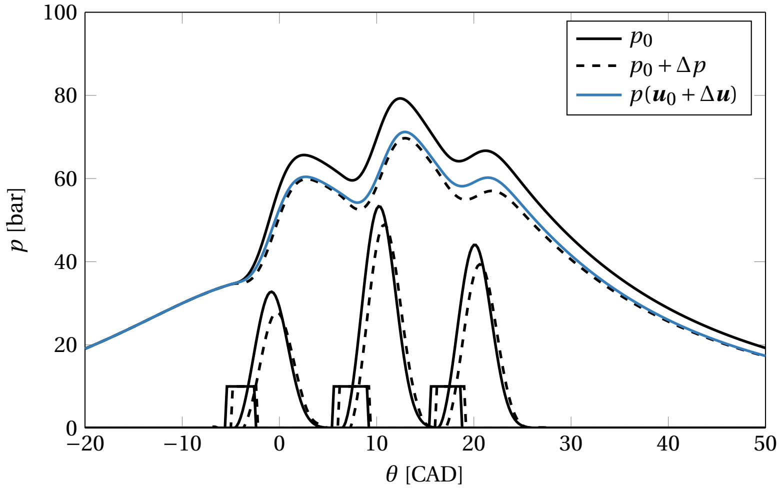

Figure 12.4 An illustration of how $\Delta \boldsymbol{u}$ affects Δp through (12.28) (dashed). The initial pressure p_0 (solid, black) is also presented together with p at $\boldsymbol{u}_0 + \Delta \boldsymbol{u}$, computed with the nonlinear model (11.2) (solid, blue).

With (12.28), the gradients with respect to p, p_{IMEP} and $dp/d\theta$ are given by

$$\begin{aligned} \nabla p &= \int_{\theta_{\mathrm{IVC}}}^{\theta} \Phi(\theta,\vartheta)\Gamma(\vartheta)\left(\nabla \frac{dQ_c(\vartheta)}{d\vartheta}\right) d\vartheta \\ \nabla p_{\mathrm{IMEP}} &= \frac{1}{V_d}\int_{\theta_{\mathrm{IVC}}}^{\theta_{\mathrm{EVO}}} \nabla p dV \\ \nabla \frac{dp}{d\theta} &= \frac{d\nabla p}{d\theta} \end{aligned} \tag{12.30}$$

Hessians are given by

$$\begin{aligned} \nabla^2 p &= \int_{\theta_{\mathrm{IVC}}}^{\theta} \Phi(\theta,\vartheta)\Gamma(\vartheta)\left(\nabla^2 \frac{dQ_c(\vartheta)}{d\vartheta}\right) d\vartheta \\ \nabla^2 p_{\mathrm{IMEP}} &= \frac{1}{V_d}\int_{\theta_{\mathrm{IVC}}}^{\theta_{\mathrm{EVO}}} \nabla^2 p dV \end{aligned} \tag{12.31}$$

Note that the gradients and Hessians above, except for ∇p_{IMEP} and $\nabla^2 p_{\mathrm{IMEP}}$, are functions of θ.

$\mathbf{NO_x}$

The NO_x constraint was linearized using the NO_x-formation model in Sec 2.5. Since this model is not easily linearized, partial derivatives of the cylinder-out

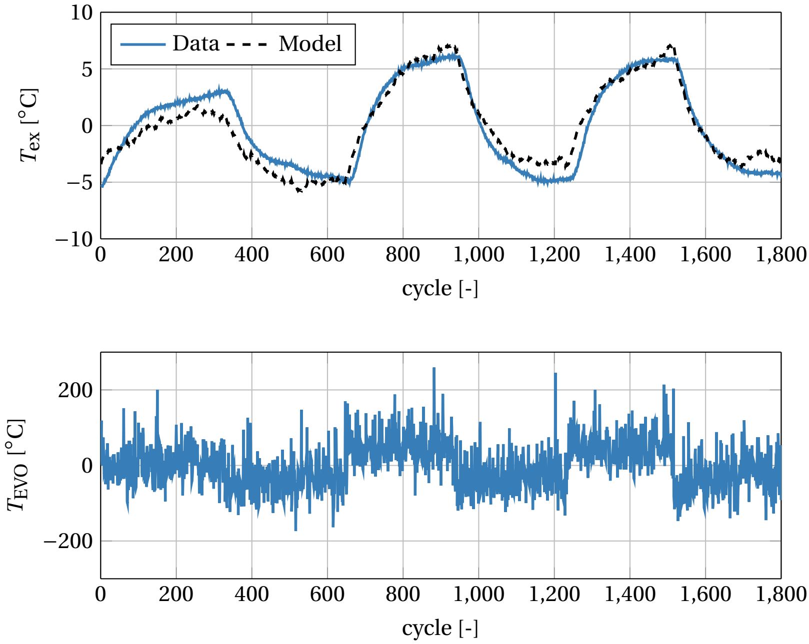

Figure 12.5 Experimental T_{ex} and T_{EVO} data (solid) together with (12.33) output (dashed) when varying θ_{SOI}. The temperature scales are relative to steady-state values at $p_{IMEP} = 5$ bar.

NO_x concentration with respect to $\boldsymbol{u}$ was obtained by solving (2.73) and applying numerical differentiation

$$\begin{aligned} \frac{\partial NO_x}{\partial m_f^i} &\approx \frac{NO_x(\boldsymbol{u}_0 + \Delta m_f^i) - NO_x(\boldsymbol{u}_0)}{\Delta m_f^i} \\ \frac{\partial NO_x}{\partial \theta_{SOI}^i} &\approx \frac{NO_x(\boldsymbol{u}_0 + \Delta \theta_{SOI}^i) - NO_x(\boldsymbol{u}_0)}{\Delta \theta_{SOI}^i} \end{aligned} \tag{12.32}$$

In the forward step, $NO_x(\boldsymbol{u}_0 + \Delta \boldsymbol{u})$ was computed by solving (2.73) with modified cylinder pressures, temperatures and heat-release rates $p(\boldsymbol{u}_0 + \Delta \boldsymbol{u})$, $T(\boldsymbol{u}_0 + \Delta \boldsymbol{u})$, $dQ_c/d\theta(\boldsymbol{u}_0 + \Delta \boldsymbol{u})$, obtained from the linearized expressions presented above. With M injections, this amounts to solving (2.73) $2M + 1$ times. The most computationally-demanding part of computing NO_x was to compute gas properties as a function of temperature. To reduce the computational load, it was decided to also use the gas properties computed at $\boldsymbol{u}_0$ in the forward steps.

Exhaust Temperature

Examples of lumped-parameter T_{ex} models, suitable for control applications are presented in [Eriksson and Nielsen, 2014]. This methodology was adopted here and used to model the relation between the temperature at exhaust-valve opening (EVO) T_{EVO} and T_{ex}

$$\Delta T_{\text{ex}}(k+1) = \Phi_{T_{\text{ex}}}\Delta T_{\text{ex}}(k) + \Gamma_{T_{\text{ex}}}\Delta T_{\text{EVO}}(k) \tag{12.33}$$

where $\Delta T_{\text{ex}}(k)$ and $\Delta T_{\text{EVO}}(k)$ are temperature deviations from an equilibrium point T^0_{ex}, T^0_{EVO}, and $\Phi_{T_{\text{ex}}}$ and $\Gamma_{T_{\text{ex}}}$ are model parameters. Differentiation with respect to T_{EVO}

$$\nabla T_{\text{EVO}} = \frac{V(\theta_{\text{EVO}})T_{\text{IVC}}}{p_{\text{IVC}}V_{\text{IVC}}}\nabla p(\theta_{\text{EVO}}) \tag{12.34}$$

establishes a relation with $\nabla p(\theta_{\text{EVO}})$, which is given by (12.30).

Experimental T_{ex} and T_{EVO} data (solid) during θ_{SOI} step changes are presented together with (12.33) output (dashed) in Fig. 12.5. The temperature scales are relative to steady-state values at $p_{\text{IMEP}} = 5$ bar. Values for $\Phi_{T_{\text{ex}}}$ and $\Gamma_{T_{\text{ex}}}$ were obtained from engine data and the MATLAB system-identification toolbox.

In order to incorporate the long time constants of T_{ex} into the MPC problem formulation, exhaust temperature was predicted over a longer horizon $H_p^{T_{\text{ex}}} = 500$ and with a longer sampling interval, ($n_{T_{\text{ex}}} = 100$ cycles). Moreover, the model was augmented with a disturbance state $d_{T_{\text{EVO}}}$ to keep track of the model steady-state offset

$$\begin{aligned}\Delta T_{\text{ex}}(k+1) &= \Phi_{T_{\text{ex}}}\Delta T_{\text{ex}}(k) + \Gamma_{T_{\text{ex}}}(\Delta T_{\text{EVO}}(k) + d_{T_{\text{EVO}}}(k))\\ d_{T_{\text{EVO}}}(k+1) &= d_{T_{\text{EVO}}}(k)\end{aligned} \tag{12.35}$$

The Kalman filter presented in Chapter 3 was then used to estimate $d_{T_{\text{EVO}}}$ using (12.35) and T_{ex} measurements.

QP Approximations

Constraint Fulfillment With gradients and Hessians available, the QP approximation of (12.3) is given by

$$\begin{array}{lll}\underset{\Delta U}{\text{minimize}} & \displaystyle\sum_{k=1}^{H_p} \hat{J}_{\theta_{\text{CT}}}(k) + \hat{J}_{p_{\text{IMEP}}}(k) + J_{\Delta \boldsymbol{u}}(k) & \\ \text{subject to} & p^0_{\max} + \nabla p_0(\theta_j)\Delta \boldsymbol{u}(k) \le p^c_{\max} & \theta_j = \theta_0,\dots,\theta_f,\ k = 1,\dots,H_p \\ & dp^0_{\max} + \nabla dp_0(\theta_j)/d\theta \Delta \boldsymbol{u}(k) \le dp^c_{\max} & \theta_j = \theta_0,\dots,\theta_f,\ k = 1,\dots,H_p \\ & \text{NO}^0_x + \nabla \text{NO}^0_x \Delta \boldsymbol{u}(k) \le \text{NO}^c_x & k = 1,\dots,H_p \\ & T^0_{\text{ex}} + \Delta T_{\text{ex}}(k) \ge T^c_{\text{ex}} & k = n_{T_{\text{ex}}},\dots,H_p^{T_{\text{ex}}} \\ & \boldsymbol{u}_0 + \Delta \boldsymbol{u}(k) \in \hat{\mathbb{U}} & k = 1,\dots,H_p\end{array} \tag{12.36}$$

The cost function $\hat{J}_{\theta_{\mathrm{CT}}}$ is given by

$$\hat{J}_{\theta_{\mathrm{CT}}}(k) = \alpha \begin{pmatrix} f^1_{\theta_{\mathrm{CT}}} \\ \vdots \\ f^M_{\theta_{\mathrm{CT}}} \end{pmatrix}^T \Delta \boldsymbol{u}(k) + \Delta \boldsymbol{u}^T(k) \begin{pmatrix} H^1_{\theta_{\mathrm{CT}}} & 0 & 0 \\ 0 & \ddots & 0 \\ 0 & 0 & H^M_{\theta_{\mathrm{CT}}} \end{pmatrix} \Delta \boldsymbol{u}(k) \tag{12.37}$$

where

$$\begin{aligned} f^i_{\theta_{\mathrm{CT}}} &= \begin{pmatrix} (\theta^{r,i}_{\mathrm{CT}} - \theta^{i,0}_{\mathrm{CT}})^2 \\ -2m^{i,0}_f(\theta^{r,i}_{\mathrm{CT}} - \theta^{i,0}_{\mathrm{CT}}) \end{pmatrix} \\ H^i_{\theta_{\mathrm{CT}}} &= \alpha \begin{pmatrix} 0 & -(\theta^{r,i}_{\mathrm{CT}} - \theta^{i,0}_{\mathrm{CT}}) \\ -(\theta^{r,i}_{\mathrm{CT}} - \theta^{i,0}_{\mathrm{CT}}) & m^{i,0}_f \end{pmatrix} \end{aligned} \tag{12.38}$$

Furthermore, the cost function $\hat{J}_{p_{\mathrm{IMEP}}}(k)$ is given by

$$\begin{aligned} \hat{J}_{p_{\mathrm{IMEP}}}(k) = -\beta(p^r_{\mathrm{IMEP}} - p_{\mathrm{IMEP},0})\big(2\nabla p^T_{\mathrm{IMEP},0}\Delta \boldsymbol{u}(k) + \Delta \boldsymbol{u}^T(k)\nabla^2 p_{\mathrm{IMEP},0}\Delta \boldsymbol{u}(k)\big) \\ + \beta \Delta \boldsymbol{u}^T(k)\nabla p_{\mathrm{IMEP},0}\nabla p^T_{\mathrm{IMEP},0}\Delta \boldsymbol{u}(k) \end{aligned} \tag{12.39}$$

Index 0 in (12.36) to (12.39) above denotes cycle $k = 0$.

Pressure Tracking The QP approximation (12.7)

$$\begin{aligned} \underset{\Delta U}{\text{minimize}} \quad & \sum_{k=1}^{H_p} \hat{J}_p(k) + J_{\Delta \boldsymbol{u}}(k) \\ \text{subject to} \quad & \boldsymbol{u}_0 + \Delta \boldsymbol{u}(k) \in \mathbb{U}, \quad k = 1, \ldots, H_p \end{aligned} \tag{12.40}$$

is obtained by computing the approximated pressure-tracking cost

$$\begin{aligned} \hat{J}_p(k) = -\sum_{\theta_j=\theta_0}^{\theta_f} \alpha_{tr}(p^r(\theta_j) - p_0(\theta_j))\big(2\nabla p^T_0(\theta_j)\Delta \boldsymbol{u}(k) + \Delta \boldsymbol{u}^T(k)\nabla^2 p_0(\theta_j)\Delta \boldsymbol{u}(k)\big) \\ + \alpha_{tr}\boldsymbol{u}^T(k)\nabla p_0(\theta_j)\nabla p^T_0(\theta_j)\Delta \boldsymbol{u}(k) \end{aligned} \tag{12.41}$$

With the QP approximations of (12.3) and (12.7) defined, the following two sections cover additional logic for adding and removing injections and practical modifications for constraint fulfillment.

12.3 Adding and Removing Injections

The optimal number of injections changes depending on operating conditions. This was shown in Chapter 10 and is also illustrated in Fig. 12.6 where optimal injection configurations for two different p^r are presented. This fact presents the problem of when to add and remove injections. Two different approaches used for (12.36) and (12.40) are presented below.

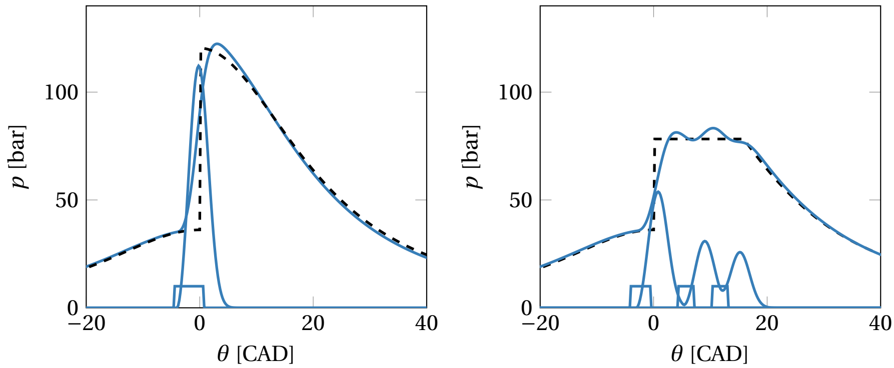

Figure 12.6 The optimal number of injections changes depending on the operating conditions. To the right, a single fuel injection is optimal for tracking the constant-volume combustion reference pressure (dashed). To the left, it is instead optimal with three fuel injections for tracking of a limited-pressure cycle (dashed).

Constraint Fulfillment

The simulation results presented in Chapter 10 suggested the following logic for adding and removing injections when solving (12.3) with up to three injections, pilot, main and post:

- Add a pilot injection if any of the predicted outputs NO_x, $p_{\max}$ or $dp/d\theta$ are larger than $x^c - \epsilon_x^{\mathrm{add}}$.
- Add a post injection if the predicted T_{ex} is smaller than $T_{\mathrm{ex}}^c + \epsilon_{T_{\mathrm{ex}}}^{\mathrm{add}}$.
- Remove the pilot injection if predicted NO_x, $p_{\max}$ and $dp/d\theta$ are smaller than $x^c - \epsilon_x^{\mathrm{rem}}$, and the pilot-fuel mass m_f^1 is sufficiently low.
- Remove the post injection if predicted T_{ex} is larger than $T_{\mathrm{ex}}^c + \epsilon_{T_{\mathrm{ex}}}^{\mathrm{rem}}$, and the post-fuel mass m_f^3 is sufficiently low.

The constraint margins should fulfill $\epsilon_x^{\mathrm{rem}} > \epsilon_x^{\mathrm{add}} > 0$ to avoid limit cycles.

Adding and removing injections introduces disturbances in p_{IMEP} and subsequent θ_{CT}. Compensation on the form

$$\begin{aligned} \theta_{\mathrm{SOI}}^2(k+1) &= \theta_{\mathrm{SOI}}^2(k) \pm \Delta\theta^{\mathrm{adj}} \\ m_f^2(k+1) &= m_f^2(k) \pm \Delta m_f^{\mathrm{adj}} \end{aligned} \tag{12.42}$$

was therefore introduced. The compensation in (12.42) adjusts $\theta_{\mathrm{SOI}}^2(k+1)$ when a pilot injection is added or removed to compensate for variation in ignition de-

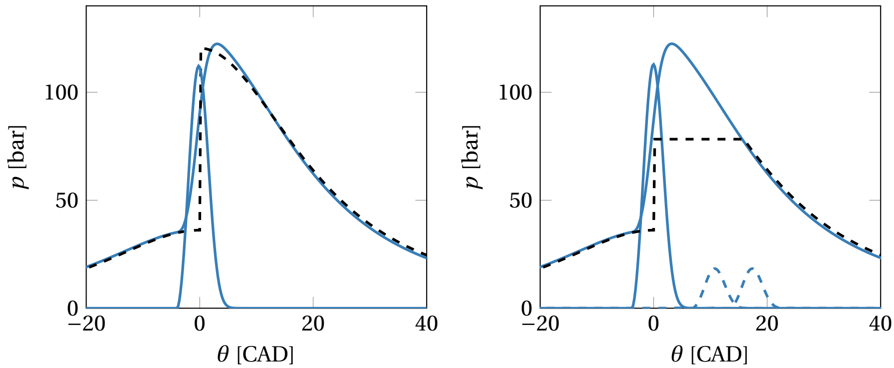

Figure 12.7 An illustration of how additional inactive injections were modeled using extrapolation. Here, the extrapolation is performed when p^r changes from a constant-volume cycle (left) to a limited-pressure cycle (right). Two additional injections are extrapolated from the currently active single-injection heat-release rate.

lay, and adjusts $m_f^2(k+1)$ when a pilot or post injections is added or removed to compensate for variation in p_{IMEP}.

Pressure Tracking

A different method was adopted in (12.40) for adding and removing injections. The method used for adding injections was to extrapolate from already active injections. For example, if injection i is inactive, $\Delta \boldsymbol{u}$ with respect to injection i is assumed to correspond to variations of a shifted ($\Delta\theta$) and rescaled (x_i) heat-release rate $dQ_c^a/d\theta$, corresponding to an already active injection

$$\frac{dQ_c^i}{d\theta} = x_i \frac{dQ_c^a}{d\theta}(\theta - \Delta\theta) \tag{12.43}$$

Extrapolation was conducted when p^r changed significantly, as presented in Fig. 12.7. Inactive injections were then turned on if the solution to (12.40) suggested that m_f^i should be increased. An alternative solution would be to instead solve (12.40) with and without extrapolated injections separately, and add injections if the corresponding cost is significantly lower. Injections were turned off once the controller reached sufficiently low m_f^i.

12.4 Constraint Handling

To guarantee feasible solutions to (12.36), output constraints were softened by introducing variables ϵ_x

$$\begin{aligned} x_0 + \nabla x_0^T \Delta \boldsymbol{u}(k) &\leq x^c + \epsilon_x \\ \epsilon_x &\geq 0 \end{aligned} \tag{12.44}$$

and adding corresponding terms

$$\rho_x \epsilon_x^2 \tag{12.45}$$

to the cost function to penalize constraint violation. This modification guarantees feasible solutions with respect to output constraints even if the constraints can not be fulfilled. By choosing ρ_x sufficiently large, the solution will however always fulfill the output constraint if possible [Maciejowski, 2002]. Constraint margins x_σ were also introduced for constraint fulfillment despite stochastic cycle-to-cycle variation

$$\begin{aligned} x_0 + \nabla x_0 \Delta \boldsymbol{u}(k) &\leq x^c + \epsilon_x + 2x_\sigma \\ \epsilon_x &\geq 0 \end{aligned} \tag{12.46}$$

The constraint margins were here pre-computed from measured output standard deviations, meaning that the margins provide probabilistic guarantees for constraint fulfillment. An alternative approach would be to estimate x_σ on-line. The reason for introducing constraint margins was to remediate the problem of stochastic constraint violation that occured in previous chapters.

12.5 Experimental Results

An experimental controller evaluation was conducted to test the controller performance in transient operation. The evaluation was done by testing the ability of MPC (12.36) to fulfill different constraints during p^r_{IMEP} step changes. MPC (12.40) was tested by varying p^r parameters. Experimental operating conditions are presented in Table 12.1. In some of the experiments, it was decided not to turn off the pilot injection completely to suppress the pressure-rise rate of the main-injection.

Constraint Fulfillment

This section presents experimental results for MPC (12.36). The controller was tuned for θ^r_{CT}- and p^r_{IMEP}-tracking response times within 10 engine cycles. Controller gains and input constraints used are presented in Table 12.2. Gain scheduling was implemented by increasing R_{SOI} (×4) for the controller to vary θ_{SOI} more cautiously in the vicinity of a constraint limit. A prediction horizon of two

Table 12.1 Operating Conditions

p_{IMEP}	4-10 bar
N_{speed}	1200 rpm
p_{rail}	1000 bar
EGR	0-30 %
fuel	80/20 vol% gasoline/n-heptane

engine cycles $H_p = 2$ was used. This enabled mean QP-solver computation times of 2 ms. The QP was constructed below 50 ms, where $\approx$ 90% of the time was used to compute the NO_x gradients in (12.32). Fulfillment of each constraint was evaluated separately during p^r_{IMEP} step changes. Experimental results are presented in the following sections.

p_{max} Handling of $p_{\max}$ constraints was investigated by letting the controller follow p^r_{IMEP} step changes from 5 to 10 bar with $p^c_{\max} = 80$ bar, see Fig. 12.8. This is far from the real $p^c_{\max}$ of the engine but was used here to illustrate the controller behavior.

As p_{IMEP} was increased from 5 to 10 bar with a single injection, $\theta^r_{\mathrm{CT}} = 8$ CAD could not be maintained without violating $p^c_{\max} = 80$ bar. The controller therefore acted by increasing m^1_f at cycle 290, as $p^c_{\max}$ was approached. This resulted in an additional detected θ^1_{CT} shortly after TDC. Moreover, θ^2_{SOI} had to be delayed 8 CAD for constraint fulfillment. As p^r_{IMEP} decreased, the controller returned to a single-injection configuration with $\theta_{\mathrm{CT}} = \theta^r_{\mathrm{CT}}$. The reason for removing the pilot injection when the constraint became inactive was because the controller prioritized the larger main injection to follow θ^r_{CT} due to the higher main-injection cost-function penalty. This controller behavior was a result of weighting θ_{CT} errors with m^i_f in (12.4). The pilot injection was then turned off once m^1_f was sufficiently low. The dashed line in the mid-left subdiagram in Fig. 12.8 indicates the level for which the pilot injection was turned off if no output constraints were active.

Table 12.2 MPC weights and constraints for (12.36), units for θ_{SOI} and m_f are [CAD] and [mg].

$\alpha = 0.0005$	$\beta = 400$	$R_{\theta_{\mathrm{SOI}}} = 5$	$R_{m_f} = 2$
$-2.5 \le \Delta\theta_{\mathrm{SOI}} \le 2.5$	$-10 \le \Delta m_f \le 10$	$-25 \le \theta_{\mathrm{SOI}} \le 20$	$0 \le m_f \le 180$

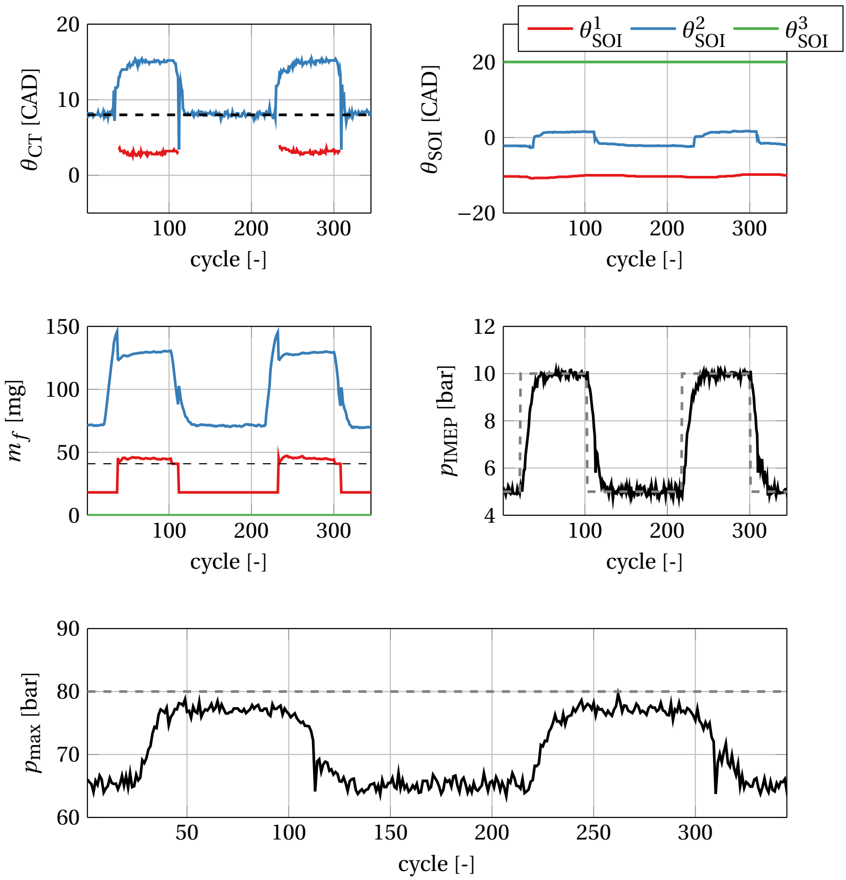

Figure 12.8 Evaluation of p_{max}-constraint fulfillment. The controller was set to follow p^r_{IMEP} step changes from 5 to 10 bar. As p_{IMEP} was increased from 5 to 10 bar with a single injection, $\theta^r_{CT} = 8$ CAD could not be maintained without violating $p^c_{max} = 80$ bar. The controller acted by increasing m^1_f as the constraint was approached. This resulted in an additional detected θ^1_{CT} (red) shortly after TDC. Moreover, θ^2_{SOI} (blue) was delayed 8 CAD for constraint fulfillment. Crank-angle resolved data for cycles 45 and 80 are presented in Fig. 12.9.

Crank-angle resolved data for cycles 45 (left) and 80 (right) are presented in Fig. 12.9. In-cylinder pressure, injector current and $dQ_c/d\theta$ are presented together with vertical lines indicating θ_{CT} and θ^r_{CT}. The dashed pressure curves visible at cycle 45 are predicted cylinder pressures for two subsequent engine cycles. The increase in predicted pressure was due to the increase in p^r_{IMEP}. Two θ_{CT} are detected at cycle 80 due to the increase in m^1_f and θ^2_{SOI}. The red and

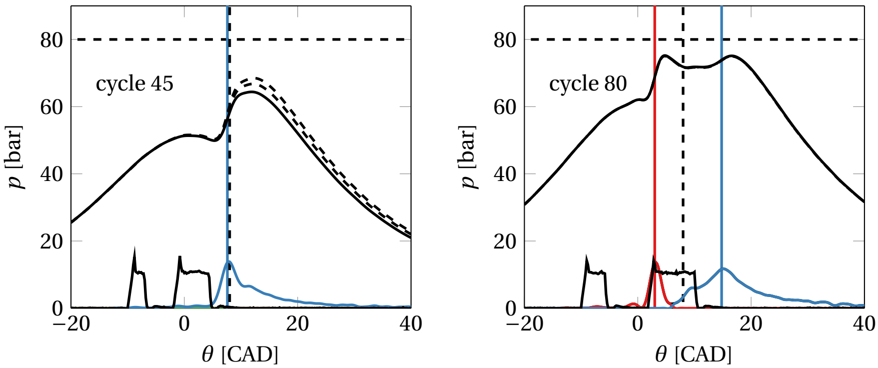

Figure 12.9 In-cycle data for cycles 45 (left) and 80 (right) in Fig. 12.8. In-cylinder pressure, injector current and $dQ_c/d\theta$ are presented together with the vertical lines indicating θ_{CT} and θ^r_{CT}. The dashed pressure curves visible at cycle 45 are predicted cylinder pressures for two subsequent engine cycles. The increase in predicted pressure was due to the increase in p^r_{IMEP}. At cycle 80, it can be seen how the controller separated $dQ_c/d\theta$ between the pilot and main injection.

blue heat-release rates indicate how the combustion detection method separated $dQ_c/d\theta$ into $dQ^1_c/d\theta$ and $dQ^2_c/d\theta$.

dp/dθ The $dp/d\theta$ limit was varied at constant p_{IMEP} in the experiment presented in Fig. 12.10. The controller increased m^1_f and delayed $\theta^{1,2}_{\mathrm{SOI}}$ as $dp^c_{\max}$ was decreased. The pilot and main fuel burned simultaneously and only one combustion timing was therefore detected, meaning that $dQ_c/d\theta$ was attributed to and controlled by the main injection. Disturbances in p_{IMEP} are visible when m^1_f changed. These disturbances could have been attenuated by improving the calibration of $\Delta m^{\mathrm{adj}}_f$ in (12.42). The $dp/d\theta$ limit was occasionally violated due to cycle-to-cycle variation.

In-cycle data for cycles 15 (left) and 150 (right) are presented in Fig. 12.11. The solid and dashed tangents correspond to $dp/d\theta_{\max}$ and $dp^c_{\max}$, respectively. The pilot fuel amount m^1_f was increased and θ^2_{CT} was delayed to fulfill $dp^c_{\max}$. The injected fuel burned simultaneously, which resulted in one combustion timing detected.

NO_x The controller was once again set to follow p^r_{IMEP} step changes to evaluate NO_x-constraint handling where the solution to (2.73) was used as a virtual NO_x sensor, see Fig. 12.12. As p^r_{IMEP} increased, θ^2_{CT} was delayed and m^1_f increased for NO_x to remain below $NO^c_x = 500$ ppm. Constraint violation occurred due to NO_x overshoots as p_{IMEP} was increased. The constraint was however later fulfilled in steady state. The NO_x overshoot could possibly be reduced by adding pilot fuel

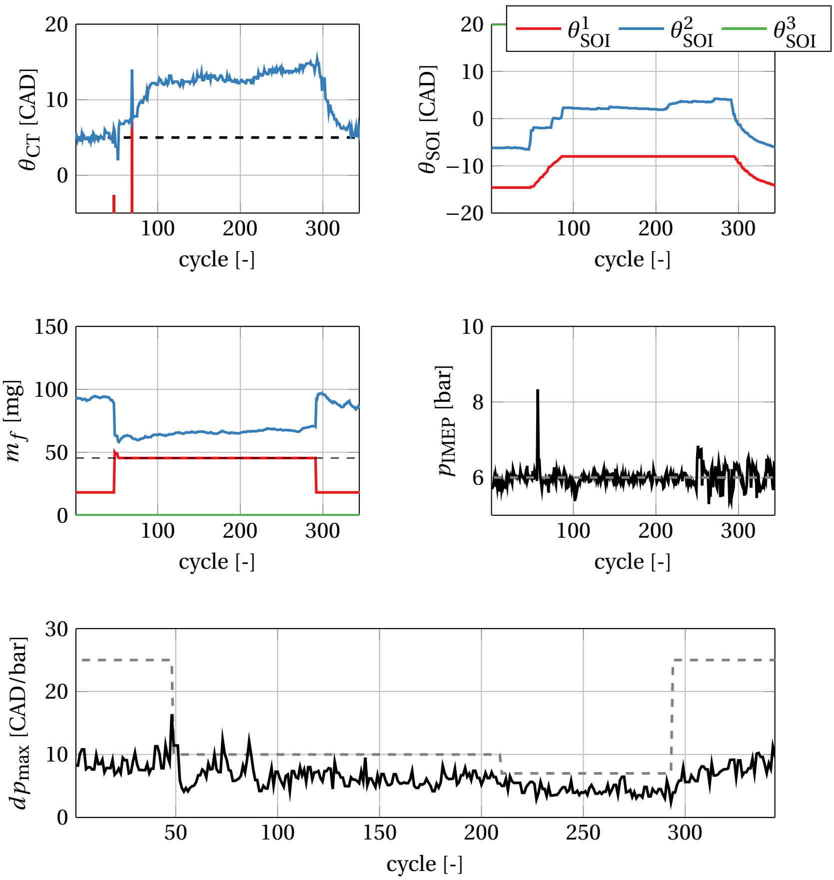

Figure 12.10 Evaluation of $dp/d\theta$ constraint fulfillment where $dp^c_{\max}$ was varied at constant p_{IMEP}. The pilot fuel amount m_f^1 was increased and $\theta_{\mathrm{SOI}}^{1,2}$ were delayed to fulfill the constraint. The pilot and main fuel burned simultaneously and only one combustion timing was detected, meanin87g that $dQ_c/d\theta$ was attributed to and controlled by the main injection. Disturbances in p_{IMEP} are visible when m_f^1 changes around cycle 60 although compensation in m_f^2 was made.

more carefully, allowing for larger θ_{SOI} changes, and/or having a longer prediction horizon. Small NO_x overshoots could however be acceptable if NO_x^c was set to regulate accumulated NO_x emissions.

In-cycle data for cycles 25 (left) and 65 (right) from the experiment in Fig. 12.12 are presented in Fig. 12.13. The solid and dashed purple lines correspond to in-cylinder NO_x and NO_x^c, respectively. The pilot-fuel mass m_f^1 was increased and θ_{CT}^2 delayed at cycle 65, in order for $NO_x^c = 500$ ppm to be fulfilled.

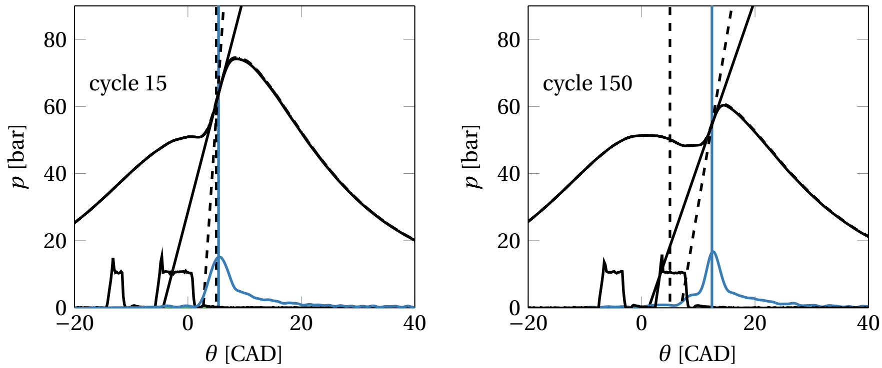

Figure 12.11 In cycle data for cycles 15 (left) and 150 (right) from the experiment in Fig. 12.10. The solid and dashed tangents correspond to $dp/d\theta_{\max}$ and $dp^c_{\max}$ respectively. The controller increased m^1_f and delayed θ^2_{CT} at cycle 150 to fulfill $dp^c_{\max} = 10$ bar/CAD.

T_{ex} Figure 12.14 shows how the controller managed to keep T_{ex} above $T^c_{\text{ex}} = 240°C$, whilst p^r_{IMEP} was varied between 5 and 7 bar. The controller introduced a post injection as T_{ex} approached T^c_{ex}. The post-injection mass m^3_f was then used to regulate T_{ex} above T^c_{ex}. A p_{IMEP} disturbance is visible when the post injection was introduced at cycles 180 and 750.

In-cycle data from cycles 5 (left) and 350 (right) in Fig. 12.14 are presented in Fig. 12.15. A post injection was introduced at cycle 350 to fulfill $T^c_{\text{ex}} = 240°C$ whilst θ^2_{CT} was kept at θ^r_{CT}. The post-injection combustion timing θ^3_{CT} and corresponding heat-release rate $dQ^3_c/d\theta$ (green) were detected by the controller.

Summary

It can be concluded that the controller was able to fulfill the different constraints as intended. Speed of convergence was higher than for the heuristic controller design in Chapter 10 with 10-20 cycles as compared to 40-50 cycles. The model-based controller presented here was also better at avoiding constraint violation. Both because of its predictive capability, and because of its constraint margins.

Pressure Tracking

This section presents experimental results with MPC (12.40). The controller was investigated by varying the pressure-reference parameters α_v, θ_{SOC} and Q^r_c. Controller parameters used are presented in Table. 12.3.

The ability to follow α_v changes with two injections is presented during a 10-cycle transition from p^r_1 with $\alpha_v = 0.5$ (red) to p^r_2 with $\alpha_v = 0.2$ (blue) in

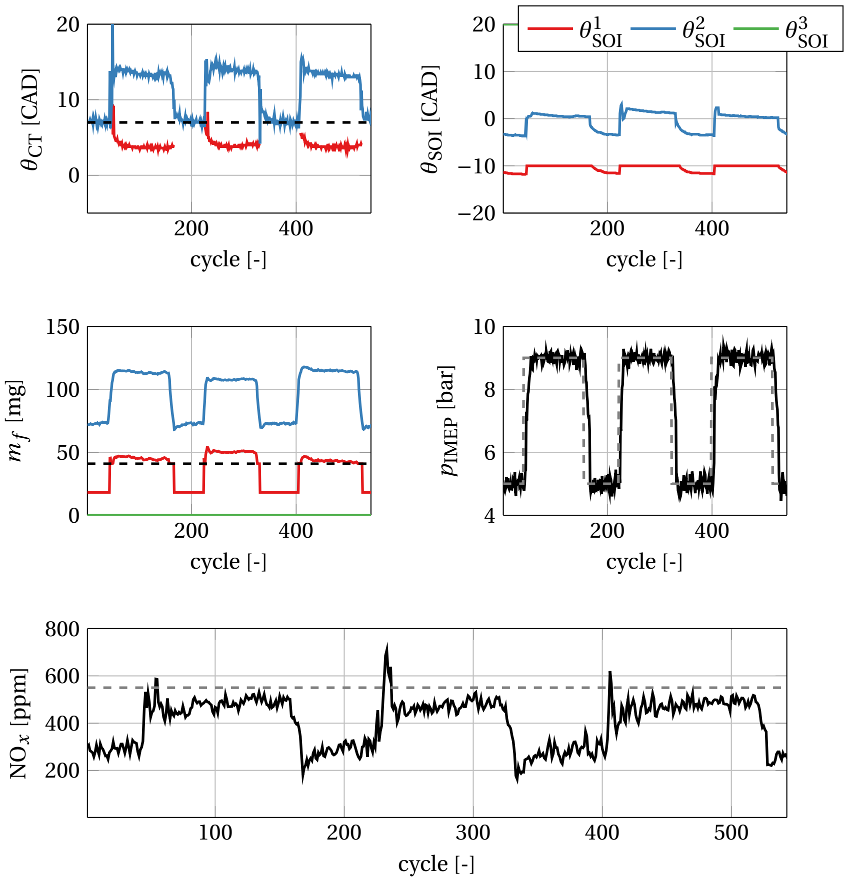

Figure 12.12 Evaluation of NO_x-constraint fulfillment. As p^r_{IMEP} increased, θ^2_{CT} was delayed and m^1_f increased for the constraint to be fulfilled. Constraint violation occured as p_{IMEP} increased. The constraint was later fulfilled in steady state.

Fig. 12.16. With $\alpha_v = 0.5$, the controller had a relatively large m^1_f. With more constant-pressure combustion, the controller increased m^2_f and delayed θ^1_{SOI} and θ^2_{SOI}.

Figure 12.17 presents in-cycle data during a transition from p^r_1 with $Q^r_c = 3000$ J (red) to p^r_2 with $Q^r_c = 6000$ J (blue) with one injection. When Q^r_c was increased, the controller increased m_f whilst θ_{CT} was kept constant.

A θ^r_{SOC} transition from p^r_1 with $\theta^r_{\mathrm{SOC}} = 10$ CAD (red) to p^r_2 with $\theta^r_{\mathrm{SOC}} = 5$ CAD (blue) is presented in Fig. 12.18. When θ^r_{SOC} was advanced, the controller adjusted θ^r_{SOI} whilst m_f was kept constant.

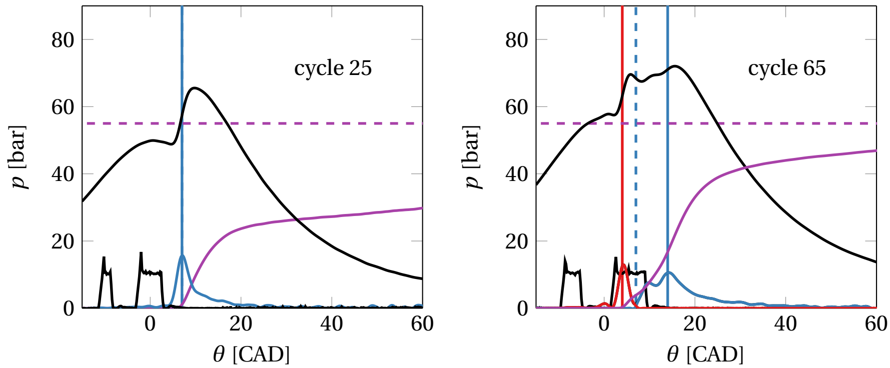

Figure 12.13 In-cycle data for cycles 25 (left) and 65 (right) from the experiment in Fig. 12.12. The solid and dashed purple lines correspond to in-cylinder NO_x and NO_x^c respectively. The pilot-fuel mass m_f^1 was increased and θ_{CT}^2 delayed at cycle 65 for $\mathrm{NO}_x^c = 500$ ppm to be fulfilled.

Data illustrating the suggested method for introducing injections during pressure tracking is shown in Fig. 12.19. For this experiment, the engine was run with diesel fuel. In the upper subdiagram, two injections were used to track a p^r with $\alpha_v = 0.3$. As α_v was changed to 0.1 and Q_c^r was increased in the middle subdiagram in Fig. 12.19, the controller extrapolated (dashed) from the first detected heat-release rate to apprehend how a post injection would affect p. The post injection was then introduced, since it would decrease p^r error cost, see the lower subdiagram in Fig. 12.19.

Summary

The pressure-tracking controller was able to adjust fuel injection as p^r parameters were varied. The ratio between m_f^1 and m_f^2 was changed to adjust the combustion duration as α_v was varied. The injected fuel m_f and θ_{SOI} were adjusted to account for changes in Q_c^r and θ_{SOC}^r, respectively. Error-free tracking could not be obtained due to limited controllability and the steep p^r increase during constant-volume combustion. It is believed that improved tracking performance could be obtained with a smoother p^r, and an adjusted γ during the expansion

Table 12.3 Controller weights and constraints for (12.40), units for θ_{SOI} and m_f are [CAD] and [mg].

$\alpha_{tr} = 1$	$R_{\theta_{\mathrm{SOI}}} = 0.5$		$R_{m_f} = 3$
$-0.5 \le \Delta\theta_{\mathrm{SOI}} \le 0.5$	$-10 \le \Delta m_f \le 10$	$-25 \le \theta_{\mathrm{SOI}} \le 20$	$0 \le m_f \le 120$

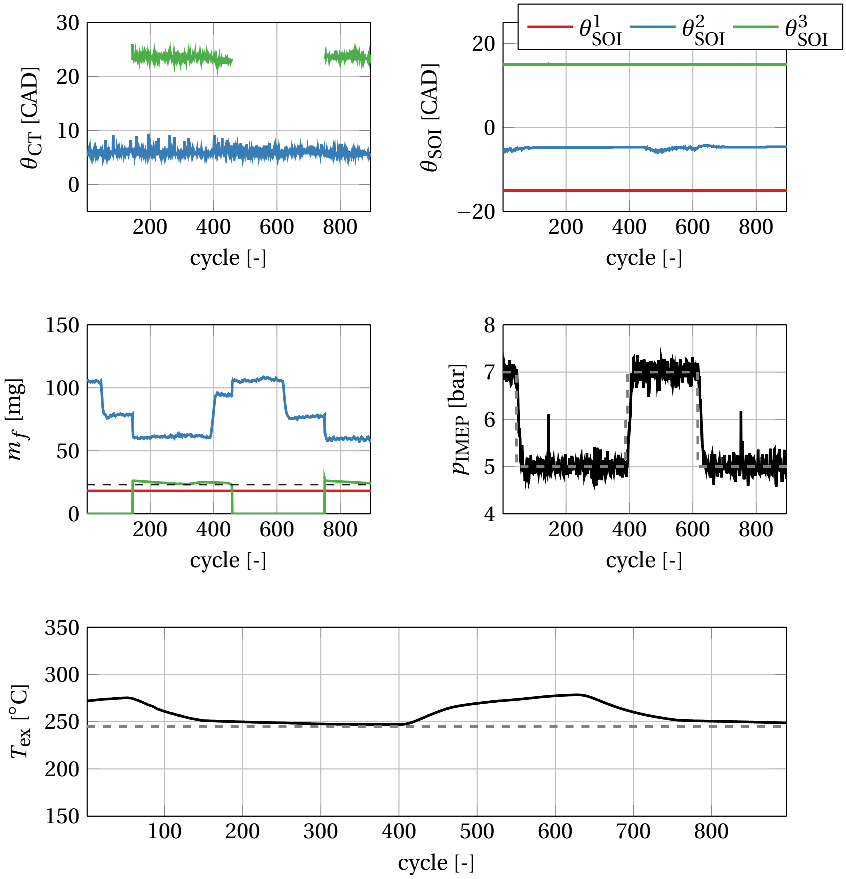

Figure 12.14 Evaluation of T_{ex}-constraint fulfillment. The ability to fulfill T_{ex} was evaluated by decreasing p_{IMEP} from 7 to 5 bar. A post-injection was introduced when T_{ex} approached $T^c_{\mathrm{ex}} = 240\ °C$. The controller then regulated T_{ex} by adjusting m^3_f.

stroke. A fuel-injection system that allows for direct control of the injection rate would improve controllability further. The controllability could also be improved by increasing the fuel-injection rate, which would allow for an increased number of injections in a shorter θ interval.

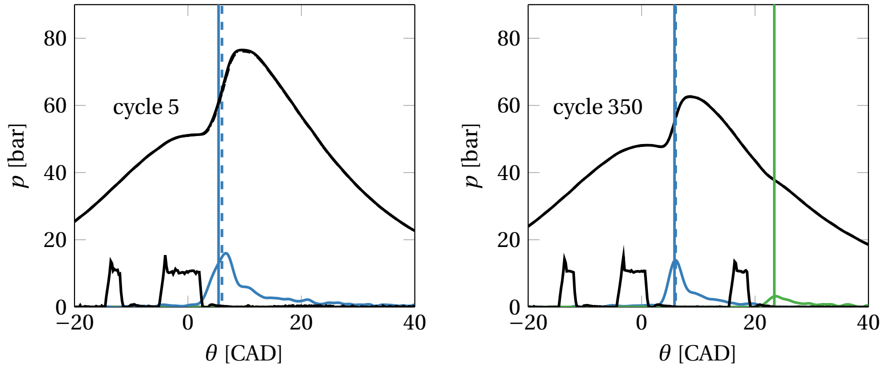

Figure 12.15 In-cycle data for cycles 5 (left) and 350 (right) from the experiment in Fig. 12.14. At cycle 350, a post injection was introduced to fulfill $T^c_{\text{ex}} = 240°C$ whilst θ^2_{CT} was kept at θ^r_{CT}. The post-injection combustion timing θ^3_{CT} and corresponding heat-release rate $dQ^3_c/d\theta$ (green) were detected by the controller.

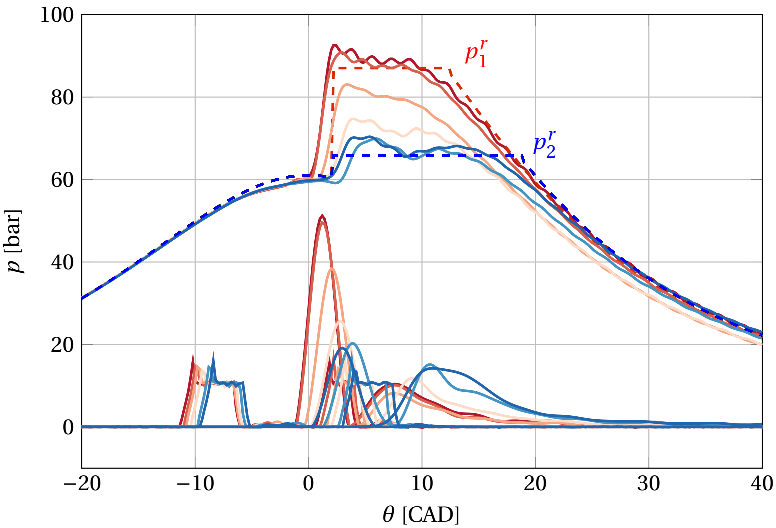

Figure 12.16 The controller's ability to follow α_v changes with two injections. During this experiment, α_v was changed from 0.5 (red) to (blue) 0.2. To obtain more constant-pressure combustion, the controller increased m^2_f and delayed θ^1_{SOI} and θ^2_{SOI}.

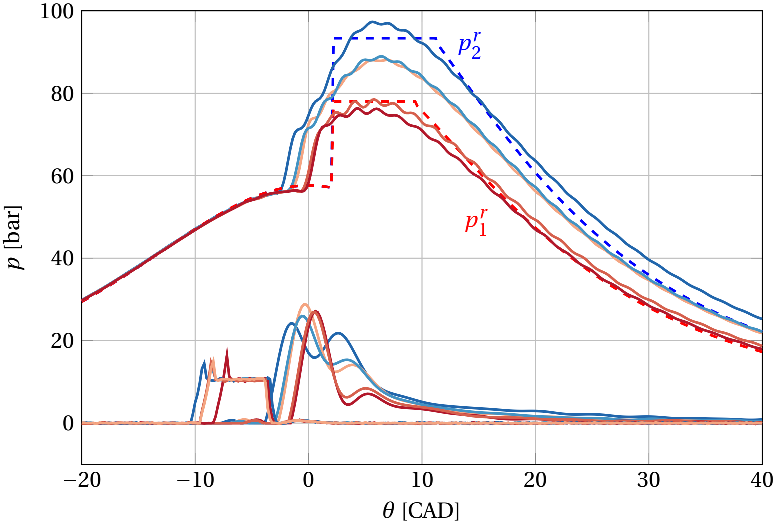

Figure 12.17 A transition from p_1^r with Q_c^r = 3000 J (red) to p_2^r with Q_c^r = 6000 J (blue), with one injection. When Q_c^r was increased, the controller increased m_f whilst θ_{CT} was kept constant.

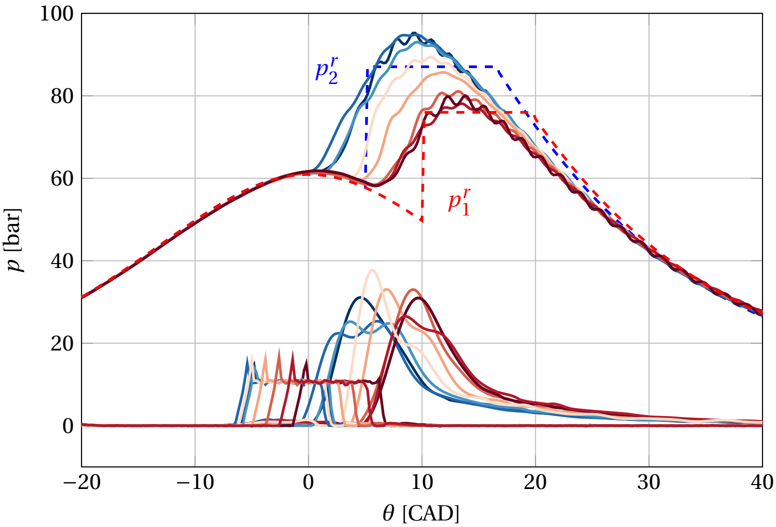

Figure 12.18 A θ_{SOC}^r transition from p_1^r with θ_{SOC}^r = 10 CAD (red) to p_2^r with θ_{SOC}^r = 5 CAD (blue). As θ_{SOC}^r was advanced, the controller adjusted θ_{SOI} whilst m_f was kept constant.

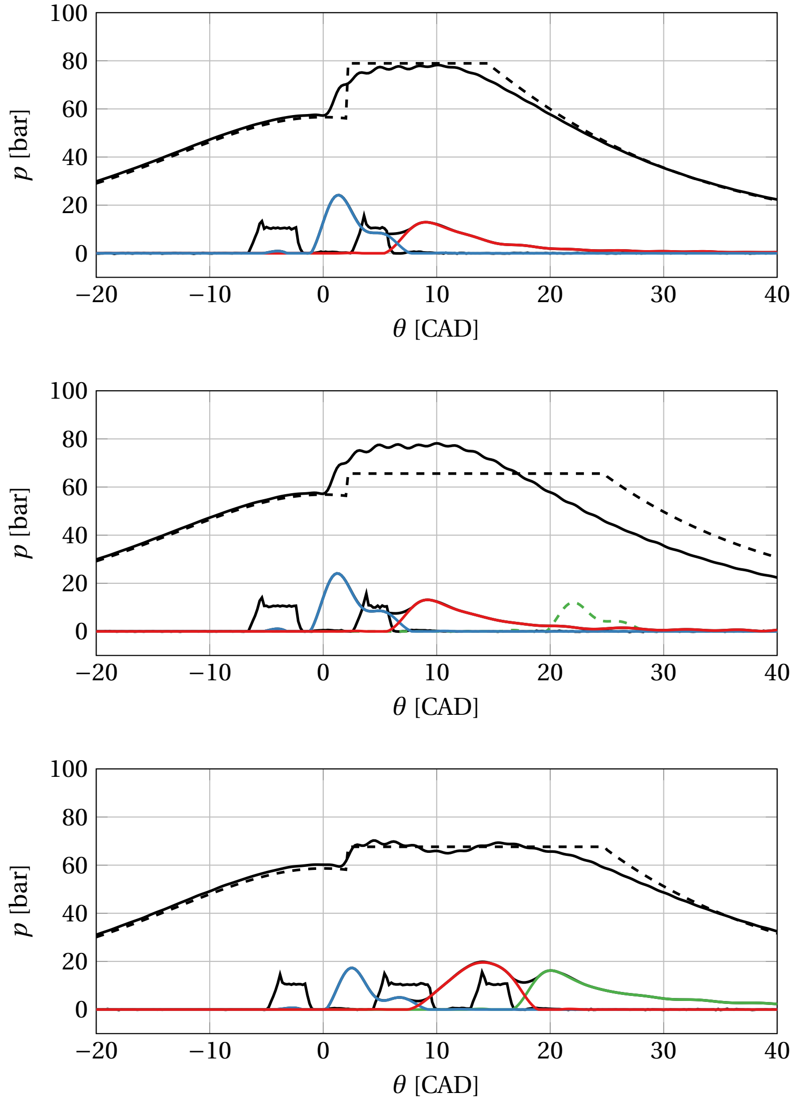

Figure 12.19 The suggested method for introducing injections during pressure tracking. In the upper subdiagram, two injections were used to track a p^r with $\alpha_v = 0.3$. As α_v was changed to 0.1 and Q_c^r was increased in the middle subdiagram, the controller extrapolated (dashed) from the first detected heat-release rate to apprehend how a third post injection would affect p. The post-injection was introduced since it was found to decrease p^r-tracking error, see the lower subdiagram.

12.6 Discussion

The use of empirical, data-based and mean-valued models to describe in-cylinder processes has been a common theme in previous works on optimal engine control for constraint fulfillment, see [Hafner et al., 2000; Stewart and Borelli, 2008; Atkinsson et al., 2009; Karlsson et al., 2010; Grahn et al., 2014].

This chapter combined the heat-release detection and separation method presented in Chapter 4 with the pressure-prediction method in Chapter 11. These methods allowed for a cycle-resolved MPC formulation, where the MPC, in contrast to previous work, can predict the effect from different injections on the cylinder pressure. To the author's knowledge, this is a novel controller-design framework that can be used for both constraint fulfillment and pressure tracking.

Constraint Fulfillment

The proposed MPC for constraint handling in (12.36) worked as intended in the experimental evaluation. It was shown in Chapter 10 that similar transient behavior could be obtained with a simpler PI-controller design. However, the model-based approach adopted in this chapter allowed the controller to predict constraint violation and in that way act beforehand. This, in combination with constraint margins, resulted in smaller NO_x overshoots, and no $p_{\max}$ overshoots, as compared to the PI controller in Chapter 10. Furthermore, the MPC had shorter settling times of 10-20 cycles, as opposed to 40-50 cycles for the PI controller. The model-based controller accounts for variation in combustion characteristics as a function of operating point which makes the feedback loop more robust. The centralized MPC design also allowed the controller to take into account for cross-coupling between control of load and other engine outputs.

Compared to the heuristic PI controller in Chapter 10, the MPC framework provided a systematic way of handling input and output constraints. All constraints were accounted for simultaneously, where it was straightforward to add or remove constraints as long as meaningful solutions existed. The controller was also flexible when adding or removing injections and adjusted the size of the optimization problems accordingly. The model-based methods for adding and removing injections could however be developed further by, for instance, also optimize timings and amounts of the injections introduced.

Even though MPC has its potential benefits, it demands careful tuning so that desired controller behavior is obtained. Poor tuning could result in pathological behavior, such as control of engine load with injection timing or control of exhaust temperature with the main-injection duration, with an offset in load tracking as a result. Further controller development would be to also incorporate gas-system dynamics and actuators. If more accurate combustion models are available, those could be incorporated for potential controller-performance improvement. This may however require a more sophisticated heat-release detection method.

Combustion Detection

The combustion detection method worked well, apart from some exceptions at cycle 60 in Fig. 12.10 and cycle 50 in Fig. 12.12. These errors occurred when a pilot injection was introduced and the controller did not detect the pilot heat-release rate properly. Instead, it detected the main-injection heat-release and a later heat-release peak. One approach to further develop the heat-release detection method would be to instead compute the likelihood of a detected peak being a combustion timing. Such a methodology could make use of a heat-release model and fuel-injection information.

Pressure Tracking

Although tracking of a cycle-resolved pressure reference is an unconventional way of controlling an engine, the results presented in this chapter showed that the presented MPC in (12.40) allowed for this approach. The convergence rate presented here (10 to 15 engine cycles) was comparable to the results in [Zweigl et al., 2015]. Control errors presented here were however somewhat larger than those reported in [Jörg et al., 2015; Zweigl et al., 2015]. With a fuel-injection systems that allows for additional injections during the engine cycle, and more direct control of the fuel-injection rate, it is possible that the controller presented in this chapter could exhibit more accurate cylinder-pressure control.

If this controller design is more favorable than conventional cylinder-pressure feedback controllers that regulate combustion-timing and indicated load remains to be investigated.

12.7 Conclusions

Two model predictive controllers were presented and experimentally evaluated. Both controllers utilized a linearized cylinder-pressure model and a novel combustion-detection method in order to predict in-cylinder pressure variation due to fuel-injection changes. Experimental results demonstrated:

- Fulfillment of constraints with respect to cylinder pressure, engine-out NO_x emissions and exhaust temperature during load changes.
- Tracking of time varying ideal-pressure-cycle trajectories.

In both cases, fuel-injections were added and removed depending on the predicted in-cylinder pressure.

13

Conclusions and Future Research

Demands for reduced emission levels and lowered fuel consumption have created a need for accurate engine control. This has been illustrated in this thesis through an investigation of how model-based closed-loop combustion control can be used to improve the reliability of a low-emission combustion concept. This thesis has also investigated how timings and durations of multiple injections can be decided with feedback control for efficient constraint fulfillment. In both contexts, feedback control reduces the amount of calibration work needed for efficient engine operation. It makes the combustion processes more robust to changes in intake conditions, hardware aging and fuel properties, and lowers the demands for precise actuators. The main results presented in the thesis are summarized below, together with suggestions for future research.

PPC

This thesis investigated model-based control for improved operation of partially premixed combustion (PPC). Designed controllers experimentally demonstrated control of ignition delay, combustion timing and pressure-rise rate in transient operation. Gas-exchange and fuel-injection actuations for improved low-load efficiency were also suggested.

The problems of regulating ignition delay and pressure-rise rate were studied separately in chapters 7 and 8. Since there is an inherent trade-off between ignition delay and pressure-rise rate, however, it would be interesting to investigate concurrent control of these variables. The controller objective could be formulated as a set-point tracking problem with respect to ignition-delay with an upper bound on pressure-rise rate. This behavior could be obtained by combining the model predictive controllers in (7.12) and (8.13).

The PPC experiments presented in the thesis were mainly limited to the low-to-mid load operating range of the engine. This suggests that future work should include a more detailed evaluation of controller performance at higher engine loads. Experiments have, however, showed that it might be difficult to create sufficiently long ignition delays at higher loads with the current experimental setup, and that the combustion characteristics approach those of conventional diesel combustion at higher loads. Manente et al. [2009] suggested that long ignition delays could be achieved at high load with large injections, located early during the compression stroke ($\theta_{\mathrm{SOI}} < -50$ CAD). This strategy was also difficult to implement in the experimental setup used due to preignition of such injections. Preignition avoidance is an interesting control problem related to PPC, that has not been discussed in this thesis. It is possible that hardware adjustments, such as a decreased compression ratio, decreased swirl, and fuels of even higher ON would facilitate high-load PPC operation. It is, however, also possible that such adjustments would make low-load performance more challenging.

Optimal Control

This thesis investigated how multiple injections should be actuated for efficient fulfillment of constraints on pressure, NO_x and exhaust temperature. A hybrid multivariate PI controller was designed and experimentally evaluated. This controller showed an experimental efficiency improvement of 4-5 % compared to a single-injection controller, as restrictive constraints on pressure and NO_x were imposed.

A predictive pressure controller was introduced, where a simple pressure model was used to directly control the in-cylinder pressure using model predictive control. This controller was capable of tracking load and efficient combustion-timing set points, as well as fulfilling constraints. The controller was also able to track ideal-cycle pressure curves. Further development of this controller include enhancement of physical model assumptions, design of a more robust heat-release-detection method, and further investigation of model-based conditions for varying the number of injections. It could also be interesting to add the common-rail pressure as a control variable for increased controllability of the heat-release shape.

Hardware that allows for additional injections and more direct control of the fuel-injection rate could also increase the usefulness of the controller. In-cycle control of the cylinder pressure with the use of similar predictive methods could also be an interesting research topic. An FPGA would be a suitable option for such an application, as the demand for computational speed increases.

Feedforward

The controllers presented in this thesis only utilized feedback control without any feedforward action. It is, however, believed that the performance of the controllers presented could be improved significantly with model-based feedforward control, especially with respect to response times in transient operation.

Design of model-based feedforward controllers that are compatible with the presented controllers is therefore an additional suggested research topic.

Model Predictive Control

Several of the controllers presented in the thesis were based on the principle of model predictive control (MPC). MPC provides a model-based framework that systematically handles output constraints, and the increasing complexity of engine control, for which the number of sensors and actuators have increased during the last decades. MPC also conveniently handled the problem of varying the number of inputs in Chapter 12, where the number of injections changed depending on the engine operating point.

The approach taken in this work was to repeatedly linearize the system model and solve a quadratic program. An alternative that would require additional memory storage but less online computations is explicit MPC, where the optimization problem is solved offline and the optimal input signal is stored in a lookup table [Bemporad et al., 2002]. It is also possible that nonlinear solvers will be fast enough in the near future for the original nonlinear optimization problems to be solved online. Moreover, the problem of deciding the number of injections is a discrete optimization problem. This suggests that a hybrid MPC solution could be used to solve the control problems studied in chapters 10 and 12. These three approaches to MPC are interesting extensions to the work presented here and deserve future investigation.

When solving constrained optimization problems, such as in MPC, one obtains Lagrangian multipliers. These can be interpreted as costs with respect to reference-tracking deviation or efficiency, that has to be paid to fulfill the different constraints. A suggestion for future work is to incorporate these multipliers in engine diagnostics, to analyze and adjust controller constraints so that the price of constraint fulfillment does not become too large. If for instance, it is noted that fulfillment of constraints on pressure-rise rate or NO_x emissions requires a late and inefficient combustion timing at a certain operating point. Then, a supervisory controller could take action by increasing the EGR set point, or by adjusting the efficiency of the after-treatment system to increase the overall engine efficiency.

An additional suggestion for future work would be to investigate how the MPC formulations presented here could be extended or adjusted to find efficient compromises between conflicting constraints such as emissions of soot and NO_x, or ignition delay and pressure-rise rate.

Bibliography

A, B. Kempinski, and J. Rife (1981). *Knock in Spark Ignition Engines*. SAE Technical Paper 810147.

Agrell, F., H.-E. Ångström, B. Eriksson, J. Wikander, and J. Linderyd (2003). *Integrated Simulation and Engine Test of Closed Loop HCCI Control by aid of Variable Valve Timings*. SAE Technical Paper 2003-01-0748.

Akihama, K., Y. Takatori, K. Inagaki, S. Sasaki, and A. M. Dean (2001). *Mechanism of the Smokeless Rich Diesel Combustion by Reducing Temperature*. SAE Technical Paper 2001-01-0655.

Annand, W. (1963). "Heat transfer in the cylinders of reciprocating internal combustion engines". *Proc. Inst. of Mech. Eng.* **177**:1, pp. 973–996.

Aoyagi, Y., T. Kamimoto, Y. Matsui, and S. Matsuoka (1980). *A Gas Sampling Study on the Formation Processes of Soot and NO in a DI Diesel Engine*. SAE Technical Paper 800254.

Askin, A. C., G. E. Barter, T. H. West, and D. K. Manley (2015). "The heavy-duty vehicle future in the United States: a parametric analysis of technology and policy tradeoffs". *Energy Policy* **81**, pp. 1–13.

Åström, K. J. and T. Hägglund (2006). *Advanced PID Control*. ISA – The Instrumentation, Systems, and Automation Society, Research Triangle Park, NC, USA.

Åström, K. J. and R. M. Murray (2010). *Feedback Systems: an Introduction for Scientists and Engineers*. Princeton University Press, Princeton, NJ, USA.

Atkinson, C. M., M. Allain, Y. Kalish, and H. Zhang (2009). *Model-Based Control of Diesel Engines for Fuel Efficiency Optimization*. SAE Technical Paper 2009-01-0727.

Bemporad, A., M. Morari, V. Dua, and E. N. Pistikopoulos (2002). "The explicit linear quadratic regulator for constrained systems". *Automatica* **38**:1, pp. 3–20.

Bengtsson, J., P. Strandh, R. Johansson, P. Tunestål, and B. Johansson (2004). "Closed-loop combustion control of homogeneous charge compression ignition (HCCI) engine dynamics". *Int. J. Adaptive Control and Signal Processing* **18**:2, pp. 167–179.

Bengtsson, J., P. Strandh, R. Johansson, P. Tunestål, and B. Johansson (2006). "Model predictive control of homogeneous charge compression ignition (HCCI) engine dynamics". In: *Proc. IEEE Int. Conf. Control Applications.* Münich, Germany, pp. 1675–1680.

Blom, D., M. Karlsson, K. Ekholm, P. Tunestål, and R. Johansson (2008). *HCCI Engine Modeling and Control using Conservation Principles.* SAE Technical Paper 2008-01-0789.

Borgqvist, P. (2013). *The Low Load Limit of Gasoline Partially Premixed Combustion (PPC)-Experiments in a Light Duty Diesel Engine.* TMHP-13/1091. PhD thesis. Dept. Energy Sciences, Lund University, Lund, Sweden.

Borgqvist, P., P. Tunestål, and B. Johansson (2012). *Gasoline Partially Premixed Combustion in a Light Duty Engine at Low Load and Idle Operating Conditions.* SAE Technical Paper 2012-01-0687.

Borgqvist, P., P. Tunestål, and B. Johansson (2013). "Comparison of negative valve overlap (NVO) and rebreathing valve strategies on a gasoline PPC engine at low load and idle operating conditions". *SAE Int. J. Engines* **6**:2013-01-0902, pp. 366–378.

BorgWarner (24, 2014). *Borgwarner equips new generation of diesel engines from Volkswagen with pressure sensor glow plugs.* press release. BorgWarner. URL: `https://cdn.borgwarner.com/docs/default-source/press-release-downloads/en_bw-equips-new-generation-of-diesel-engines-from-vw-with-psg.pdf` (visited on 2018).

Bosch, R. G. (2011). *Bosch Automotive Handbook, 8th Edition.* Wiley, Chichester, West Sussex, England.

Broy, M., I. H. Kruger, A. Pretschner, and C. Salzmann (2007). "Engineering automotive software". *Proc. IEEE* **95**:2, pp. 356–373.

Brunt, M. F. and C. R. Pond (1997). *Evaluation of Techniques for Absolute Cylinder Pressure Correction.* SAE Technical Paper 970036.

Casella, G. and R. L. Berger (2002). *Statistical Inference.* Duxbury, Pacific Grove, CA, USA.

Castellano, J., A. Chaudhari, and J. Bromham (2013). *Adaptive Temperature Control for Diesel Particulate Filter Regeneration.* SAE Technical Paper 2013-01-0517.

Chartier, C., O. Andersson, B. Johansson, M. Musculus, and M. Bobba (2011). "Effects of post-injection strategies on near-injector over-lean mixtures and unburned hydrocarbon emission in a heavy-duty optical diesel engine". *SAE Int. J. Engines* **4**:1, pp. 1978–1992.

Chiang, C. and A. Stefanopoulou (2005). "Control of thermal ignition delay in gasoline engines". In: *Proc. American Control Conf. (ACC 2005)*. Cape Town, South Africa, pp. 3847–3852.

Chiang, C. and A. Stefanopoulou (2006). "Sensitivity analysis of combustion timing and duration of homogeneous charge compression ignition (HCCI) engines". In: *Proc. American Control Conf. (ACC 2006)*. Minneapolis, MN, USA, pp. 6–12.

Chmela, F. G., G. H. Pirker, and A. Wimmer (2007). "Zero-dimensional ROHR simulation for DI diesel engines–a generic approach". *Energy Conversion and Management* **48**:11, pp. 2942–2950.

Cho, E., K. Thoney, T. Hodgson, and R. King (2003). "Rolling horizon scheduling of multi-factory supply chains". In: *Proc. 2003 Winter Simulation Conf.* New Orleans, LA, USA, pp. 1409–1416.

Contestabile, M., G. Offer, R. Slade, F. Jaeger, and M. Thoennes (2011). "Battery electric vehicles, hydrogen fuel cells and biofuels. which will be the winner?" *Energy & Environmental Science* **4**:10, pp. 3754–3772.

Curran, H. J., P. Gaffuri, W. Pitz, and C. Westbrook (2002). "A comprehensive modeling study of iso-octane oxidation". *Combustion and Flame* **129**:3, pp. 253–280.

Dawid, H. (2005). "Long horizon versus short horizon planning in dynamic optimization problems with incomplete information". *Economic Theory* **25**:3, pp. 575–597.

Dec, J. E. (1997). *A Conceptual Model of DI Diesel Combustion based on Laser-Sheet Imaging*. SAE Technical Paper 970873.

DelVescovo, D., S. Kokjohn, and R. Reitz (2016). "The development of an ignition delay correlation for PRF fuel blends from PRF0 (n-heptane) to PRF100 (iso-octane)". *SAE Int. J. Engines* **9**:1, pp. 520–535.

des Constructeurs d'Automobiles, Organisation Internationale (2017). *Production statistics*. URL: `http://www.oica.net/category/production-statistics/2017-statistics/` (visited on 2018).

Dober, G., S. Tullis, G. Greeves, N. Milovanovic, M. Hardy, and S. Zuelch (2008). *The Impact of Injection Strategies on Emissions Reduction and Power Output of Future Diesel Engines*. SAE Technical Paper 2008-01-0941.

Douaud, A. and P. Eyzat (1978). *Four-Octane-Number Method for Predicting the Anti-Knock Behavior of Fuels and Engines*. SAE Technical Paper 780080.

Egnell, R. (2001). *On Zero-Dimensional Modelling of Combustion and NOx formation in diesel engines*. PhD thesis. Dept. Heat and Power Engineering, Lund University, Lund, Sweden.

Eichmeier, J., U. Wagner, and U. Spicher (2012). “Controlling gasoline low temperature combustion by diesel micro pilot injection”. *J. Eng. for Gas Turbines and Power* **134**:7.

Ekholm, K., M. Karlsson, P. Tunestål, R. Johansson, B. Johansson, and P. Strandh (2008a). “Ethanol-diesel fumigation in a multi-cylinder engine”. *SAE Int. J. Fuels and Lubricants* **1**, pp. 26–36.

Ekholm, K., M. Karlsson, P. Tunestål, R. Johansson, B. Johansson, and P. Strandh (2008b). “Ethanol-diesel fumigation in a multi-cylinder engine”. *SAE Int. J. Fuels Lubricants* **1**, pp. 26–36.

Enkvist, P., T. Nauclér, and J. Rosander (2007). “A cost curve for greenhouse gas reduction”. *McKinsey Quarterly* **1**, p. 34.

Epping, K., S. Aceves, R. Bechtold, and J. E. Dec (2002). *The Potential of HCCI Combustion for High Efficiency and Low Emissions*. SAE Technical Paper 2002-01-1923.

Eriksson, L. (1998). *Requirements for and a Systematic Method for Identifying Heat-Release Model Parameters*. SAE Technical Paper 980626.

Eriksson, L. and L. Nielsen (2014). *Modeling and Control of Engines and Drivelines*. John Wiley & Sons, Chichester, West Sussex, England.

Eriksson, L. and M. Sivertsson (2016). “Calculation of optimal heat release rates under constrained conditions”. *SAE Int. J. Engines* **9**:2, pp. 1143–1162.

Eriksson, L. and A. Thomasson (2017). “Cylinder state estimation from measured cylinder pressure traces-a survey”. *IFAC-PapersOnLine* **50**:1, pp. 11029–11039.

European Commission (2016). *A European Strategy for Low-Emission Mobility. COM(2016) 501*. Brussels, Belgium.

European Union (2007). “Cleaner trucks and buses: tighter limits for nitrogen oxides and particulate matter (Euro VI).” *Press release, IP/07/1989*.

Fenimore, C. (1971). “Formation of nitric oxide in premixed hydrocarbon flames”. In: *Proc. Int. Symposium on Combustion*. Vol. 13. 1. Pittsburgh, PA, pp. 373–380.

Fieweger, K., R. Blumenthal, and G. Adomeit (1997). “Self-ignition of SI engine model fuels: a shock tube investigation at high pressure”. *Combustion and Flame* **109**:4, pp. 599–619.

Fiveland, S. B. and D. N. Assanis (2001). *Development of a two-zone HCCI combustion model accounting for boundary layer effects*. SAE Technical Paper 2001-01-1028.

Fridriksson, H., B. Sundén, S. Hajireza, and M. Tunér (2011). *CFD Investigation of Heat Transfer in a Diesel Engine with Diesel and PPC Combustion Modes*. SAE Technical Paper 2011-01-1838.

Garpinger, O. and T. Hägglund (2015). "Software-based optimal PID design with robustness and noise sensitivity constraints". *J. Process Control* **33**, pp. 90–101.

Gatowski, J., E. N. Balles, K. Chun, F. Nelson, J. Ekchian, and J. B. Heywood (1984). *Heat Release Analysis of Engine Pressure Data.* SAE Technical Paper 841359.

Geisser, S. (1993). *Predictive Inference.* Chapman & Hall, New York, NY, USA.

Gieshoff, J., A. Schäfer-Sindlinger, P. Spurk, J. Van Den Tillaart, and G. Garr (2000). *Improved SCR Systems for Heavy Duty Applications.* SAE Technical Paper 2000-01-0189.

Gong, J. and C. Rutland (2013). *A Quasi-Dimensional NOx Emission Model for Spark Ignition Direct Injection (SIDI) Gasoline Engines.* SAE Technical Paper 2013-01-1311.

Gordon, N. J., D. J. Salmond, and A. F. Smith (1993). "Novel approach to nonlinear/non-Gaussian Bayesian state estimation". In: *IEE Proc. F Radar and Signal Processing.* Vol. 140. 2, pp. 107–113.

Grahn, M., K. Johansson, and T. McKelvey (2014). "A transient diesel EMS strategy for online implementation". In: *Proc. IFAC Volumes.* Vol. 47. 3. Cape Town, South Africa, pp. 11842–11847.

Guardiola, C., B. Pla, A. Garcia, and V. Boronat (2017). "Optimal heat release shaping in a reactivity controlled compression ignition (RCCI) engine". *Control Theory and Technology* **15**:2, pp. 117–128.

Guzzella, L. and C. Onder (2009). *Introduction to Modeling and Control of Internal Combustion Engine Systems.* Springer-Verlag, Berlin, Germany.

Haagen-Smit, A. (1952). "Chemistry and physiology of Los Angeles smog". *Industrial & Eng. Chemistry* **44**:6, pp. 1342–1346.

Hafner, M., M. Schüler, O. Nelles, and R. Isermann (2000). "Fast neural networks for diesel engine control design". *Control Eng. Practice* **8**:11, pp. 1211–1221.

Halstead, M., L. Kirsch, A. Prothero, and C. Quinn (1975). "A mathematical model for hydrocarbon autoignition at high pressures". In: *Proc. Royal Society of London A: Mathematical, Physical and Eng. Sciences.* Vol. 346. 1647, pp. 515–538.

Halstead, M., L. Kirsch, and C. Quinn (1977). "The autoignition of hydrocarbon fuels at high temperatures and pressures—Fitting of a mathematical model". *Combustion and Flame* **30**, pp. 45–60.

Han, J.-S., P.-H. Lu, X.-B. Xie, M.-C. Lai, and N. A. Henein (2002). *Investigation of Diesel Spray Primary Break-Up and Development for Different Nozzle Geometries.* SAE Technical Paper 2002-01-2775.

Han, Z., A. Uludogan, G. J. Hampson, and R. D. Reitz (1996). *Mechanism of Soot and NOx Emission Reduction using Multiple-Injection in a Diesel Engine.* SAE Technical Paper 960633.

Hanson, R. M., S. L. Kokjohn, D. A. Splitter, and R. D. Reitz (2010). “An experimental investigation of fuel reactivity controlled PCCI combustion in a heavy-duty engine”. *SAE Int. J. Engines* **3**:1, pp. 700–716.

Haraldsson, G. (2005). *Closed-loop Combustion Control of a Multi Cylinder HCCI Engine using Variable Compression Ratio and Fast Thermal Management.* TMHP–05/1028. PhD thesis. Dept. of Heat and Power Engineering, Lund University, Lund, Sweden.

Haraldsson, G., P. Tunestål, B. Johansson, and J. Hyvönen (2002). *HCCI Combustion Phasing in a Multi Cylinder Engine using Variable Compression Ratio.* SAE Technical Paper 2002-01-2858.

Hasegawa, R. and H. Yanagihara (2003). *HCCI Combustion in DI Diesel Engine.* SAE Technical Paper 2003-01-0745.

Hast, M., K. Åström, B. Bernhardsson, and S. Boyd (2013). “PID design by convex-concave optimization”. In: *Proc. European Control Conf. (ECC 2013).* Zürich, Switzerland, pp. 4460–4465.

Hellström, E., D. Lee, L. Jiang, A. G. Stefanopoulou, and H. Yilmaz (2013). “On-board calibration of spark timing by extremum seeking for flex-fuel engines”. *IEEE Trans. Control Systems Technology* **21**:6, pp. 2273–2279.

Hendricks, E. (1986). *A Compact, Comprehensive Model of Large Turbocharged, Two-Stroke Diesel Engines.* SAE Technical Paper 861190.

Henningsson, M. (2012). *Data-Rich Multivariable Control of Heavy-Duty Engines.* PhD thesis TFRT-1092. Dept. Automatic Control, Lund University, Lund, Sweden.

Henningsson, M., K. Ekholm, P. Strandh, P. Tunestål, and R. Johansson (2012). “Dynamic mapping of diesel engine through system identification”. In: D. Alberer H. Hjalmarsson, L. (Ed.). *Identification for Automotive Systems.* Springer, London, England, pp. 223–239.

Heywood, J. B. (1988). *Internal Combustion Engine Fundamentals.* McGraw-Hill, New York, NY, USA.

Hildingsson, L., G. Kalghatgi, N. Tait, B. Johansson, and A. Harrison (2009). *Fuel Octane Effects in the Partially Premixed Combustion Regime in Compression Ignition Engines.* SAE Technical Paper 2009-01-2648.

Hohenberg, G. F. (1979). *Advanced Approaches for Heat Transfer Calculations.* SAE Technical Paper 790825.

Honardar, S., H. Busch, T. Schnorbus, C. Severin, A. F. Kolbeck, and T. Korfer (2011). “Exhaust temperature management for diesel engines assessment of engine concepts and calibration strategies with regard to fuel penalty”. In: *Proc. 10th Int. Conf. Engines Vehicles.*

Iorio, B., V. Gioglio, G. Police, and N. Rispoli (2003). *Methods of Pressure Cycle Processing for Engine Control.* SAE Technical Paper 2003-01-0352.

IPCC (2014). "Climate change 2014, synthesis report". *IPCC Fifth Assessment Report*.

Isermann, R. (2014). *Engine Modeling and Control*. Springers Berlin Heidelberg, Berlin, Germany.

Johansson, B. (2006). *Förbränningsmotorer*. Institutionen för värme-och kraftteknik, Lunds Tekniska Högskola, Lund, Sweden.

Johansson, R. (1993). *System Modeling and Identification*. Prentice Hall, Englewood Cliffs, NJ, USA.

Johansson, T. B., P. Kågesson, H. Johansson, L. Jonsson, J. Westin, H. Hejenstedt, O. Hådell, K. Holmgren, and P. Wollin (2013). "Fossilfrihet på väg". *Ministry of Enterprise, SOU* **2013**:84. Stockholm, Sweden.

Jones, J. C. P. and J. Frey (2015). "Threshold optimization and performance evaluation of a classical knock controller". *SAE Int. J. Engines* **8**:3, pp. 1021–1028.

Jörg, C., T. Schnorbus, S. Jarvis, B. Neaves, K. Bandila, and D. Neumann (2015). "Feedforward control approach for digital combustion rate shaping realizing predefined combustion processes". *SAE Int. J. Engines* **8**:2015-01-0876, pp. 1041–1054.

Julier, S. J. and J. K. Uhlmann (2004). "Unscented filtering and nonlinear estimation". *Proc. IEEE* **92**:3, pp. 401–422.

Jury, E. I. (1964). "Theory and application of the Z-transform method".

Kalghatgi, G. T., P. Risberg, and H.-E. Ångström (2006). *Advantages of Fuels with High Resistance to Auto-Ignition in Late-Injection, Low-Temperature, Compression Ignition Combustion*. SAE Technical Paper 2006-01-3385.

Källkvist, K. (2011). *Fuel Pressure Modelling in a Common-Rail Direct Injection System*. MSc Thesis LiTH-ISY-EX–11/4488–SE. Linköping University, Dept. of Electrical Engineering, Linköping, Sweden.

Kalman, R. (1959). "On the general theory of control systems". *IRE Trans. Automatic Control* **4**:3, pp. 110–110.

Kalman, R. E. et al. (1960). "Contributions to the theory of optimal control". *Bol. Soc. Mat. Mexicana* **5**:2, pp. 102–119.

Kalman, R. E. (1960). "A new approach to linear filtering and prediction problems". *J. Fluids Eng.* **82**:1, pp. 35–45.

Kamimoto, T. and M.-h. Bae (1988). *High Combustion Temperature for the Reduction of Particulate in Diesel Engines*. SAE Technical Paper 880423.

Kanda, T., T. Hakozaki, T. Uchimoto, J. Hatano, N. Kitayama, and H. Sono (2005). *PCCI Operation with Early Injection of Conventional Diesel Fuel*. SAE Technical Paper 2005-01-0378.

Karlsson, M., K. Ekholm, P. Strandh, R. Johansson, and P. Tunestål (2008). "LQG control for minimization of emissions in a diesel engine". In: *Proc. IEEE Int. Conf. Control Applications (CCA 2008)*. San Antonio, TX, USA, pp. 245–250.

Karlsson, M., K. Ekholm, P. Strandh, R. Johansson, and P. Tunestål (2010). "Multiple-input multiple-output model predictive control of a diesel engine". In: *Proc. 6th IFAC Symposium Advances in Automotive Control (AAC 2010)*. Münich, Germany, pp. 131–136.

Katare, S. R. and P. M. Laing (2009). "Hydrogen in diesel exhaust: effect on diesel oxidation catalyst flow reactor experiments and model predictions". *SAE Int. J. Fuels and Lubricants* **2**:1, pp. 605–611.

Kay, S. M. (1998). *Fundamentals of Statistical Signal Processing, Vol. II: Detection Theory*. Prentice Hall, Upper Saddle River, NJ, USA.

Kiencke, U. and L. Nielsen (2000). *Automotive Control Systems. For Engine, Driveline, and Vehicle*. Springer-Verlag, Berlin.

Killingsworth, N. J., S. M. Aceves, D. L. Flowers, F. Espinosa-Loza, and M. Krstić (2009). "HCCI engine combustion-timing control: optimizing gains and fuel consumption via extremum seeking". *IEEE Trans. Control Systems Technology* **17**:6, pp. 1350–1361.

Kim, D., I. Ekoto, W. F. Colban, and P. C. Miles (2008). *In-Cylinder CO and UHC Imaging in a Light-Duty Diesel Engine During PPCI Low-Temperature Combustion*. SAE Technical Paper 2008-01-1602.

Kimura, S., O. Aoki, H. Ogawa, S. Muranaka, and Y. Enomoto (1999). *New Combustion Concept for Ultra-Clean and High-Efficiency Small DI Diesel Engines*. SAE Technical Paper 1999-01-3681.

Kitamura, T., T. Ito, J. Senda, and H. Fujimoto (2002). "Mechanism of smokeless diesel combustion with oxygenated fuels based on the dependence of the equivalence ratio and temperature on soot particle formation". *Int. J. Engine Research* **3**:4, pp. 223–248.

Klein, M. (2007). *Single-Zone Cylinder Pressure Modeling and Estimation for Heat Release Analysis of SI Engines*. Dissertation No. 1124, Department of Electrical Engineering. PhD thesis. Linköping University, Linköping, Sweden.

Klein, M., L. Eriksson, and J. Åslund (2006). "Compression ratio estimation based on cylinder pressure data". *Control Eng. Practice* **14**:3, pp. 197–211.

Kokjohn, S. L., R. M. Hanson, D. Splitter, and R. Reitz (2011). "Fuel reactivity controlled compression ignition (RCCI): a pathway to controlled high-efficiency clean combustion". *Int. J. Engine Research* **12**:3, pp. 209–226.

Kokjohn, S. L., R. M. Hanson, D. A. Splitter, and R. D. Reitz (2009). *Experiments and Modeling of Dual-Fuel HCCI and PCCI Combustion using in-Cylinder Fuel Blending*. SAE Technical Paper 2009-01-2647.

Kook, S., C. Bae, P. C. Miles, D. Choi, and L. M. Pickett (2005). *The Influence of Charge Dilution and Injection Timing on Low-Temperature Diesel Combustion and Emissions*. SAE Technical Paper 2005-01-3837.

Krieger, R. and G. Borman (1966). “The computation of apparent heat release in IC engines”. *ASME Series* **66**.

Lee, H., Y. Park, S. Hong, M. Lee, and M. Sunwoo (2013). *EGR Rate Estimation for Cylinder Air Charge in a Turbocharged Diesel Engine using an Adaptive Observer*. SAE Technical Paper 2013-01-0246.

Leen, G. and D. Heffernan (2002). “Expanding automotive electronic systems”. *Computer* **35**:1, pp. 88–93.

Lewander, M., B. Johansson, P. Tunestål, N. Keeler, N. Milovanovic, and P. Bergstrand (2008). “Closed loop control of a partially premixed combustion engine using model predictive control strategies”. In: *Proc. of AVEC*. Vol. 8. Kobe, Japan.

Lewander, M., A. Widd, B. Johansson, and P. Tunestål (2012). “Steady state fuel consumption optimization through feedback control of estimated cylinder individual efficiency”. In: *Proc. American Control Conf. (ACC 2012)*. Fairmont Queen Elizabeth, Montreal, Canada, pp. 4210–4214.

Li, C., L. Yin, S. Shamun, M. Tunér, B. Johansson, R. Solsjö, and X.-S. Bai (2016). “Transition from HCCI to PPC: the sensitivity of combustion phasing to the intake temperature and the injection timing with and without EGR”. *SAE Technical Paper 0767*.

Livengood, J. and P. Wu (1955). “Correlation of autoignition phenomena in internal combustion engines and rapid compression machines”. In: *Proc. Int. Symposium Combustion*. Vol. 5. 1. Reinhold, NY, USA, pp. 347–356.

Lönn, S., A. Matamis, M. Tunér, M. Richter, and Ö. Andersson (2017). *Optical Study of Fuel Spray Penetration and Initial Combustion Location under PPC Conditions*. SAE Technical Paper 2017-01-0752.

Lu, T. and C. K. Law (2009). “Toward accommodating realistic fuel chemistry in large-scale computations”. *Progress in Energy and Combustion Science* **35**:2, pp. 192–215.

Maciejowski, J. M. (2002). *Predictive Control: with Constraints*. Pearson Education, Essex, England.

MacMillan, D., A. La Rocca, P. Shayler, T. Morris, M. Murphy, and I. Pegg (2009). “Investigating the effects of multiple injections on stability at cold idle for a DI diesel engine”. *SAE Int. J. Engines* **2**:1.

Majewski, W. A. and M. K. Khair (2006). *Diesel Emissions and their Control*. SAE International, Warrendale, PA, USA.

Manente, V., B. Johansson, and P. Tunestål (2009). *Partially Premixed Combustion at High Load using Gasoline and Ethanol, a Comparison with Diesel*. SAE Technical Paper 2009-01-0944.

Manente, V., B. Johansson, and P. Tunestål (2010a). "Characterization of partially premixed combustion with ethanol: EGR sweeps, low and maximum loads". *J. Eng. for Gas Turbines and Power-Transactions ASME* **132**:8.

Manente, V., P. Tunestål, B. Johansson, and W. J. Cannella (2010b). *Effects of Ethanol and Different Type of Gasoline Fuels on Partially Premixed Combustion from Low to High Load*. SAE Technical Paper 2010-01-0871.

Manente, V., A. Vressner, P. Tunestål, and B. Johansson (2008). *Validation of a Self Tuning Gross Heat Release Algorithm*. SAE Technical Paper 2008-01-1672.

Manente, V., C.-G. Zander, B. Johansson, P. Tunestål, and W. Cannella (2010c). *An Advanced Internal Combustion Engine Concept for Low Emissions and High Efficiency from Idle to Max Load using Gasoline Partially Premixed Combustion*. SAE Technical Paper 2010-01-2198.

Martinez-Frias, J., S. M. Aceves, D. Flowers, J. R. Smith, and R. Dibble (2000). *HCCI Engine Control by Thermal Management*. SAE Technical Paper 2000-01-2869.

McKinsey & Company (2014). *Electric Vehicles in Europe: Gearing up for a new phase*. Technical Report.

Meyer, J. (2011). *Calibration reduction in internal combustion engine fueling control: modeling, estimation and stability robustness*. PhD thesis. The Ohio State University.

Miller, J. A. and C. T. Bowman (1989). "Mechanism and modeling of nitrogen chemistry in combustion". *Progress in Energy and Combustion Science* **15**:4, pp. 287–338.

Murić, K., O. Stenlåås, and P. Tunestål (2014). "Zero-dimensional modeling of NOx formation with least squares interpolation". *Int. J. Engine Research* **15**:8, pp. 944–953.

Musculus, M. P. (2006). *Multiple Simultaneous Optical Diagnostic Imaging of Early-Injection Low-Temperature Combustion in a Heavy-Duty Diesel Engine*. SAE Technical Paper 2006-01-0079.

Nagatsu, K., A. Inoue, K. Matsumoto, T. Kaminaga, T. Miyamoto, and T. Youso (2017). *Control device for compression ignition-type engine*. US Patent 9,719,441.

Nilsson, Y. and L. Eriksson (2001). "A new formulation of multi-zone combustion engine models". *IFAC Proc. Volumes* **34**:1, pp. 357–362.

Noehre, C., M. Andersson, B. Johansson, and A. Hultqvist (2006). *Characterization of Partially Premixed Combustion*. SAE Technical Paper 2006-01-3412.

Okamoto, T. and N. Uchida (2016). "New concept for overcoming the trade-off between thermal efficiency, each loss and exhaust emissions in a heavy duty diesel engine". *SAE Int. J. Engines* **9**:2, pp. 859–867.

Olsson, J.-O., P. Tunestål, G. Haraldsson, and B. Johansson (2001). "A turbocharged dual-fuel HCCI engine". *SAE Special Publications* **2001**:1627.

Olsson, J.-O., P. Tunestål, and B. Johansson (2004). *Boosting for High Load HCCI*. SAE Technical Paper 2004-01-0940.

Onishi, S., S. H. Jo, K. Shoda, P. Do Jo, and S. Kato (1979). *Active Thermo-Atmosphere Combustion (ATAC)-a New Combustion Process for Internal Combustion Engines*. SAE Technical paper, 790501.

Osuka, I., M. Nishimura, Y. Tanaka, and M. Miyaki (1994). *Benefits of new Fuel Injection System Technology on Cold Startability of Diesel Engines-Improvement of Cold Startability and White Smoke Reduction by Means of Multi Injection with Common Rail Fuel System ECD-U2*. SAE Technical Paper 940586.

Ott, T., F. Zurbriggen, C. H. Onder, and L. Guzzella (2013). "Cylinder individual feedback control of combustion in a dual fuel engine". In: *Advances in Automotive Control (ACC 2013)*. Vol. 7. 1. Tokyo, Japan, pp. 600–605.

Powell, J. D. (1993). "Engine control using cylinder pressure: past, present, and future". *J. Dynamic Systems, Measurements, and Control* **115**:2B, pp. 343–350.

Randolph, A. L. (1990). *Methods of Processing Cylinder-Pressure Transducer Signals to Maximize Data Accuracy*. SAE Technical Paper 900170.

Rassweiler, G. M. and L. Withrow (1938). *Motion Pictures of Engine Flames Correlated with Pressure Cards*. SAE Technical Paper 380139.

Roelle, M. J., N. Ravi, A. F. Jungkunz, and J. C. Gerdes (2006). "A dynamic model of recompression HCCI combustion including cylinder wall temperature". In: *Proc. IMECE*. Chicago, IL, USA, pp. 415–424.

Saracino, R., M. R. Gaballo, S. Mannal, S. Motz, A. Carlucci, and M. Benegiamo (2015). *Cylinder Pressure-Based Closed Loop Combustion Control: A Valid Support to Fulfill Current and Future Requirements of Diesel Powertrain Systems*. SAE Technical Paper 2015-24-2423.

Shaver, G. M., J. C. Gerdes, and M. Roelle (2004). "Physics-based closed-loop control of phasing, peak pressure and work output in HCCI engines utilizing variable valve actuation". In: *Proc. American Control Conf. (ACC 2004)*. Vol. 1. Boston, MA, USA, pp. 150–155.

Sher, E. (1998). *Handbook of Air Pollution from Internal Combustion Engines: Pollution Formation and Control*. Academic Press, San Diego, CA, USA.

Shi, Y., H.-W. Ge, and R. D. Reitz (2011). *Computational Optimization of Internal Combustion Engines*. Springer Science & Business Media, London, England.

Sjöberg, M. and J. E. Dec (2005). "An investigation into lowest acceptable combustion temperatures for hydrocarbon fuels in HCCI engines". *Proc. Combustion Institute* **30**:2, pp. 2719–2726.

Solaka, H., U. Aronsson, M. Tunér, and B. Johansson (2012). *Investigation of Partially Premixed Combustion Characteristics in Low Load Range with Regards to Fuel Octane Number in a Light-Duty Diesel Engine*. SAE Technical Paper 2012-01-0684.

Solsjö, R. (2014). *Large Eddy Simulation of Turbulent Combustion in PPC and Diesel Engines*. PhD thesis TMHP-14/1107, Dept. Energy Sciences. PhD thesis. Lund University, Lund, Sweden.

Spadaccini, L. J. and J. A. Tevelde (1982). "Autoignition characteristics of aircraft-type fuels". *Combustion and Flame* **46**, pp. 283–300.

Sperling, D. and D. Gordon (2009). *Two Billion Cars: Driving Toward Sustainability*. Oxford University Press, New York, NY, USA.

Stas, M. J. (1996). *Thermodynamic Determination of TDC in Piston Combustion Engines*. SAE Technical Paper 960610.

Stewart, G. and F. Borrelli (2008). "A model predictive control framework for industrial turbodiesel engine control". In: *Proc. Conf. Decision and Control*. Cancun, Mexico, pp. 5704–5711.

Szekely, G. A., A. S. Solomon, and P.-H. Tsai (2004). *Optimization of the Stratified-Charge Regime of the Reverse-Tumble Wall-Controlled Gasoline Direct-Injection Engine*. SAE Technical Paper 2004-01-0037.

Takeda, Y. and N. Keiichi (1996). *Emission Characteristics of Premixed Lean Diesel Combustion with Extremely Early Staged Fuel Injection*. SAE Technical Paper 961163.

Tanov, S., R. Collin, B. Johansson, and M. Tunér (2014). "Combustion stratification with partially premixed combustion, PPC, using NVO and split injection in a LD-diesel engine". *SAE Int. J. Engines* **7**:4, pp. 1911–1919.

Tsurushima, T., E. Kunishima, Y. Asaumi, Y. Aoyagi, and Y. Enomoto (2002). *The Effect of Knock on Heat Loss in Homogeneous Charge Compression Ignition Engines*. SAE Technical Paper 2002-01-0108.

Tunestål, P. (2011). "TDC offset estimation from motored cylinder pressure data based on heat release shaping". *Oil & Gas Science and Technology–Revue d'IFP Energies nouvelles* **66**:4, pp. 705–716.

Tunestål, P., J. K. Hedrick, and R. Johansson (2001). "Model-based estimation of cylinder pressure sensor offset using least-squares methods". In: *Proc. Conf. Decision and Control*. Vol. 4. Orlando, FL, USA, pp. 3740–3745.

Turns, S. R. et al. (1996). *An Introduction to Combustion*. McGraw-Hill, New York, NY, USA.

Wahlström, J. and L. Eriksson (2011). "Modelling diesel engines with a variable-geometry turbocharger and exhaust gas recirculation by optimization of model parameters for capturing non-linear system dynamics". *Proc. Inst. Mech. Eng., Part D: J. Automobile Eng.* **225**:7, pp. 960–986.

Wang, Y. and S. Boyd (2010). "Fast model predictive control using online optimization". *IEEE Trans. Control Systems Technology* **18**:2, pp. 267–278.

Weall, A. and N. Collings (2009). *Gasoline Fuelled Partially Premixed Compression Ignition in a Light Duty Multi Cylinder Engine: a Study of Low Load and Low Speed Operation.* SAE Technical Paper 2009-01-1791.

Westbrook, C. K. and F. L. Dryer (1981). “Simplified reaction mechanisms for the oxidation of hydrocarbon fuels in flames”. *Combustion Science and Technology* **27**:1-2, pp. 31–43.

Widd, A., K. Ekholm, P. Tunestål, and R. Johansson (2009). “Experimental evaluation of predictive combustion phasing control in an HCCI engine using fast thermal management and VVA”. In: *Proc. Control Applications & Intelligent Control.* Saint Petersburg, Russia, pp. 334–339. DOI: 10.1109/CCA.2009.5281087.

Widd, A., P. Tunestål, J. Åkesson, and R. Johansson (2012). “Single-zone diesel PPC modeling for control”. In: *Proc. American Control Conf. (ACC 2012).* Montréal, Canada, pp. 5731–5736.

Widd, A., P. Tunestål, and R. Johansson (2008). “Physical modeling and control of homogeneous charge compression ignition HCCI engines”. In: *Proc. Conf. Decision and Control.* Cancun, Mexico, pp. 5615–5620.

Wiebe, I. I. (1970). *Brennverlauf und Kreisprozess von Verbrennungsmotoren.* VEB Verlag Technik, Berlin, Germany.

Willems, F., E. Doosje, F. Engels, and X. Seykens (2010). *Cylinder Pressure-Based Control in Heavy-Duty EGR Diesel Engines using a Virtual Heat Release and Emission Sensor.* SAE Technical Paper 2010-01-0564.

Woshni, G. (1967). *A Universally Applicable Equation for the Instantaneous Heat Transfer Coefficient in the Internal Combustion Engine.* SAE Technical Paper 670931.

Yang, T., L. Yin, G. Ingesson, P. Tunestål, R. Johansson, and W. Long (2017). “Simultaneous control of soot emissions and pressure rise rate in gasoline PPC engine”. In: *Proc. IEEE Conf. Control Technology and Applications (CCTA 2017).* Hawaii, USA, pp. 572–577.

Yin, L., G. Ingesson, S. Shamun, P. Tunestål, R. Johansson, and B. Johansson (2015). *Sensitivity Analysis of Partially Premixed Combustion (PPC) for Control Purposes.* SAE Technical Paper 2015-01-0884.

Zeldovich, Y. B., P. Y. Sadovnikov, and D. A. Frank-Kamenetskii (1947). *Oxidation of Nitrogen in Combustion.* Academy of Sciences of USSR, Institute of Chemical Physics, Moscow-Leningrad.

Zheng, M., G. T. Reader, D. Wang, J. Zuo, R. Kumar, M. C. Mulenga, U. Asad, D. S. Ting, and M. Wang (2005). *A Thermal Response Analysis on the Transient Performance of Active Diesel Aftertreatment.* SAE Technical Paper 2005-01-3885.

Zhou, K. and J. C. Doyle (1998). *Essentials of Robust Control.* Vol. 104. Prentice Hall, Upper Saddle River, NJ, USA.

Zweigel, R., F. Thelen, D. Abel, and T. Albin (2015). “Iterative learning approach for diesel combustion control using injection rate shaping”. In: *Proc. European Control Conf. (ECC 2015)*, pp. 3168–3173.

Videos

Videos showing cycle-resolved data for some of the experiments presented are available in the entry for this thesis in the Lund University Research Portal: `http://portal.research.lu.se/portal/`

These videos are also available on the author's youtube channel:
`https://www.youtube.com/channel/UCCsMeCRDrzoJF_wm41X1xuA`

Videos of in-cylinder data aid understanding of the controller behavior and can be used as a complement to the figures presented in the thesis. The videos present data from the following experiments:

- Closed-loop θ_{50} and τ experiments in Chapter 7.
- dp_{max}-controller experiments in Chapter 8.
- A comparison between the low-load controllers in Chapter 9.
- Constraint-fulfillment experiments in Chapters 10 and 12.
- Pressure-tracking experiments in Chapter 12.